CHARLES UNIVERSITY PRAGUE

faculty of mathematics and physics

INTERACTING GALAXIES
MAGELLANIC CLOUDS AND MILKY WAY

Thesis submitted for the degree of Philosophiae Doctor

Adam Růžička

Supervisor: Prof. RNDr. Jan Palouš, DrSc.

Prague, June 2006

To my parents

CONTENTS

PREFACE

This thesis focuses on the dynamical evolution of the Milky Way–Large Magellanic Cloud (LMC)–Small Magellanic Cloud (SMC) group. We perform an analysis of the parameter space for the interaction of the Magellanic System with the Milky Way. The studied parameters cover the phase space parameters, the masses, the structure and the orientation of both Magellanic Clouds as well as the flattening of the dark matter halo of the Milky Way. The analysis is done by a specially adopted optimization code searching for a best match between numerical models and the detailed H I map of the Magellanic System. Unique high–resolution H I survey of the entire Magellanic System provides detailed information about the kinematics and morphology of the Magellanic Clouds. We use the data to compare the extended H I structures of both LMC and SMC (Magellanic Stream, Leading Arm) to our numerical model of the Magellanic System evolving in an extended dark matter halo of the Milky Way. The applied search algorithm is a genetic algorithm (GA) combined with a code based on the fast restricted N–body method. By this, we are able to analyze more than 10^6 models which makes this study one of the most extended ones for the Magellanic System.

I would like to thank to my supervisor, Jan Palouš, and to my adviser, Christian Theis, for all their helpful advice, useful ideas and pertinent comments on this work and my research. I also wish to thank Christian Brüns who kindly provided excellent observational data. Many thanks go to everyone whom I worked with at the Astronomical Institute of the Academy of Sciences for their valuable contributions to this project. I gratefully acknowledge the support by the Czech–Austrian cooperation scheme AKTION (funded by the Austrian Academic Exchange Service ÖAD and by the program Kontakt of the Ministery of Education of the Czech Republic) under grant A–13/2005, by the grant of the Fulbright Commission in the Czech Republic, by the Institutional Research Plan AV0Z10030501 of the Academy of Sciences of the Czech Republic and by the project LC06014 Center for Theoretical Astrophysics.

INTRODUCTION

Galaxies are systems of gravitationally bound stars, interstellar medium and dark matter showing considerably complex dynamics. A large number of observational surveys of deep-sky objects denote that galaxies generally tend to form larger configurations. Interacting pairs, galactic groups, clusters and super clusters cover a wide range of masses and dimensions. Thus, one may suggest that encounters and collisions play a significant role in the process of evolution of members of these systems. Such a hypothesis is supported by numerous observations bringing a clear evidence for existence of various types of extended galactic bridges, tails and asymmetrical arm–like structures that can only hardly be products of internal dynamical evolution of an isolated galaxy. Furthermore, some observed galactic pairs are in the phase of a violent interaction or merger.

Modeling of galactic evolution, interactions and mergers shows that they lead to a substantial energy, mass and angular momentum redistribution. Significant changes in structure and distortion of original shapes are apparent consequences of such processes (see TOOMRE & TOOMRE, 1972). Because of quite a complex nature of galactic dynamics, theoretical approaches are based on methods of numerical mathematics employed in computational models, since analytic solutions to such problems would suffer from unavoidable simplification of the description of explored systems. Even though numerical models are processed by powerful computers, approximations always have to be accepted for the description of real physical systems. Under such circumstances we are constrained to test quality and efficiency of our models by comparing theoretical results with numerical simulations and observationally obtained data. Solution to a given problem of dynamics of a galactic system cannot be obtained without determination of initial conditions and parameters for the model. Hence, it can be easily inferred that knowledge in current values of dynamical quantities of the studied galactic system is a basic presumption for its successful numerical modeling. A large amount of observational data has been collected for some galactic groups. In principle, this wealth of information should be sufficient to define the history of the interaction or to draw conclusions on the structure. Unfortunately, observations are affected by extreme intergalactic distances and so exact measurements of physical parameters are usually substituted by estimates. Moreover, models of interactions between galaxies depend on a large number of free parameters and it is very difficult to find their right set if we want to process a detailed analysis with reliable results. Thus, it is not surprising that a relatively small number of papers focus on simulations of real observed galactic systems.

It can be seen that a detailed exploration of the parameter space is a basic presumption for successful modeling of interacting galaxies. We need an optimization tool offering an efficient search strategy to find a good solution for the simulated galactic system. Obviously, such a search demands a very fast numerical model of the investigated galactic system to explore the parameter space properly within a reasonable time interval. In this respect, it was proposed by THEIS (1999) to employ *genetic algorithms* together with a *restricted N-body model* as a very powerful and general optimization scheme for galactic dynamics of interacting systems.

A remarkable amount of observational data has been collected for the Local Group (VAN DEN BERGH, 2000) and mainly for the Large Magellanic Cloud and Small Magellanic Cloud - dwarf galactic satellites of the Milky Way (MW). However, these data also allowed only for an estimate of important physical parameters necessary for building up the proper numerical model. To overcome such a complication most of the previous studies to this galactic system (see MURAI & FUJIMOTO, 1980; LIN & LYNDEN-BELL, 1982; GARDINER ET AL., 1994, 1996) adopted some assumptions on the orbital and other parameters of the MW–LMC–SMC system. Such considerations were based on observational data but no detailed parameter space search was performed.

We investigate the dynamical evolution of the MW–LMC–SMC system and perform the first detailed analysis of the entire parameter space of the interaction. A very precise, high-resolution neutral hydrogen (H I) survey of the Magellanic System (see BRÜNS ET AL., 2005) was available, becoming a unique challenge for a GA–based search for the preferred evolutionary scenario of the galactic system. Such an investigation can be performed using the observational H I data for detailed comparison and evaluation of the series of numerical models. Quality of the model corresponding to the given set of parameters has to be evaluated by comparing its output to known morphological features of the galactic objects. To avoid artificial assumptions on the LMC and SMC orbital parameters, the spatial velocities and position vectors are restricted by accessible astrometric measurements (see e.g. JONES ET AL., 1994; KROUPA & BASTIAN, 1997; KALLIVAYALIL ET AL., 2006A,B). Typically, the GA approach is limited by the insufficient information provided by the observational data. Fortunately, this is not the case of LMC and SMC. For these galaxies, a large number of detailed surveys have been performed allowing for constraints on their structure, kinematics, and the distribution of matter.

We propose a project focusing on numerical modeling the dynamical evolution of the Magellanic System, based on automated search of the entire parameter space of the MW–LMC–SMC interaction. The study comprises several steps, that are reviewed and discussed in this thesis.

The dwarf galaxies LMC and SMC are introduced In Chapter 1. We focus on observations comprising both gaseous and stellar components of the Clouds. Special attention is paid to the results of H I surveys of the entire Magellanic System, because the corresponding data provide the crucial information about the kinematics and morphology of the Clouds on various scales. Chapter 2 clarifies and summarizes the specific problems of modeling observed galactic systems. It also offers an extended review of previous attempts to model the evolution of the Magellanic System. The adopted numerical model of the galactic interaction is discussed in Chapter 3. Since the GA search process demands

10^4 runs of the optimized model typically, a very fast numerical code is desired for such a task. Thus, the 3 D test–particle model of the LMC–SMC interaction gravitationally influenced by the MW devised by MURAI & FUJIMOTO (1980) and GARDINER ET AL. (1994) was improved. Chapter 4 introduces the parameter space of the interaction between the Magellanic Clouds and MW. We discuss the specific choices for each of the parameters involved. Chapter 5 explains the general scheme and principles of GA. Also the application of GA to the problem of a galactic interaction made by THEIS & KOHLE (2001) is briefly introduced in order to demonstrate the abilities of GA with respect to astrophysical problems. Finally, we describe our implementation of GA based on the *GAlib* library of various GA components developed by WALL (1996) in Chapter 5. Using the H I observations by BRÜNS ET AL. (2005) and the current velocity and position vector estimates for LMC and SMC, we perform numerous GA runs to search the extended parameter space and verify the uniqueness of obtained solutions. However, the GA optimization is very sensitive to the choice for the comparison method between the models and observations. The work by THEIS & KOHLE (2001) clearly demonstrated that GAs might fail if important features of the investigated system are omitted. To avoid such complications, the GA has to be customized for the purposes of this specific task which is the topic of Chapter 6. The same chapter also discusses the results of GA search of the parameter space with respect to the quality (fitness) of the corresponding models. Chapters 7 and 8 offer a detailed analysis of the influence of various parameters on the evolution of the Magellanic System. We showed a crucial role of the spatial velocities of the Clouds on the distribution of matter in the Magellanic System, and the corresponding results are introduced in Chapter 7. Finally, we introduce our findings concerning the shape of the dark matter halo of Galaxy (Chapter 8), that was also a free parameter of the MW–LMC–SMC interaction. A discussion of the desirable future improvements and extensions of our study is offered at the end of the thesis (Chapter "Summary and Future Prospects").

CHAPTER 1

Magellanic Clouds

The aim of this chapter is to provide a brief review of our present knowledge in the dwarf galactic neighbors of the Milky Way named the Large Magellanic Cloud and the Small Magellanic Cloud. We concentrate on their internal structure, on the composition and distribution of interstellar matter and on stellar component of both the Clouds. The Large Magellanic Cloud is the largest and brightest galaxy in the plane of sky, situated on the southern hemisphere. Because of its proximity ($D \simeq 50\,\mathrm{kpc}$) the stellar content can be studied in more detail than that of any other external galaxy and the same remains valid if we concentrate on SMC. That is the reason for our choice of both LMC and SMC to be the subjects of the exploration.

The Large Cloud belongs to the barred sub–type of Hubble's irregular class. Its classification is Ir III–IV, i.e. it has a morphology intermediate between that of giant (III) and sub–giant (IV) galaxies. Based on the presence of a faint streamer of nebulosity that extends from $(\alpha, \delta) = (5^h, -73^\circ)$ to $(\alpha, \delta) = (3.5^h, -55^\circ)$ LMC has often been described as a late–type spiral. However, this spiral arm–like feature actually appears to be a faint streamer of galactic foreground nebulosity. Furthermore, published star counts show no evidence for a statistically significant number of stars being associated with this "spiral arm" (VAN DEN BERGH, 2000). The Large Magellanic Cloud is a disc that is seen almost pole–on. According to LIN & LYNDEN–BELL (1982) $i = 27^\circ \pm 7^\circ$ and $p = 170^\circ \pm 10^\circ$. From the wide–field imaging of LMC (see VAN DEN BERGH, 2000) the disc scale–length of $101' \pm 3'$ (1.5 kpc) was found. Asymmetrically embedded within this disc is a bar with a length of $\sim 3^\circ$. Bar is mainly outlined by intermediate–age stars, while young clusters and associations are mostly located in the outer disc.

The Small Magellanic Cloud is an irregular dwarf of type Ir IV–V that has a low mean metallicity and a high mass fraction remaining in gaseous form. This suggests that SMC is, from an evolutionary point of view, a more primitive and less evolved galaxy than LMC. At the present time SMC is forming stars less actively than LMC. It can be seen from the fact that LMC presently contains 110 Wolf–Rayet (WR) stars, while there are only 9 WR stars in SMC (VAN DEN BERGH, 2000). The main body (bar[1]) of SMC has $i = 60° \pm 15°$ and $p = 45° \pm 5°$. However, these inclination and position angle are not reliable if the space orientation of SMC "disk" is needed. Thus in our model introduced in following chapters, we have relied on the theoretically obtained data given by GARDINER ET AL. (1996). According to VAN DEN BERGH (2000) SMC disk scale–length has possible values ranging from 51' to 76'. The intrinsic shape of SMC remains unambiguous. Observations of the distances to Cepheids by CALDWELL & LANEY (1991) indicated that SMC has a large depth along the line of sight. The results of GARDINER & HAWKINS (1991) suggest that SMC has a tidal tail, as seen from the Milky Way, appears projected on the main body of SMC. A compilation of data on LMC and SMC is given in Tab. 1.1.

Information about the history of star formation may be derived from star clusters, field stars and from the age–metallicity relation of stars or clusters. The first burst of activity in the Large Magellanic Cloud, which produced 13 globular clusters and a field population including stars that are now RR Lyrae variables, occurred more than 11 Gyr ago. This was followed by a period of quiescence that lasted for ~ 8 Gyr, i.e. for at least half of its lifetime. During these "dark ages" LMC might have resembled a low surface brightness galaxy. This low activity phase was terminated ~ 3 Gyr ago by a violent burst of star formation that continues to the present day. The observation that 53 clusters are known to have ages of ~ 2 Gyr, while only one is known to have an age of ~ 4 Gyr, suggests that the rate of cluster formation ~ 3 Gyr ago may have increased by one or two orders of magnitude. However, the rate of star formation might have increased by a smaller factor than the rate of cluster formation. Clusters formed during the first burst of star creation in LMC occupied a much larger area than that which formed during the last 3 Gyr. This shows that the region of active star formation in LMC shrank with time.

No clusters older than 1 Gyr appear to be associated with the bar of LMC. Furthermore, a considerable fraction of the stars in the bar are younger than 0.5 Gyr (VAN DEN BERGH, 2000). These observations suggest that the bar may be a relatively young morphological feature. The absence of evidence for star and cluster formation associated with a bow–shock suggests that the Large Cloud is moving through a region of the outer galactic halo that is presently essentially free of interstellar material that is kinematically tied to the Galaxy (see VAN DEN BERGH, 2000).

The stars and clusters with ages ≤ 1 Gyr are mainly concentrated in the main body of SMC, whereas the older populations appear to be distributed throughout a larger volume of space. On the whole, the distribution of luminous young stars, of emission nebulosity and of young clusters appears rather similar to that of neutral hydrogen gas. The rate of cluster formation in SMC appears to have remained more–or–less constant over time. The fact that LMC exhibits a star formation burst, but SMC does not, speaks against the suggestion that the starburst in LMC was triggered by a close encounter with SMC. The ages of star clusters and the color–magnitude diagrams of field stars do not appear any

---

[1] The term bar usually refers to the brightest portion of the major axis of the rather chaotic main body of SMC. Although SMC is not a barred sub–type of an Ir type, GARDINER ET AL. (1996) assumed in their N–body model the existence of the real bar in SMC.

evidence for major bursts of star and cluster formation in the history of SMC. No evidence for spiral arms is seen in SMC. This shows that spiral density waves are not required to trigger star formation. Both the low metallicity of SMC gas and the high fraction of its total mass remaining in gaseous form show that SMC is still a relatively unevolved galaxy.

1.1 Magellanic Clouds and Milky Way Interacting System

The centers of LMC and of SMC are separated in the sky by 20.7°. HIPPARCOS proper motion (Kroupa & Bastian, 1997) show that both these galaxies are moving approximately parallel to each other on the plane of sky, with the Magellanic Stream trailing behind. Orbital simulations by Byrd et al. (1994) suggest that the Magellanic Clouds may have left the neighborhood of M 31 $\sim$ 10 Gyr ago and were captured by the Galaxy $\sim$ 6 Gyr ago. However, it should be emphasized that such computations are uncertain because they contain a large number of free parameters. A number of lines of evidence point to a recent tidal interaction which has affected the morphology of the outer regions of SMC:

Parameter	**LMC**	**SMC**
$\alpha\,(2000)$	$5^{h}\,19.6^{m}$	$0^{h}\,52.6^{m}$
$\delta\,(2000)$	$-69^{\circ}\,27.1'$	$-72^{\circ}\,48'$
$D_{\mathrm{Heliocentric}}$	49 kpc	57 kpc
Type	Ir III-IV (barred subtype of Ir class)	Ir IV-V (a high mass fraction remaining in gaseous form; so it seems to be less evolved than LMC)
Mass	$(0.6 - 2.5) \cdot 10^{10}\,M_{\odot}$	$(0.8 - 2.0) \cdot 10^{9}\,M_{\odot}$
Inclination	27° – 45°	60°
Position angle	170°	45°

Table 1.1: Table of basic observational data on the Magellanic Clouds (Van den Bergh, 2000).

1. Observations of young Cepheids and of old red giant stars appear to show that SMC has a considerable depth along the line of sight. This depth is probably caused by a tidal arm behind the main body of SMC.

2. A bridge containing gas and associations of young luminous stars links LMC and SMC. The fact that the young stars in the bridge have SMC–like metallicities suggests that this bridge was tidally drawn out of the Small Cloud.

3. The cluster ESO 121–SC03 which is located in the outermost part of LMC may have been tidally detached from SMC.

1.2 Interstellar Matter

Hindman et al. (1963) observed the *Magellanic Bridge* connecting the Clouds in the emission line of neutral hydrogen (H I). It was also the first indication of possible interaction in the Magellanic System. Another significant argument for the LMC–SMC–MW interaction was brought Wannier & Wrixon (1972) and Wannier et al. (1972). Their H I observations of the Magellanic Clouds discovered large filamentary structures projected on the plane of sky close to the Clouds, and extended to both high negative and positive radial LSR velocities. Mathewson et al. (1974) detected another H I structure and identified a narrow tail emanating from the space between LMC and SMC, spread over

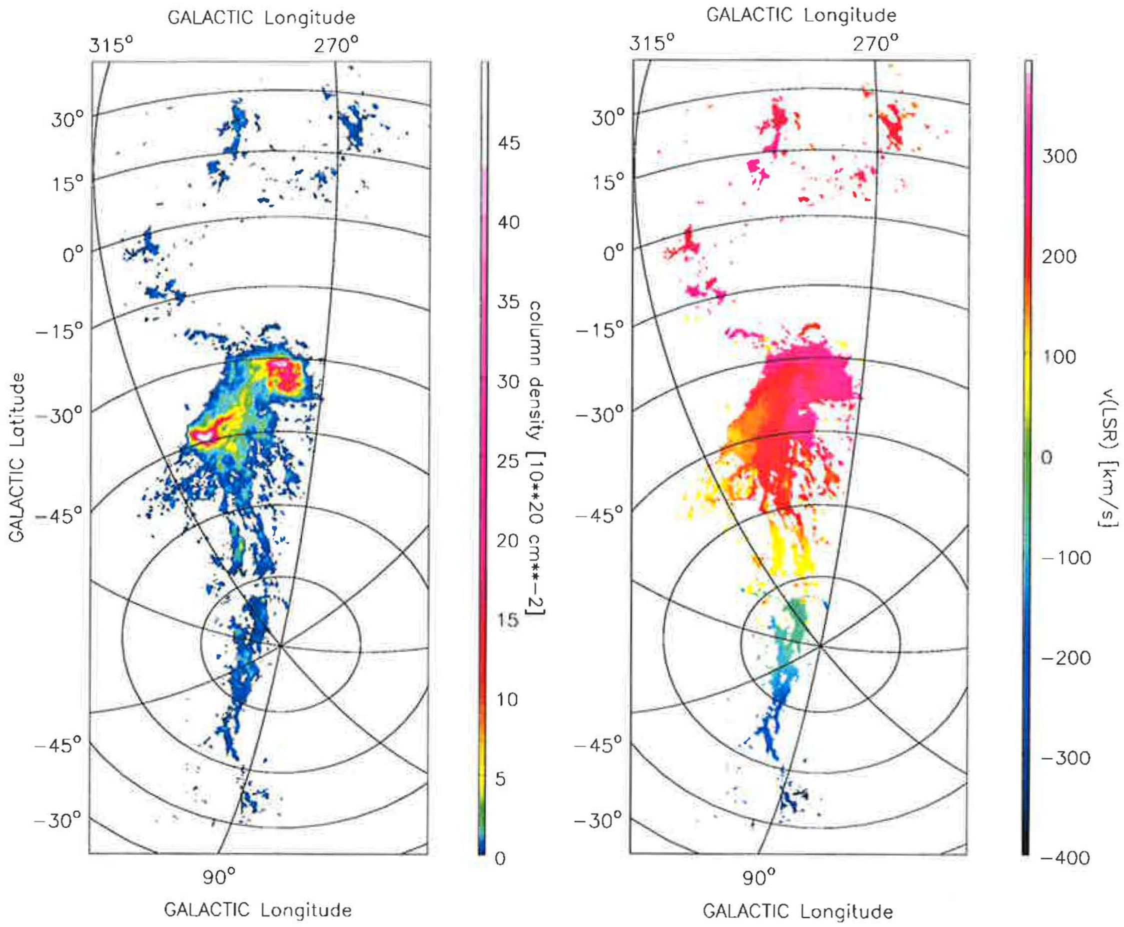

Figure 1.1: H I observations of the Magellanic Clouds by Brüns et al. (2005). Left plot shows integrated H I column densities that are in logarithmic scale and range from $5 \cdot 10^{18}\,\mathrm{cm}^{-2}$ (black) to $5 \cdot 10^{21}\,\mathrm{cm}^{-2}$ (white). Right plot depicts mean LSR radial velocity map of the entire Magellanic System. Velocities range from $-400\,\mathrm{km\,s}^{-1}$ (black) to $+400\,\mathrm{km\,s}^{-1}$ (pink). Figure by Brüns et al. (2005) is shown.

the South Galactic Pole. The tail was named the *Magellanic Stream*. A similar H I structure called the *Leading Arm* extends to the north of the Clouds, crossing the Galactic plane. A high–resolution, spatially complete H I survey of the entire Magellanic System done by Brüns et al. (2005) gives detailed kinematic information about the Clouds and the connected extended structures. It indicates that the observed features consist of the matter torn off the Magellanic Clouds and spread out due to the interaction between LMC, SMC and MW. Since the Leading Arm and the Stream are the most significant structures for our study, the H I data will be the particular subject to this section.

Undoubtedly the best currently available study of H I distribution in the Magellanic System was introduced by Brüns et al. (2005). They made the first fully and uniformly sampled, spatially complete H I survey of the entire Magellanic System with high velocity resolution ($\Delta v = 1.0\,\mathrm{km\,s^{-1}}$), performed with the Parkes Telescope. The Magellanic System was covered by this survey on a $\approx 5'$ grid with an angular resolution of $HPBW = 14.1'$. The overall distribution of H I in the Magellanic System is depicted in Fig. 1.1, together with the map of mean LSR radial velocity over the observed area. In addition to the previously introduced morphological features of the System observed in H I, Brüns et al. (2005) identified a complex structure that appears like a filamentary

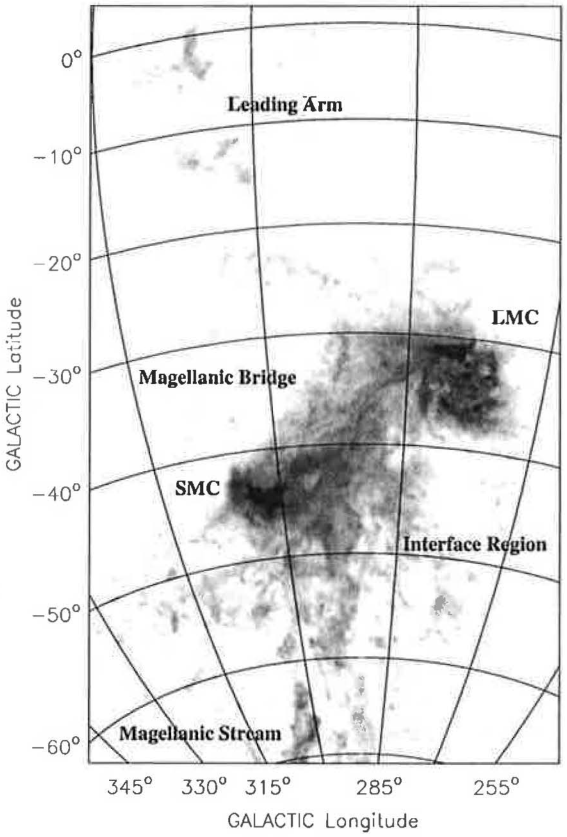

Figure 1.2: H I column density around LMC and SMC. Important structures are labeled. The gray–scale is logarithmic and represents column densities between $5 \cdot 10^{18}\,\mathrm{cm^{-2}}$ (light gray) and $1 \cdot 10^{22}\,\mathrm{cm^{-2}}$ (black). Density map from the paper Brüns et al. (2005).

web of H I clouds and was named *Interface Region.* Most of its filaments point toward the South Galactic Pole. The high column density filament between Galactic longitude $l = 290°$ and $l = 300°$ near $b \approx 55°$ is connected to the Magellanic Stream (see Fig. 1.2).

Since the Magellanic Clouds are embedded in a common H I envelope, there is no obvious way to define borders between LMC, SMC, the Magellanic Bridge or the Interface Region. BRÜNS ET AL. (2005) used both column density and kinematic features to define a subdivision of the region around the Magellanic Clouds into complexes. Definition of the parts is depicted in Fig. 1.3. Then, the total LMC and SMC masses within the above defined borders are $M(\mathrm{H\,I}) = (4.41 \pm 0.09) \cdot 10^8\,\mathrm{M}_\odot$ and $M(\mathrm{H\,I}) = (4.02 \pm 0.08) \cdot 10^8\mathrm{M}_\odot$, respectively (BRÜNS ET AL., 2005). Comparison of the results by BRÜNS ET AL. (2005) with older determinations of the LMC and SMC masses has to be treated with care, because the values obviously depend on the definition of the borders between the Clouds. STAVELEY–SMITH ET AL. (2003) determined an H I mass of $M(\mathrm{H\,I}) = (4.8 \pm 0.2) \cdot 10^8$ M. for LMC, also using the Parkes multi-beam facility. BRÜNS ET AL. (2005) derived a total H I mass of $M(\mathrm{H\,I}) = (4.6 \pm 0.1) \cdot 10^8$ M. for LMC, if the same borders between the emission from LMC and the neighboring gas are used as in STAVELEY–SMITH ET AL. (2003). The derived masses from both observations agree within their uncertainties. The estimated total amount of H I gas in LMC by ISRAEL (1997) is $7 \cdot 10^8\,\mathrm{M}_\odot$, which exceeds the above introduced values. However, definition of the LMC border in H I is unclear for ISRAEL (1997). The distribution of neutral hydrogen in LMC seems to be very clumpy and the center of mass of the H I gas is displaced from the center of rotation of LMC. Detailed studies of H I in LMC (see VAN DEN BERGH, 2000) showed that most of the gas in LMC forms part of a rotating disc with mass of $(2.2 \pm 0.4) \cdot 10^8\,\mathrm{M}_\odot$. An additional component with a mass of $(0.6 \pm 0.1) \cdot 10^8\,\mathrm{M}_\odot$ appears to be located in front of this disk. It is obvious that the interstellar medium in LMC has the turbulent and fractal structure on small scales. The structure of this gas is dominated by H I filaments, shells and holes.

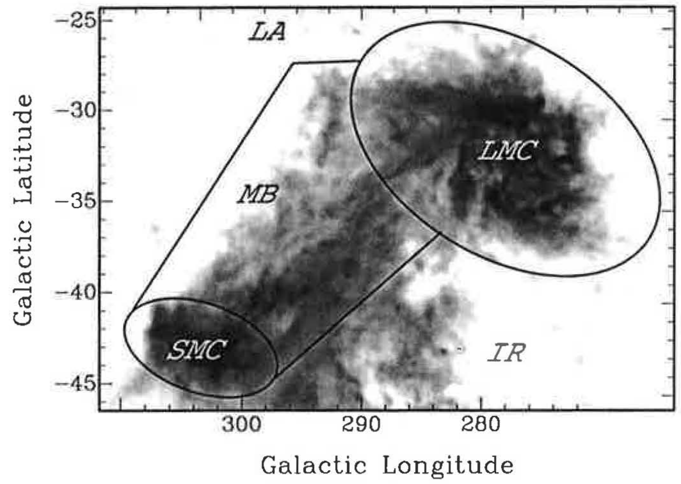

Figure 1.3: Image by BRÜNS ET AL. (2005) shows the definition of the borders between LMC, SMC, the Magellanic Bridge and the Interface Region used for calculation of total H I masses.

STANIMIROVIC ET AL. (1999) derived an H I mass of $M(\mathrm{H\,I}) = (3.8 \pm 0.5) \cdot 10^8\,\mathrm{M}_\odot$

for SMC, which is in a good agreement with the value by BRÜNS ET AL. (2005). Their mass increases to $M(\mathrm{H\,I}) = 4.2 \cdot 10^8\,\mathrm{M}_\odot$ after applying a self–absorption correction. H I in the Small Cloud has rather a smooth distribution and so it differs from that in the Large Cloud. Possibly the clumpier distribution of the LMC gas is due to the fact that the higher metallicity in LMC produced more dust, which in turn resulted in more intense gas cooling. An estimated total H I mass by VAN DEN BERGH (2000) is $\approx 5 \cdot 10^8\,\mathrm{M}_\odot$. Since the total mass of SMC is $\gtrapprox 8 \cdot 10^8\,\mathrm{M}_\odot$ (VAN DEN BERGH, 2000) it follows that a large fraction of the total SMC mass is in the form of gas.

To summarize the information about various H I morphological features of the Magellanic System, we offer review of the results by BRÜNS ET AL. (2005) in Tab. 1.2. The mass estimates assume distances of 50 kpc and 60 kpc for LMC and SMC, respectively.

region	$\Sigma(\mathrm{H\,I})_\mathrm{max}$ $[10^{20}\,\mathrm{cm}^{-2}]$	$M(\mathrm{H\,I})_\mathrm{max}$ $[10^7\,\mathrm{M}_\odot]$
LMC	54.5	44.1
SMC	99.8	40.2
Magellanic Bridge	16.4	18.4
Interface Region	5.5	14.9
Magellanic Stream	5.1	12.4
Leading Arm I	1.6	1.0
Leading Arm II + III	2.8	2.0

Table 1.2: The peak column densities and H I masses of the single parts of the Magellanic System (BRÜNS ET AL., 2005). The division of the Leading Arm into the parts labeled as I, II and III is explained by Fig. 1.5.

Undoubtedly, one of the most interesting large–scale H I morphological features of the Magellanic System is the Magellanic Stream (see Fig. 1.1 or Fig. 1.2). First observations by WANNIER & WRIXON (1972) discovered the famous linear LSR radial velocity profile of the Magellanic Stream that can be seen in Fig. 1.4, which illustrates the distribution of gas in the Magellanic Stream relative to MW gas (strong emission at $v_\mathrm{LSR} \approx 0\,\mathrm{km\,s^{-1}}$). The radial velocity changes dramatically over the extent of the Magellanic Stream starting at $v_\mathrm{LSR} \approx +250\,\mathrm{km\,s^{-1}}$ near the Magellanic Bridge and decreasing to $v_\mathrm{LSR} \approx -400\,\mathrm{km\,s^{-1}}$ near $(l, b) = (90°, -45°)$, forming an almost linear structure in the position/velocity space. Thus, the velocity difference is $\Delta v_\mathrm{LSR} = 650\,\mathrm{km\,s^{-1}}$.

Concerning the morphology of the Magellanic Stream, the first low–resolution survey by WANNIER & WRIXON (1972) indicated rather a smooth H I distribution of decreasing column density toward the far end of the Magellanic Stream. However, newer observations by MATHEWSON ET AL. (1974) showed local peaks of H I column densities and identified six dominant clumps in the Magellanic Stream, named MS I–VI. As we will see in Chapter 2, the nature of H I distribution over the Stream is considered to be a key factor that allows to evaluate reliability of two competing classes of evolutionary models of the system LMC–SMC–MW: tidal stripping versus ram pressure stripping models. The data depicted in Fig. 1.1 clearly show that a simple subdivision of the Stream in six clouds MS I–VI is not appropriate with the current resolution and sensitivity. BRÜNS ET AL. (2005) also pointed out that H I emission from the middle part of the Magellanic Stream, where v_{LSR} is close to that of the MW gas, may be contaminated by the contribution of Galaxy. Fortunately, this part of the Stream is located close to the southern Galactic Pole, where the column density of the local gas is lower than the column density of the Magellanic Stream.

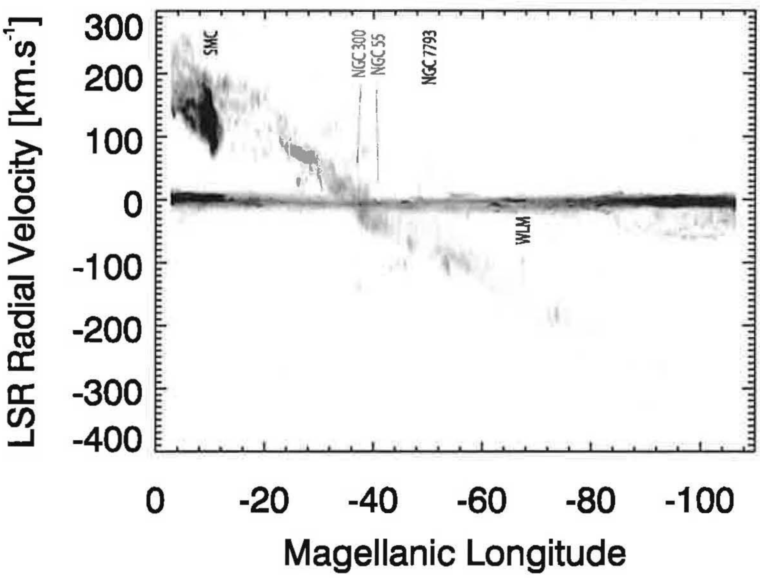

Figure 1.4: Image by BRÜNS ET AL. (2005) that shows the LSR radial velocity of the Magellanic System as function of Magellanic Longitude (for definition see WANNIER & WRIXON, 1972). The gray–scale indicates the peak intensity of H I emission (white corresponds to $T_{\mathrm{B}} = 0\,\mathrm{K}$ and black corresponds to $T_{\mathrm{B}} > 20\,\mathrm{K}$). The strong emission at $v_{\mathrm{LSR}} \approx 0\,\mathrm{km\,s^{-1}}$ is caused by MW. The map also shows the emission from SMC, the galaxies NGC 300, NGC 55, and NGC 7793 from the Sculptor Group, and the Local Group galaxy WLM.

Finally, we will pay attention to the Leading Arm, that also played very important role in our parameter study of the interaction of LMC, SMC and MW. H I observations of the Leading Arm by BRÜNS ET AL. (2005) are depicted in Fig. 1.5. The Leading Arm is a complex of high–velocity clouds (HVC) that can be grouped into three structures LA I–III. First, a complex that is located between the Magellanic Clouds and the Galactic Plane. This complex was described by MATHEWSON ET AL. (1979). Second, a filament that is part of HVC–complex observed by WANNIER ET AL. (1972). Third, a clumpy complex located at $265° \leq l \leq 280°$, $0° < b < 30°$. Detailed observational information about the Leading Arm complex can be found in BRÜNS ET AL. (2005).

From the point of view of numerical studies of dynamical evolution of the System, there is a critically important question that has not been satisfactorily answered by any of the mentioned H I surveys of the Magellanic Clouds. The question is related to the origin of H I gas in the structures LA I–III. Development of reliable models of the LMC–SMC–MW interaction requires clear information whether the HVCs in the Leading Arm belong evolutionary to either of the Clouds. The paper by BRÜNS ET AL. (2005) argues that LA I should be considered H I matter torn–off from the Clouds. However, doubts still remain concerning the complexes LA II and LA III that might originate in MW (the same result was indicated in a private communication with Christian Brüns). It will become obvious in the next sections, that reliability of observational data is crucial for parameter studies of observed galactic systems. Thus, we decided to exclude the Leading Arm parts LA II and LA III from the data used for comparison to the modeled H I distribution in the Magellanic System.

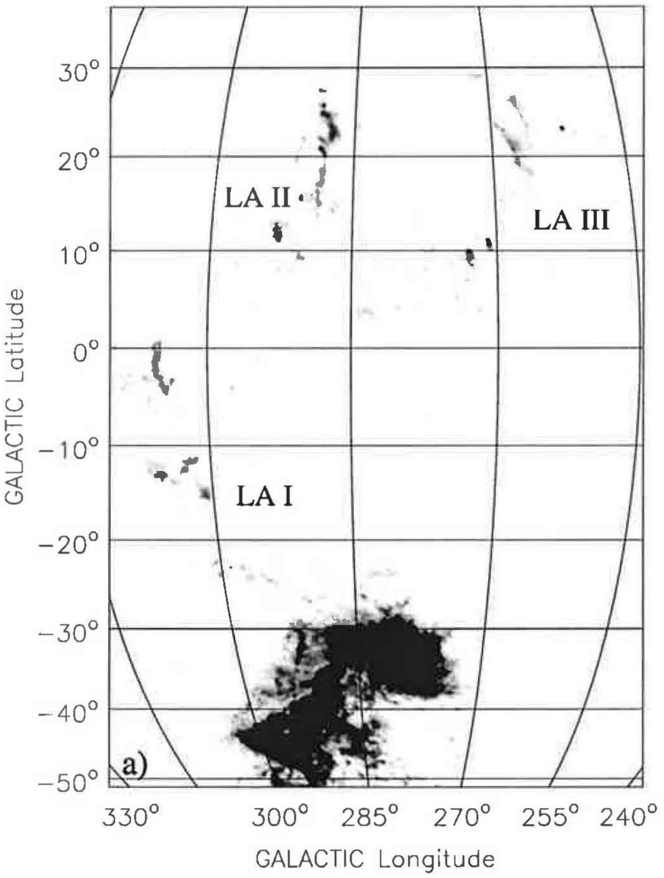

Figure 1.5: H I column density distribution of the Leading Arm integrated over the velocity interval $170\,\mathrm{km\,s^{-1}} < v_{\mathrm{LSR}} \leq 400\,\mathrm{km\,s^{-1}}$. Gray scales are linear ranging from 0 (white) to $1.5 \cdot 10^{20}\,\mathrm{cm^{-2}}$ (black). Plot from Brüns et al. (2005).

We have payed a particular attention to the information about about the Magellanic System that was acquired due to observations in the H I emission line. It is quite understandable if one realizes the composition of LMC, SMC and the connected extended structures. While various stellar populations and multi–component interstellar matter have been observed in the main bodies of the Magellanic Clouds and the connecting Magellanic Bridge, the only significant component of the remarkable Magellanic Stream and Leading Arm is H I. Numerical studies have clearly indicated that it is morphology and kinematics of those two extended structures, that allow for constraints on the dynamical evolution of the Magellanic Clouds (details will be offered in Chapter 2). Thus, we found desirable to offer the reader detailed information about the composition of the Magellanic

Stream and the Leading Arm, since they play a key role in our search for evolutionary scenarios of the Magellanic System.

A brief review of another components of the interstellar matter in the Magellanic Clouds will be offered before we close this chapter. Remarkable progress has been achieved over the last decade concerning observations of CO in the Magellanic Clouds. There is usually a strong correlation between the distribution of CO and star formation regions in galaxies, and CO is then a valuable source of information about stellar populations in the Clouds. MUELLER ET AL. (2003) detected and partially mapped a region of 12 CO(1–0) line emission within the Magellanic Bridge. They argue that the observed region is of a low metallicity, supporting earlier findings that the Magellanic Bridge is not as evolved as SMC and Magellanic Stream, which are themselves of a lower metallicity than the Galaxy. Notable results have been obtained by the Japanese NANTEN group, concerning distribution of CO in LMC. KAWAMURA ET AL. (2005) used the NANTEN facility to make a CO survey toward the Magellanic Clouds to map giant molecular clouds (GMCs) in the System, including the Magellanic Bridge, with angular resolution of 40 pc. The mass spectrum and the line–width distribution of the GMCs in the Galactic plane and in LMC are similar to each other. Nevertheless, GMCs without any signs of massive star formation were detected in the Clouds, which is surprising, since almost all the GMCs show massive star formation in the Solar vicinity. Further data about star formation regions have been obtained from observations of molecular clouds in the absorption line of H_2. For more detailed information about detection of H_2 in the Magellanic Clouds see e.g. ISRAEL (1997) or VAN DEN BERGH (2000).

1.3 Stars and Clusters

This section is just a brief introduction to our knowledge in the stellar content of the Magellanic System, with suggestions for further reading. It is due to marginal role of the stellar component of the System in this study of the LMC–SMC–MW interaction. However, in some respects – e.g. the problem of the age gap in the globular cluster formation – features of stellar populations in the Clouds have to be considered.

Research of star clusters in the Magellanic Clouds possesses a great significance for our knowledge of the LMC and SMC evolutionary history as we will see later. The LMC cluster system has dimensions of 11° x 15° and is centered at $5^h 32^m$, $-69.3°$. In LMC there is a wide gap between true globular clusters with ages $>$ 12 Gyr and open clusters with ages $<$ 4 Gyr. The only cluster is known to have an age between 4 Gyr and 12 Gyr, but this one may be an interloper from SMC. The centroid of LMC globular cluster system is located at $\alpha = 5^h 17^m \pm 12^m$, $\delta = -69.5° \pm 1.5°$ (Epoch 2000). It is sometime concluded that the oldest clusters in LMC rotate with an amplitude comparable to that of young disc objects and their velocity dispersion is small. This suggests that the globular clusters in LMC form a disk rather than a halo. If this conclusion is correct, and if LMC and galactic globular clusters have the same age, then LMC would already have collapsed to a disc at the time when the Galaxy was still forming halo clusters (VAN DEN BERGH, 2000). For information about the recent progress in studies of LMC globular clusters see e.g. DE

Grijs & Anders (2006) and references therein. Young clusters and associations can be mainly found in several LMC regions with a high star–formation activity. At present the *30 Doradus complex* appears to be the most active region of star formation in LMC.

Van den Bergh (2000) suggests that young associations in the ***bridge*** between the Magellanic Clouds evolutionary belong to SMC. Distances of these associations decrease from the SMC side to the LMC side which is compatible with the hypothesis that they form a bridge between LMC and SMC. The main sequences of these associations indicate that a burst of star formation occurred in the bridge between 10 Myr and 25 Myr ago.

CHAPTER 2

Modeling Observed Galaxies

The theoretical understanding of interacting galaxies suffered for a long time from the lack of computational power allowing for a numerical solution of the gravitational N-body problem. To reduce the computational costs of N-body models, *restricted N-body simulations* were introduced. They are based on the assumption that the potential of interacting galaxies can be modeled by two potentials that correspond to the galactic masses and move on Keplerian orbits. With these assumptions all the other particles are just *test-particles*, and the complete N-body problem is reduced to N single body problems for a time-dependent potential. This method was successfully applied on the problem of interacting galaxies by TOOMRE & TOOMRE (1972).

With increase of accessible computational power, new N-body techniques were proposed. They usually treat the gravitational interaction self-consistently. However, various approaches are used to overcome the $O(N^2)$ bottleneck of direct N-body simulations. *TREE-method* by BARNES & HUT (1986) scales as $O(N \log N)$ with the number of particles The organization of the force calculation - the most time-consuming part of N-body calculations - adapts to clumpy mass distributions. By this, BARNES & HUT (1986) were able to simulate encounters of disc galaxies including all dynamical components, i.e. the disc, the bulge, and the halo as N-body systems. Faster *grid-based methods* (see e.g. SELLWOOD, 1980) or *expansion methods* (HERNQUIST & OSTRIKER, 1992) compared to direct N-body or TREE methods are more flexible with respect to strongly varying geometries and scale lengths. An alternative to these techniques are special-purpose computers such as the GRAPE project (SUGIMOTO ET AL., 1990). They implemented Newton's law of gravity in the hardware which allows for a very fast direct determination of the gravitational forces.

2.1 Magellanic System

TOOMRE & TOOMRE (1972) have shown the applicability of *restricted N–body* models on interacting galaxies. In restricted N–body simulations, gravitating particles are replaced by *test–particles* moving in a time–dependent potential which is a superposition of analytic potentials of the individual galaxies. Such an approach maps the gravitational potential with high spatial resolution for low CPU costs due to the linear CPU scaling with the number of particles. However, the self–gravity of the stellar systems is not considered directly. E.g. the orbital decay of the Magellanic Clouds due to dynamical friction cannot be treated self–consistently in restricted N–body simulations, but has to be considered by (semi–)analytical approximative formulas.

First papers on the physical features of the interacting system LMC, SMC and Galaxy used 3 D restricted N–body simulations to investigate the *tidal origin* of the extended Magellanic structures. LIN & LYNDEN–BELL (1977) pointed out the problem of the large parameter space of the LMC–SMC–MW interaction. To reduce the parameter space, they neglected both the SMC influence on the System and dynamical friction within the MW halo, and showed that such configuration allows for the existence of a LMC trailing tidal stream. The interaction between the Clouds was analyzed by FUJIMOTO & SOFUE (1976) who assume LMC and SMC to form a gravitationally bound pair for several Gyr, moving in a flattened MW halo. They identified some LMC and SMC orbital paths leading to creation of a tidal tail. Following studies by MURAI & FUJIMOTO (1980), MURAI & FUJIMOTO (1984), LIN & LYNDEN–BELL (1982), GARDINER ET AL. (1994) and LIN ET AL. (1995) extended and developed test–particle models of the LMC–SMC–MW interaction. The Magellanic Stream was reproduced as a remnant of the LMC–SMC encounter that was mostly placed to the time of −2 Gyr. The matter torn off was spread along the paths of the Clouds. The simulations also indicate that the major fraction of the Magellanic Stream gas stems from SMC. The observed radial velocity profile of the Stream was modeled remarkably well. However, the smooth H I column density distribution did not agree with observations indicating apparently clumpy Magellanic Stream structure. Test–particle models place matter to the Leading Arm area naturally (see the study on the origin of tidal tails and arms by TOOMRE & TOOMRE (1972)), but correspondence with observational data cannot be considered sufficient. GARDINER ET AL. (1996) devised a scheme of the Magellanic System interaction implementing the full N–body approach. SMC was modeled by a self–gravitating sphere moving in LMC and MW analytic potentials. It was shown that the evolution of the Magellanic Stream and the Leading Arm is dominated by tides which supports the applicability of test–particle codes for modeling of extended Magellanic structures. Recently, the study by CONNORS ET AL. (2005) investigated the evolution of the Magellanic Stream as a process of tidal stripping of gas from SMC. Their high–resolution N–body model of the Magellanic System based on ideas of GARDINER ET AL. (1996) is compared to the data from the HIPASS survey. Involving pure gravitational interaction allowed for remarkably good reproduction of the Magellanic Stream LSR radial velocity profile. They were able to improve previous models of the Leading Arm. Similarly to the previous tidal scenarios, difficulties remain concerning overestimating of the H I column density toward the far tip of the Magellanic Stream.

Connors et al. (2005) approximate both the LMC and Milky Way by rigid potentials and also do not study influence of non–spherical halo of MW.

Meurer et al. (1985) involved continuous ram pressure stripping into their simulation of the Magellanic System. This approach was followed later by Sofue (1994) who neglected presence of SMC, though. The Magellanic Stream was formed of the gas stripped from outer regions of the Clouds due to collisions with the MW extended ionized disk. Heller & Rohlfs (1994) argue for a LMC–SMC collision 500 Myr ago that established the Magellanic Bridge. Later, gas spread to the inter–cloud region was stripped off by ram pressure as the Clouds moved through a hot MW halo. Generally, continuous ram pressure stripping models succeeded reproducing the decrease of the Magellanic Stream H I column density towards the far tip of the Stream. However, they are unable to explain the evidence of gaseous clumps in the Magellanic Stream. Gas stripping from the Clouds caused by isolated collisions in the MW halo was studied by Mathewson & Ford (1984). The resulting gaseous trailing tail consisted of fragments, but such a method did not allow for reproduction of the column density decrease along Magellanic Stream. Recently, Bekki & Chiba (2005) applied a complex gas–dynamical model including star–formation to investigate the dynamical and chemical evolution of LMC. They include self–gravity and gas dynamics by means of sticky particles, but they are also not complete: they assume a live LMC system, but SMC and MW were treated by static spherical potentials. Thus, dynamical friction of LMC in the MW halo is only considered by an analytical formula and a possible flattening of the MW halo is not involved. Their model cannot investigate possible SMC origin of Magellanic Stream neither. Mastropietro et al. (2005) introduced a model of the Magellanic System including hydrodynamics (SPH) and full N–body treatment of gravity. They studied the interaction between LMC and MW. Similarly to Lin & Lynden–Bell (1977) and Sofue (1994) the presence of SMC was not taken into account. It was shown that the Stream, which sufficiently reproduces the observed H I column density distribution, might have been created without an LMC–SMC interaction. However, the history of the Leading Arm was not investigated.

In general, hydrodynamical models allow for better reproduction of the Magellanic Stream H I column density profile than tidal schemes. However, they constantly fail reproducing the Magellanic Stream radial velocity measurements and especially the high–negative velocity tip of Magellanic Stream. Both families of models suffer from serious difficulties when modeling the Leading Arm.

In order to model the evolution of the Magellanic System, the initial conditions and all parameters of their interaction have to be determined. Such a parameter space becomes quite extended. In the Magellanic System we have to deal with the orbital parameters and the orientation of the two Clouds, their internal properties (like the extension of the disk) and the properties of the MW potential. In total we have about 20 parameters (the exact number depends on the adopted sophistication of the model). Previous studies on the Magellanic Clouds, however, argued for very similar evolutionary scenarios of the system (e.g. Lin & Lynden–Bell (1982), Gardiner et al. (1994), Bekki & Chiba (2005)). These calculations are based on additional assumptions concerning the orbits, or the internal structure and orientation of the Clouds, the potential of the Milky Way (mass distribution and shape), the treatment of dynamical friction in the Galactic halo or the treatment of self–gravity and gas dynamics in the Magellanic Stream. Some of them can be motivated by additional constraints. E.g. LIN & LYNDEN–BELL (1982) and IRWIN ET AL. (1990) argue that the Clouds should have been gravitationally bound over the last several Gyr. However, in general the uniqueness of the adopted models is unclear, because a systematic analysis of the entire parameter space is still missing.

CHAPTER 3

Numerical Model of the Magellanic System

3.1 Introduction

We attempt to explore the LMC–SMC–MW interaction parameter space that is compatible with the observations of the Magellanic System available up to date. Regarding the dimension and size of the parameter space, a large number of the numerical model runs have to be performed to test possible parameter combinations – no matter which kind of search technique is selected for the task. In such a case, despite their physical reliability, full N–body models are of little use, due to their computational costs (see Chapter 2).

Necessity to employ an approximative restricted N–body scheme for the purpose of this study is apparent. However, in order to cope with the extended parameter space, neither a complete catalog of even computationally very fast models nor a large number of computationally expensive self–consistent simulations can be performed – both due to numerical costs. However, a new numerical approach based on evolutionary optimization methods combined with efficient N–body integrators turned out to be a promising tool. In case of encounters between two galaxies, WAHDE (1998) and THEIS (1999) showed that a combination of GA with restricted N–body simulations is able to reproduce the parameters of the interaction. GA is a robust optimizer that selects possible parameter combinations according to their ability to match observations. The parameters serve as input for a numerical model of the interacting system. Regarding the above made notes, together with the review of various attempts to model the interaction of MW, LMC and SMC provided in Sec. 2.1, we suggest to apply a ***3D restricted N–body model with test–particles*** to study the evolution of the Magellanic System.

3.2 Physical Features

In order to optimize the performance of GA, a computationally fast model of the Magellanic System is required. Therefore, complex N–body schemes involving self–consistent description of gravity and hydrodynamics (see BEKKI & CHIBA, 2005; MASTROPIETRO ET AL., 2005) are discriminated. On the other hand, correct description of physical processes dominating the evolution of the System remains a crucial constraint on the model.

In Sec. 2.1 we discussed applicability of restricted N–body schemes on problems of galactic encounters and showed that they allow for modeling of extended streams and tails. Thus, we devised a restricted N–body code based on the numerical models by MURAI & FUJIMOTO (1980) and GARDINER ET AL. (1994). The test–particle code interprets the observed large–scale structures such as the Magellanic Stream or the Leading Arm as products of tidal stripping in the Magellanic System.

Except tidal schemes, there have been used also ram pressure models in the previous studies on the Magellanic System (see Sec. 2.1). However, employing even a simple formula for ram pressure stripping would introduce other parameters including structural parameters of the distribution of gas in the MW halo and description of the gaseous clouds in LMC and SMC. It would increase the dimension of the parameter space of the interaction and make the entire GA optimization process even more complex. Moreover, ram pressure models did not improve the results of tidal schemes (see Sec. 2.1).

The dark matter (DM) halo of the Milky Way is considered axisymmetric and generally flattened in our model. It is a significant improvement of previous studies of the Magellanic System that assumed spherical halos. We were able to investigate the influence of the potential flattening parameter q on the evolution of the Magellanic System. However, both the mass and shape of the MW DM halo were fixed for the entire evolutionary period of 4 Gyr.

We did not take into account possible changes in mass and shape of the Clouds. Shape modification might become important for very close LMC–SMC encounters that are typical for the models with nearly–spherical MW DM halos. PEÑARRUBIA ET AL. (2004) demonstrated that a relative mass–loss of a satellite galaxy moving through an extended halo strongly differs for various combination of its orbital parameters, shape and mass distribution of the halo, and cannot be described reliably by a simple analytic formula.

3.3 Magellanic Clouds

Even when the functions describing density profiles of the Magellanic Clouds are estimated insufficiently, some plausible approximation of the mass distribution has to be adopted. In agreement with MURAI & FUJIMOTO (1980) and GARDINER ET AL. (1994) the Magellanic Clouds are described as *Plummer spheres* with density distribution

$$\rho_{\mathrm{P}} = \frac{3m}{4\pi} \frac{\epsilon^2}{(r^2 + \epsilon^2)^{5/2}}, \tag{3.1}$$

generating the following gravitational potential:

$$\Phi_P = -\frac{Gm}{\sqrt{r^2+\epsilon^2}}, \tag{3.2}$$

where r is the distance to the center of mass of the Cloud, ϵ is a free parameter, and m is the total mass. Both the Magellanic Clouds posses a large number of test–particles that are initially distributed in the form of 2 D disks surrounding the center of mass of LMC and SMC, respectively. The particles are set to circular orbits in the potential (3.2) with the surface number density of an exponential disk:

$$\Sigma(R) = \Sigma_0 \exp^{-R/R_D}, \tag{3.3}$$

where Σ_0 is a constant and R_D is a disk scale factor. The total number of test–particles inside the radius R is then

$$n(R) = 2\pi\Sigma_0 R_D^2 \left[1 - \exp(-R/R_D)\left(1+\frac{R}{R_D}\right)\right]. \tag{3.4}$$

3.4 Milky Way

MW DM halo is modeled as an axisymmetric logarithmic potential (BINNEY & TREMAINE, 1987)

$$\Phi_L = \frac{1}{2}{v_0}^2 \ln\left({R_c}^2 + R^2 + \frac{z^2}{q^2}\right) \tag{3.5}$$

with the density distribution

$$\rho_L = \left(\frac{{v_0}^2}{4\pi G q^2}\right) \frac{(2q^2+1){R_c}^2 + R^2 + \left(2-q^{-2}\right)z^2}{\left({R_c}^2 + R^2 + z^2 q^{-2}\right)^2}. \tag{3.6}$$

To reproduce the rotation curve of MW, we set $R_c = 12\,\mathrm{kpc}$, $v_0 = \sqrt{2}\cdot 131.5\,\mathrm{km\,s^{-1}}$, and q describes the flattening of the MW halo potential. There is no upper limit for the values of q, while it is necessary that $q \geq 1/\sqrt{2}$ to avoid negative values of ρ_L on z–axis. The corresponding flattening q_ρ of the density distribution associated with the halo potential follows

$${q_\rho}^2 = q^2\left(2 - \frac{1}{q^2}\right) \quad (R \gg R_c). \tag{3.7}$$

The relation expressed by (3.7) is plotted in Fig. 3.1. Note, that the mass distribution is substantially more flattened than the corresponding potential, as q becomes different from 1.0. Variation of the flattening parameter q influences effects of tides exerted on a body moving through the Galactic halo.

Tides between points at the positions $\boldsymbol{R}$ and $\boldsymbol{R}_1$ are defined as

$$\Delta\boldsymbol{F} \equiv \boldsymbol{F}(\boldsymbol{R}) - \boldsymbol{F}(\boldsymbol{R}_1). \tag{3.8}$$

If a special polar plane ($\phi = \phi_1 = 0$) is assumed, we obtain the cylindrical components of $\Delta\boldsymbol{F}$ for a logarithmic potential (3.5):

$$\Delta F_R = v_0^2 \left(\frac{R}{R_c^2 + R^2 + \frac{z^2}{q^2}} - \frac{R_1}{R_c^2 + R_1^2 + \frac{z_1^2}{q^2}} \right) \tag{3.9}$$

$$\Delta F_\phi = 0 \tag{3.10}$$

$$\Delta F_z = \frac{v_0^2}{q^2} \left(\frac{z}{R_c^2 + R^2 + \frac{z^2}{q^2}} - \frac{z_1}{R_c^2 + R_1^2 + \frac{z_1^2}{q^2}} \right). \tag{3.11}$$

To investigate the features of a tidal interaction in a logarithmic halo, we calculated tidal acceleration for points at $\boldsymbol{R}$, $\boldsymbol{R}_1$ of a constant radial distance $\Delta R = 10\,\mathrm{kpc}$ moving on galactocentric polar circular orbits. In Fig. 3.2 we show the mean, maximal and minimal tidal acceleration per one orbital cycle for different galactocentric radii as functions of the potential flattening parameter q.

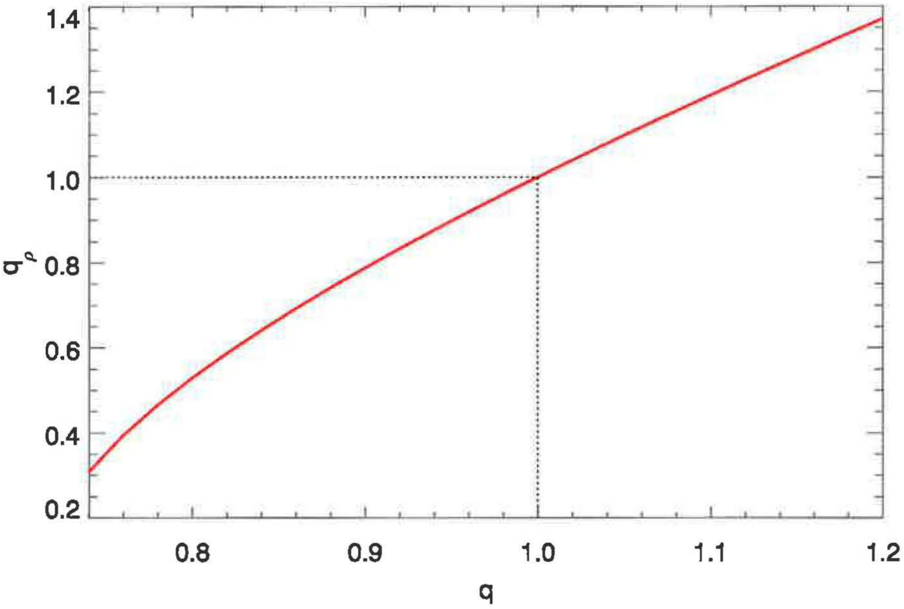

Figure 3.1: MW DM halo density flattening q_ρ as function of the potential flattening q (3.7).

Typical relaxation time of galaxies implies that their dynamics is that of a *collision–less system*, where stars move under the potential generated by the entire system. Long–term galactic evolution is driven by its overall gravitational field, not by two–body encounters. The state of a collision–less system at any time is described by the *distribution*

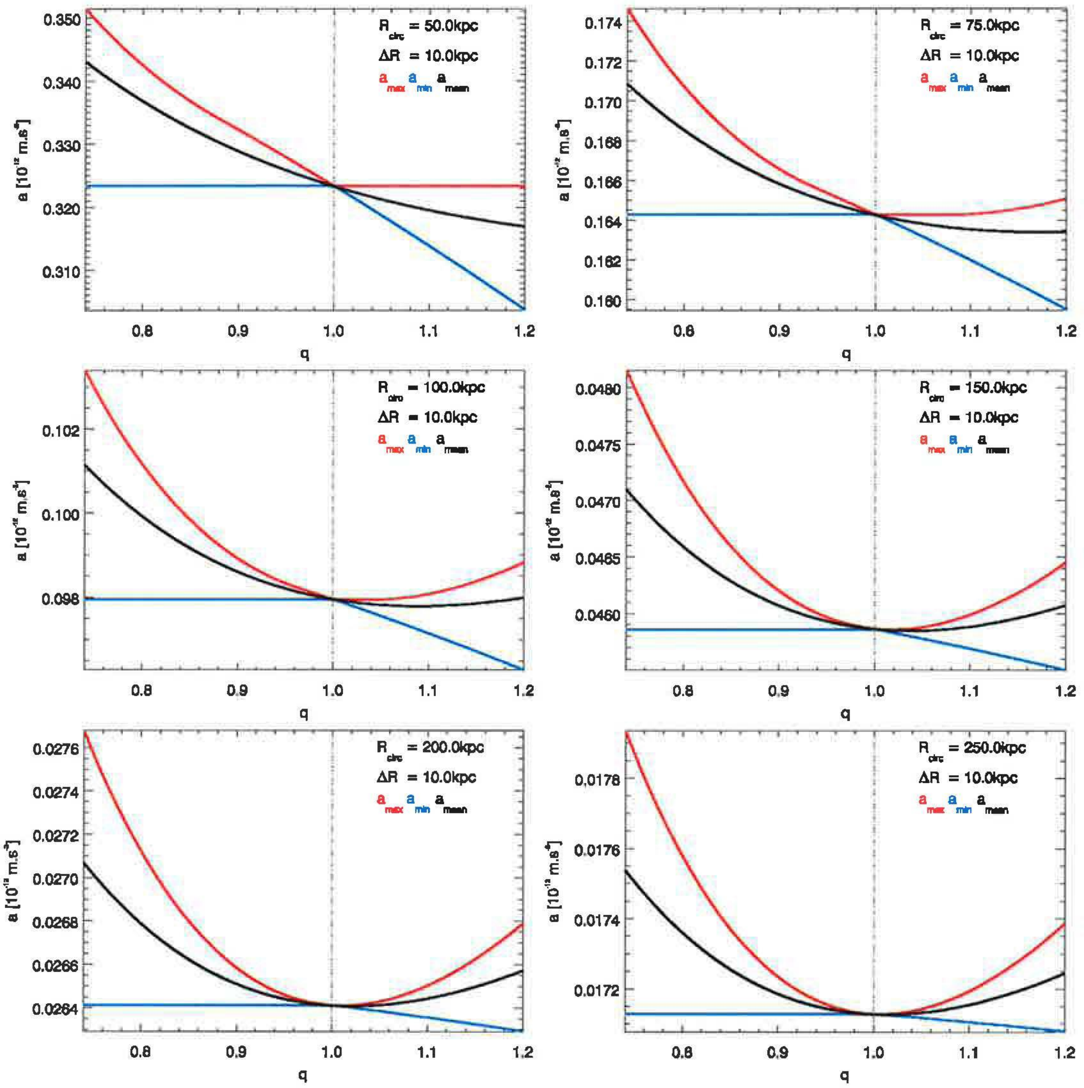

Figure 3.2: Tidal acceleration for a logarithmic potential as function of flattening q. Values are calculated for two points on circular polar orbits of a constant radial distance $\Delta R = 10\,\mathrm{kpc}$.

function $f(\boldsymbol{x}, \boldsymbol{v}, t)$, that satisfies the *collision–less Boltzmann equation*

$$\frac{\mathrm{d}f}{\mathrm{d}t} = 0. \tag{3.12}$$

If we consider the gravitational field of MW modeled by the logarithmic potential Φ_{L}, (3.12) becomes

$$\frac{\partial f}{\partial t} + \boldsymbol{v} \cdot \nabla f - \nabla \Phi_{\mathrm{L}} \cdot \frac{\partial f}{\partial \boldsymbol{v}} = 0. \tag{3.13}$$

To avoid usual difficulties arising from attempts to solve (3.13) directly, it is a common practice to deal with the zeroth and the first moments of (3.13), that are called *Jeans equations.* If the collision–less Boltzmann equation is integrated over all possible velocities, we get the first Jeans equation (continuity equation)

$$\frac{\partial \nu}{\partial t} + \frac{\partial (\nu \overline{v}_i)}{\partial x_i} = 0, \tag{3.14}$$

where

$$\nu \equiv \int f \mathrm{d}^3 \boldsymbol{v}; \qquad \overline{v}_i \equiv \frac{1}{\nu} \int f v_i \mathrm{d}^3 \boldsymbol{v}. \tag{3.15}$$

Multiplying (3.13) by $\boldsymbol{v}$ and integrating over all velocities leads to the second Jeans equation

$$\nu \frac{\partial \overline{v}_j}{\partial t} + \nu \overline{v}_i \frac{\partial \overline{v}_j}{\partial x_i} = -\nu \frac{\partial \Phi_{\mathrm{L}}}{\partial x_j} - \frac{\partial (\nu \sigma_{ij}^2)}{\partial x_i}, \tag{3.16}$$

where

$$\sigma_{ij}^2 \equiv \overline{v_i v_j} - \overline{v}_i \overline{v}_j \tag{3.17}$$

is a ***stress tensor***, which is symmetric, and so orthogonal axes exist in which $\sigma_{ij}^2 = \sigma_{ii}^2 \delta_{ij}$. Then, the ellipsoid with σ_{11}, σ_{22} and σ_{33} for its semi–axes is called the ***velocity ellipsoid*** at $\boldsymbol{x}$. Semi–axes of the velocity ellipsoid correspond to observationally measurable velocity dispersion of stellar populations in galaxies. Apparently, the Jeans equations (3.14) and (3.16) do not allow for unique determination of all the variables ν and σ_{ij}^2. Such a difficulty is usually resolved by adopting assumptions on the tensor σ_{ij}^2. That approach will be introduced in the following paragraphs where the Jeans equations for a logarithmic halo are analyzed. Obtaining a solution to the Jeans equations is a necessary step toward proper treatment of ***dynamical friction*** in the Galactic halo (see Sec. 3.5).

The adopted model of a flattened logarithmic halo of MW is axisymmetric and hence it is natural to express (3.14) and (3.16) in cylindrical coordinates. Assuming axial symmetry ($\partial/\partial\phi = 0$), we may rewrite (3.14) as

$$\frac{\partial \nu}{\partial t} + \frac{1}{R}\frac{\partial (R \nu \overline{v}_R)}{\partial R} + \frac{\partial (\nu \overline{v}_z)}{\partial z} = 0. \tag{3.18}$$

Similarly, from (3.16) we obtain

$$\frac{\partial (\nu \overline{v}_R)}{\partial t} + \frac{\partial (\nu \overline{v_R^2})}{\partial R} + \frac{\partial (\nu \overline{v_R v_z})}{\partial z} + \nu \left(\frac{\overline{v_R^2} - \overline{v_\phi^2}}{R} + \frac{\partial \Phi_{\mathrm{L}}}{\partial R} \right) = 0, \tag{3.19}$$

$$\frac{\partial (\nu \overline{v}_\phi)}{\partial t} + \frac{\partial (\nu \overline{v_R v_\phi})}{\partial R} + \frac{\partial (\nu \overline{v_\phi v_z})}{\partial z} + \frac{2\nu}{R} \overline{v_\phi v_R} = 0, \tag{3.20}$$

and

$$\frac{\partial (\nu \overline{v}_z)}{\partial t} + \frac{\partial (\nu \overline{v_R v_z})}{\partial R} + \frac{\partial (\nu \overline{v_z^2})}{\partial z} + \frac{\nu \overline{v_R v_z}}{R} + \nu \frac{\partial \Phi_{\mathrm{L}}}{\partial z} = 0. \tag{3.21}$$

In order to achieve further simplification of the Jeans equations, we consider the system to be in a steady state when

$$\partial/\partial t = 0, \tag{3.22}$$

and only tangential flow of mass is admitted, which means that

$$\overline{v}_R = \overline{v}_z = 0. \tag{3.23}$$

Binney (1977) assumes a bi–axial Maxwellian velocity distribution function (Schwarzschild spheroid) for a generally tri–axial flattened galactic potential:

$$f(\boldsymbol{x},\boldsymbol{v}) = f(\boldsymbol{x})\left(\frac{1}{2\pi}\right)^{3/2}\frac{1}{\sigma_\parallel^2\sigma_z}e^{-(v_\parallel^2/2\sigma_\parallel^2+v_z^2/2\sigma_z^2)}, \tag{3.24}$$

where $v_\parallel = v_\phi$ and

$$\sigma_\parallel = \sigma_R = \sigma_\phi. \tag{3.25}$$

If we introduce the following notation based on the definition (3.17):

$$\sigma_R^2 = \overline{v_R^2} \qquad \sigma_\phi^2 = \overline{v_\phi^2} - \overline{v}_\phi^2 \qquad \sigma_z^2 = \overline{v_z^2}, \tag{3.26}$$

and apply (3.22), (3.23), and (3.25) on the Jeans equation for an axially symmetric system, the equations (3.18) and (3.20) vanish, while (3.19) and (3.21) are significantly simplified:

$$\frac{\partial(\nu\sigma_R^2)}{\partial R} + \nu\left(\frac{\partial\Phi_\mathrm{L}}{\partial R} - \frac{\overline{v}_\phi^2}{R}\right) = 0, \tag{3.27}$$

and

$$\frac{\partial(\nu\sigma_z^2)}{\partial z} + \nu\frac{\partial\Phi_\mathrm{L}}{\partial z} = 0. \tag{3.28}$$

Unfortunately, (3.27) and (3.28) do not provide sufficient information to find unique solution for the unknown variables $\overline{v}_\phi^2$ and σ_R^2. To resolve such a difficulty, we consider the radial velocity dispersion σ_R^2 a function of the circular streaming velocity $\overline{v}_\phi^2$ that is a measure of rotation of the Galactic halo. In general, the velocity $\overline{v}_\phi^2$ lies within the range $\langle 0, v_\mathrm{circ}^2\rangle$, where $v_\mathrm{circ}^2 = R\frac{\partial\Phi_\mathrm{L}}{\partial R}$ is a circular velocity in the equatorial plane. Regarding the mentioned fact, it is feasible to define the following parametrization:

$$\overline{v}_\phi^2 = XR\frac{\partial\Phi_\mathrm{L}}{\partial R}, \tag{3.29}$$

where $X \in \langle 0, 1\rangle$. Then, substitution of (3.29) into (3.27) and its subsequent formal integration lead to

$$\sigma_R^2 = (1-X)\frac{1}{\nu}\int\limits_R^\infty \nu\frac{\partial\Phi_\mathrm{L}}{\partial R'}\mathrm{d}R'. \tag{3.30}$$

Finally, we obtain the relation for σ_R^2 from (3.30):

$$\sigma_R^2 = (1-X)\frac{v_0^2}{4}\left(1+\frac{R_c^2+R^2+z^2q^{-2}}{(2q^2+1)R_c^2+R^2+(2-q^{-2})z^2}\right). \tag{3.31}$$

Apparently, the free parameter $0 \leq X \leq 1$ determines the fraction of the total kinetic energy of the collision–less system that is in the form of streaming motion – rotation. Studies of matter distribution in galaxies, that are available up to date, do not introduce any particular arguments for presence of macroscopic rotation of galactic halos. Therefore, we assume a *non–rotating halo* of MW, i.e. we put $X = 0$.

Derivation of σ_z^2 is very similar to the above performed calculation of σ_R^2. Formal integration of (3.28) allows for expression of the axial velocity dispersion σ_R^2 as

$$\sigma_z^2 = \frac{1}{\nu}\int\limits_z^{\infty} \nu\frac{\partial\Phi_{\mathrm{L}}}{\partial z'}\mathrm{d}z', \tag{3.32}$$

which results into

$$\sigma_z^2 = \frac{v_0^2}{4}\left(1+\frac{(2q^2-1)(R_c^2+R^2+z^2q^{-2})}{(2q^2+1)R_c^2+R^2+(2-q^{-2})z^2}\right). \tag{3.33}$$

As an illustration of basic features of the velocity dispersion in a non–rotating logarithmic halo (3.5), we plot both σ_R^2, σ_z^2 as functions of distance in the equatorial plane and on the axis of symmetry, respectively (see Fig. 3.3).

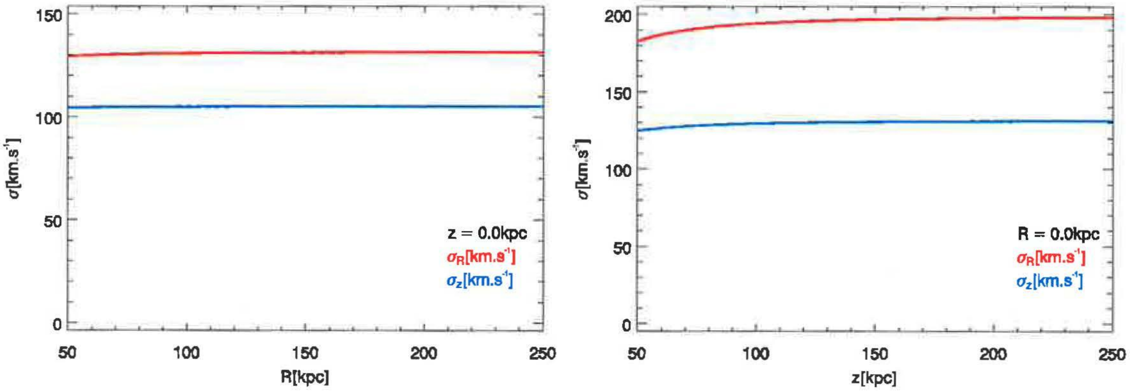

Figure 3.3: Radial velocity dispersion σ_R and axial velocity dispersion σ_z in the equatorial plane (left plot) and on the z–axis of a non–rotating Galactic halo. The corresponding value of the halo flattening is $q = 0.8$.

3.5 Dynamical Friction

It is well known that if a mass body moves through a region populated by a large number of stars, it is retarded due to a gravitational interaction with this particle background. The moving body loses its kinetic energy and a wake in the star field is induced. Such a kind of an interaction has been named ***dynamical friction*** by CHANDRASEKHAR (1943). The derivation of the commonly used analytic formula for the corresponding deceleration has been performed after doing several basic assumptions (see BINNEY & TREMAINE, 1987):

1. the mutual interaction between a moving body and background stars is treated as a pure two–body encounter, i.e. the mutual attraction of the background stars with each other is neglected
2. the body passes each of the stars on a Keplerian hyperbola
3. the moving body is considered to be a mass point
4. the background stars move isotropically

With respect to the first three assumptions, one may evaluate the drag $\delta \boldsymbol{F}_{\mathrm{DF}}$ which is experienced by a mass M (e.g. a satellite galaxy) as it moves at a velocity $\boldsymbol{v}_{\mathrm{M}}$ through a background population of lighter particles (e.g. a massive galaxy), mass m, velocity $\boldsymbol{v}_{\mathrm{m}}$, distribution function $f(\boldsymbol{x},\boldsymbol{v})$:

$$\delta \boldsymbol{F}_{\mathrm{DF}} = -\frac{4\pi G^2 \bar{f}(\boldsymbol{v}) \mathrm{d}^3\boldsymbol{v}_{\mathrm{m}} m M (m+M) \ln\Lambda}{v_{\mathrm{M}}^3} \boldsymbol{v}_{\mathrm{M}}, \tag{3.34}$$

where $\ln\Lambda$ is the *Coulomb logarithm* (see BINNEY & TREMAINE, 1987) and

$$\bar{f}(\boldsymbol{v}) \equiv \frac{\int_V f(\boldsymbol{x},\boldsymbol{v}) \mathrm{d}^3\boldsymbol{x}}{\int_V \mathrm{d}^3\boldsymbol{x}}. \tag{3.35}$$

If isotropic velocity distribution of background particles is taken into account, $\bar{f}(\boldsymbol{v})$ becomes Maxwellian with dispersion σ, and after integration of (3.34) over all velocities, the classical formula for dynamical friction (CHANDRASEKHAR, 1943) can be expressed as

$$\boldsymbol{F}_{\mathrm{DF}} = -\frac{4\pi \ln\Lambda G^2 \rho_{\mathrm{h}}(R,z) M}{v_{\mathrm{M}}^3} \frac{2}{\sqrt{\pi}} \left[-Y \exp\left(-Y^2\right) + \int_0^Y \exp\left(-t^2\right) \mathrm{d}t \right] \boldsymbol{v}_{\mathrm{M}}, \tag{3.36}$$

where $Y \equiv v_M/\sqrt{2}\sigma$.

We have solved the Jeans equations for an axially symmetric logarithmic potential. The relations (3.31) and (3.33) describe velocity ellipsoid for such a configuration. It is obvious that the velocity distribution is generally anisotropic (see Fig. 3.3). In that case, one has to ask if (3.36) is an appropriate and reliable approximation of the drag force. PEÑARRUBIA ET AL. (2004) focused on various approaches to the problem of dynamical friction and introduced a comparative study of (3.36), analytic formula by BINNEY (1977) applicable on systems with an axially symmetric velocity dispersion, and self–consistent N–body simulations of sinking satellites. They showed, that solution by BINNEY (1977) is a significant improvement to the standard approach with Chandrasekhar's formula, if deviation from an isotropic velocity distribution exists. The analytic prescription for dynamical friction by BINNEY (1977) is based on the previously listed assumptions, but it allows for axial symmetry of the velocity distribution. Regarding (3.25)(axial symmetry), and the results by PEÑARRUBIA ET AL. (2004), we consider the Binney's model a suitable description of dynamical friction exerted on a satellite galaxy as it moves through the extended logarithmic halo of MW.

Identically to the approach by CHANDRASEKHAR (1943), the Binney's formula is derived from (3.34) by its integration over the entire velocity space, when one has to substitute (3.24) for $f(\boldsymbol{x}, \boldsymbol{v})$ in (3.35). Then, the zeroth order specific friction force is (for details see BINNEY, 1977):

$$F^{i}_{\mathrm{DF}} = -\frac{2\sqrt{2\pi}\rho_{\mathrm{h}}(R,z)G^{2}M\sqrt{1-{e_v}^{2}}\ln\Lambda}{{\sigma_R}^{2}\sigma_z}B_R v^{i}_{\mathrm{M}}, \tag{3.37}$$

$$F^{z}_{\mathrm{DF}} = -\frac{2\sqrt{2\pi}\rho_{\mathrm{h}}(R,z)G^{2}M\sqrt{1-{e_v}^{2}}\ln\Lambda}{{\sigma_R}^{2}\sigma_z}B_z v^{z}_{\mathrm{M}}, \tag{3.38}$$

where $i = x, y$ and (σ_R, σ_z) is the velocity dispersion ellipsoid with ellipticity ${e_v}^2 = 1 - (\sigma_z/\sigma_R)^2$, and

$$B_R = \int_0^\infty \frac{\exp\left(-\frac{v_R^2/2\sigma_R^2}{1+q} - \frac{v_z^2/2\sigma_R^2}{1-e_v^2+q}\right)}{(1+q)^2(1-e_v^2+q)^{1/2}}dq, \tag{3.39}$$

$$B_z = \int_0^\infty \frac{\exp\left(-\frac{v_R^2/2\sigma_R^2}{1+q} - \frac{v_z^2/2\sigma_R^2}{1-e_v^2+q}\right)}{(1+q)(1-e_v^2+q)^{3/2}}dq, \tag{3.40}$$

where (v_R, v_z) are the components of the satellite velocity in cylindrical coordinates.

After summarizing the features of our model of the LMC–SMC–MW interaction introduced in Sec. 3.3, Sec. 3.4 and Sec. 3.5, we get the following equations of motion of the Magellanic Clouds:

$$\frac{\mathrm{d}\boldsymbol{v}_{\mathrm{LMC}}}{dt} = -(\nabla\Phi_{\mathrm{L}} + \nabla\Phi_{\mathrm{P}}^{\mathrm{SMC}}) + \frac{\boldsymbol{F}_{\mathrm{DF}}}{m_{\mathrm{LMC}}}, \tag{3.41}$$

$$\frac{\mathrm{d}\boldsymbol{v}_{\mathrm{SMC}}}{\mathrm{d}t} = -(\nabla\Phi_{\mathrm{L}} + \nabla\Phi_{\mathrm{P}}^{\mathrm{LMC}}) + \frac{\boldsymbol{F}_{\mathrm{DF}}}{m_{\mathrm{SMC}}}, \tag{3.42}$$

where $\Phi_{\mathrm{P}}^{\mathrm{LMC}}$, $\Phi_{\mathrm{P}}^{\mathrm{SMC}}$ are the LMC, SMC Plummer potentials, and $\boldsymbol{F}_{\mathrm{DF}}$ is the dynamical friction force exerted on the Clouds as they move in the MW DM halo. Initial conditions for the starting point of the evolution of the System at the time –4 Gyr were obtained by the standard backward integration of equations of motion (3.41, 3.42) (see e.g. MURAI & FUJIMOTO, 1980; GARDINER ET AL., 1994). Basically, the choice for the starting epoch of this study originates in the fact that MW, LMC and SMC form an isolated system in our model. Such an assumption was very common in previous papers on the Magellanic System (e.g. MURAI & FUJIMOTO, 1980; GARDINER ET AL., 1994, 1996) and was motivated by insufficient kinematic information about the Local Group, that did not allow to estimate the influence of its members other than MW on the evolution of the Magellanic System. Our detailed analysis of the orbits of the LMC and SMC showed that the galactocentric distance of either of the Clouds did not exceed 300 kpc within the last 4 Gyr. Investigation of the kinematic history of the Local Group by BYRD ET AL. (1994) indicates, that the restriction of the maximal galactocentric radius of the Magellanic System to $R_{\rm max} \approx 300\,{\rm kpc}$ for $T > -4\,{\rm Gyr}$ corresponds to the assumption that the orbital motion of the Clouds is gravitationally dominated by MW.

Our simulations are performed with the total number of 10 000 test–particles equally distributed to both Clouds. We start the simulation with test–particles in a disk–like configuration with an exponential particle density profile (3.3), and compute the evolution of the test–particle distribution up to the present time. Regarding the nature of test–particles, they serve as objects mapping the underlying gravitational potential of MW+LMC+SMC, and allow for analysis of tidal processes in the interacting system. The equation of motion of the i–th test–particle involves pure gravitational interaction:

$$\frac{{\rm d}\boldsymbol{v}_i}{{\rm d}t} = -(\nabla\Phi_{\rm L} + \nabla\Phi_{\rm P}^{\rm LMC} + \nabla\Phi_{\rm P}^{\rm SMC}). \tag{3.43}$$

Together with (3.41) and (3.42), the equation of motion (3.43) form a full set of equations describing the evolution of the system LMC–SMC–MW in our model. The equations are integrated from $T = -4\,{\rm Gyr}$ up to present.

CHAPTER 4

Parameter Space of the MW–LMC–SMC Interaction

In this chapter we introduce the parameters of the Magellanic System interaction that are subject to our GA search. The parameters involve the initial conditions of the LMC and SMC motion, their total masses, parameters of mass distribution, particle disc radii and orientation angles, and also the MW dark matter halo potential flattening parameter. Tab. 4.1 summarizes the parameters of the interaction and introduces their limiting values. Models are described in a right–handed Cartesian coordinate system with the origin in the Galactic center. This system is considered to be an inertial frame, because we assume that $m_{\mathrm{MW}} \gg m_{\mathrm{LMC}}, m_{\mathrm{SMC}}$. Therefore, the center of mass of the system may be placed at the Galactic center. We assume the present position vector of the Sun $\boldsymbol{r}_{\odot} = (-8.5, 0.0, 0.0)$ kpc. In the following paragraphs we discuss the parameters of the LMC–SMC–MW interaction and the determination of their ranges.

The nature and distribution of dark matter in the Galaxy has been subject to intense research and a large number of models have been proposed. We probe the DM distribution by investigating the redistribution of matter in the Magellanic System due to the MW–LMC–SMC interaction, paying special attention to the features of the Magellanic Stream. That is similar to the method applied by HELMI (2004), who studied kinematic properties of the Sagittarius stream. In order to enable comparison with the results by HELMI (2004), we also adopted the axially symmetric logarithmic halo model of MW (3.5) and the same values of the halo structural parameters R_{c}, v_0 with a similar range of studied values of the flattening q (see Tab. 4.1). We extended the range of q values tested by HELMI (2004) to the lower limit of $q = 0.74$, which is the minimal value acceptable for the model of a logarithmic halo (for a detailed explanation see BINNEY & TREMAINE (1987). For every value of q a time–consuming calculation of parameters of dynamical friction is required (see Sec. 3.5). To reduce the computational difficulties, the flattening q was treated as a discrete value with a step of $\Delta q = 0.02$, and the parameters of dynamical friction were tabulated. The upper limit of $q = 1.20$ was selected to enable testing of prolate halo configurations. Extension of the halo flattening range to higher values was not considered due to the computational performance limits of our numerical code.

Param.	Value	
$\boldsymbol{r}_{\mathrm{LMC}}$[kpc]	$\begin{pmatrix} \langle -1.5,-0.5\rangle \\ \langle -41.0,-40.0\rangle \\ \langle -27.1,-26.1\rangle \end{pmatrix}$	Current galactocentric position vectors
$\boldsymbol{r}_{\mathrm{SMC}}$[kpc]	$\begin{pmatrix} \langle 13.1,14.1\rangle \\ \langle -34.8,-33.8\rangle \\ \langle -40.3,-39.3\rangle \end{pmatrix}$	
$\boldsymbol{v}_{\mathrm{LMC}}[\mathrm{km\,s^{-1}}]$	$\begin{pmatrix} \langle -3,85\rangle \\ \langle -231,-169\rangle \\ \langle 132,206\rangle \end{pmatrix}$	Current velocity vectors
$\boldsymbol{v}_{\mathrm{SMC}}[\mathrm{km\,s^{-1}}]$	$\begin{pmatrix} \langle -112,232\rangle \\ \langle -346,-2\rangle \\ \langle 45,301\rangle \end{pmatrix}$	
$m_{\mathrm{LMC}}[10^9\mathrm{m}_\odot]$	$\langle 15.0,25.0\rangle$	Masses
$m_{\mathrm{SMC}}[10^9\mathrm{m}_\odot]$	$\langle 1.5,2.5\rangle$	
ϵ_{LMC}[kpc]	$\langle 2.5,3.5\rangle$	Plummer sphere scale radii
ϵ_{SMC}[kpc]	$\langle 1.5,2.5\rangle$	
$r^{\mathrm{disk}}_{\mathrm{LMC}}$[kpc]	$\langle 9.0,11.0\rangle$	Particle disk radii
$r^{\mathrm{disk}}_{\mathrm{SMC}}$[kpc]	$\langle 5.0,7.0\rangle$	
$\Theta^{\mathrm{disk}}_{\mathrm{LMC}}$	$\langle 87^\circ,107^\circ\rangle$	Disk orientation angles
$\Phi^{\mathrm{disk}}_{\mathrm{LMC}}$	$\langle 261^\circ,281^\circ\rangle$	
$\Theta^{\mathrm{disk}}_{\mathrm{SMC}}$	$\langle 35^\circ,55^\circ\rangle$	
$\Phi^{\mathrm{disk}}_{\mathrm{SMC}}$	$\langle 220^\circ,240^\circ\rangle$	
q	$\langle 0.74,1.20\rangle$	MW DM halo potential flattening

Table 4.1: Parameters of the MW–LMC–SMC interaction.

The estimated ranges of the values of the remaining parameters are based on our observational knowledge in the Magellanic System. A very detailed review of distance determinations of the Magellanic Clouds is given in VAN DEN BERGH (2000, p. 185–191 for LMC, p. 267–271 for SMC). From observations of Cepheids, RR Lyrae stars, Mira variables, red stars, open clusters, planetary nebulae and SN 1987A unweighted mean distance moduli were found. Tables summarizing recent distance determinations to LMC (Tab. 4.2) and SMC (Tab. 4.3) follow. These data yield unweighted mean values of the distance moduli of the Magellanic Clouds that are $\overline{(m-M)_0} = 18.50 \pm 0.05$ for

Method	$(m-M)_0$	References and comments
Cepheids	18.46 ± 0.06	Gieren et al. (1997)
Cepheids	18.51 ± 0.05	Wood et al. (1997)
Cepheids	18.56 ± 0.08	Oudmaijer et al. (1998)
RR Lyrae	18.48 ± 0.19	Alcock et al. (1997)
RG tip	18.64 ± 0.14	Salaris & Cassisi (1998) (Tip of red giant branch)
Red clump	18.36 ± 0.17	Cole (1998)
SX Phe	18.56 ± 0.10	McNamara (1997) (Period–Luminosity relation for SX–Phe stars was used in order to calibrate M_V(RR Lyr))
Miras	18.60 ± 0.05	van Leeuwen et al. (1997) (Period–Luminosity relation in K–band)
Miras	18.47 ± 0.05	van Leeuwen et al. (1997) (Period–Luminosity relation in $M_{\rm bol}$)
Miras	18.50 ± 0.17	Bergeat et al. (1998) (Period–Luminosity relation for carbon–rich long–period variables observed with the HIPPARCOS satellite)
Planetary nebulae	18.44 ± 0.18	Jacoby (1997) (PN luminosity function)
SN 1987A	18.58 ± 0.05	Panagia et al. (1998) (Combination of IUE light curves of SN 1987A with HST imaging gave absolute and angular sizes of the SN ring)
SM 1987A	$< 18.37 \pm 0.04$	Gould & Uza (1998) (Obtained from the "light echo" times to the near and far side of the ring around SN 1987A)

Table 4.2: Results of various methods employed in order to find distance modulus of LMC. For more detailed explanation see Van den Bergh (2000) and works cited above.

LMC and $\overline{(m-M)_0} = 18.85 \pm 0.10$ for SMC, corresponding to Heliocentric distances of (50.1 ± 1.2) kpc and (58.9 ± 2.6) kpc, respectively. However, the significance of the value of the distance modulus of SMC is open to question because all of the Cepheid–based distance estimates are greater than this value, whereas all of those obtained from RR Lyrae stars are smaller than this value. Cartesian coordinates of the position vectors of the Magellanic Clouds are listed in Tab. 4.1. Only 2 of the 6 components of the position vectors enter the GA search as free parameters, because the rest of them is determined by the projected position of the Clouds on the plane of sky, that is $(l,b)_{\rm LMC} = (280^\circ\,27', -32^\circ\,53')$ and $(l,b)_{\rm SMC} = (302^\circ\,47', -44^\circ\,18')$.

Method	$(m-M)_0$	References and comments
Cepheids	18.94 ± 0.05	VAN DEN BERGH (2000)
Cepheids	18.87	LANEY & STOBIE (1994) (Period–Luminosity relation in V–band)
Cepheids	19.02	LANEY & STOBIE (1994) (Period–Luminosity relation in K–band)
Surface brightness	18.90 ± 0.20	BARNES ET AL. (1993) (They used their visual surface brightness technique)
RR Lyrae	18.73 ± 0.17	WALKER & MACK (1988) (Observation of RR Lyr stars in NGC 121)
RR Lyrae	18.78 ± 0.20	REID & STRUGNELL (1986) (Field RR Lyrae in SMC)
RR Lyrae	18.73	SMITH ET AL. (1992) (Field RR Lyrae in the vicinity of NGC 121)
RR Lyrae	18.66	SMITH ET AL. (1992) (Field RR Lyrae in the vicinity of NGC 361)
RR Lyrae	18.76	KALUZNY ET AL. (1998) (RR Lyr variables in the field of 47 Tucanae)
Planetary nebulae	19.09 ± 0.29	JACOBY (1997) (PN luminosity function)

Table 4.3: List of distance moduli of SMC obtained in different ways from observational data. Used methods are commented in VAN DEN BERGH (2000) in a detailed manner.

Previous studies by MURAI & FUJIMOTO (1980) and GARDINER ET AL. (1994) found out that the correct choice for the spatial velocities is crucial for reproducing the observed H I structures. In order to obtain present spatial velocities of the Magellanic Clouds, knowledge in their proper motion is essential. However, proper motion measurements demand appreciable precision because of the distance to the Clouds that implies extremely small annual change of their positions on the plane of sky.

Generally, more precise determination of proper motion was achieved for LMC. It is a natural fact, regarding larger Heliocentric distance to SMC and a small number of stellar objects in SMC that can serve for astrometric measurements. In the following paragraphs a brief introduction into available observational estimates of the LMC and SMC proper motions is provided. The statistically correctly obtained mean values of the proper motion components are summarized in Tab. 4.4.

Our overview starts with the study by JONES ET AL. (1994), who introduced an estimate of the proper motion of LMC based on 21 photographic plates spanning 14 yr. Kroupa et al. (1994) used a relatively small sample of 35 LMC and 8 SMC stars listed in the Position and Proper Motion Catalogue to derive proper motions of the centers of the analyzed sets of LMC and SMC stars, respectively. Later, the information about the LMC and SMC stars collected by the HIPPARCOS satellite was investigated by Kroupa & Bastian (1997).

	LMC	SMC	Reference
$\mu_\alpha \cos\delta$	$+1.37 \pm 0.28$	–	Jones et al. (1994)
μ_δ	-0.18 ± 0.27	–	Jones et al. (1994)
$\mu_\alpha \cos\delta$	$+1.3 \pm 0.6$	$+0.5 \pm 1.0$	Kroupa et al. (1994)
μ_δ	$+1.1 \pm 0.7$	-2.0 ± 1.4	Kroupa et al. (1994)
$\mu_\alpha \cos\delta$	$+1.94 \pm 0.29$	1.23 ± 0.84	Kroupa & Bastian (1997)
μ_δ	-0.14 ± 0.36	-1.21 ± 0.75	Kroupa & Bastian (1997)
$\mu_\alpha \cos\delta$	$+1.8 \pm 0.2$	–	Pedreros et al. (2002)
μ_δ	$+0.3 \pm 0.2$	–	Pedreros et al. (2002)
$\mu_\alpha \cos\delta$	–	$+0.6 \pm 0.6$	Anderson & King (2004)
μ_δ	–	-1.9 ± 0.6	Anderson & King (2004)
$\mu_\alpha \cos\delta$	$+2.03 \pm 0.08$	–	Kallivayalil et al. (2006a)
μ_δ	$+0.44 \pm 0.05$	–	Kallivayalil et al. (2006a)
$\mu_\alpha \cos\delta$	–	$+1.16 \pm 0.18$	Kallivayalil et al. (2006b)
μ_δ	–	-1.17 ± 0.18	Kallivayalil et al. (2006b)

Table 4.4: Independently measured proper motions in mas/yr.

Operating from 1989 to 1993, astrometry satellite HIPPARCOS performed optical astrometry with typical mean errors smaller than 1 mas (milliarcsec) and systematic errors smaller than 0.1 mas. Also a large number of observations with lower precision were realized. It is important that HIPPARCOS also observed 36 LMC and 11 SMC stars and their astrometric parameters, i.e. coordinates α_i, δ_i at epoch 1991.25, the proper motion components $\mu_{\alpha,i} \cos\delta_i$, $\mu_{\delta,i}$, the parallax π_i and their standard errors, are comprised in The HIPPARCOS Catalogue. Due to the special measurement approach of HIPPARCOS, the astrometric parameters for a given star are not statistically independent, but mutually correlated. Unfortunately, also correlations between the astrometric parameters of different stars have to be taken into account. These correlations are significant for stars with their separation less than 5° on the sphere. Therefore, an elaborate analysis of the proper motions in the case of the LMC and SMC stars is required. It is also necessary to point out that three LMC stars were excluded from the statistical set because their HIPPARCOS measurements are disturbed and two SMC stars had to be excluded because of a suspicion that they lie in a region of SMC which may be tidally disturbed by LMC. For the detailed explanation see Kroupa & Bastian (1997) and works cited therein.

Analysis of proper motion of LMC relatively to the selected background quasi–stellar periodic object (QPO) located on 44 CCD frames made by Pedreros et al. (2002).

The data was obtained from 1989.0 to 2000.0 at the Cassegrain focus of the Cerro Tololo Inter–American Observatory 1.5 m telescope. Anderson & King (2004) measured a very accurate relative proper motion between SMC and the globular cluster 47 Tucanae of $\overline{\mu_\alpha \cos\delta} = +4.176 \pm 0.035\,\mathrm{mas\,yr^{-1}}$ and $\overline{\mu_\delta} = -1.357 \pm 0.021\,\mathrm{mas\,yr^{-1}}$. When combined with an estimate of the absolute proper motion of 47 Tucanae by Freire et al. (2003), who report $\overline{\mu_\alpha \cos\delta} = +5.3 \pm 0.6\,\mathrm{mas\,yr^{-1}}$ and $\overline{\mu_\delta} = -3.3 \pm 0.6\,\mathrm{mas\,yr^{-1}}$, that implies the values of the proper motion listed in Tab. 4.4. Similarly to the approach by Pedreros et al. (2002), the LMC proper motion on the background of 21 QPOs was studied by Kallivayalil et al. (2006a). They used the astrometric data coming from the High

	LMC	SMC	Reference
$\left(\overline{\mu_\alpha \cos\delta}\right)^{\mathrm{a}}$	$+1.65 \pm 0.20$	-	Kroupa & Bastian (1997) + Jones et al. (1994)
$(\overline{\mu_\delta})^{\mathrm{a}}$	-0.17 ± 0.22	-	Kroupa & Bastian (1997) + Jones et al. (1994)
$\left(\overline{\mu_\alpha \cos\delta}\right)^{\mathrm{b}}$	-	$+0.91 \pm 0.19$	Kroupa & Bastian (1997) + Anderson & King (2004)
$(\overline{\mu_\delta})^{\mathrm{b}}$	-	-1.28 ± 0.36	Kroupa & Bastian (1997) + Anderson & King (2004)
$\left(\overline{\mu_\alpha \cos\delta}\right)^{\mathrm{c}}$	$+1.94 \pm 0.09$	-	Kallivayalil et al. (2006a) + Jones et al. (1994) + Kroupa et al. (1994) + Kroupa & Bastian (1997) + Pedreros et al. (2002)
$(\overline{\mu_\delta})^{\mathrm{c}}$	$+0.43 \pm 0.06$	-	Kallivayalil et al. (2006a) + Jones et al. (1994) + Kroupa et al. (1994) + Kroupa & Bastian (1997) + Pedreros et al. (2002)
$\left(\overline{\mu_\alpha \cos\delta}\right)^{\mathrm{d}}$	-	$+1.04 \pm 0.13$	Kallivayalil et al. (2006b) + Anderson & King (2004) + Kroupa & Bastian (1997)
$(\overline{\mu_\delta})^{\mathrm{d}}$	-	-1.19 ± 0.16	Kallivayalil et al. (2006b) + Anderson & King (2004) + Kroupa & Bastian (1997)
$\left(\overline{\mu_\alpha \cos\delta}\right)^{\mathrm{e}}$	$+1.61 \pm 0.19$	$+0.93 \pm 0.64$	Kroupa & Bastian (1997) + Jones et al. (1994) + Kroupa et al. (1994)
$(\overline{\mu_\delta})^{\mathrm{e}}$	-0.06 ± 0.21	-1.39 ± 0.66	Kroupa & Bastian (1997) + Jones et al. (1994) + Kroupa et al. (1994)

Table 4.5: Proper motion of the Magellanic Clouds. Weighted mean values with standard deviations of the mean.

Resolution Camera (HRC) of the Advanced Camera for Surveys on the Hubble Space Telescope. The QPOs are distributed homogeneously behind the central area of LMC. The same method was employed in order to obtain the proper motion of SMC (Kallivayalil et al., 2006b). However, only the sample of 5 QPOs observed by HRC could be used for SMC.

Several combinations of the above mentioned independent measurements result in an improved estimate of the proper motions reviewed in Tab. 4.5. The LMC proper motion components $\overline{\mu_\alpha \cos\delta}^{\mathrm{c}}$, $\overline{\mu_\delta}^{\mathrm{c}}$ and the values $\overline{\mu_\alpha \cos\delta}^{\mathrm{d}}$, $\overline{\mu_\delta}^{\mathrm{d}}$ obtained for SMC are the most precise estimates that are currently available. Even though the precision of the proper motion measurements of both Clouds has been improved remarkably during the last 10 years, it still does not allow for clear statements on the dynamical evolution and interaction scenario of the Magellanic System (see Kallivayalil et al., 2006a,b). With respect to that, we decided to select the entire relatively large area of the LMC and SMC velocity space defined by the ranges of $\overline{\mu_\alpha \cos\delta}^{\mathrm{e}}$, $\overline{\mu_\delta}^{\mathrm{e}}$ to be a subject to the automated search of the parameter space of the LMC–SMC–MW interaction, since a detailed analysis of the corresponding models might establish additional constraints on the proper motions.

The proper motion ranges for SMC include the improved intervals $\overline{\mu_\alpha \cos\delta}^{\mathrm{d}}$, $\overline{\mu_\delta}^{\mathrm{d}}$. The adopted proper motion ranges for LMC do not entirely intersect with the compiled results by Jones et al. (1994); Kroupa et al. (1994); Kroupa & Bastian (1997); Pedreros et al. (2002) when the corrections by Kallivayalil et al. (2006a) are taken into account ($\overline{\mu_\alpha \cos\delta}^{\mathrm{c}}$, $\overline{\mu_\delta}^{\mathrm{c}}$). The study by Kallivayalil et al. (2006a) was not available for the purpose of our first detailed analysis of the parameter space that is presented here. However, it will be shown later that the velocity vectors of the Magellanic Clouds play a crucial role in the process of the dynamical evolution of the System, which implies necessity of further analysis of the velocity space with clear request for new improved data on proper motions.

Thus, the galactocentric space motion of the Magellanic Clouds is estimated following the measurement of the proper motion components $\overline{\mu_\alpha \cos\delta}^{\mathrm{e}}$, $\overline{\mu_\delta}^{\mathrm{e}}$ (see Tab. 4.5), considering the position and velocity vectors of the Sun and of the position and measured radial velocity of both Magellanic Clouds. Then, the galactocentric velocity vectors and the galactocentric radial and tangential velocity components of LMC and SMC are:

$$\boldsymbol{v}^{\mathrm{e}}_{\mathrm{LMC}} = \begin{pmatrix} +41 \pm 44 \\ -200 \pm 31 \\ +169 \pm 37 \end{pmatrix} \mathrm{km\,s^{-1}}, \tag{4.1}$$

$$\boldsymbol{v}^{\mathrm{e}}_{\mathrm{rad,LMC}} = 74 \pm 33\,\mathrm{km\,s^{-1}}, \tag{4.2}$$

$$\boldsymbol{v}^{\mathrm{e}}_{\mathrm{tang,LMC}} = 255 \pm 33\,\mathrm{km\,s^{-1}}, \tag{4.3}$$

$$\boldsymbol{v}^{\mathrm{e}}_{\mathrm{SMC}} = \begin{pmatrix} +60 \pm 172 \\ -174 \pm 172 \\ +173 \pm 128 \end{pmatrix} \mathrm{km\,s^{-1}}, \tag{4.4}$$

$$v^{\mathrm{e}}_{\mathrm{rad,SMC}} = -2 \pm 150\,\mathrm{km\,s^{-1}}, \tag{4.5}$$

$$v^{\mathrm{e}}_{\mathrm{tang,SMC}} = 253 \pm 150\,\mathrm{km\,s^{-1}}. \tag{4.6}$$

The corresponding galactocentric velocity vector of the Sun is

$$\boldsymbol{v}_{\odot} = \begin{pmatrix} +9 \\ +232 \\ +12 \end{pmatrix} \mathrm{km\,s^{-1}}. \tag{4.7}$$

To derive the actual initial conditions at the starting time of the simulation from the current positions and velocities of the Clouds, we employed the backward integration of equations of motion.

Another serious uncertainty in the input parameters for our model arises from the wide range of possible LMC and SMC masses. Their determinations are usually based on a various scale of kinematic studies and it may be useful to review recent works concerning masses of the Magellanic Clouds.

Observations demand such an interpretation that LMC is a galaxy with a differentially rotating disk and possessing a dark halo extending at least beyond 10 kpc (see KUNKEL ET AL., 1997). The inner part of LMC inside a radius of approximately 6 kpc was a subject of interest of HUGHES, WOOD & REID (1991) who found out that velocity distribution of the old long–period variables indicates that $m_{\mathrm{LMC}} \lesssim (6.2 \pm 1.5) \cdot 10^{9}\,\mathrm{m}_{\odot}$. From HI rotation curve and radial velocities of planetary nebulae MEATHERINGHAM ET AL. (1988) derived an estimate for the LMC mass within 6 kpc to be $6 \cdot 10^{9}\,\mathrm{m}_{\odot}$. One of the most complete works treating the periphery of LMC is that of SCHOMMER ET AL. (1992) estimating the mass of LMC from kinematics of star clusters. According to this work $m_{\mathrm{LMC}} \in (1.5, 2.5) \cdot 10^{10}\,\mathrm{m}_{\odot}$ which is in a well agreement with the value $m_{\mathrm{LMC}}(r < 10\,\mathrm{kpc}) = 1.51 \cdot 10^{10}\,\mathrm{m}_{\odot}$ obtained by KUNKEL ET AL. (1997) from the rotation curve of carbon stars lying from 3 to 12 kpc. All these results have been collected by VAN DEN BERGH (2000) who inferred that $m_{\mathrm{LMC}} \in (0.6, 2.5) \cdot 10^{10}\,\mathrm{m}_{\odot}$.

For SMC, a lower mass limit of $1 \cdot 10^{9}\,\mathrm{m}_{\odot}$ is suggested from observations of carbon stars (HARDY ET AL., 1989) and planetary nebulae (DOPITA ET AL., 1985) in both cases lying within 3 kpc from center. Since the carbon star halo and the planetary nebulae halo extend out to 6 kpc from the center (VAN DEN BERGH, 2000), the total mass is again probably much larger. The estimate by (VAN DEN BERGH, 2000) is $m_{\mathrm{SMC}} \in (0.8, 2.0) \cdot 10^{9}\,\mathrm{m}_{\odot}$.

In general, masses of the Clouds are functions of time and evolve due to the LMC–SMC exchange of matter, and as a consequence of the interaction between the Clouds and MW. Our test–particle model does not allow for a reasonable treatment of a time–dependent mass–loss. Therefore, masses of the Clouds are considered constant in time and their initial values at the starting epoch of our simulations are approximated by the current LMC and SMC masses. The mass ranges that we investigated can be found in Tab. 4.1. Our estimates are based on those by VAN DEN BERGH (2000), but the limits are slightly shifted toward larger values, regarding the fact that the Clouds do not experience any mass–loss in our model. Based on the large range of the LMC and SMC mass estimates available (for details see VAN DEN BERGH, 2000), $m_{\rm LMC}$ and $m_{\rm SMC}$ are also treated as free input parameters of our model that become subjects to the GA optimization.

Scale radii of the LMC and SMC Plummer potentials $\epsilon_{\rm LMC}$, $\epsilon_{\rm SMC}$ are input parameters of the model describing the radial mass distribution in the Clouds. The study by GARDINER ET AL. (1994) used the values $\epsilon_{\rm LMC} = 3\,{\rm kpc}$ and $\epsilon_{\rm SMC} = 2\,{\rm kpc}$. In order to investigate the influence of this parameter on the evolution of the Magellanic System, the Plummer radii were involved into the GA search and their values were varied within the ranges of the width of 1 kpc, including the estimates by GARDINER ET AL. (1994)) (see Tab. 4.1).

GARDINER ET AL. (1994) analyzed the H I surface contour map of the Clouds to estimate the initial LMC and SMC disk radii entering their model of the Magellanic System. Regarding the absence of a clearly defined disk of SMC, and possible significant mass redistribution in the Clouds during their evolution, the results require a careful treatment and a further verification. We varied the current estimates of disk radii $r^{\rm disk}_{\rm LMC}$, $r^{\rm disk}_{\rm SMC}$ as free parameters within the ranges introduced in Tab. 4.1, containing the values derived by GARDINER ET AL. (1994), and used them as initial values at the starting point of our calculations.

The orientation of the disks is described by two angles Θ and Φ defined by GARDINER ET AL. (1996). Several observational determinations of the LMC disk plane orientation were collected by LIN ET AL. (1995). Its sense of rotation is assumed clockwise (LIN ET AL., 1995; KROUPA & BASTIAN, 1997). Position angle of the bar structure in SMC was used by GARDINER ET AL. (1996) to investigate the current disk orientation. Their results allow for wide ranges of the LMC, SMC disk orientation angles (see Tab. 4.1) and so we investigated Θ and Φ by the GA search method, too. Similarly to GARDINER ET AL. (1996) we use the current LMC and SMC disk orientation angles (Tab. 4.1) to approximate their initial values.

CHAPTER 5

Genetic Algorithms

Genetic Algorithms are a family of computational models inspired by evolution (evolutionary algorithms). These algorithms encode a potential solution to a specific problem on a simple chromosome–like data structure and apply recombination operators to these structures so as to preserve critical information. GAs are often viewed as function optimizers, although the range of problems to which GAs have been applied is quite broad. Algorithms that mimic the process of natural evolution were proposed and studied by RECHENBERG (1965), RECHENBERG (1973) and especially by HOLLAND (1975). This chapter introducing the principles of evolutionary computing brings an excellent review of the theory of GA by WHITLEY (1994).

The principle of the natural evolution suggests that GA is not a plausible tool for the tasks that require identification of the optimal solution. The evolutionary process should be viewed as an iterative search for the best result to the given problem. The best solution is very unlikely to be identified, but a very good result may be achieved on a relatively short time–scale. GA becomes a very robust optimizer if the space of possible solutions does not allow for testing every candidate. Then, GA is capable to reach a remarkably fast progress by preserving and collecting features of good solutions, which drives the algorithm to identification of generally better solutions in the next iterative steps. The point is that as long as the number of "good solutions" to a problem are sparse with respect to the size of the search space, then random search or search by enumeration of a large search space is not a practical form of problem solving. On the other hand, any search other than random search introduces some bias in terms of how it looks for better solutions and where it looks in the search space. GAs indeed introduce a particular bias in terms of what new points in the space will be sampled. Nevertheless, GA belongs to the class of methods known as "weak methods" because it makes relatively few assumptions about the problem that is being solved.

Of course, there are many optimization methods that have been developed in mathematics and operations research. What role do GAs play as an optimization tool? GAs are often described as a global search method that does not use gradient information. Thus, nondifferentiable functions as well as functions with multiple local optima represent classes of problems to which GAs might be applied. GAs, as a weak method, are robust but very general. If there exists a good specialized optimization method for a specific problem, then GA may not be the best optimization tool for that application. On the other hand, some researchers work with hybrid algorithms that combine existing methods with GAs.

5.1 Following the Nature

An implementation of GA begins with a *population* of *chromosomes* (individuals). Creation of that first population is often called *initialization* (follow the schematic view of GA in Fig. 5.1). One then evaluates these structures and allocates reproductive opportunities in such a way that those chromosomes which represent a better solution to the target problem are given more chances to reproduce than those chromosomes which are poorer solutions. The quality of a solution is typically defined with respect to the current population. Following the evaluation, *selection* of chromosomes is made proportionally to their quality. Subsequently, genetic operators, such as *crossover* or *mutation*, are applied to produce the next population (generation). The iterative process continues until the defined convergence criterion is satisfied. This particular description of GA is intentionally abstract because in some sense, the term GA has two meanings. In a strict interpretation, GA refers to a model introduced and investigated by HOLLAND (1975) and DEJONG

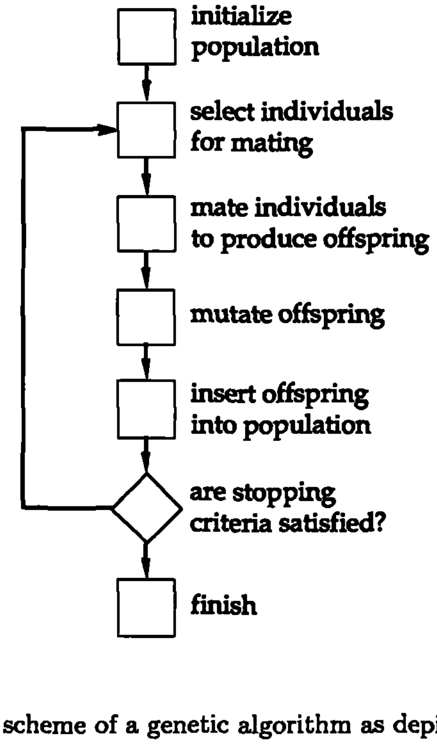

Figure 5.1: General scheme of a genetic algorithm as depicted in WALL (1996).

(1975). It is still the case that most of the existing theory for GAs applies either solely or primarily to the model introduced by Holland (1975), as well as variations on what will be referred to in this thesis as the *canonical genetic algorithm.* In a broader usage of the term, GA is any population–based model that uses selection and recombination operators to generate new sample points in a search space.

5.1.1 Encoding, Evaluation and Optimization Problems

This section refers to the remarkable fact that there are only two components of GA that are problem dependent: the problem *encoding* and *evaluation function.*

Consider a parameter optimization problem where we must optimize a set of variables either to maximize some target such as profit, or to minimize cost or some measure of error. We might view such a problem as a black box with a series of control dials representing different parameters; the only output of the black box is a value returned by an evaluation function indicating how well a particular combination of parameter settings solves the optimization problem. The goal is to set the various parameters so as to optimize some output. In more traditional terms, we wish to minimize (or maximize) some function $f(x_1, x_2, \dots, x_m)$ of m variables.

Most users of GAs typically are concerned with problems that are nonlinear. This also often implies that it is not possible to treat each parameter as an independent variable which can be solved in isolation from the other variables. There are interactions such that the combined effects of the parameters must be considered in order to maximize or minimize the output of the black box.

The first assumption that is typically made is that the variables representing parameters can be represented by bit strings. This means that the variables are discretized, and that the range of the discretization corresponds to some power of 2. For example, with 10 bits per parameter, we obtain a range with 1024 discrete values. If the parameters are

Encoding	Typical chromosome
binary	0111010001101001110010101 0100101100110100111001110 1000000000000000010000000
permutation	0132654897 3210698547 8564230917
tree	(()(()))((()()())(()())()) (x+(x+x))+((x+x)+(x+x))
real	0.123 1.2365 9856.0 5.032145 0.36 1.0 0.1 0.11 0.111 0.2 0.22 0.222

Table 5.1: Common encoding schemes used for GAs.

actually continuous then this discretization is not a particular problem. This assumes, of course, that the discretization provides enough resolution to make it possible to adjust the output with the desired level of precision. It also assumes that the discretization is in some sense representative of the underlying function.

If some parameter can only take on an exact finite set of values then the coding issue becomes more difficult. For example, what if there are exactly 1200 discrete values which can be assigned to some variable x_i. We need at least 11 bits to cover this range, but this codes for a total of 2048 discrete values. The 848 unnecessary bit patterns may result in no evaluation, a default worst possible evaluation, or some parameter settings may be represented twice so that all binary strings result in a legal set of parameter values. Regarding the above discussed drawbacks of the binary coding, a large number of encoding schemes have been proposed. A brief review of the most commonly used coding options is offered in Tab. 5.1. Solving such coding problems is usually considered to be a part of the design of the evaluation function.

Aside from the coding issue, the evaluation function is usually given as part of the problem description. On the other hand, developing an evaluation function can sometimes involve developing a simulation. In other cases, the evaluation may be performance based and may represent only an approximate or partial evaluation. For example, consider a control application where the system can be in any one of an exponentially large number of possible states. Assume a genetic algorithm is used to optimize some form of control strategy. In such cases, the state space must be sampled in a limited fashion and the resulting evaluation of control strategies is approximate and noisy (see WHITLEY, 1994, and references therein).

The evaluation function must also be relatively fast. This is typically true for any optimization method, but it may particularly pose an issue for GAs. Since GA works with a population of potential solutions, it incurs the cost of evaluating this population. Furthermore, the population is replaced (all or in part) on a generational basis. The members of the population reproduce, and their offspring must then be evaluated. If it takes 1 hour to do an evaluation, then it takes over 1 year to do 10 000 evaluations. This would be approximately 50 generations for a population of 200 strings.

5.2 The Canonical Genetic Algorithm

This section introduces the classical scheme of GA devised by HOLLAND (1975). However, the features of the canonical GA apply on a wide class of evolutionary algorithms that are often variations of the basic structure of GA as it was suggested by HOLLAND (1975). The first step in the implementation of any GA is to generate an initial population. In the canonical GA each member of this population will be a binary string of length L which corresponds to the problem encoding. Strings are sometimes called ***genotypes*** (see HOLLAND, 1975) or chromosomes. Typically, the initial population is generated randomly. After creating an initial population, each string is then evaluated and assigned a ***fitness*** value.

Concerning evaluation and fitness, it is necessary to distinguish between the *evaluation function* and the *fitness function* used by GA. The evaluation function (objective function), is a measure of performance with respect to a particular set of parameters. The fitness function transforms that measure (objective score) into an allocation of reproductive opportunities. Objective score of a string representing a set of parameters is independent of the evaluation of any other string. However, the fitness of that string is defined with respect to other members of the current population. Thus, let FF_i be the evaluation of the string i and fit_i its fitness. Then we can write $fit_i = f(FF_1, \ldots, FF_i, \ldots, FF_n)$, where n is the population size. We will see later in this section, that the canonical GA as described by GOLDBERG (1989) uses a linear fitness scaling $fit_i = aFF_i + b$, which becomes a special case $fit_i = FF_i$ here. It is desirable to keep in mind the formal difference between the fitness function and the evaluation function for correct understanding the principle of GA. Nevertheless, it is an usual attitude to speak in terms of fitness, when implementing GA and developing the evaluation function for a specific problem. There is no risk of confusion because the fitness function is apparently an internal prescription of GA for scaling the raw scores returned by the evaluation function. Thus, the term "fitness" will always refer to an objective score assigned by the evaluation function, and the evaluation function itself will be called the fitness function, starting in Chapter 6.

It is useful to view the run of the GA as a two-stage process. It starts with the current population. Selection is applied to the current population to create an intermediate population. Then recombination and mutation are applied to the intermediate population to create the next population. The process of going from the current population to the next population establishes one generation in the GA run (see Fig. 5.1). GOLDBERG (1989) refers to this basic implementation as a Simple Genetic Algorithm.

We will first consider the construction of the intermediate population from the current population. In the first generation the current population is also the initial population. After calculating the target sampling rate (tsr) $FF_i/\overline{FF}$ for all the strings in the current population, selection is performed. In the canonical GA the probability that strings in the current population are copied and placed in the intermediate generation is proportional to their tsr. A selection process that satisfies the expected fitness values better is *remainder stochastic sampling*. For each string i, where $FF_i/\overline{FF} > 1.0$, the integer portion of this number indicates how many copies of that string are directly placed in the intermediate population. All the strings (including those with $FF_i/\overline{FF} < 1.0$) then place additional copies in the intermediate population with a probability corresponding to the fractional portion of $FF_i/\overline{FF}$. For example, a string with $FF_i/\overline{FF} = 1.36$ places 1 copy in the intermediate population and then receives a 0.36 chance of placing a second copy. A string with a fitness of $FF_i/\overline{FF} = 0.54$ has a 0.54 chance of placing one string in the intermediate population.

After selection has been made the construction of the intermediate population is complete and recombination can occur. This can be viewed as creating the next population from the intermediate population. Crossover is applied to randomly paired strings with a probability p_c. A pair of strings is picked and recombined with probability p_c to form two new strings that are inserted into the next population.

Assume the following binary string: 1101001100101101. The string would represent a possible solution to some optimization problem. New sample points in the space are generated by recombining two parent strings. Consider the string 1101001100101101 and another binary string, yxyyxyxxyyyxyxxy, in which the values 0 and 1 are denoted by x and y. Using a single randomly chosen recombination point, *1-point crossover* occurs as follows.

11010 \/ 0110010110
yxyyx /\ yxxyyyxyxxy

Swapping the fragments between the two parents produces the following offspring:

11010yxxyyyxyxxy and yxyyx0110010110

After recombination, we can apply a mutation operator. For each bit in the population, mutation occurs with some low probability p_m. Typically, the mutation rate is applied with probability of order 10^{-2}. In some cases, mutation is interpreted as randomly generating a new bit, in which case, only 50% of the time will the mutation actually change the bit value. In other cases, mutation is interpreted to mean actually flipping the bit.

Finally the process of selection, recombination and mutation is complete and the next population can be evaluated. The process of evaluation, selection, recombination and mutation forms one generation in the run of GA.

5.3 Why Does It Work?

The answer which is most often given to explain the computational behavior of GAs came from work by HOLLAND (1975), where several arguments are developed to explain how GA can result in complex and robust search by implicitly sampling partitions of a search space. For a bit string encoding of length L, the size of the search space is 2^L and forms a *hypercube*. The GA samples the corners of this L-dimensional hypercube and tries to allocate *hyperplanes* containing high-quality solutions. It is easy to show that $3^L - 1$ hyperplanes exist over the entire L-dimensional space. In the next sections, we will show the way GA searches for the optimal solution by sampling hyperplanes. Subsequently, the result will be formalized by the schema theorem.

5.3.1 Hyperplane Sampling

The best way to understand how a genetic algorithm can sample hyperplanes is to consider a simple 3-dimensional space (see Fig. 5.2). Assume we have a problem encoded with just 3 bits - this can be represented as a simple cube with the string 000 at the origin. The corners in this cube are numbered by bit strings and all adjacent corners are labeled by bit strings that differ by exactly 1-bit. The front plane of the cube contains all the points that begin with 0. If "*" is used as a wild card match symbol, then this plane can also be represented by the special string 0**. Strings that contain "*" are called *schemata*, each schema corresponds to a hyperplane in the search space. The order of a hyperplane refers to the number of actual bit values that appear in its schema. Thus, 1** is order–1 while 1**1******0** would be of order–3. A binary string matches a particular schema if that bit string can be constructed from the schema by replacing the "*" symbol with the appropriate bit value. In general, all bit strings that match a particular schema are contained in the hyperplane partition represented by that particular schema. Every binary encoding is a chromosome which corresponds to a corner in the hypercube and is a member of $2^L - 1$ different hyperplanes, where L is the length of the binary encoding.

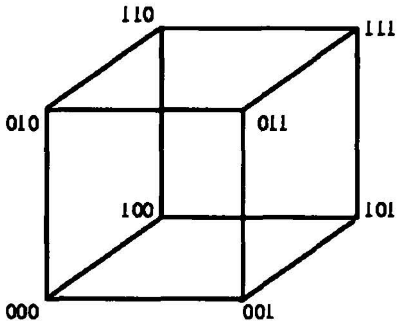

Figure 5.2: Simple example of a 3 D hyperspace established by binary encoding of possible solutions into strings of length 3 (WHITLEY, 1994).

Stating that each string is a member of $2^L - 1$ hyperplanes does not provide useful information if each point in the space is examined in isolation. This is why the idea of a population based search is critical for GAs. A population of sample points provides information about numerous hyperplanes. Moreover, low order hyperplanes should be sampled by a large number of points in the population. Thus, many hyperplanes are sampled when a population of strings is evaluated (see HOLLAND, 1975) which is the key to understanding the principle and remarkable performance of GAs as procedures allocating efficiently high–quality schemata (hyperplanes) in the entire searched space. This feature of GAs is often called *intrinsic (internal) parallelism* (HOLLAND, 1975).

5.3.2 Schema Theorem

The principle of GA was explained as parallel sampling of numerous hyperplanes (schemata) in the searched space of possible solutions. This idea was introduced by HOLLAND (1975), who also suggested the *schema theorem* that provides a reasonable estimate of the change in the sampling rate for a single hyperplane from a generation t to a generation $t+1$.

To start formalizing the idea of hyperplane sampling, lets define $M(H,t)$ as the number of binary strings sampling the hyperplane H at the current generation t, $FF(H,t)$ is the average objective score of the strings in H of the population t. First, the selection occurs, which leads to a modified sampling of H for the intermediate generation $M(H,t+\Delta t)$:

$$M(H,t+\Delta t) = M(H,t)\frac{FF(H,t)}{\overline{FF}}. \tag{5.1}$$

To obtain the sample of H for the next generation, evolutionary operators have to be applied. First, we will consider the effects of crossover. The crossover influences the population with the probability p_c, which means that the fraction $(1-p_c)$ of the population remains unchanged together with the corresponding portion of the sample $M(H,t)$. One has to be aware, that some strings do not fit the schema H anymore due to disruption by the crossover operator. On the other hand, an inflow of strings from other schemata generally occurs for the same reason. Then, the sample of H for the next generation is

$$M(H,t+1) = (1-p_c)M(H,t)\frac{FF(H,t)}{\overline{FF}} + p_c\left[M(H,t)\frac{FF(H,t)}{\overline{FF}}(1 - \mathit{losses}) + \mathit{gains}\right], \tag{5.2}$$

where *losses* equals to the number of strings lost due to disruption and *gains* counts the strings obtained from other hyperplanes.

It can be shown that application of crossover does not necessarily lead to a loss of the disrupted strings, which is expressed as *losses* $\leq$ *disruptions*, where *disruptions* quantifies the disruptive nature of crossover. At this point (5.2) is simplified by making an assumption that *gains* will be ignored, which then leads to the lower estimate of the resulting sampling of H:

$$M(H,t+1) \geq (1-p_c)M(H,t)\frac{FF(H,t)}{\overline{FF}} + p_c\left[M(H,t)\frac{FF(H,t)}{\overline{FF}}(1 - \mathit{disruptions})\right]. \tag{5.3}$$

Now we would like to estimate the number of disruptions, which is crossover–dependent, however. In order to explain the problem, lets assume application of a 1–point crossover on the following order–2 schemata of 12 bits:

11********** and 1**********1

The probability that the defining bits in the first schema will be separated due to a 1–point crossover (and thus the schema will be disrupted) is $1/(L-1)$, because there are $(L-1)$ crossover points. Obviously, the disruption probability for the second schema is $(L-1)/(L-1) = 1.0$. Following that result, we will define a measure $\Delta(H)$ of resistance of a schema H to a disruption by a 1–point crossover called *defining length.* If I_x is the index of the rightmost occurrence of either 0 or 1 in the schema H, and I_y is the index of the leftmost occurrence of either 0 or 1 in H, we can write $\Delta(H) = I_x - I_y$. For example, the schema ****1**0**10** has a defining lenght $\Delta(H) = 12 - 5 = 7$.

Following the previous paragraph, one can easily see that it is the defining length $\Delta(H)$ that determines the number of disruptive crossover operations. If the representation of H

is divided by the population size, we obtain the relative sample $P(H,t)$ of H. Then, we can write

$$\textit{disruptions} = \frac{\Delta(H)}{(L-1)}(1 - P(H,t)). \tag{5.4}$$

If the definition of $P(H,t)$ is taken into account, together with the relation (5.4), the expression (5.3) can be rearranged with respect to p_c:

$$P(H,t+1) \geq P(H,t)\frac{FF(H,t)}{FF}\left[1 - p_c\frac{\Delta(H)}{L-1}(1 - P(H,t))\right]. \tag{5.5}$$

It is often considered that both parents are chosen based on fitness, i.e. from the intermediate population $t + \Delta t$. One can see, that (5.5) transforms into

$$P(H,t+1) \geq P(H,t)\frac{FF(H,t)}{FF}\left[1 - p_c\frac{\Delta(H)}{L-1}\left(1 - P(H,t)\frac{FF(H,t)}{FF}\right)\right]. \tag{5.6}$$

To obtain the final version of the schema theorem, it is only mutation left to be involved. Assume that $o(H)$ is a function returning the order of the hyperplane H. The order of H corresponds to a count of the number of bits in the schema representing H that have a value either 0 or 1. If the mutation probability is p_m, the relative number of strings belonging to H that are affected by mutation is $(1-p_m)^{o(H)}$. Then, we get the resulting expression of the schema theorem:

$$P(H,t+1) \geq P(H,t)\frac{FF(H,t)}{FF}\left[1 - p_c\frac{\Delta(H)}{L-1}\left(1 - P(H,t)\frac{FF(H,t)}{FF}\right)\right](1-p_m)^{o(H)}. \tag{5.7}$$

Apparently, the schema theorem emphasizes the role of hyperplane sampling and crossover in the GA search. If we take a look at (5.7), it denotes that the preservation of hyperplane samples after selection is maximal when the disruptive effects of crossover and influence of mutation are minimized. However, that raises a question about the actual advantages of employing the genetic operators in the GA scheme. While the importance of crossover as operator allowing for exchange of genetic operation is clear, the role of mutation deserves a more detailed explanation.

The motivation for using mutation is to prevent the permanent loss of any particular bit. After several generations it is possible that selection will drive all the bits in some position to a single value: either 0 or 1. If this happens without the GA converging to a satisfactory solution, then the algorithm has ***prematurely converged.*** This may particularly be a problem if one is working with a small population. Without a mutation operator, there is no possibility for reintroducing the missing bit value. Also, if the optimized function is nonstationary and the fitness landscape changes over time (which is certainly the case in real biological systems), then there needs to be some source of continuing genetic diversity. Mutation, therefore acts as a background operator, occasionally changing bit values and allowing alternative hyperplane partitions to be tested again.

We should also mention that another points of view of the principle of GA exist, besides the idea of the schema theorem. The presence of mutation is treated as necessary evil in (5.7), and it is only involved due to its preventive influence concerning the premature convergence of the system. However, several experimental researchers analyzing performance of various GA schemes point out that GA optimization using mutation and no crossover often produces a fairly robust search.

Another problem related to premature convergence is the need for scaling the population fitness. As the average evaluation of the strings in the population increases, the variance in fitness decreases in the population. There may be little difference between the best and worst individual in the population after several generations, and the selective pressure based on fitness is correspondingly reduced. Nevertheless, this problem can be successfully addressed by using an alternative form of fitness scaling. Several scaling schemes will be introduced in the next section.

5.4 GA Variations

5.4.1 Fitness – Scaling Schemes

It has been already emphasized, that there is an important difference between evaluation of individuals (strings) and their fitness. The fitness of every population individual is always defined with respect to other members of the population, and its calculation is often referred to as scaling. A wide variety of scaling schemes have been devised. We will offer a brief review of commonly used schemes. Note, that the proper choice for the fitness function (scaling scheme) may be crucial for performance of the GA and is typically problem–dependent.

The simplest version of fitness calculation is accepting the objective scores (sometimes called "raw scores") without any scaling. Fitness fit_i of the i–th individual can be expressed as

$$fit_i = FF_i, \tag{5.8}$$

where FF_i is the evaluation of the individual i.

Linear scaling was introduced by GOLDBERG (1989). It is relatively simple but applies on positive objective scores only. One has to define the evaluation function properly, then. Objective scores are converted to fitness scores using the relation

$$fit_i = a \cdot FF_i + b, \tag{5.9}$$

where a and b are calculated based upon the objective scores of the individuals in the population as described in GOLDBERG (1989).

Sigma truncation scaling is a common replacement of linear scaling if negative values of the objective score have to be allowed. It scales based on the variation from the population average and truncates arbitrarily at 0. The mapping from objective to fitness score for each individual is given by

$$fit_i = FF_i \cdot (\overline{FF} - c \cdot \Delta FF). \tag{5.10}$$

Power law scaling maps objective scores to fitness scores using an exponential relationship defined as

$$fit_i = (FF_i)^k. \tag{5.11}$$

Sharing is a scaling method used to do speciation. The fitness score is derived from its objective score by comparing the individual against the other individuals in the population. If there are other similar individuals then the fitness is derated. The distance function $s(d_j)$ is used to specify how similar to each other two individuals are. A distance function must return a value of 0 or higher, where 0 means that the two individuals are identical (no diversity). For a given individual,

$$fit_i = \frac{FF_i}{\sum_{j=1}^{n} s(d_j)} \tag{5.12}$$

$$s(d_j) = \begin{cases} d_j < \sigma \rightarrow 1 - \left(\frac{d_j}{\sigma}\right)^\alpha \\ d_j \geq \sigma \rightarrow 0 \end{cases} \tag{5.13}$$

where d_j is the distance between current individual i and individual j, n is the population size, and σ is a cutoff value that is to be specified by the user. α controls the curvature of the sharing function (5.12). When $\alpha = 1.0$ the sharing function is a straight line (triangular sharing). Notice that the sharing scaling differs depending on whether the objective function is to maximized or minimized. If the goal is to maximize the objective score, the raw scores will be divided by the sharing factor. If the goal is to minimize the objective score, the raw scores will be multiplied by the sharing factor.

5.4.2 Selection Schemes

Selection schemes are used to pick chromosomes from a population for mating. We have introduced the term *target sampling rate* (*tsr*) in Sec. 5.2, which basically refers to ability of every individual to produce offspring. Generally, two classes of selection operators are distinguished. *Selective algorithm* calculates *tsr* of an individual and it is considered to be the expected size of its offspring. *Sampling algorithm* also evaluates *tsr*, but it does not refer directly to the number of copies of the individual. The value of *tsr* is used by a sampling algorithm to calculate the size of offspring. The difference between the two approaches to selection will be clarified in the following paragraph.

First, we will offer several schemes of selective algorithms. The selection scheme employed in the original canonical GA by HOLLAND (1975) is usually called the *proportional* *selection.* Formally, we can write:

$$tsr_i = \frac{fit_i}{\overline{fit}}, \tag{5.14}$$

where tsr_i refers to the i–th individual.

Rank selector calculates the index (rank) of every individual assuming that the population members are sorted in descending order with respect to their objective score. For a given individual, we get

$$tsr_i = \frac{2}{n+1}\frac{rank_i}{n}, \tag{5.15}$$

where $rank_i$ is the index of the i–th individual and n is the population size. This algorithm is resistant to premature convergence and every individual can be picked for mating. However, the rank selector may lead to a very slow convergence in some cases.

Sampling algorithms are generally based on the principle of the roulette wheel. Every individual is assigned a part of the wheel of a size proportional to its tsr. Apparently higher values of tsr correspond to a higher probability of selection after the wheel stops spinning. There is a wide variety of sampling algorithms and so we will review several of them that are most often used.

The basic sampling algorithm is the pure *roulette wheel selection.* This selection method picks an individual based on the magnitude of the fitness score relative to the rest of the population. The higher the score, the more likely an individual will be selected. Any individual has a probability p of being chosen where p is equal to the fitness of the individual divided by the sum of the fitnesses of each individual in the population.

The *tournament selector* uses the roulette wheel method to select two individuals, then it picks the one with the higher score. The tournament selector typically chooses higher valued individuals more often than the roulette wheel selector.

The *deterministic sampling selector* uses a two–staged selection procedure. In the first stage, each individual's expected representation is calculated. A temporary population is filled using the individuals with the highest expected numbers. Any remaining positions are filled by first sorting the original individuals according to the decimal part of their expected representation, then selecting those highest in the list. The second stage of selection is uniform random selection from the temporary population. A very similar scheme is used by *stochastic remainder sampling selector* that was introduced in Sec. 5.2

The *stochastic uniform sampling selector* picks randomly from the population. Any individual in the population has a probability p of being chosen where p is equal to 1 divided by the population.

5.4.3 Genetic Operators

It is often the crossover operator that is considered to be the critical operator influencing the performance of GA. The role of crossover was demonstrated in Sec. 5.3.2 that introduced the schema theorem. Crossover operator consists of two algorithms: a mating algorithm and a combination algorithm. The following mating schemes are commonly used:

- *random mating* – parents are selected randomly with the same probability
- *inbreeding* – individuals of similar genes (e.g. bits if a binary encoding is used) are picked for mating
- *outbreeding* – strongly diverse individuals are mated
- *line breeding* – a set of high–quality individuals is selected for mating with the rest of the population, and children are also allowed for mating
- *asexual mating* – a single individual can produce its offspring

The random mating is usually employed in implementations of GA. However, it is desirable to prevent the system from mating of copies of the same individual since it increases the tendency to premature convergence.

Now, we will offer the reader several interesting combination algorithms that produce the actual offspring. Only chromosomes of a fixed length will be considered. Then, all the combination schemes may be treated as application of a Boolean mask on a pair of chromosomes, where the genes masked by 1s come out of the first parent, while those ones masked by 0s are picked from the second parent.

The simplest *1–point crossover* has already been discussed in Sec. 5.2 and is depicted again in Fig. 5.3. The *2–point crossover* uses two randomly chosen crossover points.

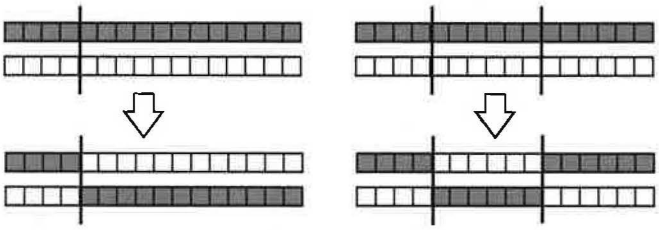

Figure 5.3: 1–point crossover (left plot) and 2–point crossover (WALL, 1996).

Individuals exchange the segment that falls between these two points. This crossover scheme is illustrated by Fig. 5.3. It was first shown by DEJONG (1975) that the 2–point crossover treats the chromosomes as if they form a ring. When viewed this way, 1–point crossover is a special case of 2–point crossover where one of the crossover points always occurs at the wrap–around position between the first and last gene. Apparently, the *n–point crossover* is a generalization of the above described schemes.

The scheme of the *uniform crossover* will be introduced at the end of this overview. Uniform crossover works as follows: for each gene position 1 to L, randomly pick each gene from either of the two parent individuals. This means that each gene is inherited independently from any other genes and that there is, in fact, no linkage between genes. It also means that uniform crossover is unbiased with respect to defining length (for more details see WHITLEY, 1994). Many researchers point out that GAs employing uniform crossover are often more efficient than either 1–point or 2–point crossover operators. However, mutation operators may also significantly influence GA performance.

5.4.4 Generation Replacement

There is a certain diversity in GA schemes introduced by replacement algorithms. They refer to the way the next generation replaces the current one during the progress of GA. The basic canonical GA uses non–overlapping populations which means that every generation is entirely replaced by the next one. This scheme is often modified by ***elitism***, which always preserves the best individual of each generation and copies it into the subsequent population. It is often argued that elitism increases performance of GAs.

Generally, only defined fraction of the current population is replaced by the next generation. GAs with a significant overlap of populations (only 1 or 2 individuals are replaced each generation) were studied e.g. by DEJONG (1975). Such schemes are based on so–called Genitor–style algorithms discussed by WHITLEY (1994). Implementation of overlapping GAs may stabilize oscillations of the average population evaluation $\overline{FF}$, but it strongly depends on the problem to be solved.

5.4.5 Parallel GA – Island Model

Island model of GA is a parallel algorithm that has multiple, independent populations (subpopulations). Each population evolves using GA with overlapping generations, but each generation some individuals migrate from one population to another. By introducing migration, the island model is able to exploit differences in the various subpopulations.

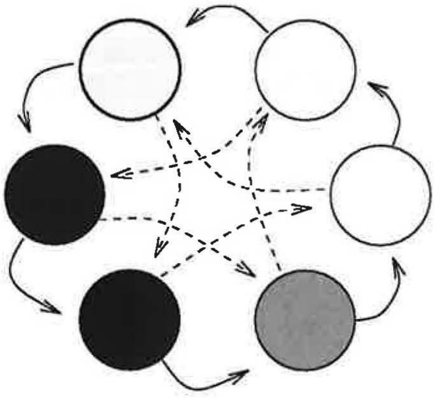

Figure 5.4: Island model of parallel GA. Scheme by (WHITLEY, 1994).

This variation in fact represents a source of genetic diversity. If a large number of strings migrate each generation, then global mixing occurs and local differences between islands will be driven out. If migration is too infrequent, it may not be enough to prevent each small subpopulation from prematurely converging. The general scheme of the island model is offered in Fig. 5.4.

5.5 Implementation

In this section implementation of GA for the purpose of investigation of observed galactic systems will be introduced. Many branches of astrophysical research require application of efficient optimization tools if successful modeling of observationally explored system is deserved. Specialized search schemes such as the simplex method are commonly used by the astrophysical community, since they can address specific problems with high efficiency. However, it is often the case that information about the distribution of quality solutions over the explored space is quite poor. Then, a robust optimization algorithm is necessary to perform a complete search of the entire space of possible solutions, without a tendency to converge to local extremes. A typical example of such a task is numerical modeling of observed galaxies, and namely the systems in interaction. To build up a successful and reliable model, the input parameters and initial conditions have to be determined. However, THEIS (1999) showed that even the parameter space of a two–body galactic interaction becomes remarkably extended. In addition, the wealth of information provided by observations is still insufficient to restrict such a parameter space significantly, which is caused by large distances to extragalactic objects. Regarding the previous arguments, THEIS (1999) and THEIS & KOHLE (2001) suggested application of GAs for studies of observed galaxies in interaction as a promising method to overcome the difficulties related to the size and dimension of the corresponding parameter spaces. The results by THEIS & KOHLE (2001) will be briefly introduced in the next section.

5.5.1 Interacting Galaxies

THEIS & KOHLE (2001) introduced an interesting analysis of possible evolutionary scenarios of the galaxy NGC 4449. They used H I observations of the extended gaseous halo and disk of NGC 4449 and investigated the interaction between NGC 4449 and DDO 125, a close companion in projected space. The spatial resolution of the available H I observational data did not allow for direct search of the parameter space of the interaction, because the observationally established volume of the parameter space exceeded performance limits of applicable search methods. Observationally, only three kinematic quantities – the projected position on the sky and the line–of–sight velocity - can be measured. Another parameter, the galactic mass, depends on the availability of velocity data, the determination of the distance, and the reliability of the conversion from velocity to masses. Neglecting the center–of–mass data of the interacting system, these 14 parameters reduce to 7 parameters containing the relative positions and velocities. These 7 values just fix the orbit in the case of a two–body interaction. Moreover, one has to specify the parameters that characterize both stellar systems, e.g. characteristic scales, orientation, or rotation. The final result is a high–dimensional parameter space which is in general too large for a standard search method. For instance, the interaction of a galactic disk with a point–mass galaxy is described at least by 7 parameters. A regular grid with a poor coverage of 10 grid points per dimension demands 10^7 models.

To overcome the above described difficulties, THEIS & KOHLE (2001) proposed a three–level modeling of the interaction. In a first step, restricted N–body simulations were performed to constrain the model parameters. In the case of insufficient data, one can use the restricted N–body models to obtain a first guess of the parameters, creating an artificial HI intensity map and then apply a plausible search method (THEIS & KOHLE (2001) suggested and tested GA) to check its uniqueness.

In the second step, self–consistent models are used in order to tune the parameters and to check the applicability of the restricted N–body method. These checks address two questions: if the neglecting of self–gravity is acceptable, and if gas dynamics alters the results significantly. Technically this means that self–consistent simulations with and without gas should be performed, which introduces the third level to the numerical study of the interacting pair of NGC 4449 and DDO 125.

Restricted N–body simulations aim to reduce the N–body problem to N 1–body problems by assuming that the gravitational potential is given by a simple relation. E.g. two– or a few–body problems have known (semi–)analytical solutions or can be solved by fast standard methods. Test–particles that mimic HI gas were arranged in a flat disk moving on circular orbits. The disk itself was characterized by its orientation, i.e. its inclination and position angle, the scale–length and the outer edge. In a series of simulations the orbital parameters as well as the disk parameters were varied. The details of the analysis of the parameter space for the NGC 4449–DDO 125 can be found in THEIS & KOHLE (2001).

After several evolutionary scenarios satisfying observational data were identified, GA optimization was employed in order to investigate uniqueness of such models. The scenarios served as reference models and the GA searched the parameter space to reach the global extreme of the evaluation function that was a measure of similarity between the tested models and the reference models. The evaluation function in the study of THEIS & KOHLE (2001) compared the observed (i.e. reference) and modeled column densities of HI on a grid of 7x7 pixels and was defined as follows:

$$FF \equiv \frac{1}{1+\delta} \tag{5.16}$$

$$\delta \equiv \sum_i \frac{|I_{\mathrm{ref},i} - I_{\mathrm{mod},i}|}{MAX(I_{\mathrm{ref},i}, I_{\mathrm{mod},i})}, \tag{5.17}$$

where $I_{\mathrm{ref},i}$ is the HI column density in the i–th pixel of the reference model, and $I_{\mathrm{mod},i}$ refers to the same quantity for the tested model (GA individual). For more detailed explanation of the actual GA scheme see THEIS & KOHLE (2001). Reliability of such a uniqueness test, together with the demonstration of the used GA scheme can be found in Fig. 5.5. THEIS & KOHLE (2001) showed that the relative deviation of the derived parameters from the original values was less than 15% in all cases, and for many was better than 5%.

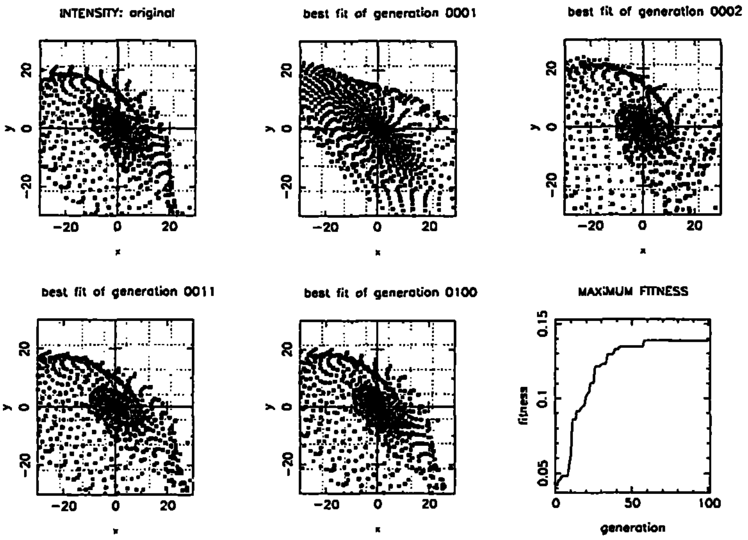

Figure 5.5: Demonstration of GA convergence as offered in THEIS & KOHLE (2001). The original data (upper left), the best fit of the GA after initialization (upper middle), after the first breeding (upper right), after 11 generations (lower left) and at the end of the fitting procedure after 100 generations (lower middle) are plotted above. The evolution of the maximum fitness is shown in the lower right diagram.

Finally, the self–consistent models were performed by a direct N–body integration to investigate reliability of test–particle schemes for such tasks. THEIS & KOHLE (2001) bring comparison of restricted N–body simulations with self–consistent models. Except for the more diffuse structure in the latter, the large–scale features are very similar in both simulations.

The results by THEIS & KOHLE (2001) denote that combination of standard N–body methods and GAs as robust search tools, in order to develop a method for the determination of the parameters of interacting galaxies is a promising method, and became a strong motivation for the parameter study of the Magellanic System that is the subject to this thesis. In the next section, the GA scheme employed for the purpose of our study will be introduced.

5.5.2 Magellanic System

In contrast to the case of NGC 4449 studied by THEIS & KOHLE (2001), the observational resources for the Magellanic Clouds include numerous high–resolution observations of various gaseous components of both dwarf galaxies, and also detailed information about stellar populations present in LMC and SMC is available (see Chapter 1). Especially, precision of proper motion measurements of the Clouds has been improved remarkably during the last 15 years (see e.g. JONES ET AL., 1994; KROUPA ET AL., 1994; KROUPA & BASTIAN, 1997; KALLIVAYALIL ET AL., 2006A,B), which is the crucial factor in order to establish the space of the current LMC and SMC velocity vectors. Discussion in Chapter 4 introduces the volume of the parameter space of the interaction LMC–SMC–MW as it was confined following the observations available up–to–date. The wealth of information allowed for the first complete automated search for possible parameter combinations of the interaction by the means of GA. The results of the analysis will be introduced in the following chapters.

Our implementation of GA is based on the excellent library of GA components by WALL (1996). The composition of the selected GA scheme are summarized in Tab. 5.2. The final scheme was developed after extended testing of numerous GA variations. The termination of GA does not occur upon a convergence of a per–generation averaged fitness function, because the averaged fitness shows a progress with the number of generations similar to the case depicted in the rightmost lower plot of Fig. 5.5. Thus, the GA is terminated when the generation number corresponds to the turn–point in fitness function. The evaluation function (fitness function hereafter) consists of two parts. First, the restricted N–body model introduced in Chapter 3 is run for the selected parameter values (chromosome). Subsequently, the resulting distribution of particles is converted into column densities of HI and compared to the high–resolution HI data by BRÜNS ET AL. (2005). The comparison scheme is a significant extension of (5.17) by THEIS & KOHLE (2001). Detailed introduction to the fitness calculation employed in this study is offered in Chapter 6.

general scheme	canonical GA *with* elitism
encoding	real number encoding (Tab. 5.1)
fitness function	linear scaling (5.9)
selection scheme	roulette wheel selection
crossover	uniform crossover (Sec. 5.4.3)
GA termination	after 120 generations
population size	150 individuals

Table 5.2: Setup of the GA used for our parameter study of the Magellanic System.

CHAPTER 6

Fitness Function

6.1 Heart of Genetic Algorithm

As described, GA is a very general optimization scheme. Most of its components are problem independent, which makes it a powerful tool for a wide variety of tasks. The connection between the investigated system and the GA itself is established by a *fitness function* (FF). The function is responsible for evaluation of quality of population individuals – possible solutions. It is critically important for the proper behavior of the whole GA. Unfortunately, there is no unique way to define such a driver. It is left on a user completely how to measure quality of solutions.

Our study is focused on the search for evolutionary scenarios of the Magellanic System reproducing its observations. In principle, the wealth of information provided by the H I Parkes survey (BRÜNS ET AL., 2005) of the entire system is sufficient for performing a detailed automatic GA search. However, a consideration has to be given to the fact that our test–particle model unavoidably does not describe all the physical processes involved in the formation of the Magellanic System. Test–particle numerical simulations of interacting galaxies incorporate neither self–gravity nor a description of the dynamics of the gaseous medium. They are primarily designed for recognizing ***tidal structures***. Previous attempts to use such a kind of simulations for the Magellanic System (e.g. GARDINER ET AL., 1994; RUZICKA, 2001) showed that the overall H I distribution of the system (Magellanic Stream, Leading Arm area) can be considered a tidal feature.

Following that result an elaborate scheme of the original H I data processing has to be proposed to emphasize extended H I features of the observed interacting galaxies. Also small–scale structures are supposed to be suppressed since they were formed due to physical processes missing in the restricted N–body model.

6.2 Data Processing

It is a common practice in observational astronomy to store data as a *Flexible Image Transport System* (FITS) format. Then, application of advanced methods of *image processing* in order to customize the data is quite natural. Process of the 3 D H I data-set preparation for the purposes of our GA–based study will be explained in this section. Basically, three common methods are considered as possible candidates – resizing, rescaling and filtering. Typically, their application on 2 D images is assumed, but extension to higher dimensions is allowed.

Resizing is the simplest possibility, nevertheless the least suitable one. Generally, to resize an image consisting of N pixels, a regularly spaced grid with I nodes is laid over the image. Assuming the relation $I < N$, image pixels matching grid nodes are copied into a new image. Although such an operation is capable to remove details, each pixel is treated without any respect to the neighboring pixels. But it clearly denotes that our H I data images cannot be treated that way. Each pixel represents an amount of H I gas which is obviously related to the surrounding matter due to physical interaction.

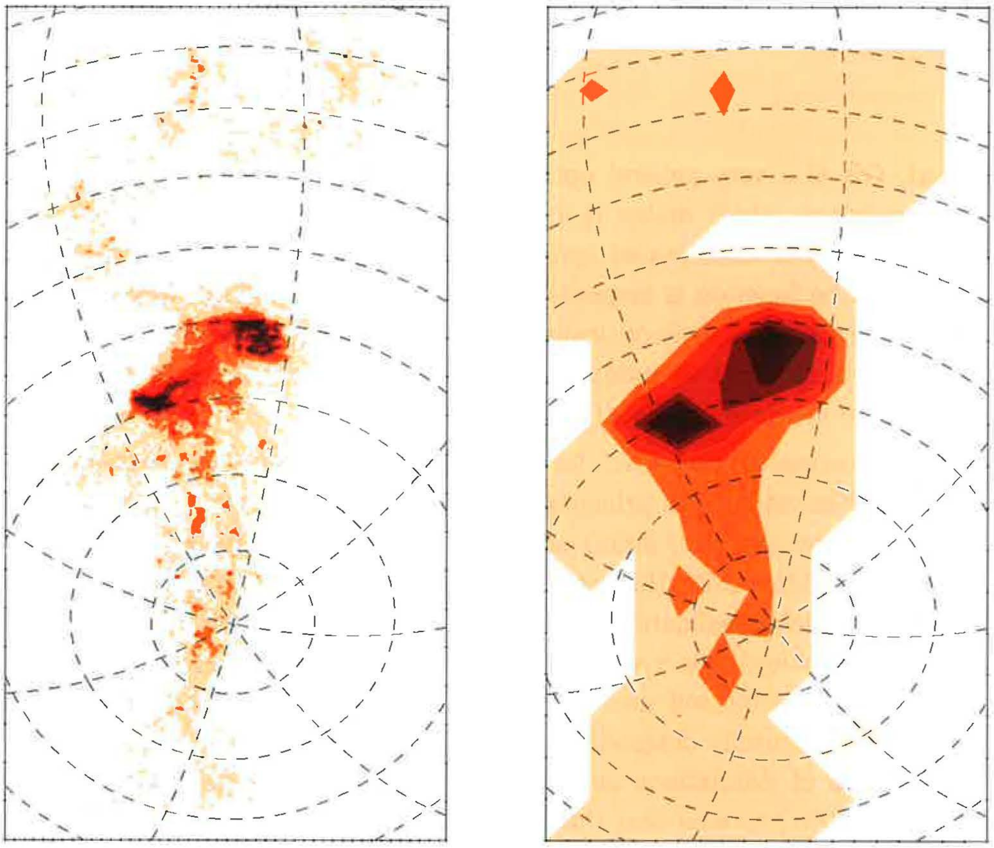

Figure 6.1: Demonstration of image rescaling. The left plot shows the original FITS image – integrated H I column density in the Magellanic System (Brüns et al., 2005) – of the spatial resolution 452 x 1079 pixels. The right plot illustrates the typical result of a rescaling procedure. The original resolution was decreased to 10 x 20 pixels.

Rescaling of an image means a decrease in resolution without removing pixels permanently. Similarly to the resizing process, a grid is defined to cover the original image. For each grid cell values of the pixels fitting the cell are summed over its entire area. It can be expressed as

$$P_i' = \sum_{j=1}^{N_i} P_i^j, \tag{6.1}$$

where

N_i number of original pixels fitting the i–th grid cell
P_i^j value of the j–th original pixel in the i–th grid cell
P_i' i–th pixel of the new image

Even though a relation between close pixels is taken into account and small–scale intensity variations no longer exist in the new image, requirements of test–particle simulations are not fully met. Image rescaling is not sensitive to structures. Features of size not exceeding the grid spacing vanish while large–scale distribution is distorted significantly. Regarding the special case of the Magellanic System (Fig. 6.1), substantial widening of the Magellanic Stream area occurs. But it is a change affecting the global matter distribution which is supposed to remain conserved.

Image **filtering** is used to remove noise, sharpen contrast, or highlight structures. Two of the most common classifications of filters are based on their linearity and frequency response. The third classifier distinguishes filters that are applied spatially from frequency domain filters, which are applied to a Fourier–transformed representation of an image.

6.2.1 Image Filters

Linearity

Linear filters, also known as *convolution filters*, are so named because they can be represented in linear algebra using a matrix multiplication. The matrix defining the neighborhood of the pixel also specifies the weight assigned to each neighbor. This matrix is called the *convolution kernel*. For each pixel P_{ij} in an image (where i and j represent the coordinates of the pixel), the convolution kernel is centered on P_{ij}. Each pixel masked by the kernel is multiplied by the coefficient placed on top of it. P_{ij} becomes the sum of these products. In the case of a 3 x 3 neighborhood, you can index the pixels surrounding P_{ij} and the coefficients of the kernel, K, as follows:

$$\mathbf{P} = \begin{pmatrix} P_{i-1,j-1} & P_{i,j-1} & P_{i+1,j-1} \\ P_{i-1,j} & P_{i,j} & P_{i+1,j} \\ P_{i-1,j+1} & P_{i,j+1} & P_{i+1,j+1} \end{pmatrix}, \mathbf{K} = \begin{pmatrix} K_{i-1,j-1} & K_{i,j-1} & K_{i+1,j-1} \\ K_{i-1,j} & K_{i,j} & K_{i+1,j} \\ K_{i-1,j+1} & K_{i,j+1} & K_{i+1,j+1} \end{pmatrix} \tag{6.2}$$

Then

$$P'_{ij} = \frac{1}{N} \sum_{k=i-1}^{i+1} \sum_{l=j-1}^{j+1} P_{kl} K_{kl}, \tag{6.3}$$

where

$$N = MAX\left(1, \sum_{k=i-1}^{i+1} \sum_{l=j-1}^{j+1} K_{kl}\right).$$

Non–linear filters are any other filters that cannot be represented using a matrix formulation. Thresholding and equalization are typical non–linear operations. Other operations that are more commonly thought of as "filtering" include various edge detection (high–pass) operations and *median filtering*, which is a low–pass filter well-suited for the removal of noise from images (see Fig. 6.2).

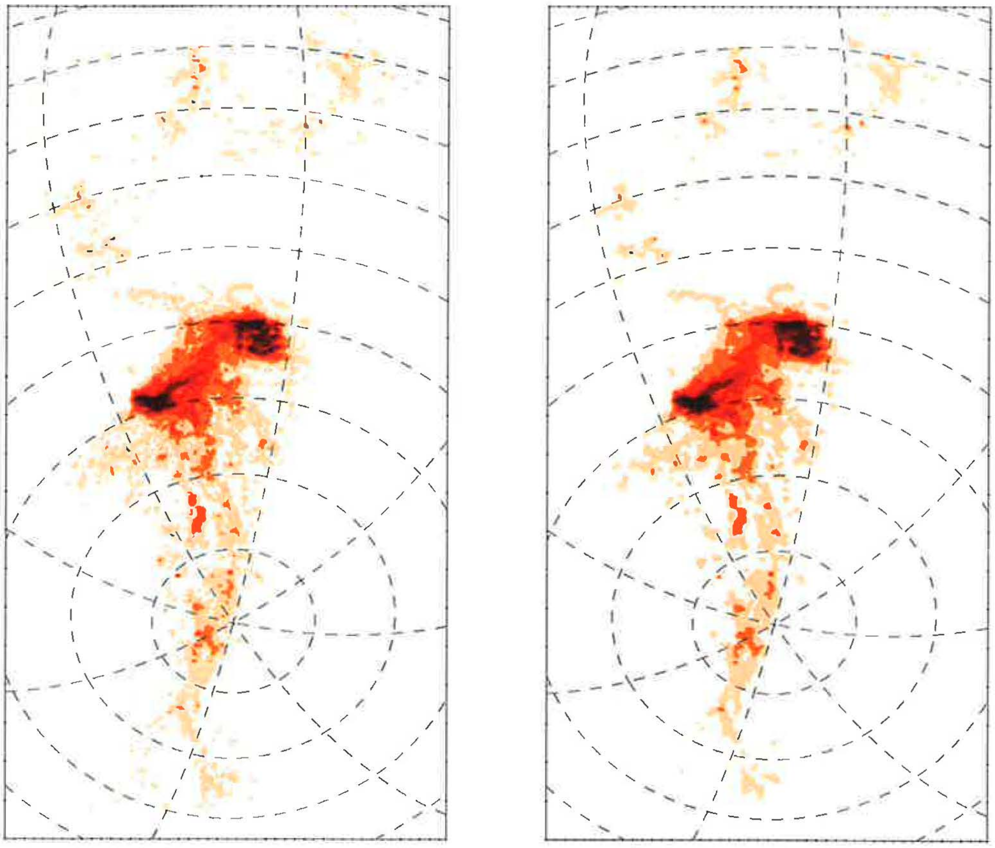

Figure 6.2: Median filtering is an efficient noise–removal technique. The above plot shows comparison between the original image (left) and the image after median filtering with the kernel 3 x 3.

Median filter is a special case of *N–th order non–linear filters*. Such filters define a kernel similarly to linear filters. However, each cell has the same weight. The values of the pixels masked by the kernel are sorted in increasing order. Then, the value of the kernel's central pixel is replaced by the N–th value in the order.

Frequency Response

A fundamental way to characterize filters is by how they attenuate or amplify certain frequency ranges. In general, there are many different classes of frequency responses, but for images, the broad categories of *low–pass* or *high–pass* are sufficient. Low–pass filters can be used for operations like noise removal or image smoothing. High–pass filters respond to abrupt changes in intensity in an image, so they can be applied to enhance details in the image.

Note that frequency response can be used to classify both spatial and frequency filters. The next section explains these terms, which refer only to how the filter is implemented. All filters can be described by some kind of frequency response.

Spatial versus Frequency Filters

Spatial filters alter pixel values with respect to variations in intensity in their neighborhood, while *frequency filters* operate in the frequency domain on images that have been Fourier–transformed. After the filtering operation, the inverse transform is applied to get back to an enhanced version of the original image. It is also possible to classify both spatial and frequency filters as linear or non–linear, and low–pass or high–pass.

Frequency filters have the advantage of being extremely easy to design and implement, but they can introduce artifacts into the image when the inverse transform is applied. These artifacts typically appear as "ringing" or ripples that emanate from edges in the image (Fig. 6.3). Such effects are present when values of pixels vary substantially over a small spatial range, or the selected filter is not smooth enough.

Lets demonstrate the influence of the filter function on the resulting data considering a Fourier frequency low–pass filter. The basic choice usually is a low–pass *rectangular filter*

Figure 6.3: Filtering of a 2D step function (left plot). A low–pass rectangular filter is defined (middle plot) and convolved with the function. Typical "ringing" appears after the inverse Fourier transform is applied (right plot).

defined as follows:

$$Filter(f_x, f_y) = \begin{cases} 1, & \sqrt{f_x^2 + f_y^2} \leq f_{\text{cutoff}} \\ 0, & \sqrt{f_x^2 + f_y^2} > f_{\text{cutoff}} \end{cases} \tag{6.4}$$

Fig. 6.3 shows the performance of the rectangular filter when a step function is the target of filtering. To reduce undesirable artifacts of Fourier filtering, one can smooth the transition between the stop and pass band. This is often done using *Hanning (Hamming) filters* which are rectangular filters smoothed by cosine functions.

$$Filter(f_x, f_y) = \begin{cases} 1, & \sqrt{f_x^2 + f_y^2} \leq f_{\text{cutoff}} - \omega \\ 0, & \sqrt{f_x^2 + f_y^2} > f_{\text{cutoff}} - \omega \\ \frac{1}{2}\left(1 - sin\left(\frac{\pi(\sqrt{f_x^2+f_y^2} - f_{\text{cutoff}})}{2\omega}\right)\right), & \text{else} \end{cases} \tag{6.5}$$

Application of a Hanning filter given by (6.5) with gradual transition between the stop and pass band is illustrated by Fig. 6.4.

Figure 6.4: A smooth Fourier filter (middle plot) and a 2 D step function (left plot). Filtering artifacts strongly present in Fig. 6.3 are reduced remarkably.

6.3 Observational Data Filtering

A comparison of possible data manipulation techniques showed that data filtering leads to the best satisfaction of constraints coming from the restricted N–body model's features, that do not allow for reliable modeling of structures on small scales. Application of a low–pass image filter enables suppression of small–scale H I line intensity variations while overall matter distribution remains unaffected. Generally, both spatial and frequency filtering should be taken into account. However, a decision has to be made which possibility promises better performance for a specific task.

Spatial filtering is a popular approach to tasks that do not pay particular attention to global features of processed data. Noise removal from raw spectra is a good example. Filters in the spatial domain deal with values of individual units (pixels) and computational burden scales as N_{u}^2 with the number of units involved in one step, because convolution of the filter and data has to be performed. Hence, spatial filtering can only hardly be helpful for highlighting of large–scale structures. On the other hand, spatial filters can suppress extreme fragmentation and presence of isolated pixels (see Fig. 6.2).

Actually, also frequency filters mostly use a convolution principle. However, due to the availability of the *Fast Fourier Transform* algorithm, Fourier filtering in frequency domain offers a high computational performance when implemented properly. Moreover, it brings an excellent control over the scale range of image's structures to be conserved or filtered out. Apparently, this is due to a direct connection between a structure–scale level of the image and the frequency that is particularly responsible for features of that scale level. Concerning our request for a low–pass filter, a cut–off frequency can be selected easily prior to defining a frequency filter function *Filter*(f). The filter function will then conserve frequencies lower than the cut–off, while frequencies above the level are suppressed. On the other hand, the presence of abrupt changes in the intensity of neighboring pixels or

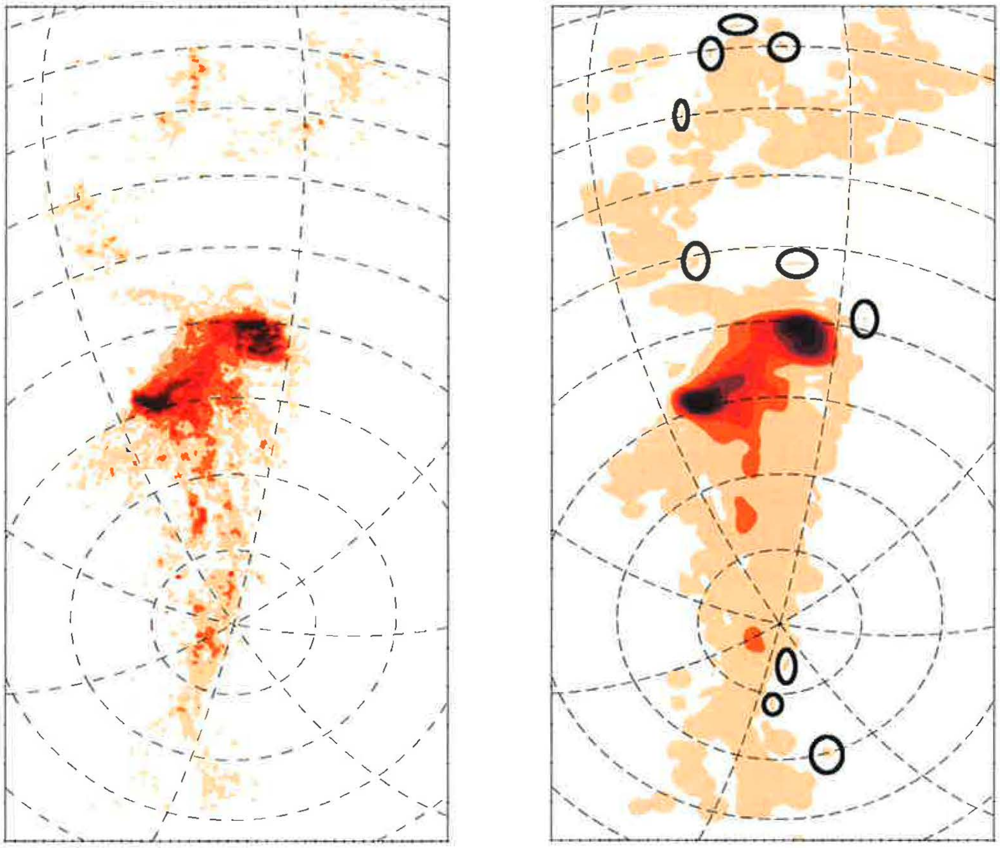

Figure 6.5: Fourier filtering of the original integrated H I column density map of the entire Magellanic System (Brüns et al., 2005). The filtered image suffers from undesired artifacts – "ringing".

a large number of isolated fragments often cause unwanted artifacts in Fourier–filtered images (see Fig. 6.5). However, we have shown that such small–scale intensity variations can be smoothed out well by a reasonably selected spatial filter.

Following the previous discussion, we suggest a *two–level data filtering* to be employed for all image processing (Fig. 6.6).

- A *median filter* is applied on the raw data image to remove isolated pixels and steep intensity variations. Such features cannot be handled by frequency filters reliably. Among spatial filters, the median filter shows considerable efficiency for such tasks.
- As a second step, a low–pass smooth Hanning *Fourier filter* (6.5) is convolved with the Fourier transform of the H I data.

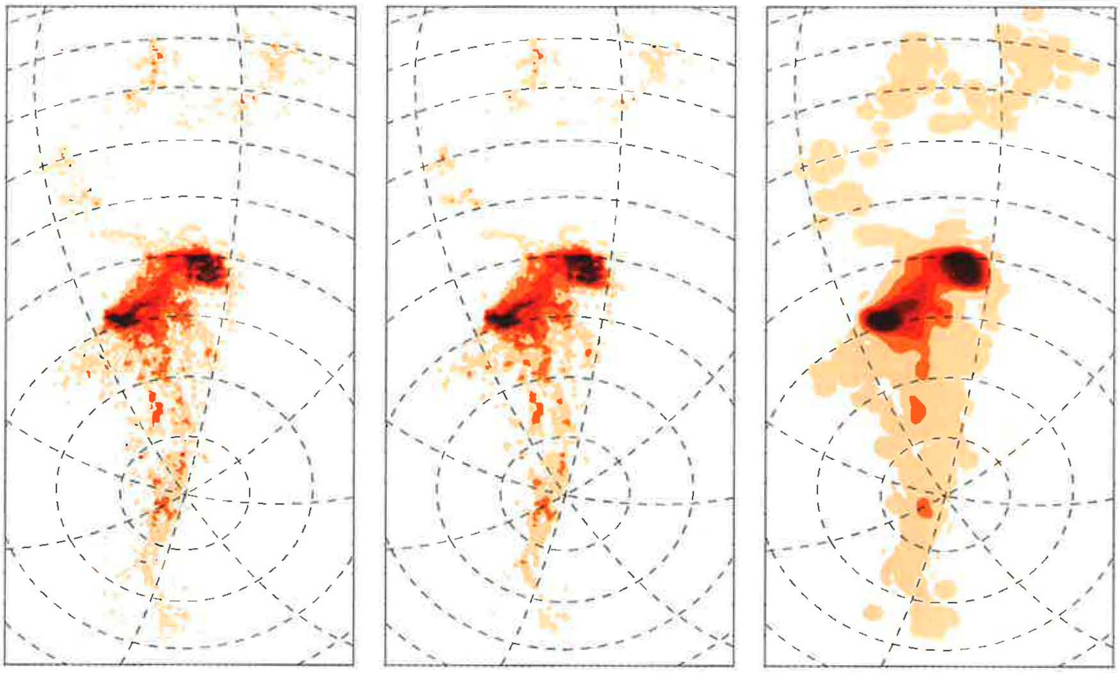

Figure 6.6: Demonstration of a two–level image filtering. In order to suppress abrupt changes in intensity of neighboring pixels and reduce the number of isolated fragments, the original image (left plot) is processed by a median filter to get a corrected map (middle plot). Subsequently, a Fourier frequency filter is used.

6.4 Fitness Function of the Magellanic System

The behavior of the 3 D test–particle model of the Magellanic System is determined by a large set of initial conditions and parameters that can be viewed as a point (individual) in the system's high–dimensional parameter space. In the case of our task, the fitness of an individual means the ability of the numerical model to reproduce the observed H I distribution in the Magellanic Clouds if the individual serves as the input parameter set for the model. It is well known, that a proper choice for FF is critical for the efficiency of the GA and its convergence rate to quality solutions. After extended testing, we devised a three–component FF scheme. In order to discover possible unwanted dependencies of our GA on the specific choice for the FF, both following FF definitions were employed:

$$FF_a = FF_1 \cdot FF_2 \cdot FF_3, \tag{6.6}$$

$$FF_b = \frac{\sum\limits_{i=1}^{i=3} c_i \cdot FF_i}{\sum\limits_{i=1}^{i=3} c_i}, \tag{6.7}$$

where the components FF_1, FF_2 and FF_3 reflect significant features of the observational data and $c_1 = 1.0$, $c_2 = 4.0$ and $c_3 = 4.0$ are weight factors. Both the FFs return values from the interval $\langle 0.0, 1.0 \rangle$. The specific choice for c_1, c_2 and c_3 is based on testing the efficiency of the resulting FF as of a driver of the GA. In general, the weight of FF_1 is lower, because it does not apply on the entire distribution of H I in the Magellanic System. Further discussion of the components of FF follows in the next paragraphs.

FF compares observational data with its models. In order to do that, the resulting particle distribution has to be treated as neutral hydrogen and converted into H I emission maps for the defined radial velocity channels. In the following paragraphs we briefly introduce both the observed and modeled data processing.

It was shown by Gardiner et al. (1996) that the overall H I distribution in the Magellanic System (Magellanic Stream, Leading Arm) can be considered as a tidal feature. Following that result, an elaborate scheme of the original data (Brüns et al., 2005) manipulation was devised to emphasize large–scale features of the Magellanic H I distribution on one hand, and suppress small–scale structures on the other hand, since they originate in physical processes missing in our simple test–particle model. The data

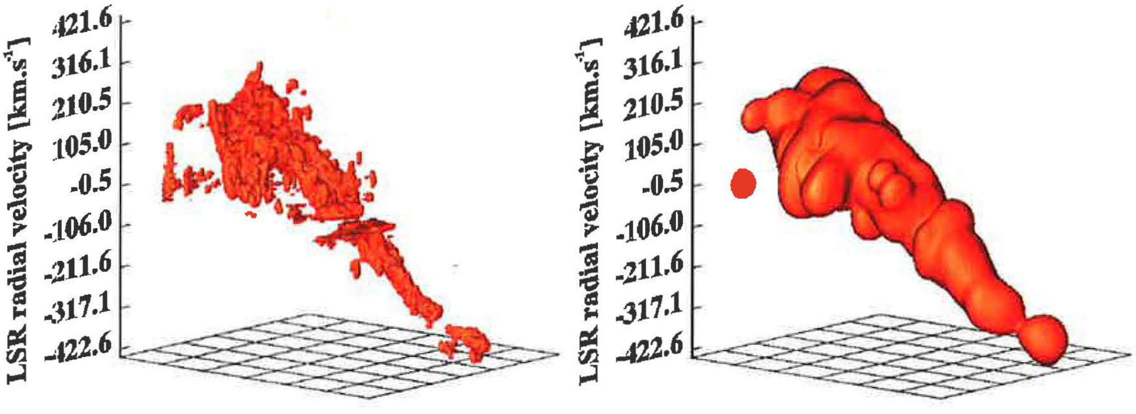

Figure 6.7: The figure depicts the original 3D H I data cube by Brüns et al. (2005) (left plot) together with the resulting data after median and Fourier filtering. Both images offer 3D visualization of the column density isosurface $\Sigma_{\mathrm{HI}} = 0.2 \cdot 10^{18}\,\mathrm{cm}^{-2}$.

kindly provided by Brüns et al. (2005) was obtained from observations of the Magellanic System in the emission line of H I. The observations reached notable spatial and velocity resolution (for details see Brüns et al., 2005), and the data can be viewed as 3 D (position–position–LSR radial velocity) array of H I column densities, stored as an image in FITS format. That lets us apply standard image processing methods naturally. Fourier filter was selected for our task. It represents a frequency domain filter, and so it allows for an excellent control over the scale range of the image's structures to be conserved or filtered out. We removed the wavelengths below the limit of ≈ 10° projected on the plane of sky. The performance of Fourier filters suffers from the presence of abrupt changes of intensity, such as edges and isolated pixels. In order to enhance the efficiency of frequency filtering, it was preceded by an application of a spatial median filter to smear the original image on small scales. Subsequently, the H I column density is normalized. The resulting 3 D H I column density data cube together with the original data by Brüns et al. (2005) can be seen in Fig. 6.7. To compare the modeled particle distribution with H I observations, we convert the distribution to a 3 D FITS image of column densities that are proportional to particle counts, since all the test–particles have the same weight factor assigned. Then, we have to interpolate missing data which is due to a limited number of particles in our simulations. Finally, the column density is normalized to the maximal value.

After discussing the data processing and manipulation, we will introduce the individual FF components FF_1, FF_2 and FF_3.

6.4.1 FF_1

The observed H I LSR radial velocity profile measured along the Magellanic Stream is a notable feature of the Magellanic System. It shows a linear dependence of LSR radial velocity on Magellanic Longitude, and a high negative velocity of $-400\,\mathrm{km\,s^{-1}}$ is reached at the Magellanic Stream far tip (Brüns et al., 2005). From the studies by Murai & Fujimoto (1980), Gardiner et al. (1994) and our modeling of various Magellanic evolutionary scenarios we know, that the linearity of the Magellanic Stream velocity profile shows low sensitivity to a variation of initial conditions of the models. On the other hand, the slope of the LSR radial velocity function is a very specific feature, strongly dependent especially on the features of the orbital motion of the Clouds. Therefore, it turned out to be an efficient approach to test whether our modeled particle distribution was able to reproduce the high negative LSR radial velocity tip of the Magellanic Stream. Then, the first FF component FF_1 was defined as follows:

$$FF_1 = \frac{1}{1 + \left| \frac{v_{\mathrm{min}}^{\mathrm{obs}} - v_{\mathrm{min}}^{\mathrm{mod}}}{v_{\mathrm{min}}^{\mathrm{obs}}} \right|}, \tag{6.8}$$

where $v_{\mathrm{min}}^{\mathrm{obs}}$ and $v_{\mathrm{min}}^{\mathrm{mod}}$ are the minima of the observed LSR radial velocity profile of the Magellanic Stream and its model, respectively.

6.4.2 FF_2 and FF_3

The FF components FF_2 and FF_3 compare the observed and modeled H I column density distributions in the Magellanic System for 64 separate LSR radial velocity channels with a width $\Delta v = 13.2\,\mathrm{km\,s^{-1}}$. For every velocity channel, H I column density values are available for (64 x 128) pixels covering the entire System. The above introduced 3 D data was obtained by modification of the original high-resolution H I data-cube by BRÜNS ET AL. (2005). Since the test-particle model is not capable to reproduce small-scale features of the explored system, filtering and reduction of resolution of the original data were necessary prior to its use for the purpose of our GA search.

The second FF component analyzes whether there is a modeled H I emission present at the positions and LSR radial velocities where it is observed. Thus, we measure the relative spatial coverage of the System observed in H I emission by the modeled matter distribution for every LSR radial velocity channel. No attention is paid to specific H I column density values here. We only test, whether both modeled and observed emission is present at the same pixel of the position-velocity space. It can be expressed as

$$FF_2 = \frac{\sum\limits_{i=1}^{N_v}\sum\limits_{j=1}^{N_y}\sum\limits_{k=1}^{N_x} pix_{ijk}^{\mathrm{obs}} \cdot pix_{ijk}^{\mathrm{mod}}}{MAX\left(\sum\limits_{i=1}^{N_v}\sum\limits_{j=1}^{N_y}\sum\limits_{k=1}^{N_x} pix_{ijk}^{\mathrm{obs}}, \sum\limits_{i=1}^{N_v}\sum\limits_{j=1}^{N_y}\sum\limits_{k=1}^{N_x} pix_{ijk}^{\mathrm{mod}}\right)}, \tag{6.9}$$

where $pix_{ijk}^{\mathrm{obs}} \in \{0, 1\}$ and $pix_{ijk}^{\mathrm{mod}} \in \{0, 1\}$ indicate whether there is matter detected at the position [i, j, k] of the 3 D data on the observed and modeled Magellanic System, respectively. $N_v = 64$ is the number of separate LSR radial velocity channels in our data. $(N_x \mathrm{x} N_y) = (64 \mathrm{x} 128)$ is the total number of positions on the plane of sky for which observed and modeled H I column density values are available.

This binary comparison between the observed and modeled data introduces a problem of pure noise pixels present in the observed data cube, because they posses the same weight as the other data, despite their typically very low intensity. However, our treatment of the original high-resolution data by BRÜNS ET AL. (2005) involves spatial median filtering. It smears abrupt intensity changes and removes isolated pixels which handles the problem of pure-noise data pixels naturally. The subsequent Fourier filtering decreases the data resolution significantly, and that also strongly suppresses the influence of original noise pixels.

As the last step we compare the modeled matter density distribution to the observation. To do that, both modeled and observed H I column density values are scaled relatively to their maxima to introduce dimensionless quantities. Then, we get

$$FF_3 = \frac{1}{N_v \cdot N_y \cdot N_x} \sum_{i=1}^{N_v}\sum_{j=1}^{N_y}\sum_{k=1}^{N_x} \frac{1}{1 + \left|\sigma_{ijk}^{\mathrm{obs}} - \sigma_{ijk}^{\mathrm{mod}}\right|}, \tag{6.10}$$

where $\sigma_{ijk}^{\mathrm{obs}}$, $\sigma_{ijk}^{\mathrm{mod}}$ are normalized column densities measured at the position [j, k] of the i–th velocity channel of the observed and modeled data, respectively.

6.5 Analysis of the Fitness Function

We try to reproduce as closely as possible the column density and velocity distribution of H I in the Magellanic Stream and in the Leading Arm. The influence of actual distances to the LMC and SMC and of their present space velocity vectors is considered together with their masses and the past sizes and space orientation of the original disk–like configuration of matter (test–particles). Here, we give the results of the search in the parameter space with the GA using the 3–component fitness function defined by (6.7). In principle, the GA is able to find the global maximum of the *FF* if enough time is allowed for the evolution of the explored system (see HOLLAND, 1975). However, it may be very time–consuming to identify the single best fit due to a possibly slow convergence of the *FF*. Therefore, to keep the computational cost reasonable, the maximum number of 120 GA generations to go through was defined.

In order to explore the *FF* of our system, we collected 123 GA fits of the Magellanic System resulting from repeated runs of our GA optimizer. The best model is introduced in Tab. 6.1. Typically, identification of a single GA fit requires $\approx 10^4$ runs of the numerical model. Thus, due to the application of GA we were able to search the extended parameter space of the interaction and discover the most successful models of the System over the entire parameter space by testing $\approx 10^6$ parameter combinations. In the case of our 20–dimensional parameter space, simple exploration of every possible combination of parameters even on a sparse grid of e.g. 10 nodes per dimension means 10^{20} runs of the model. Such a comparison clearly shows necessity of using optimization techniques and demonstrates the computational efficiency of GA.

FF	0.496	q	0.84
r_{LMC}[kpc]	$\begin{pmatrix} -1.26 \\ -40.50 \\ -26.87 \end{pmatrix}$	r_{SMC}[kpc]	$\begin{pmatrix} 13.16 \\ -34.26 \\ -39.77 \end{pmatrix}$
$v_{\mathrm{LMC}}[\mathrm{km\,s^{-1}}]$	$\begin{pmatrix} 44.0 \\ -169.8 \\ 146.7 \end{pmatrix}$	$v_{\mathrm{SMC}}[\mathrm{km\,s^{-1}}]$	$\begin{pmatrix} -37.2 \\ -60.2 \\ 204.3 \end{pmatrix}$
$m_{\mathrm{LMC}}[10^9\mathrm{M_\odot}]$	24.46	$m_{\mathrm{SMC}}[10^9\mathrm{M_\odot}]$	2.06
$r^{\mathrm{disk}}_{\mathrm{LMC}}$[kpc]	9.62	$r^{\mathrm{disk}}_{\mathrm{SMC}}$[kpc]	6.54
$\Theta^{\mathrm{disk}}_{\mathrm{LMC}}$	89°	$\Phi^{\mathrm{disk}}_{\mathrm{LMC}}$	274°
$\Theta^{\mathrm{disk}}_{\mathrm{SMC}}$	36°	$\Phi^{\mathrm{disk}}_{\mathrm{SMC}}$	229°

Table 6.1: Parameters of the best model identified by the GA optimizer.

6.5.1 Features of *FF*

In the following paragraphs we will introduce the *FF* of the MW–LMC–SMC interaction as function of the parameters listed in Tab. 4.1. First, consideration will be given to the coverage of the parameter space by the above mentioned fits of the System. If the fitness values of the solutions are printed against a selected single parameter, we receive a series of 1 D plots that are shown in Fig. 6.8. It is a remarkable fact that all the points are located within the fitness range of $\langle 0.438, 0.496 \rangle$, which is equivalent to the relative difference between the best and worst solution $\Delta FF = 12\%$. Such a narrow range indicates rather presence of an extended plateau than of a significant single global maximum in the fitness landscape. Another notable result is related to the coverage of the studied area of the parameter space by the solutions. The volume of the parameter space was set up according to various observational constraints on each parameter (see Chapter 4). In most cases, the GA fits are spread over the entire ranges of parameters with various deviations from homogeneous distribution for different parameters (Fig. 6.8). Nevertheless, for the Cartesian components v^y_{LMC}, v^x_{SMC} and v^y_{SMC} of the current LMC/SMC spatial velocity vectors, the GA-based search substantially restricted their ranges derived from observational data (see KROUPA & BASTIAN, 1997). The GA fits occupy $\approx 50\%$ of the intervals for v^x_{SMC} and v^y_{SMC}, with no increase of the coverage density toward either of the limits. However, the distribution of the fits over the LMC velocity component v^y_{LMC} is significantly concentrated to the upper limit of the interval, suggesting that an interesting region of the *FF* landscape remained hidden beyond the observationally established limit.

Distribution of the points identified by GA in the parameter space (fits of maxima of *FF*) suggests the existence of an extended plateau of slow convergence in the fitness landscape. It may be treated as justification of the adopted approach to the optimization problem, when repeated runs of GA for a restricted number of generations were performed. The above introduced features of *FF* are based on Fig. 6.8, which does not allow for further conclusions on either local or global behavior of *FF* outside the region populated by the localized GA fits, though. As the next step toward better understanding of the *FF* (6.7), we studied 1 D projections of *FF* to the plane of the j-th parameter $FF - p_j$:

$$FF^i_j \equiv f(p^i_1, \ldots, p_j, \ldots, p^i_n), \tag{6.11}$$

where $p^i_1, \ldots, p^i_n$ are specific values of the parameters of the i-th GA fit (point in the parameter space) and the parameter p_j is varied within its range as it is specified in Tab. 4.1. The function FF^i_j for all the parameters studied, except for the MW halo flattening q, is plotted in Fig. 6.9 for the point of the highest fitness that we identified by GA (see Tab. 6.1). Undoubtedly the most interesting and significant qualitative result coming out of Fig. 6.9 is the remarkable sensitivity of *FF* to some parameters, namely to the LMC and SMC current spatial velocities, but on the other hand also very small changes in *FF* as other parameters vary. Similarly to Fig. 6.8, there is a notable indication that the observationally derived range of the LMC velocity component v^y_{LMC} (see the left-most plot in the second row of Fig. 6.9) does not include values that would eventually lead to a better reproduction of the H I observations of the Magellanic System. The projection of *FF* for

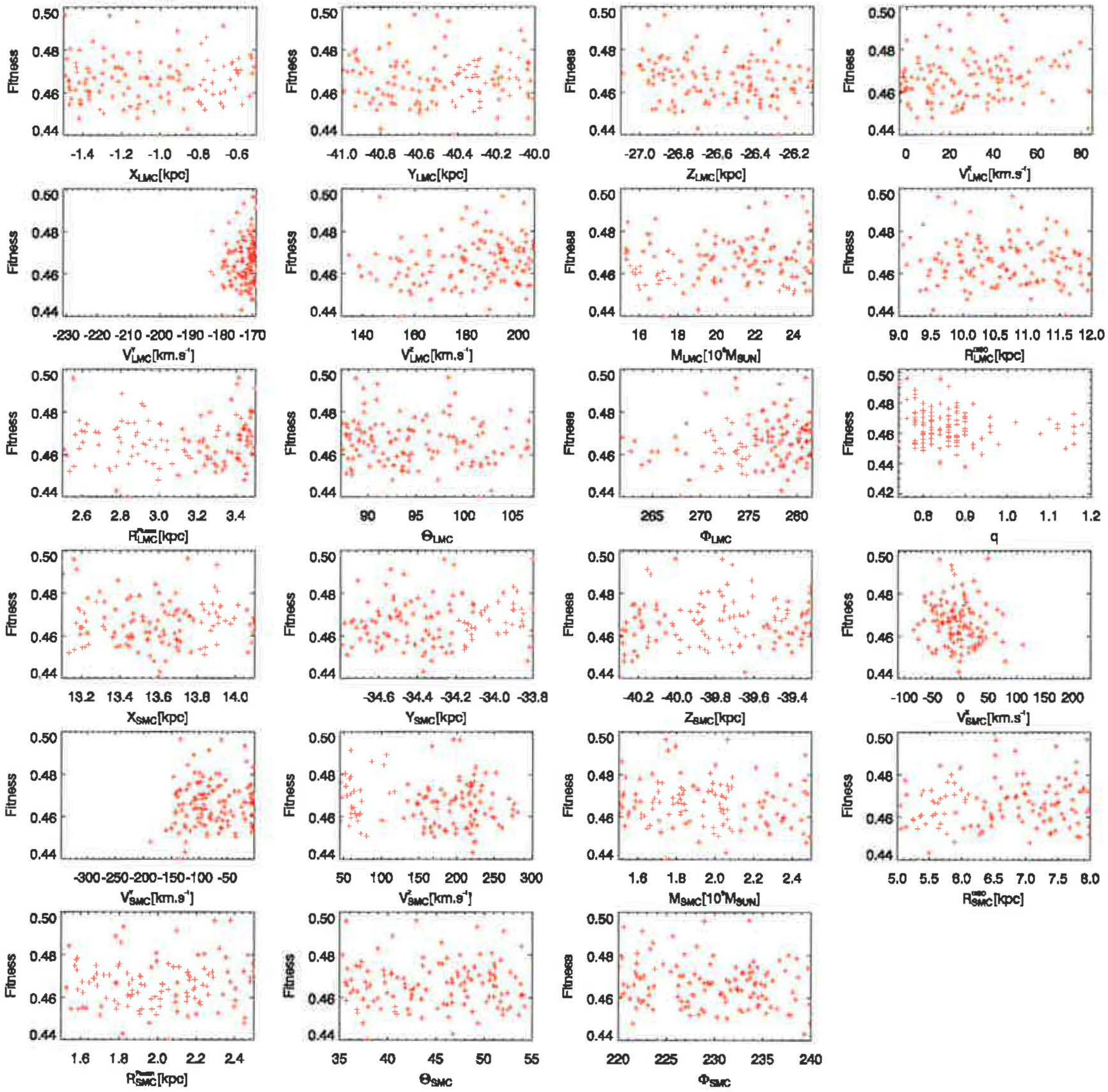

Figure 6.8: Distribution of GA fits of the Magellanic System over the analyzed ranges of variables (parameters of the interaction). Each plot depicts 123 points in the parameter space.

$v^y_{\rm LMC}$ grows well monotonously toward the upper limit of the velocity component, where the best GA fit was located. The plots in Fig. 6.9 are based on a rather sparse coverage of the parameter ranges by 21 points where FF was evaluated. Thus, relevant information about how FF depends on the parameters locally is missing. In order to fix the drawback of Fig. 6.9, we analyzed FF close to the points of the 123 GA fits on intervals of half-width of 1 % of the entire range of each parameter (see Tab. 4.1). The resulting 1 D slices of FF obtained at the position of the best GA fit are depicted in Fig. 6.10. Qualitative differences in local sensitivity of FF to variations of different parameters are not so remarkable, compared to the global case. Mostly, FF shows oscillations of the relative amplitude of only 2–5 % around the mean value. It is notable, that the orientation angles of the LMC disk $\Theta_{\rm LMC}$ and $\Phi_{\rm LMC}$ do significantly influence the FF values neither on a global nor on a local scale. To quantify the sensitivity of FF to changes in different

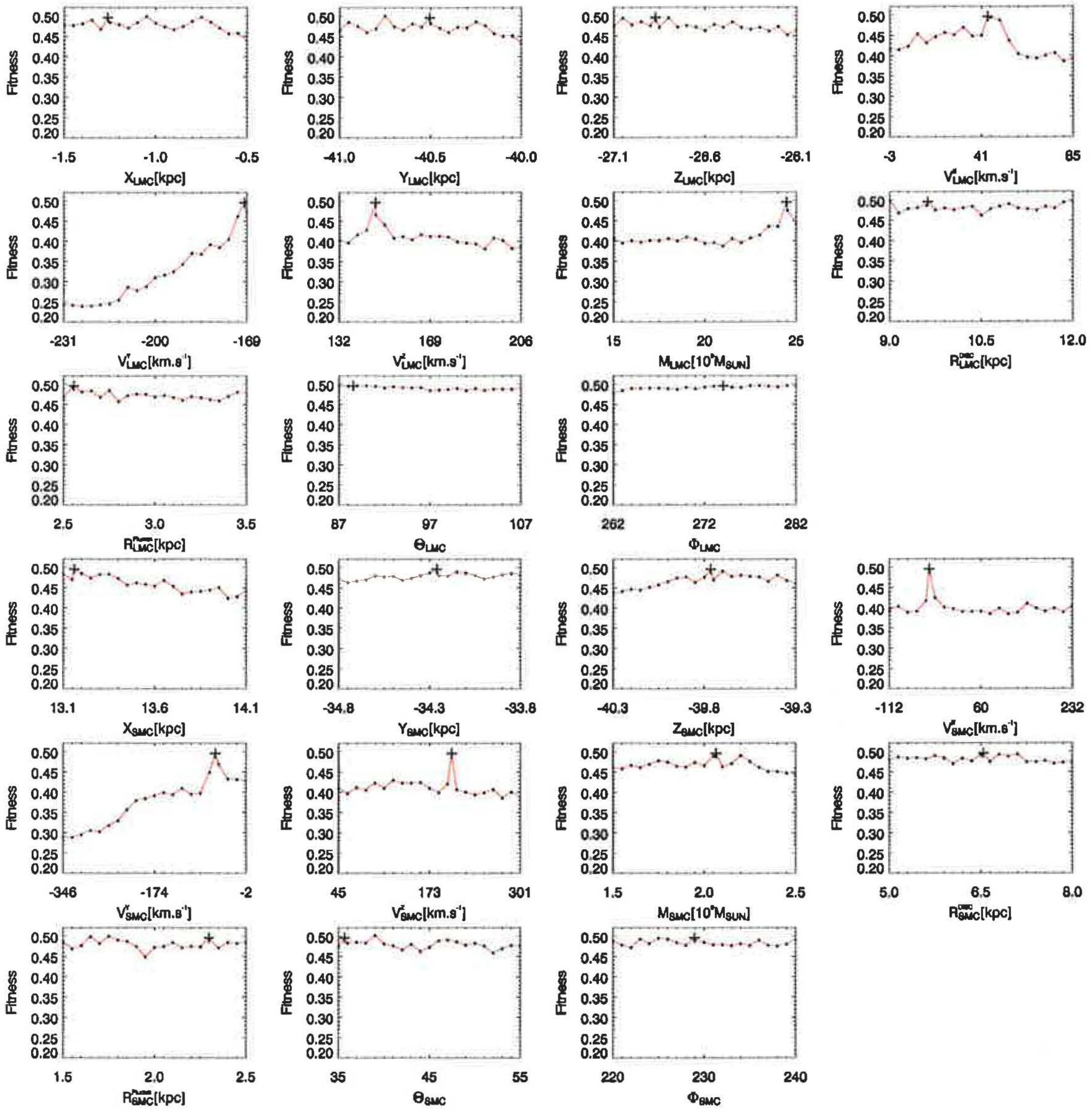

Figure 6.9: Projection of FF (6.7) to the planes of the parameters of the MW–LMC–SMC interaction. For every single plot, the parameter of interest is varied within its range introduced in Tab. 4.1, while the remaining parameters are kept fixed to the values of the best GA fit that was identified (marked by a cross).

variables (parameters), the following functions were defined:

$$\delta_j \equiv \frac{1}{N} \sum_{i=0}^{N-1} \frac{\sigma_j^i}{\overline{FF_j^i}}, \tag{6.12}$$

is *mean relative deviation* of the 1 D projected fitness FF_j^i calculated over N GA fits for the j–th parameter, where

$$\sigma_j^i \equiv \frac{1}{N_\mathrm{P}} \sum_{k=0}^{N_\mathrm{P}-1} (FF_j^i(x_k) - \overline{FF_j^i})^2 \tag{6.13}$$

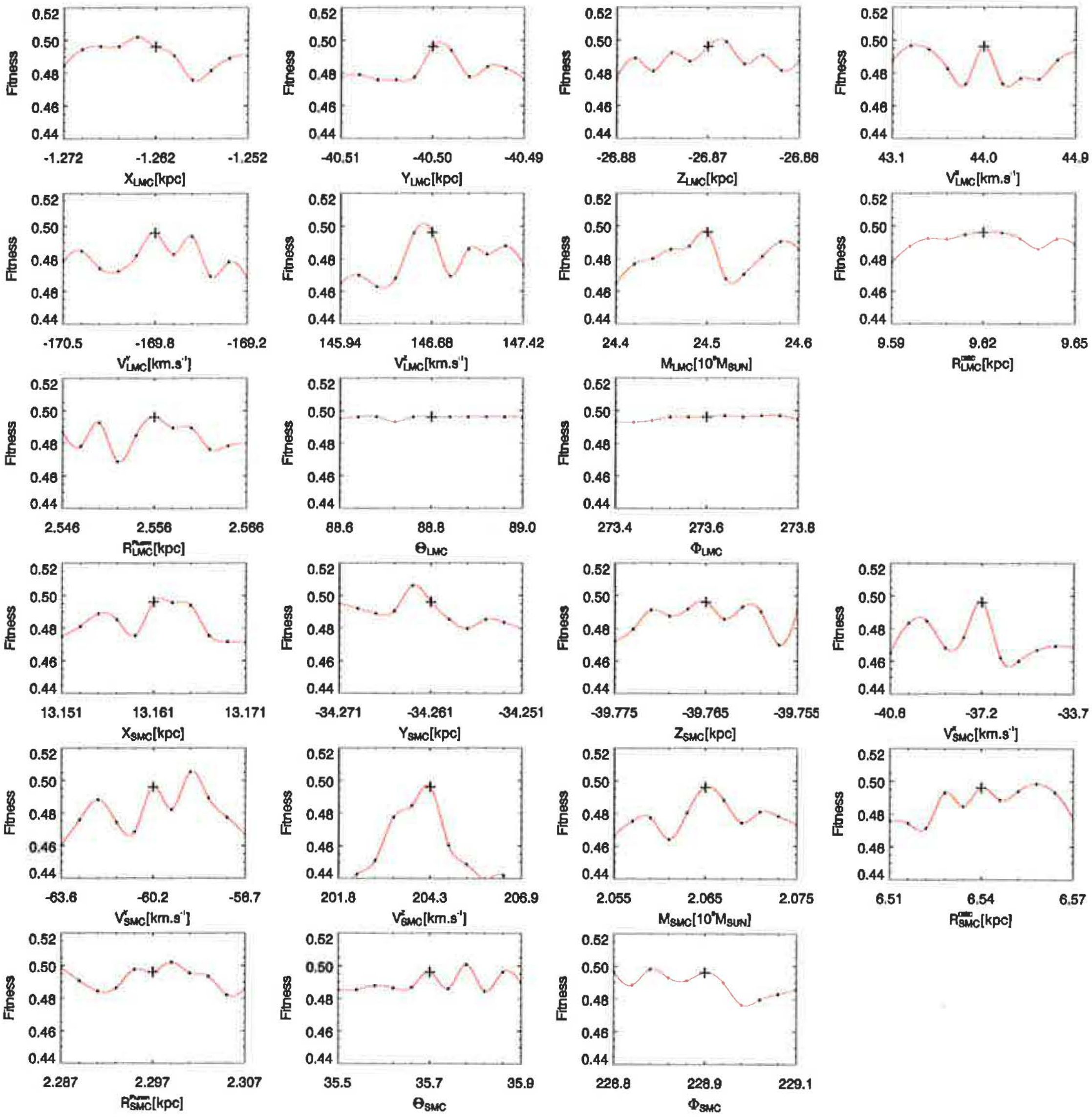

Figure 6.10: Local projection of FF (6.7) to the planes of the parameters of the MW–LMC–SMC interaction. FF is studied locally around the best GA fit (black cross). For every single plot, the parameter of interest is varied within the total of 2% of the range introduced in Tab. 4.1, while the remaining parameters are kept fixed to the values of the best GA fit that was identified. The cubic spline interpolation was performed between the calculated fitness values (black marks).

is the corresponding standard deviation calculated for $N_{\rm P}$ points of the projected FF^i_j, and $\overline{FF^i_j}$ is the mean value of the FF on the defined interval of the j–th variable. Similarly to (6.12) we specify a *maximal relative deviation* of FF for the j–th parameter:

$$\delta_j^{\rm MAX} \equiv \frac{1}{N} \sum_{i=0}^{N-1} \frac{MAX(|FF^i_j - \overline{FF^i_j}|)}{\overline{FF^i_j}}. \qquad (6.14)$$

Finally, we calculate *relative change in FF_j*:

$$\delta_j^{\mathrm{FF}} \equiv \frac{1}{N}\sum_{i=0}^{N-1} \frac{MAX(FF_j^i) - MIN(FF_j^i)}{\overline{FF_j^i}}. \tag{6.15}$$

If the values of the above defined relations are calculated for every parameter of the FF and for the entire set of 123 GA fits, we obtain Fig. 6.11. It consists of two plots of the same meaning, but valid for global (upper plot) or local features of FF studied in its 1 D projections. The parameters are ordered along the horizontal axis in decreasing order regarding the values of (6.12). In general, Fig. 6.11 confirms the previously reviewed qualitative results. Relative differences between the parameters are less apparent on the local scale than if their entire intervals are studied. However, the order of the parameters remains almost unaltered as we switch between the plots of Fig. 6.11. It indicates similar features of FF on either scale. Unlike Fig. 6.9 or Fig. 6.10, Fig. 6.11 describes the behavior of FF "averaged" over all the GA fits, which lets us conclude general facts about the FF. The analysis of 1 D projections of FF strongly suggests to pay special attention to the current velocity vectors of both Clouds, since they turned out to be crucial factors influencing the MW–LMC–SMC interaction.

As a part of the FF analysis, we also calculated the *Spearman's rank correlation* and its significance value of every combination of the parameters. Investigation of possible linear relation between the model's parameters is a very basic but a desirable procedure, once we have efficiency of GA in mind. If a parameter (variable) determining the behavior of the system studied by GA depends on the choice for some other parameter(s), it usually increases the tendency of GA to prematurely converge (see e.g. GOLDBERG, 1989, and references therein). Even though the correlation check does not allow for verification of more complex dependencies in the parameter space, it may introduce valuable information about the optimized system with respect to achieving maximal performance and reliability of GA. The Spearman's rank correlation coefficient ρ is defined as

ρ	Sig	a	b
−0.329	2.10^{-4}	v^x_{SMC}	v^y_{SMC}
+0.356	6.10^{-5}	v^z_{SMC}	m_{SMC}

Table 6.2: Spearman's rank correlation coefficients of parameters a and b calculated according to (6.16). The above table shows the maximum anti-correlation (upper row) and correlation of the studied parameters, together with the significance values of the correlation.

$$\rho = \frac{\sum_{i=0}^{N-1}(R_a^i - \overline{R_a})(R_b^i - \overline{R_b})}{\sqrt{\sum_{i=0}^{N-1}(R_a^i - \overline{R_a})^2}\sqrt{\sum_{i=0}^{N-1}(R_b^i - \overline{R_b})^2}}, \tag{6.16}$$

where R_a^i, R_b^i are magnitude–based ranks among the parameters a and b, respectively.

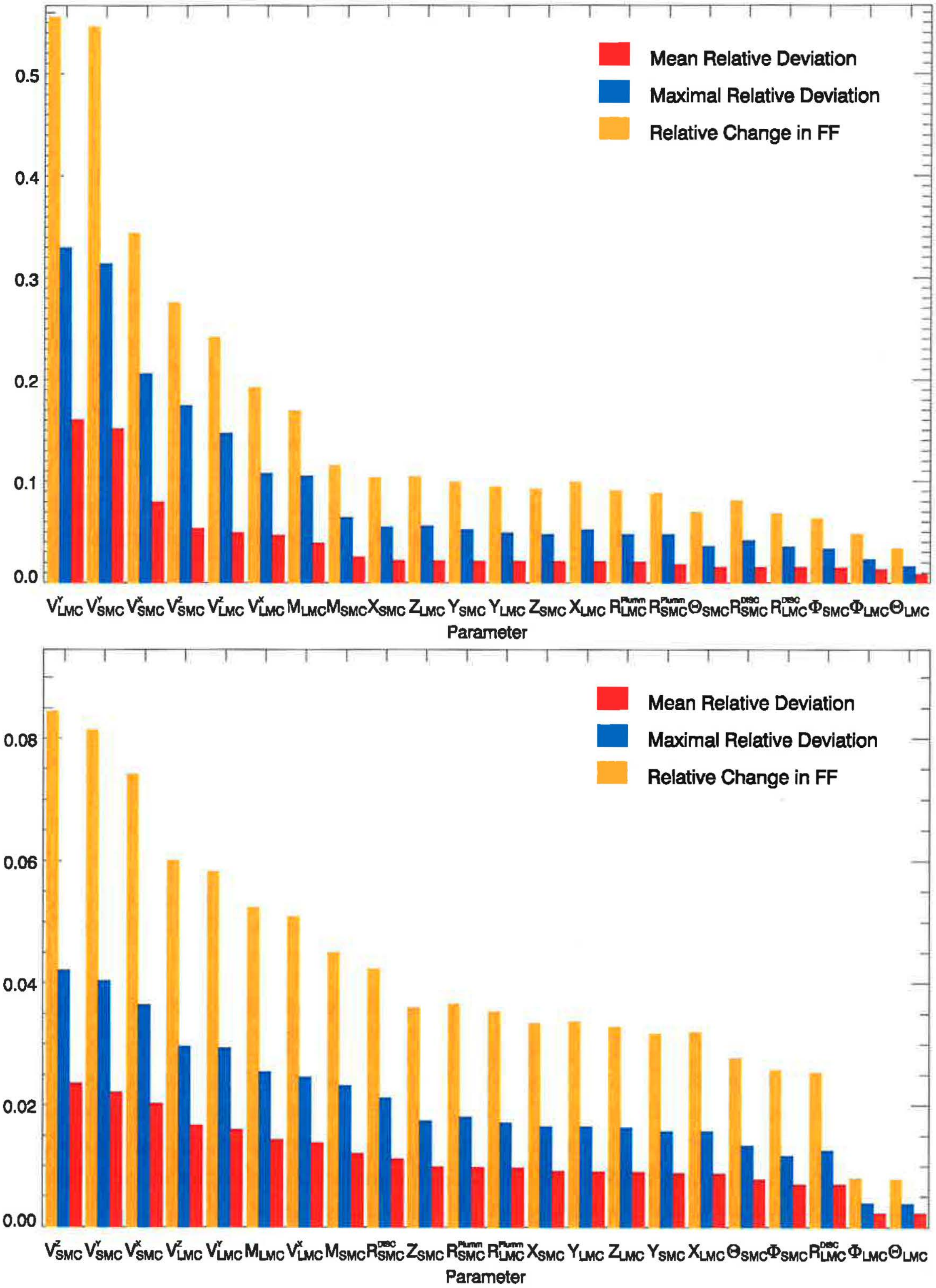

Figure 6.11: Global (upper plot) and local features of FF in 1 D projections. Figure shows values of the relations (6.12) (red), (6.14)(blue) and (6.15) for each of the studied parameters. The obtained values quantify sensitivity of FF to variations in different parameters.

For correlation ρ we define its significance Sig. The significance is a value in the interval $\langle 0.0, 1.0 \rangle$. A small value of Sig indicates a significant correlation. The extreme values of the correlation coefficient are listed in Tab. 6.2. Thus, basic search for dependencies between the parameters of the interaction by the means of a correlation check did not discover any indication of a linear relation for an arbitrary choice of two parameters.

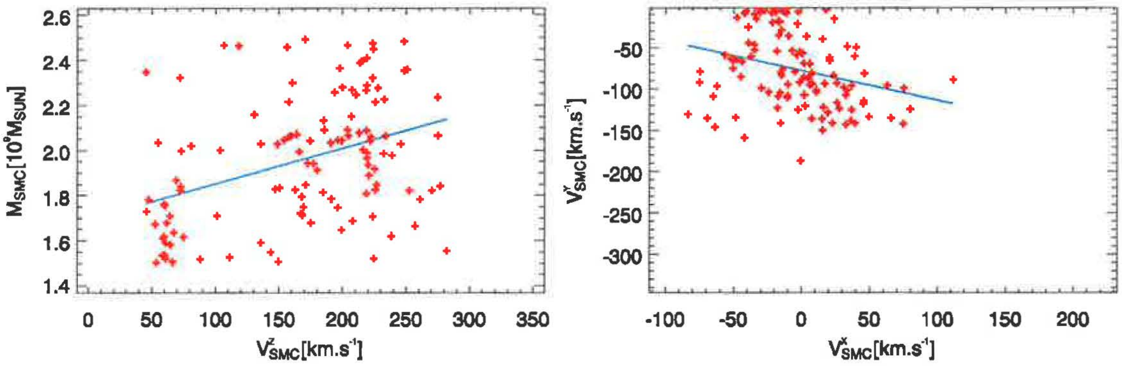

Figure 6.12: GA fits in the $V^z_{\mathrm{SMC}} - M_{\mathrm{SMC}}$ (left plot) and $V^x_{\mathrm{SMC}} - V^y_{\mathrm{SMC}}$ planes of the parameter space of the interaction. Maximum Spearman's rank correlation (left plot) and anti-correlation exists for the above depicted parameter pairs (see also Tab. 6.2).

We discussed the influence of the parameters of the interaction in the Magellanic System on the resulting value of FF. The analysis of 1 D projections of FF clearly indicated that a specific choice for a value of a given parameter means different impact on the fitness of our model for different parameters. While variations in the positioning of the LMC particle disk do not influence significantly the structure and velocity distribution of matter in the System, sensitivity of the interaction scenario to the LMC and SMC spatial velocity vectors is apparent. Results introduced in this chapter became a strong motivation for the following part of this thesis. Special attention will be paid to the motion of the Magellanic Clouds and also to the structure of the MW halo, that enters the problem via the potential flattening q. The MW halo flattening was omitted in the discussion of FF, since it was allowed to change in discrete steps only, which would not allow for all the comparison procedures. Nevertheless, the flattening parameter and the physical consequences of its choice on the evolution of the System will be studied in the next chapter. The above picked parameters will be treated from the point of view of their physical meaning and the way they influence the actual distribution of H I in the Magellanic System.

Before closing this chapter, we would like to offer the reader selected 2 D projections of the FF (Fig. 6.13) to illustrate notably different features of FF as we switch between different parameters. To emphasize the contrast in behavior of various 2 D FF projections, the planes $v^y_{\mathrm{LMC}} - v^y_{\mathrm{SMC}}$ and $\Theta_{\mathrm{LMC}} - \Phi_{\mathrm{LMC}}$ are displayed in Fig. 6.13. The remaining parameters are always fixed to the values of the best GA fit, that was introduced previously. For either of the plots one may get a good feeling of what is often called "fitness landscape".

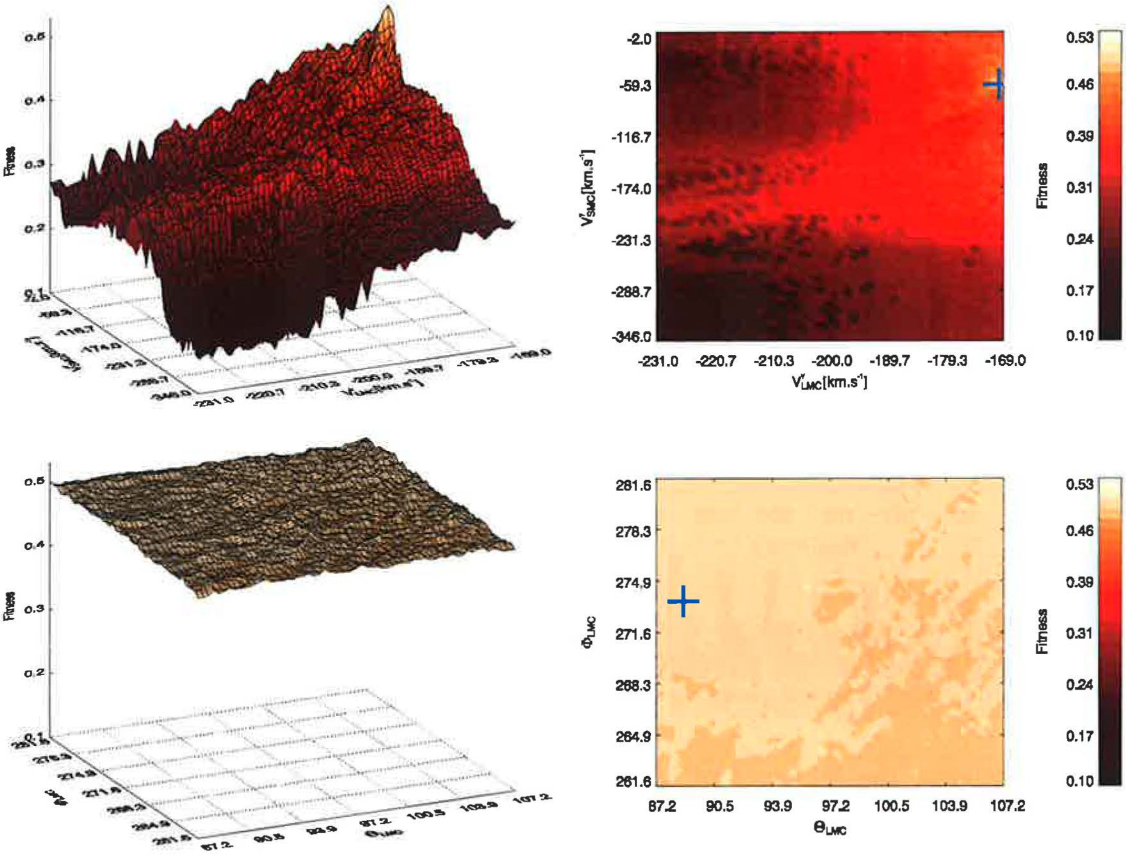

Figure 6.13: Selected 2 D projections of FF. The upper row shows the $v^y_{\rm LMC} - v^y_{\rm SMC}$ slice of FF, while the lower row presents the dependence of fitness on the orientation angles $\Theta_{\rm LMC}$ and $\Phi_{\rm LMC}$ of the initial LMC particle disk. The coordinates of the best GA fit are marked by the blue cross.

CHAPTER 7

Spatial Motion of the Magellanic Clouds

Chapter 6, and namely Sec. 6.5 introduced the features of FF formally defined by (6.7). It was employed in order to quantify agreement between our models of the interacting galactic system LMC–SMC–MW and observations of the System. Review of the knowledge in the Magellanic Clouds based on observational data available up to date (see Chapter 1) indicates a remarkable variety in information about the main bodies of LMC and SMC, respectively. However, structures such as extended arms/tails or intergalactic bridges consisting of stars and gaseous components, that have been observed in numerous galactic systems and explained as remnants of their interaction (see e.g. TOOMRE & TOOMRE, 1972), are what is considered a notable and promising way to investigate dynamical evolution of galaxies in interaction. Since the discovery of the Magellanic Bridge, that was identified in H I data by HINDMAN ET AL. (1963), a clear indication of intense interaction between the Magellanic Clouds has been existing. Later, extended H I filaments of the Magellanic Stream and Leading Arm were detected (WANNIER & WRIXON, 1972; WANNIER ET AL., 1972; MATHEWSON ET AL., 1974), which was a crucial argument supporting the view of the system of LMC, SMC and Galaxy as a group of interacting galaxies. Despite numerous observational studies, it is still only H I that serves as a source of information about the outer regions of the Magellanic Clouds, including the Magellanic Stream and Leading Arm. There was no other gaseous component detected in the extended structures. Stellar populations reside in LMC, SMC and connecting Magellanic Bridge exclusively, and their absence in the Magellanic Stream still deserves reliable explanation. Regarding the previous notes, it is apparent that the comparison between models and observations of the Magellanic System, that we made using FF, was based on H I data only, because other applicable observational information is currently unavailable. From a mathematical point of view, a search for a model satisfying H I observations of the Magellanic Clouds was treated as a process of maximization of a model–to–observation comparison function FF.

The application of a GA allowed for very fast and efficient analysis of FF over the entire volume of the parameter space of the interaction (see Chapter 4). The GA–based search for extremal values of FF lead to the discovery of an extended plateau in the "fitness landscape". We collected 123 fits of maxima of FF. The analysis of their distribution over the studied ranges of parameters became the first indication of the possibly very different influence of various parameters on the result of the model. Especially the choice for the components $v^y_{\rm LMC}$ and $v^y_{\rm SMC}$ of the spatial velocity vectors of the Magellanic Clouds turned out to be critically important. Additionally, significant concentration of the GA fits to the upper limit of the searched interval of $v^y_{\rm LMC}$ (see Fig. 6.8) suggested that a very promising region of the parameter space remains hidden beyond that parameter limit. Subsequently, features of FF were studied on both local and global scales (for details see Sec. 6.5). A detailed analysis of 1 D projections of FF (6.11) obtained at the positions of all the GA fits of FF maxima was performed. A statistical analysis of the resulting information confirmed differences in sensitivity of FF (i.e. of the distribution of H I gas) to the parameters of the interaction (Fig. 6.11). Generally, the outstanding role of the velocity vectors of the Magellanic Clouds was emphasized again, and became a natural motivation for further analysis of influence of the LMC and SMC spatial velocity on the evolution of the Magellanic System. In this chapter, we study physical properties of our models of the LMC–SMC–MW interaction with respect to variations in spatial motion of the Magellanic Clouds. Particular attention is paid to the distribution of H I in the position–velocity space (see BRÜNS ET AL., 2005) and to the evolution of the galactic group over the last 4 Gyr.

It was mentioned, that a decomposition of the current velocity vectors of the Magellanic Clouds into their components with respect to the Cartesian frame introduced in Chapter 4 indicates notable sensitivity of the interacting system to the y–components $v^y_{\rm LMC}$ and $v^y_{\rm SMC}$. In order to illustrate the impact of different components of the velocity vectors on the resulting value of FF, we offer series of 2 D projections of FF at the position of the best model (Tab. 6.1). Fig. 7.1 depicts the 2 D "fitness landscape" for all the combinations of the LMC velocity components $v^x_{\rm LMC}$, $v^y_{\rm LMC}$ and $v^z_{\rm LMC}$. Similar plots for SMC are introduced in Fig. 7.2. Every contour plot contains black dotted lines drawn through the point showing the position of the best GA fit. The lines mark the 1 D projections of FF gathered in Fig. 6.8 for every velocity component of LMC and SMC, respectively. One can easily note that the FF slices $v^x_{\rm LMC}-v^z_{\rm LMC}$ and $v^x_{\rm SMC}-v^z_{\rm SMC}$ that are plotted as the middle row of Fig. 7.1 and Fig. 7.2, respectively, differ from the 2 D projections of FF to the planes involving the spatial velocity components $v^y_{\rm LMC}$ and $v^y_{\rm SMC}$. Remarkable sensitivity of FF may be described quantitatively by the relative change in 1 D projection of FF for the j–th parameter $\delta^{\rm FF}_j$ defined by (6.15). (Note, that the 1 D slices we want to discuss here are marked by black dotted lines in Fig. 7.1 and Fig. 7.2.) While $\delta^{\rm FF}_j \approx 55\,\%$ for $j = v^y_{\rm LMC}, v^y_{\rm SMC}$, it does not exceed $\approx 35\,\%$ for either of the remaining velocity components. Undoubtedly, the discussion of the current spatial velocity vectors of the Magellanic Clouds showed their crucial importance for successful modeling of the observational data, and especially the influence of their y–components deserves further analysis. Therefore, we focus on the velocity components $v^y_{\rm LMC}$ and $v^y_{\rm SMC}$ in the following sections in order to analyze their impact on the evolution of the Magellanic System.

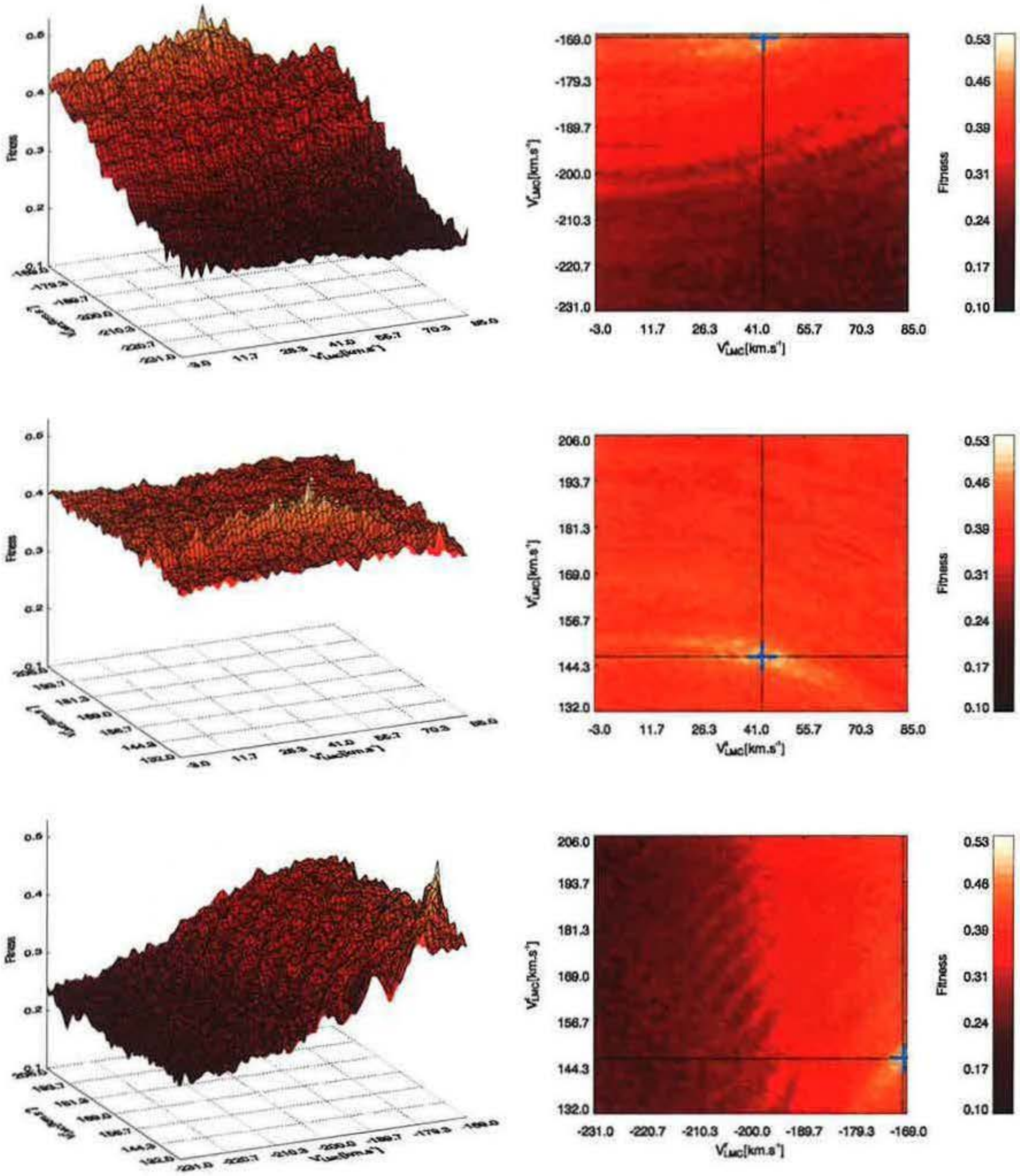

Figure 7.1: 2D projections of FF. The planes of every combination of the LMC velocity vector components are plotted above in the following order (from top to bottom): $\upsilon^x_{\rm LMC} - \upsilon^y_{\rm LMC}$, $\upsilon^x_{\rm LMC} - \upsilon^z_{\rm LMC}$ and $\upsilon^y_{\rm LMC} - \upsilon^z_{\rm LMC}$. The figure demonstrates strong influence of the choice for the velocity component $\upsilon^y_{\rm LMC}$ on the value of FF. The coordinates of the best GA fit are marked by the blue cross. The remaining parameters are fixed to the values of the best GA fit.

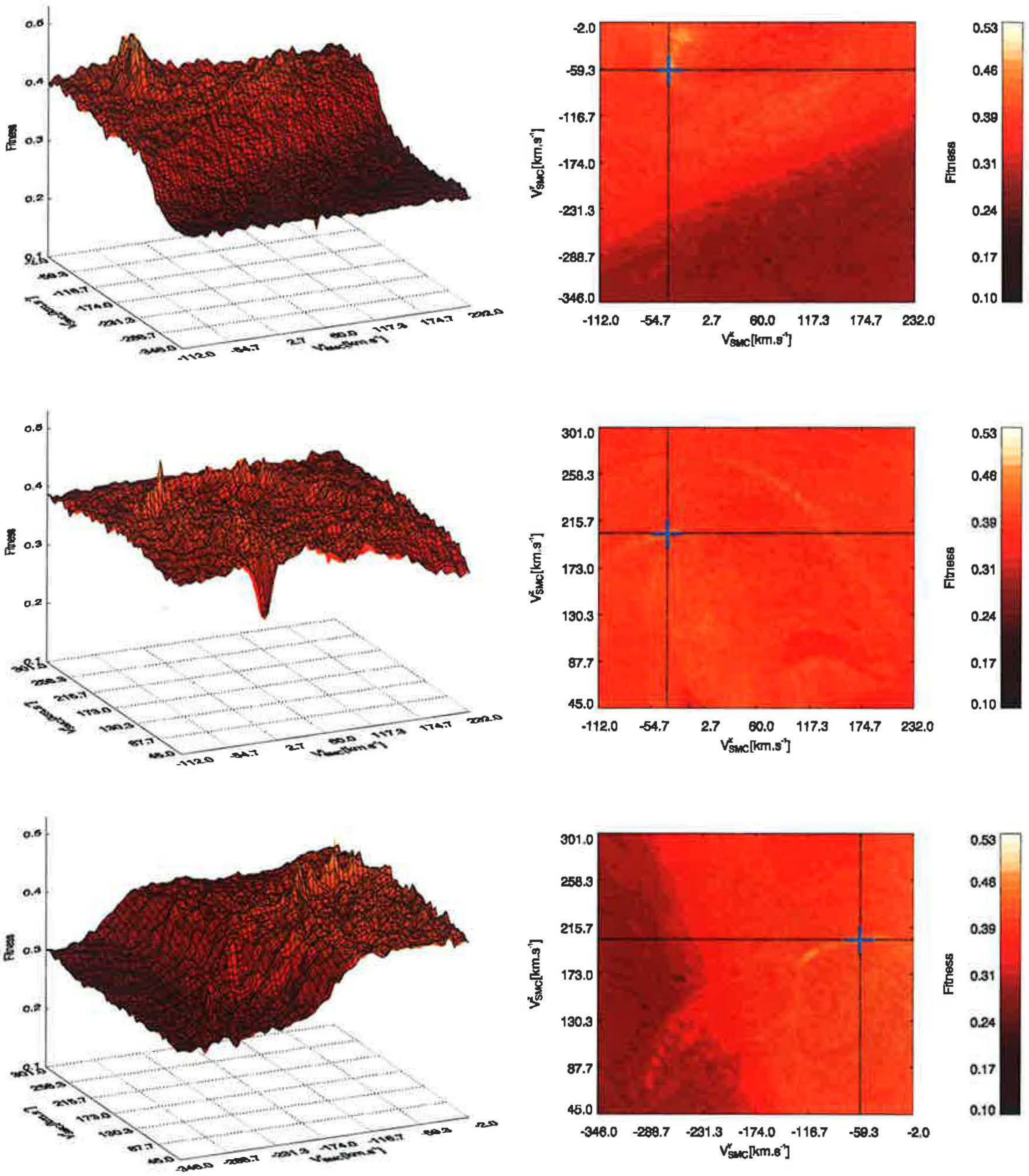

Figure 7.2: 2 D projections of FF. The figure shows the planes of every combination of the components of the SMC velocity vector. The plots are ordered as follows (from top to bottom): $v^x_{\mathrm{SMC}} - v^y_{\mathrm{SMC}}$, $v^x_{\mathrm{SMC}} - v^z_{\mathrm{SMC}}$ and $v^y_{\mathrm{SMC}} - v^z_{\mathrm{SMC}}$. Strong influence of the choice for the velocity component v^y_{SMC} on the value of FF is apparent. The coordinates of the best GA fit are marked by the blue cross. The remaining parameters are fixed to the values of the best GA fit.

7.1 Velocity versus Reproduction of the Magellanic System

We selected the LMC and SMC velocity vectors to investigate the way they affect the dynamical evolution of the Magellanic Clouds and the resulting distribution of H I together with its kinematic features. Both parameters turned out to be responsible for significant changes in FF on either a local or a global scale. The modeled distribution of H I quantified by the value of FF is highly sensitive to the choice for the spatial velocities of the Magellanic Clouds. Insufficient reproduction of the H I observational data over significant fractions of the studied ranges of v^y_{LMC}, v^x_{SMC} and v^y_{SMC} is reflected in the clumpy distribution of the 123 GA fits of extremal values of FF in Fig. 6.8. It suggests that we might try to set up a restriction of the LMC and SMC velocity ranges that were derived from the best currently available astrometric measurements (see the review in Chapter 4). Such a restriction would be based on the first detailed search of the entire parameter space of the Magellanic System that was performed by a robust and automated optimizing method.

As we noted above, the collection of 123 fits contains useful information about the range of every parameter value, that allows for acceptable agreement between models and observations of the Magellanic System. Obviously, the term "acceptable" requires establishing of a threshold level of FF. To allow for quantitative statements concerning the parameters of the interaction, the models of $FF \geq FF_{\mathrm{lim}} = 0.438$, where FF_{lim} corresponds to the worst of the 123 GA fits, will be considered a satisfactory approximation of the observed System. After the limiting quality of a model for the Magellanic System was defined, it is possible to delimit sub–intervals of the studied LMC and SMC velocity ranges (Tab. 4.1), that allowed for models of $FF \geq FF_{\mathrm{limit}}$. The corrected ranges for the spatial velocity components of the Magellanic Clouds are listed in Tab. 7.1. Obviously, significant restriction of acceptable values of the velocity components v^y_{LMC}, v^x_{SMC} and v^y_{SMC} occurred, while the remaining components lead to satisfactory models ($FF \geq FF_{\mathrm{lim}}$) over their entire ranges that we analyzed.

Param. \ ***FF* value**	$FF \geq 0$	$FF \geq FF_{\mathrm{lim}}$
$v_{\mathrm{LMC}}[\mathrm{km\,s^{-1}}]$	$\begin{pmatrix} \langle -3,85 \rangle \\ \langle -231,-169 \rangle \\ \langle 132,206 \rangle \end{pmatrix}$	$\begin{pmatrix} \langle -3,84 \rangle \\ \langle -183,-169 \rangle \\ \langle 135,206 \rangle \end{pmatrix}$
$v_{\mathrm{SMC}}[\mathrm{km\,s^{-1}}]$	$\begin{pmatrix} \langle -112,232 \rangle \\ \langle -346,-2 \rangle \\ \langle 45,301 \rangle \end{pmatrix}$	$\begin{pmatrix} \langle -84,111 \rangle \\ \langle -187,-2 \rangle \\ \langle 45,281 \rangle \end{pmatrix}$

Table 7.1: Restriction of the observationally derived estimates for the ranges of the current spatial velocity vectors of the Magellanic Clouds. The velocity ranges in the middle column are equal to the entire intervals searched by GA where always $FF \geq 0$. The right column offers sub–intervals of the original ranges for which models of $FF \geq FF_{\mathrm{lim}}$ exist.

We have mentioned that there was a remarkable distribution of the 123 GA fits obtained over the range of the LMC velocity component v^y_{LMC} (see Sec. 6.5.1). The number density of the points in the parameter space, that correspond to the GA fits, grows toward the upper limit of the interval for v^y_{LMC} as depicted in Fig. 6.8. The 1 D projection of FF at the position of the best fit (Tab. 6.1) shows a very steep slope as it approaches the upper v^y_{LMC} limit, which one may see in Fig. 6.9. Thus, strong indications exists, that an extension of the studied parameter space concerning the LMC velocity (the component v^y_{LMC} specifically) is highly desirable, since it might allow for even more successful models ($FF \geq FF_{\mathrm{lim}}$) of the Magellanic System. A detailed GA–based search of the redefined parameter space will be left for the next study on the System, because of high when

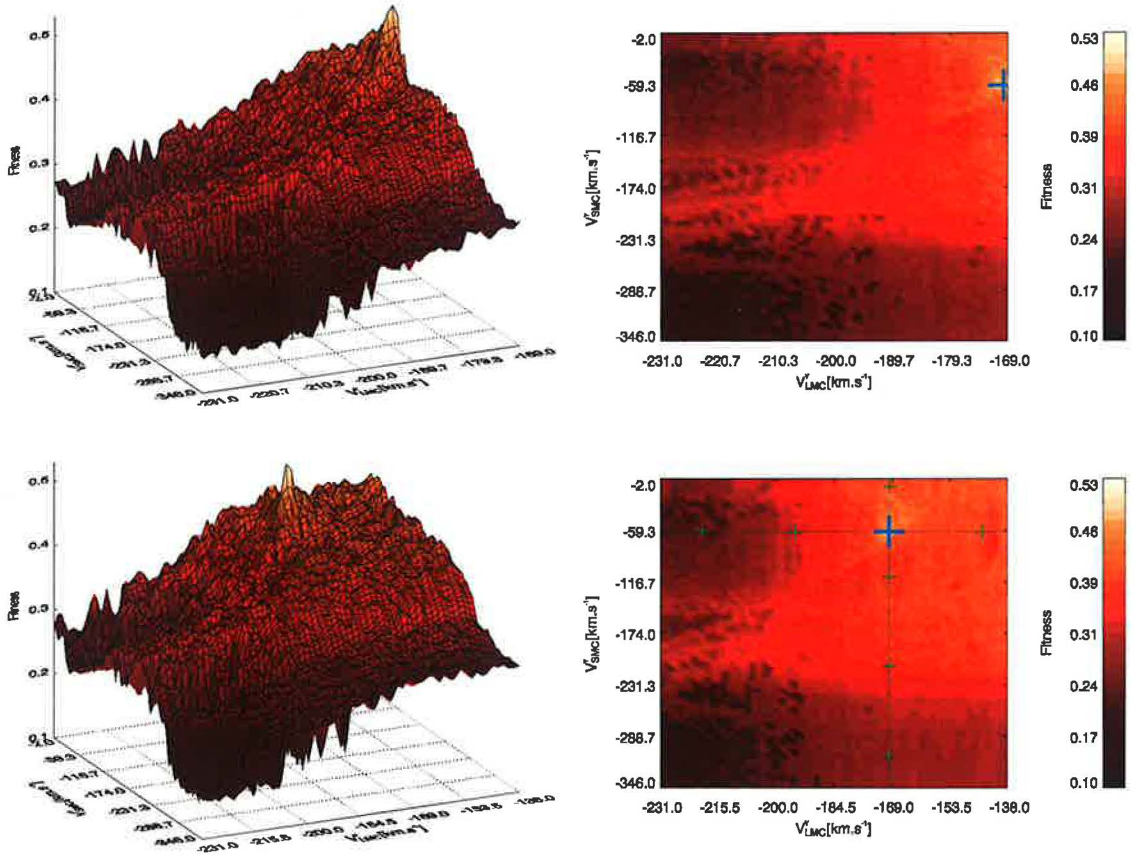

Figure 7.3: Projection of FF to the plane $v^y_{\mathrm{LMC}} - v^y_{\mathrm{SMC}}$. computational cost of such a task. However, useful insight into the features of FF for the velocity extension of the parameter space may be obtained by the means of interpolation of the FF values calculated on a grid. The upper limit of the LMC velocity component v^y_{LMC} was changed from $-169\,\mathrm{km\,s^{-1}}$ to $-139\,\mathrm{km\,s^{-1}}$. Subsequently, FF was evaluated on the 2 D grid in the plane $v^y_{\mathrm{LMC}} - v^y_{\mathrm{SMC}}$ (that shows the strongest variations in FF), The upper plot corresponds to the original GA searched parameter space (Tab. 4.1). It is compared to the 2 D FF projection for the space extended in the LMC velocity component v^y_{LMC}. The blue cross marks the highest value of FF that was identified by GA (Tab. 6.1). Additional green crosses show the points that were picked for further analysis of the corresponding models.

the remaining parameters were fixed to the values in Tab. 6.1. After interpolation we obtained the 2 D projection of FF for the extended parameter space. The new 2 D "fitness landscape" is depicted in Fig. 7.3, that offers comparison with the original portion of the parameter space. The first look at the extended 2 D FF plane discovers a turn–point located right at the edge of the original range of $\upsilon^{y}_{\mathrm{LMC}}$, where the maximal known value of FF was identified. The projected FF becomes rather flat beyond the mentioned limit, and oscillates between the values of ≈ 0.42 and ≈ 0.48, when $\upsilon^{y}_{\mathrm{SMC}} \gtrsim -230\,\mathrm{km\,s^{-1}}$. Thus, similarly to all the other parameters of the interaction, that were studied, there is an interval of $\upsilon^{y}_{\mathrm{LMC}}$ values where FF reaches its plateau. If such an analysis of the projected FF is made for every of the 123 GA fits (local maxima of FF), one obtains the same result. It has to be considered a very remarkable result, since it allows for speculations about the global maximum of FF (6.7) for the Magellanic System. The investigation of the FF brought a significant indication that a fraction of the parameter space exists, where the dependence of FF on the specific parameter combination becomes weak, and values of FF oscillate with the relative amplitude of order 10^{-2} around a typical value of ≈ 0.46. Then, there is no particular reason to expect a model of fitness exceeding significantly the quality of the best GA fit (Tab. 6.1) in the volume of the parameter space that is the subject to this study.

We have analyzed the dependence of FF on the LMC and SMC spatial velocity components. The previous discussion emphasized importance of the choice for the velocity vector, regarding the dynamical evolution of the System and namely the resulting distribution of H I. Values of FF measure the overall H I column density and kinematics, but do not offer any information about the local agreement between models and the H I observations. That raises an interesting question about sensitivity of the observed H I structures to the choice for the parameters of the interaction (LMC and SMC velocities here). Since main focus has been given to the major structures connected to the Magellanic Clouds – the Magellanic Stream and the Leading Arm – we analyzed the 1 D FF slices in $\upsilon^{y}_{\mathrm{LMC}}$, $\upsilon^{y}_{\mathrm{SMC}}$ separately for both the mentioned structures. The FF defined by (6.7) was employed. The 1 D projections of FF are marked by green dotted lines in the lower left plot in Fig. 7.3. The resulting dependence of the 1 D FF for the velocity parameters $\upsilon^{y}_{\mathrm{LMC}}$ and $\upsilon^{y}_{\mathrm{SMC}}$ is depicted in Fig. 7.4. Together with the values of FF_{Tot} for the entire system (marked as "Total"), we plot also the FF calculated separately for the Magellanic Stream

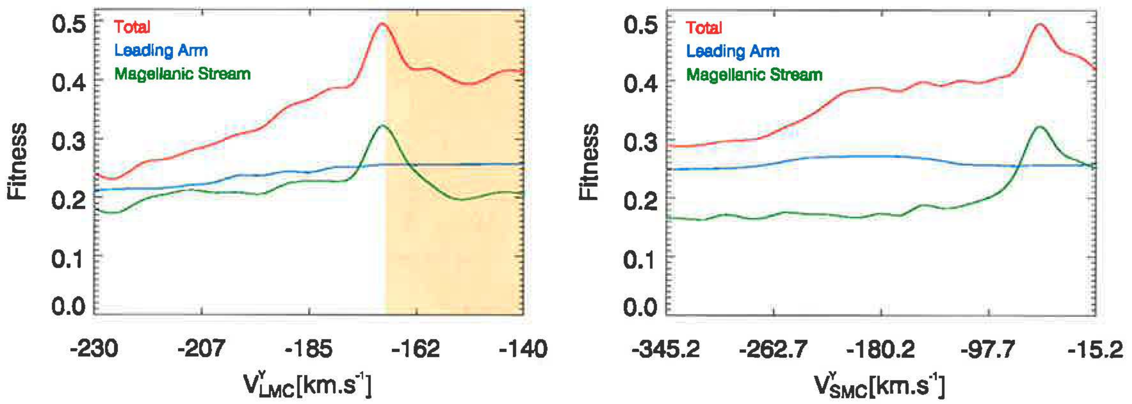

Figure 7.4: Fitness functions of the entire Magellanic System (FF_{Tot}), of the Leading Arm area (FF_{LA}) and of the Magellanic Stream (FF_{MS}) are plotted versus the velocity components $\upsilon^{y}_{\mathrm{LMC}}$ and $\upsilon^{y}_{\mathrm{SMC}}$ of LMC and SMC, respectively.

(FF_{MS}) and the Leading Arm (FF_{LA}) areas. Note, that FF always returns values in the range of $\langle 0, 1\rangle$ and so $FF_{\mathrm{Tot}} \neq FF_{\mathrm{LA}} + FF_{\mathrm{MS}}$. Apparently, the profile of the FF_{Tot} strongly dependent on behavior of the component FF_{MS}. That is based on the relative fraction of the entire H I data–cube belonging to the Magellanic Stream area (it is $\approx 3/4$ of the volume). However, detailed look at Fig. 7.4 suggests, that the contribution of FF_{LA} is not negligible and is able to compensate variations in FF_{MS}. It is due to remarkably different sensitivity of the FF components for the Magellanic Stream and the Leading Arm. Regarding the overview of the previous tidal models of the Magellanic System in Chapter 2.1, it is not surprising that the fitness of the Leading Arm reaches the maximum of ≈ 0.25 which has to be considered insufficient. The flatness of FF_{LA} reflects the fact, that tidal models are unable to reproduce the Leading Arm satisfactorily.

7.2 Morphology and Kinematics of H I Distribution

We have analyzed the role of the LMC and SMC spatial velocity components v^{y}_{LMC} and v^{y}_{SMC} as input parameters of the numerical model of the interacting system LMC–SMC–MW. Particular attention was paid to the way the choice for the velocity components affects the resulting distribution of H I in the position–LSR radial velocity

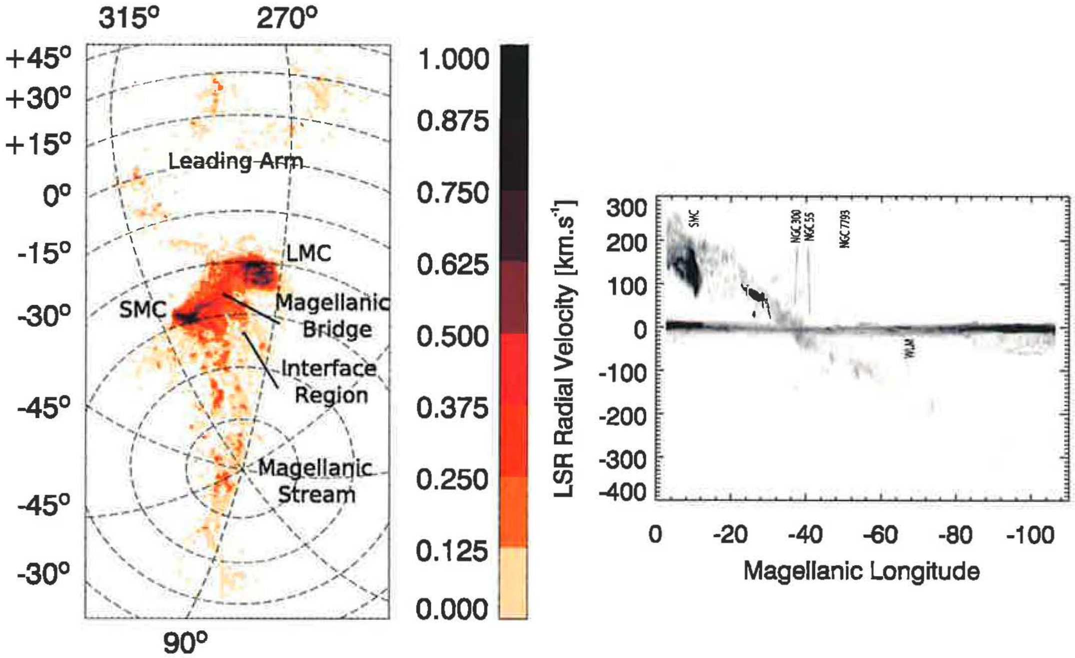

Figure 7.5: Left plot: Contour map of the observed H I integrated relative column density in the Magellanic System. Data by Brüns et al. (2005) is projected on the plane of sky. Galactic coordinates are used. Right plot: LSR radial velocity of the Magellanic Stream as a function of Magellanic Longitude (Wannier & Wrixon, 1972). The observational data Brüns et al. (2005) is plotted. Strong H I emission observed for $v_{\mathrm{LSR}} \approx 0\,\mathrm{km\,s^{-1}}$ comes from the MW. The map also shows the emission from the SMC, the galaxies NGC 300, NGC 55, and NGC 7793 from the Sculptor Group, and the Local Group galaxy WLM.

space, which was discussed in terms of the fitness function FF. The values of FF reflect the overall agreement between the observational information about kinematics and column density of H I and the results of our simulations. To investigate the individual contributions of the most notable H I features – the Magellanic Stream and the Leading Arm – the FF was evaluated separately for each of the mentioned structures. A remarkable difference was discovered between the parts of the Magellanic System, concerning behavior of FF_{MS} and FF_{LA}, respectively. Values of FF_{MS} turned out to be highly sensitive to variations in spatial velocities of the Clouds, while FF_{LA} did not show significant dependence on the input velocities (see Fig. 7.4). Such an interesting result became a strong motivation to investigate the morphology of the H I distribution together with its large-scale kinematic features. Therefore, we offer Fig. 7.5 that depicts the integrated observed column density of H I projected on the plane of sky, and also the famous LSR velocity profile of the entire Magellanic System as seen in H I, discovered by MATHEWSON ET AL. (1974). Actually, the plots introduce two different views of the original 3 D data-cube obtained by BRÜNS ET AL. (2005) and kindly provided for our GA search. The high-resolution data was

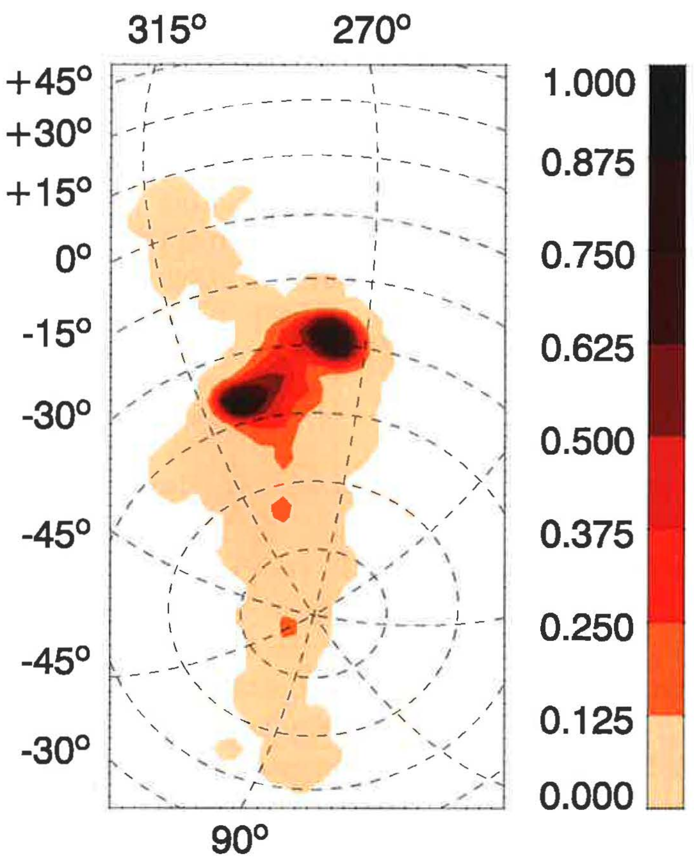

Figure 7.6: Contour map of the observed H I integrated column density. The original data cube by BRÜNS ET AL. (2005) is modified by frequency filtering (see Sec. 6.3) and integrated over all radial velocity channels. Contour map is projected on the plane of sky. Galactic coordinates are used.

filtered and degraded in resolution (see Sec. 6.3), since the simple test-particle model does not allow for reliable investigation of details offered by the original data. Then, the corresponding 2 D contour map changes from the right plot in Fig. 7.5 into Fig. 7.6.

In order to study the distribution of H I in the Magellanic System and its changes with respect to variations of the spatial velocities of the Clouds, we selected 8 points in the parameter space, located in the 2 D slice of FF that contains the maximum discovered by GA (see Tab. 6.1). The plane covers the entire range of the SMC velocity component $v^y_{\rm SMC}$ (Tab. 4.1), and the extension of the original interval for $v^y_{\rm LMC}$ and is depicted in Fig. 7.3. The selected velocity combinations are marked by green crosses, and we also included the position of the best fit (blue cross). The corresponding models will be referenced as A, B, C, D, E, F, G and H hereafter (see Tab. 7.2).

Model	$v^y_{\rm LMC}$ [km s^{-1}]	$v^y_{\rm SMC}$ [km s^{-1}]	FF
A	-219.8	-60.2	0.258
B	-194.8	-60.2	0.319
C	-169.8	-60.2	0.496
D	-144.8	-60.2	0.414
E	-169.8	-310.2	0.292
F	-169.8	-210.2	0.378
G	-169.8	-110.2	0.397
H	-169.8	-10.2	0.421

Table 7.2: Selected velocity combinations for the current motion of the Magellanic Clouds.

First, the y–component of the LMC velocity vector was varied, while $v^y_{\rm SMC} = -60.2\,{\rm km\,s^{-1}}$. The resulting morphology of H I distribution and the LSR radial velocity profile of the System are plotted in the first two rows of Fig. 7.7 for every parameter combination. That set of models contains also the best GA fit discovered for $v^y_{\rm LMC} = -169.8\,{\rm km\,s^{-1}}$. Similarly, the SMC velocity vector was kept fixed and 4 simulations were run for different values of $v^y_{\rm LMC}$. The corresponding density distribution of H I and its kinematic properties are illustrated by the lower two rows of Fig. 7.7.

A notable relation between the relative fraction of H I mass transported from the Clouds into the region of the Magellanic Stream and the quality of the model can be inferred from the contour plots. In general, the Stream becomes more massive and also its morphology gets more similar to the observational results for the models close to the best GA fit. That fact is reflected by the increasing values of both the $FF_{\rm MS}$ and the total fitness of the Magellanic System in Fig. 7.4. However, as either of the velocity components approaches its upper limit, the discrepancy of the model and observational data grows due to systematic overestimating of the H I column densities and also of the spatial extent of the matter distribution to the areas with no H I emission observed (see D and H), which results into lower values of FF compared to the best GA fit (see Fig. 7.3 or Fig. 7.4). One should also raise a question about composition of the Magellanic Stream, regarding

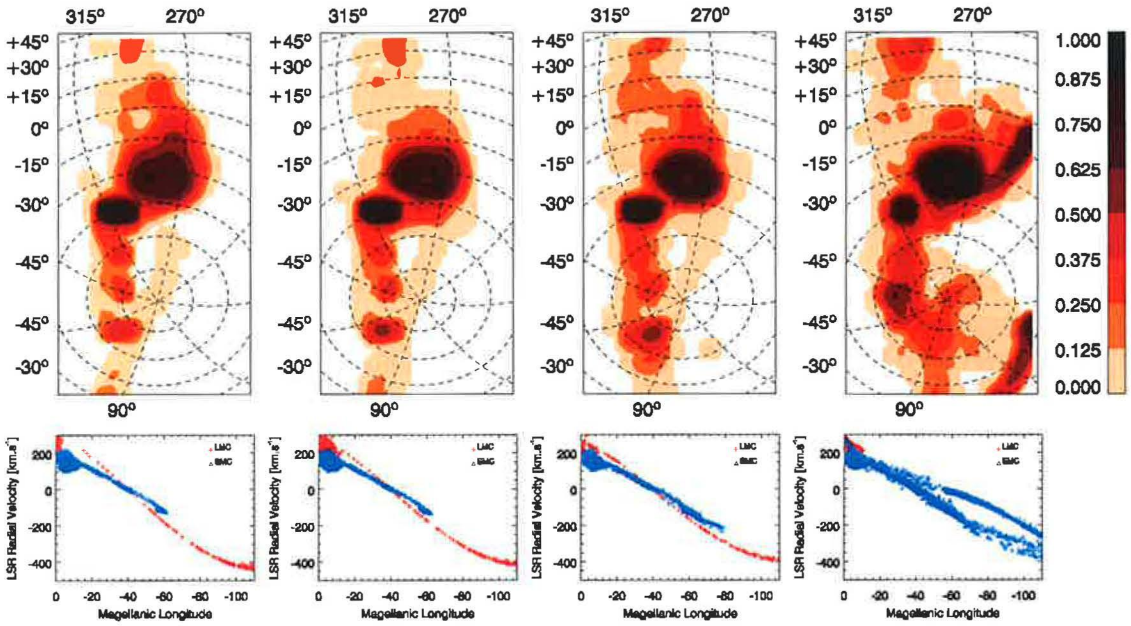

$v^y_{\mathrm{LMC}} = -219.8\,\mathrm{km\,s^{-1}}$ $v^y_{\mathrm{LMC}} = -194.8\,\mathrm{km\,s^{-1}}$ $v^y_{\mathrm{LMC}} = -169.8\,\mathrm{km\,s^{-1}}$ $v^y_{\mathrm{LMC}} = -144.8\,\mathrm{km\,s^{-1}}$

$v^y_{\mathrm{SMC}} = -60.2\,\mathrm{km\,s^{-1}}$ $v^y_{\mathrm{SMC}} = -60.2\,\mathrm{km\,s^{-1}}$ $v^y_{\mathrm{SMC}} = -60.2\,\mathrm{km\,s^{-1}}$ $v^y_{\mathrm{SMC}} = -60.2\,\mathrm{km\,s^{-1}}$

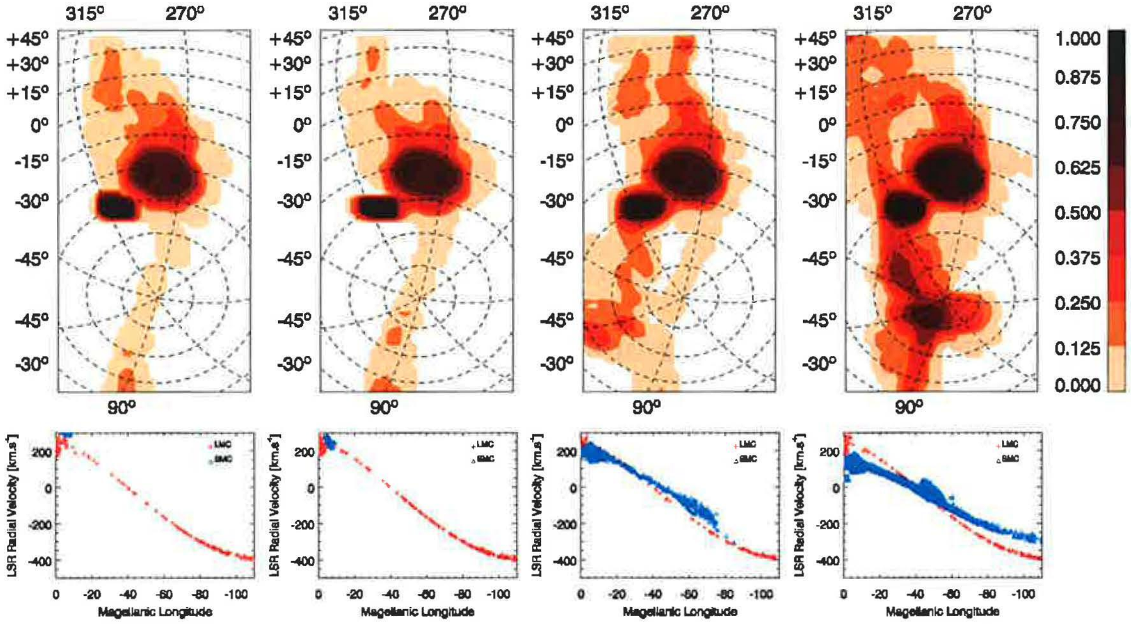

$v^y_{\mathrm{LMC}} = -169.8\,\mathrm{km\,s^{-1}}$ $v^y_{\mathrm{LMC}} = -169.8\,\mathrm{km\,s^{-1}}$ $v^y_{\mathrm{LMC}} = -169.8\,\mathrm{km\,s^{-1}}$ $v^y_{\mathrm{LMC}} = -169.8\,\mathrm{km\,s^{-1}}$

$v^y_{\mathrm{SMC}} = -310.2\,\mathrm{km\,s^{-1}}$ $v^y_{\mathrm{SMC}} = -210.2\,\mathrm{km\,s^{-1}}$ $v^y_{\mathrm{SMC}} = -110.2\,\mathrm{km\,s^{-1}}$ $v^y_{\mathrm{SMC}} = -10.2\,\mathrm{km\,s^{-1}}$

Figure 7.7: Modeled distribution of H I in the Magellanic System. The plots in the first and the third row show contour maps of the integrated relative column densities of H I. Data is projected on the plane of sky and galactic coordinates are used. Important kinematic information about the H I distributions is offered in the figures depicting the LSR radial velocity of H I as function of Magellanic Longitude (for definition see WANNIER & WRIXON, 1972).

contributions to the H I content coming from LMC and SMC, respectively. To answer, we may use the LSR radial velocity plots that provide interesting information about origin of matter in the Magellanic Stream. Obviously, it is SMC that is responsible for the previously discussed enrichment of the Magellanic Stream for the models situated at the plateau of FF (Fig. 7.3). The low-density trailing tail consisting of LMC particles turned out to be rather a general structure that was created over a wide range of LMC and SMC velocities. The matter distribution in the LMC stream is smooth, which indicates the influence of a long-term continuous tidal stripping. On the other hand, sensitivity of the SMC component of the Magellanic Stream to the choice for the velocity vectors of the Clouds, together with its clumpy structure, point to the important role of LMC–SMC and SMC–MW encounters in the process of disruption of SMC. We have touched the relation of the present distribution of H I in the Magellanic System and the past evolution of the interacting group LMC–SMC–MW. That undoubtedly interesting topic will be discussed in the next section. The observations by MATHEWSON ET AL. (1974) discovered the Magellanic Stream and introduced its remarkable large-scale kinematics. The LSR radial velocity profile of H I along the Magellanic Stream is linear and reaches a high negative value of $\approx -400\,\mathrm{km\,s^{-1}}$ at its far tip (see Fig. 7.5). LSR radial velocity profiles in Fig. 7.7 always succeed concerning the slope and the velocity value at the far tip of the Magellanic Stream. Basically, it is the LMC component of the Stream that is responsible for the good agreement of the models and observations of the LSR radial velocity profile. Exception exists for the scenario D, where the SMC tail became dominant. However, a significant H I structure appears in the model at the velocity–position region where no emission has been detected so far, which discriminates that scenario. If a SMC component exists, its LSR radial velocity is also well linear, but the slope slightly differs from the profile of the LMC stream, which causes a small separation of the components in velocities, and so the SMC tail does not reach the observed high–negative LSR radial velocity.

7.3 Notes on the Dynamical Evolution

Analysis of the contributions by the Magellanic Stream and the Leading Arm to FF of the entire Magellanic System discovered the sensitivity of the H I distribution in the area of the Stream to variations in the spatial velocities of the Clouds (see Fig. 7.4). In the previous section, we noted that the Magellanic Stream typically consists of both the LMC and SMC components, which respond to the choice for the LMC and SMC velocity vectors in significantly different ways. Such facts allowed for general speculations about the dynamical evolution of the interacting system LMC–SMC–MW. We suggested that the features of the LMC tail point to its possible origin as a product of a continuous tidal stripping, while the strong dependence of the SMC contribution to the Magellanic Stream on the motion of the Clouds indicates a very likely role of close SMC–LMC and SMC–MW encounters. Thus, the investigation of the orbital motion of the Magellanic Clouds and its influence on redistribution of matter in the Magellanic System will be the subject to this section.

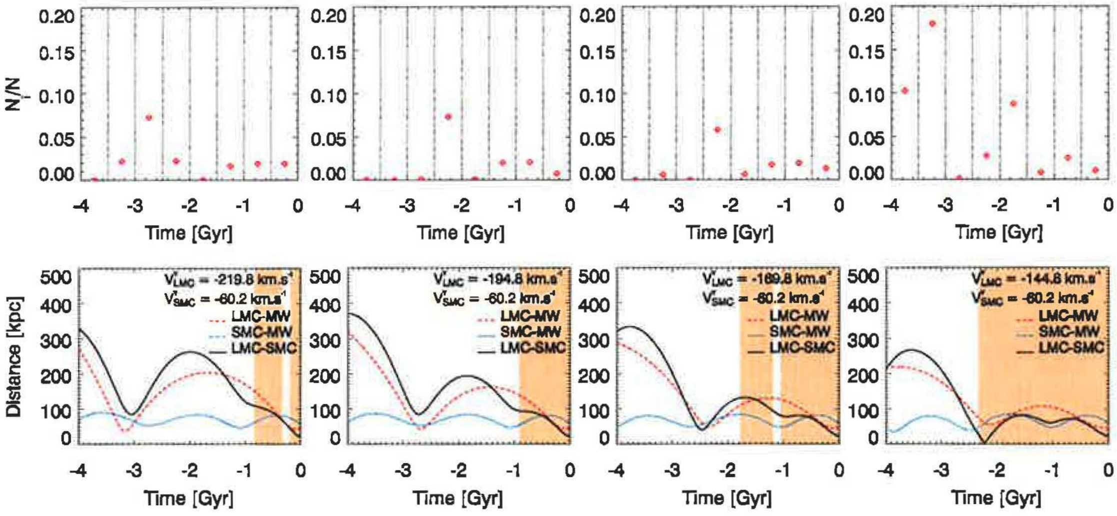

$v^y_{\rm LMC} = -219.8\,{\rm km\,s^{-1}}$
$v^y_{\rm SMC} = -60.2\,{\rm km\,s^{-1}}$

$v^y_{\rm LMC} = -194.8\,{\rm km\,s^{-1}}$
$v^y_{\rm SMC} = -60.2\,{\rm km\,s^{-1}}$

$v^y_{\rm LMC} = -169.8\,{\rm km\,s^{-1}}$
$v^y_{\rm SMC} = -60.2\,{\rm km\,s^{-1}}$

$v^y_{\rm LMC} = -144.8\,{\rm km\,s^{-1}}$
$v^y_{\rm SMC} = -60.2\,{\rm km\,s^{-1}}$

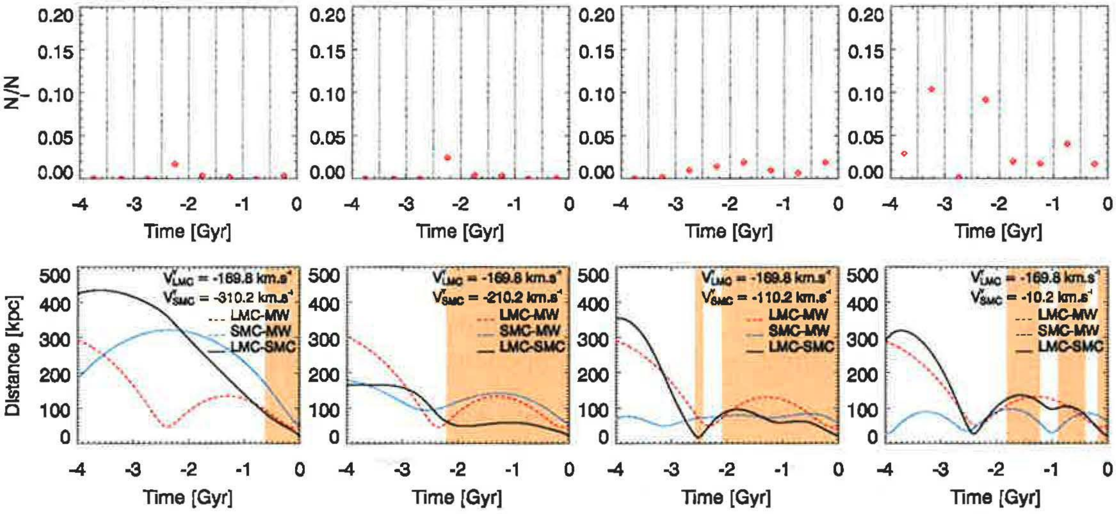

$v^y_{\rm LMC} = -169.8\,{\rm km\,s^{-1}}$
$v^y_{\rm SMC} = -310.2\,{\rm km\,s^{-1}}$

$v^y_{\rm LMC} = -169.8\,{\rm km\,s^{-1}}$
$v^y_{\rm SMC} = -210.2\,{\rm km\,s^{-1}}$

$v^y_{\rm LMC} = -169.8\,{\rm km\,s^{-1}}$
$v^y_{\rm SMC} = -110.2\,{\rm km\,s^{-1}}$

$v^y_{\rm LMC} = -169.8\,{\rm km\,s^{-1}}$
$v^y_{\rm SMC} = -10.2\,{\rm km\,s^{-1}}$

Figure 7.8: Evolution of the Magellanic System during the last 4 Gyr. The plots in the second and the fourth row show the orbital evolution of the Clouds. Time dependence of of the LMC (red dashed line), SMC (blue dotted line) galactocentric distances, and the LMC–SMC relative distance are plotted above. Filled areas of the plots correspond to time intervals when LMC and SMC formed a gravitationally bound couple. For each of the 8 models, we also calculated the relative number of the LMC/SMC particles strongly disturbed due to the interaction in the Magellanic System. Counts within 8 time intervals of 500 Myr are made and plotted in the first and the third row.

We studied orbital paths of the Magellanic Clouds during the last 4 Gyr. The evolution of the separation between the Clouds and their galactocentric distances as functions of time are plotted in Fig. 7.8 for each of the selected points in the parameter space (see Fig. 7.3). Filled parts of the mentioned plots in Fig. 7.8 indicate the periods when the Magellanic Clouds reached the state of a gravitationally bound system. We define gravitational binding by the sum of the relative kinetic and gravitational potential energy of LMC and SMC:

$$E_{\mathrm{tot}} = \frac{m_{\mathrm{LMC}}\, m_{\mathrm{SMC}}}{m_{\mathrm{LMC}} + m_{\mathrm{SMC}}} \left(|\boldsymbol{v}_{\mathrm{LMC}} - \boldsymbol{v}_{\mathrm{SMC}}|^2 - G \frac{m_{\mathrm{LMC}} + m_{\mathrm{SMC}}}{|\boldsymbol{r}_{\mathrm{LMC}} - \boldsymbol{r}_{\mathrm{SMC}}|} \right) . \tag{7.1}$$

The Clouds are bound when E_{tot} is negative. Another point of interest is redistribution of matter in the Magellanic System during the process of its dynamical evolution. Therefore, every orbital plot is accompanied by a figure depicting the relative number of the LMC and SMC particles strongly disturbed, i.e. particles that reached the minimal distance of twice the original radii of their circular orbits around the LMC, SMC center, respectively, for each of 8 time intervals of 500 Myr.

First of all, lets explore the galactocentric distances of the Clouds and their dependence on the velocity components v^y_{LMC} and v^y_{SMC}. The current velocity of LMC was varied and we obtain the series of 4 models with the corresponding plots shown in the upper half of Fig. 7.8. Apparently, significant changes in the LMC velocity vector do not induce a strong response in the time dependence of the LMC–MW distance. In every case, two perigalactic approaches of LMC occurred during the last 4 Gyr. Their time separation decreased from $\approx$ 3 Gyr in the model A to $\approx$ 2 Gyr for the model D. A very similar decreasing tendency was noted for the apogalactic distances of LMC as v^y_{LMC} grows. One should also note an interesting detail concerning the first perigalactic approach of LMC. It is slightly increased (by $\approx$ 15 kpc) toward the upper limit of v^y_{LMC}, which will turn out to be important with respect to the LMC component of the Magellanic Stream.

As we expected, the orbital evolution of SMC was altered only when a close approach to LMC occurred (the rightmost plot in the second row of Fig. 7.8). A similar result was obtained for the LMC galactocentric distance when the SMC velocity vector became the subject to modification (the fourth row of Fig. 7.8). Moreover, sensitivity of LMC to perturbations by SMC is less that vice–versa due to the ratio of their masses. On the other hand, the SMC–MW separation as function of v^y_{LMC} is really remarkable. The interval of the subsequent perigalactic approaches of SMC well exceeds 4 Gyr for E, while it becomes $<$ 1.5 Gyr for the model H. Such a change is accompanied by an apparent drop of the maximal apogalactic distance of SMC from $\approx$ 300 kpc to $\approx$ 100 kpc.

Now, the attention will be paid to the time dependence of the LMC–SMC separation for different velocity combinations. The orbital plots in Fig. 7.8 indicate that the global minimum of the relative distance between the Clouds drops as we reach the high–fitness plateau in Fig. 7.4. Also the average LMC–SMC distance decreases which is reflected by the generally increasing total length of the periods when the Clouds form a gravitationally bound pair. Such a trend in the LMC–SMC separation suggests rising intensity and efficiency of their interaction, concerning redistribution of matter in the System, which deserves a further investigation. The plots in Fig. 7.8, depicting the relative counts of the disturbed LMC/SMC particles, may serve as plausible sources of information for such an analysis.

We have already noted that the LMC component of the Magellanic Stream is present over a wide range of possible initial velocity combinations. Except the scenario D, the LMC tail is present in each of the models studied here. The perigalactic approach of LMC at $T < -2\,\mathrm{Gyr}$ was crucial for its creation, and so the major raise of the number of disturbed particles for $-3.5 < T < -2\,\mathrm{Gyr}$ is due to distortion of the outer regions of the LMC initial disk. The matter torn–off was spread along the orbit of LMC due to the tidal stripping by MW. Previously, it was pointed out that the LMC–MW distance for the first perigalactic approach slightly increases as we switch from A to D. Now, it became clear that it is a crucial factor for the creation of the LMC trailing tail. It should be mentioned, that also a LMC leading stream always evolves as a counterpart to the trailing component (for general notes on test–particle models of galactic interactions see TOOMRE & TOOMRE, 1972). It contributes to the Leading Arm, but the agreement with the observed distribution of H I is constantly insufficient (see Fig. 7.4).

Concerning the SMC contribution to the H I structures, it varies due to both SMC–MW approaches and SMC–LMC encounters. However, the orbital motion of SMC turned out to be highly sensitive to the choice for v^y_{SMC} (affects especially timing and distance of perigalactic approaches) but also to the motion of LMC (due to changes in the resulting gravitational perturbations). Thus, it is not surprising that the SMC content of the Magellanic Stream strongly fluctuates over the studied models. Generally, outflow of particles from SMC dominates the process of matter redistribution for $T > -2\,\mathrm{Gyr}$. In the case of the models D and H, very intense destruction of the initial particle disk–like configuration for $T < -3\,\mathrm{Gyr}$ is apparent for SMC. The corresponding plots in Fig. 7.8 clearly explain such a fact by tidal stripping caused by MW due to the proximity of SMC. Similarly to the LMC particles, a certain fraction of the SMC matter stripped–off contributes to the Leading Arm.

7.4 Summary and Conclusions

We investigated the properties of the modeled distribution of H I in the Magellanic System with respect to the choice for the current velocities of LMC and SMC. The detailed search of the entire parameter space of the interaction (Tab. 4.1) discovered the outstanding role of the spatial velocity of the Clouds regarding the dynamical evolution of the System. Due to the specific selection of the Cartesian frame, the velocity components v^y_{LMC} and v^y_{SMC} became the parameters critically influencing the results of the corresponding models. Their impact on agreement between our numerical models and observations of H I in the Magellanic System are discussed in Sec. 7.1.

Interesting behavior of FF as function of v^y_{LMC} became a motivation for an additional exploration of the parameters space beyond the upper limit of v^y_{LMC} defined in Tab. 4.1. We studied the FF of the Magellanic System over the selected plane of the velocity components $v^y_{\rm LMC} - v^y_{\rm SMC}$, when the remaining parameters were kept fixed to the values of the best GA fit (Tab. 6.1). The deserved extension of the range for $v^y_{\rm LMC}$ lead to the discovery of a flat region of the "fitness landscape", which was previously noticed for all the other parameters. A further insight into the Magellanic System was achieved by decomposition of FF into the parts for the Magellanic Stream and the Leading Arm. It was found out that the distribution of H I in the Magellanic Stream area is the main factor contributing to FF of the entire System and is notably sensitive to the variations in the spatial velocities. In contrast to that, satisfaction of observational data is constantly insufficient for the region of the Leading Arm, and the corresponding $FF_{\rm LA}$ does not vary with changing velocities of the Clouds. The last note introduces an expectable result, since serious difficulties reproducing the Leading Arm occurred in every simulation of the Magellanic System introduced so far (see the discussion in Sec. 2.1). After the influence of the current spatial velocities of LMC and SMC on agreement between the modeled and observed distribution of H I was investigated, the physical properties of the models need to be clarified in terms of H I column densities, kinematics, and the past orbital motion of the Clouds.

We have shown that the models of low values of FF (the models A, B, E, F) generally miss intense encounters that would lead to a significant disruption of either the LMC or SMC initial disk–like configuration of a particle distribution. However, the LMC–MW encounters at $-3.5 < T < -2$ Gyr are efficient enough to disturb the outer region of the LMC disk, which leads to creation of a smooth low–density trailing tail, that satisfies the observed LSR radial velocity profile of the Magellanic Stream well (Fig. 7.5). When the plateau of FF (see Fig. 7.3) is reached (the models C, D, G, and H), the mutual approaches of SMC and MW, together with the LMC–SMC encounters lead to a very intense tidal stripping of the SMC particles. The encounters cause a very strong tidal force acting for a short time interval, which results into large variations of the stripping rates for SMC (see Fig. 7.8). Such a process is reflected by the clumpy distribution of H I column density, as illustrated by Fig. 7.7. Comparison with the H I observations by BRÜNS ET AL. (2005) (Fig. 7.5 and Fig. 7.6) shows the expected discrepancy between the observed and modeled H I maps. However, the best models studied here (C and G) were able to produce trailing tails of correct large–scale kinematics and also of an inhomogeneous distribution of H I, which should be considered a notable reproduction of the Magellanic Stream. We show that the choice for the LMC and SMC orbits may suppress common drawbacks of both the tidal (absence of clumps in the Magellanic Stream) and ram pressure (insufficient slope of the LSR radial velocity profile) models. Nevertheless, the obvious excess of H I column density at the far tip of the Magellanic Stream and also its spatial extent at some regions cannot be ignored and require further investigation.

It is highly desirable to take look at our models with respect to the results of previous studies (for review see Sec. 2.1). The tidal scenarios of the LMC–SMC–MW interaction predict the beginning of the evolution of the Magellanic Stream at $T \lesssim -1.5$ (see e.g. MURAI & FUJIMOTO, 1980; GARDINER ET AL., 1994, 1996), which is in a good agreement with our results. Ram pressure models often argue for younger Streams (HELLER & ROHLFS, 1994; MASTROPIETRO ET AL., 2005), but it is mostly due to a necessity for a time limitation of the continuous stripping not to exceed the total mass of the Stream. Age of the Leading Arm is comparable to the age of the Magellanic Stream, since it appears as its natural counterpart in our models (detailed explanation in TOOMRE & TOOMRE, 1972).

It turned out to be a very common result, that both the LMC and SMC particles contribute to the extended structures of the Magellanic System, namely to the Magellanic Stream. Moreover, we discovered a remarkably different influence of the LMC and SMC components on the kinematics and morphology of the System. It is very interesting that most studies published so far deal with pure either LMC or SMC Streams. That result is natural since often only LMC (e.g. LIN & LYNDEN–BELL, 1977; SOFUE, 1994; MASTROPIETRO ET AL., 2005; BEKKI & CHIBA, 2005) or SMC (see GARDINER ET AL., 1996; CONNORS ET AL., 2005) are treated as live systems. However, our study shows that creation of a one–component Magellanic Stream is a very unlikely case since both Clouds can serve as sources of matter.

Now, we would like to pay attention to the actual velocity vectors of the Clouds. The LMC and SMC velocity components of our best model can be found in Tab. 6.1, and we argue for the velocity ranges in Tab. 7.1, since they allow for a satisfactory reproduction of HI observations ($FF \geq FF_{\mathrm{lim}}$). One of the most often cited papers by GARDINER ET AL. (1994), concerning the evolution of the Magellanic System, introduces a detailed analysis of the LMC and SMC motion and suggests the current velocity vectors $\boldsymbol{v}_{\mathrm{LMC}} = (-5, -225, +194)\,\mathrm{km\,s^{-1}}$ and $\boldsymbol{v}_{\mathrm{SMC}} = (+40, +185, +171)\,\mathrm{km\,s^{-1}}$. However, a very strong and restrictive constraint was adopted by GARDINER ET AL. (1994), assuming that the LMC and SMC have formed a gravitationally bound couple for over 10 Gyr. In fact, such a condition is common in studies on the Magellanic Clouds, but its clear justification has not been introduced. Our analysis of a wide area of the velocity space denotes that a continuous long–term gravitational binding of the Clouds is an extremely unlikely case and we did not discover any dependence between the duration of the bound phase and the quality of the model. Moreover, the velocity analysis by GARDINER ET AL. (1994) was performed for a spherical potential of MW. However, we found out, that a flattened MW halo allowed for the best model, and in the next section it will be shown that aspherical halo configurations generally lead to better satisfaction of observational data.

CHAPTER 8

Flattening of the MW Dark Matter Halo

The idea of *dark matter* was introduced by ZWICKY (1933). His dynamical measurements of the mass–to–light ratio of the Coma cluster gave larger values than those known from luminous parts of nearby spirals. That discrepancy was explained by presence of DM. OSTRIKER ET AL. (1974) proposed that DM is concentrated in a form of extended galactic halos. Analysis of rotation curves of spiral galaxies (BOSMA, 1981; BURSTEIN & RUBIN, 1985) denotes that their profiles cannot be explained without presence of non–radiating DM. Hot X–ray emitting halos have been used to estimate total galactic masses (MCLAUGHLIN, 1999). Corresponding mass–to–light ratios exceed the maximum values for stellar populations, and DM explains the missing matter naturally. The presence of DM halos is expected by the standard CDM cosmology model of hierarchical galaxy formation. The classical CDM halo profile (NFW) is simplified to be spherical. However, most CDM models expect even significant deviations from spherical symmetry of DM distribution in halos. The model of formation of DM halos in the universe dominated by CDM by FRENK ET AL. (1988) produced triaxial halos with preference for prolate configurations ($c/a > 1.0$). Numerical simulations of DM halo formation by DUBINSKI & CARLBERG (1991) are consistent with halos that are triaxial and flat, with $(c/a) = 0.50$ and $(b/a) = 0.71$. There are roughly equal numbers of dark halos with oblate and prolate forms.

Observationally, the measurement of the shape of a DM halo is a difficult task. A large number of various techniques found notably different values, and it is even not clear if the halo is prolate or oblate. OLLING & MERRIFIELD (2000) use two approaches to investigate the DM halo shape of the Milky Way (MW), a rotation curve analysis and the radial dependence of the thickness of the H I layer. Both methods lead consistently to flattened oblate halos.

Recently, the nearly planar distribution of the observed MW satellites, which is almost orthogonal to the Galactic plane, raised the question, if they are in agreement with cosmological CDM models (KROUPA ET AL., 2005) or if other origins have to be invoked. ZENTNER ET AL. (2005) claim that the disk–like distribution of the MW satellites can be explained, provided the halo of the MW is sufficiently prolate in agreement with their CDM simulations. On the other hand, it is not clear, if there exists a unique prediction of the axis ratios from CDM simulations, as the scatter in axis ratios demonstrates DUBINSKI & CARLBERG (1991). Based on ΛCDM simulations KAZANTZIDIS ET AL. (2004) emphasize that gas cooling strongly affects halo shapes with the tendency to produce rounder halos.

Another promising method to determine the Galactic halo shape are stellar streams, because they are coherent structures covering large areas in space. Thus, their shape and kinematics should be strongly influenced by the overall properties of the underlying potential. A good candidate for such an analysis is the stellar stream associated with the Sagittarius dwarf galaxy. By comparison with simulations IBATA ET AL. (2001) found that the DM halo is almost spherical in the galactocentric distance range from 16 to 60 kpc. However, HELMI (2004) warned that the Sagittarius stream might be dynamically too young to allow for constraints on the halo shape.

We use the Magellanic Stream in order to derive constraints on the halo shape of the MW. The basis are the new detailed H I observations of the Magellanic System (including LMC and SMC) by BRÜNS ET AL. (2005). As remnants of the LMC–SMC–MW interaction, extended structures connected to the System are observed. We employed a simple fast numerical model of the Magellanic System combined with an implementation of a GA to perform the first very extended search of the parameter space for the interaction between LMC, SMC and MW. Here we present our results about the MW DM halo flattening values compatible with most detailed currently available H I Magellanic survey (BRÜNS ET AL., 2005, see Fig. 7.5).

8.1 Results of the GA Search

The fitness distribution for different values of the halo flattening parameter q is shown in Fig. 8.1. For every value of q, the model of the highest fitness is selected and its fitness value is plotted. Fig. 8.1 indicates that better agreement between the models and observational data was achieved generally for oblate halo configurations than for nearly spherical or prolate halos. The relative difference between the worst ($FF_{\mathrm{MIN}} = 0.450; q = 1.14$) and

Group	A	B	C
	$0.74 \le q \le 0.92$	$0.94 \le q \le 1.06$	$1.08 \le q \le 1.20$
N_i	101	10	12

Table 8.1: Three major groups according to the halo flattening q

the best ($FF_{\mathrm{MAX}} = 0.496; q = 0.84$) model shown in Fig. 8.1 is $\Delta FF = 0.09$. It reflects the fact, that each of the GA fits contains a trailing tail (Magellanic Stream) and a leading stream (Leading Arm), but there are fine differences between the resulting distributions of matter.

We want to discuss our results with respect to the shape of the MW halo. Thus, all the GA fits are divided into three groups according to the halo flattening (see Tab. 8.1) to show differences or common features of models for oblate, nearly spherical and prolate halo configurations. The actual borders between the groups A, B and C were selected by definition and the way, so that the number of models in each of the groups allows for statistical treatment of the LMC, SMC orbital features and particle redistribution which will be introduced in Sec. 8.2.

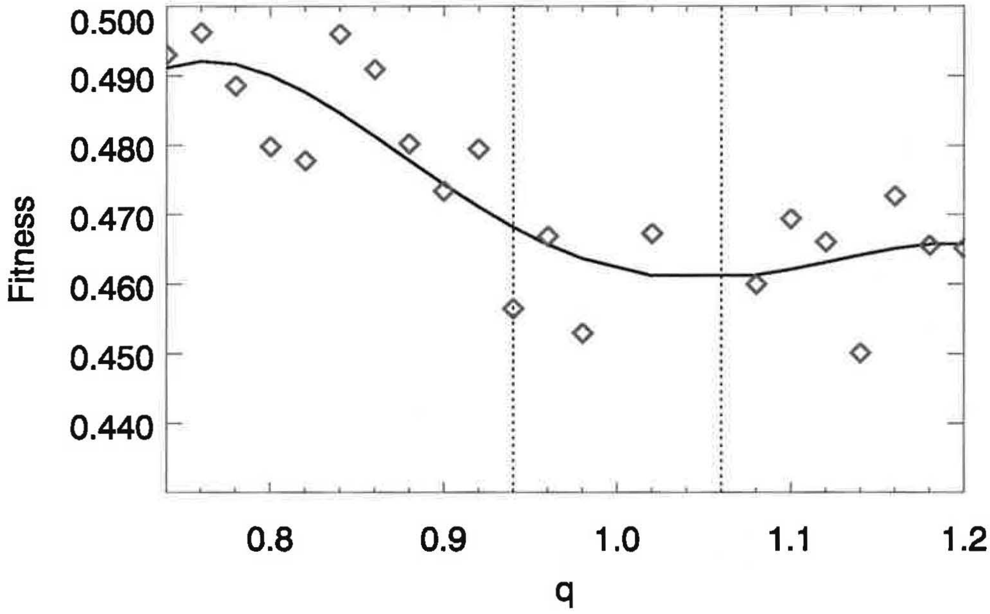

Figure 8.1: Maximum values of fitness as function of the MW dark matter halo flattening q. The plot depicts the fitness of the best GA fit of the Magellanic System that was found for each of the MW dark matter halo flattening values that entered the GA search. The function is also approximated by its least–square polynomial fit. The values of q delimiting the model groups A, B and C (see Tab. 8.1) are emphasized by dotted lines.

8.2 DM Halo Shape and Evolution of the Magellanic System

Close encounters of interacting galaxies often lead to substantial disruption of their particle disks forming tidal arms and tails subsequently (TOOMRE & TOOMRE, 1972). Regarding that, the time dependence of the relative distance of the interacting pair is an interesting source of information on the system.

First of all, we examine the time distribution of the minima of the LMC–SMC relative distance. For each of the model groups mentioned in Tab. 8.1, we calculate the relative number of GA solutions having a minimum of the LMC–SMC relative distance within a given interval of 500 Myr. Fig. 8.2 shows such a distribution of fits for the total time interval of our simulations, which is 4.0 Gyr. The local maxima of the time distribution of the LMC–SMC distance minima are within the intervals $\langle -3.0, -2.0 \rangle$ Gyr and $\langle -0.5, 0.0 \rangle$ Gyr. For prolate halos ($q \geq 1.08$) there is no LMC–SMC distance minimum between –2.0 Gyr and –0.5 Gyr.

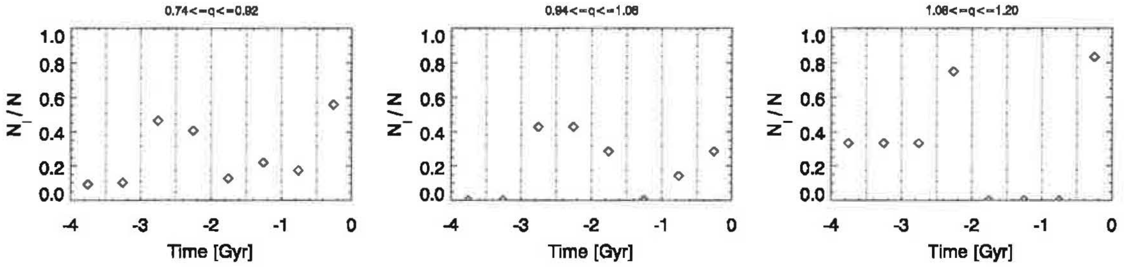

Figure 8.2: Relative numbers of the Magellanic System GA models with LMC–SMC relative distance minima at given time interval for model groups A (left), B (middle) and C (right). The counts were made for 8 time intervals of 500 Myr covering the entire Magellanic evolution period of 4 Gyr investigated in our study.

Subsequently, the mean values of the LMC–SMC distance minima are calculated for each of the time intervals defined above. Comparison of the results for oblate, nearly spherical and prolate DM halo configuration is available in Fig. 8.3. It was found that close ($\Delta r \approx 10$ kpc) LMC–SMC encounters do not occur in models with either oblate or prolate halos. If the MW DM halo shape is nearly spherical, disruption of the LMC and SMC initial particle distribution leading to creation of the observed H I structures occurred due to strong LMC–SMC interaction typically.

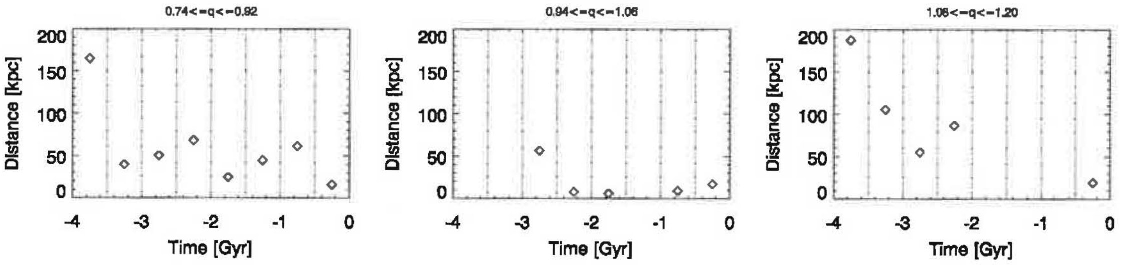

Figure 8.3: Mean values of the LMC–SMC distance minima for model groups A (left), B (middle) and C (right) (Tab. 8.1) and for 8 time intervals of 500 Myr.

Another point of interest is the time dependence of the LMC and SMC test–particle redistribution during the evolutionary process. Fig. 8.4 offers the relative number of test–particles strongly disturbed, i.e. particles that reached the minimal distance of twice the original radii of their circular orbits around the LMC, SMC center, respectively, by the LMC–SMC–MW interaction in the defined time–intervals. Comparison between the plots in Fig. 8.3 and Fig. 8.4 shows that encounters of the Clouds are followed by delayed raise of the number of particles shifted to different orbits, typically. Another such events are induced by the interaction of the Clouds and MW. Disruption of the LMC and SMC disks triggers formation of the extended structures of the Magellanic System. Particles are assigned new orbits in the superimposed gravitational potential of the LMC, SMC and MW, and spread along the orbital paths of the Clouds. Our study shows that the formation of the Magellanic Stream and other observed H I features did not begin earlier than 2.5 Gyr ago for model groups A and B (see Fig. 8.4). Prolate halos (group C) allow for a mass redistribution in the system that started at $T < -3.5$ Gyr.

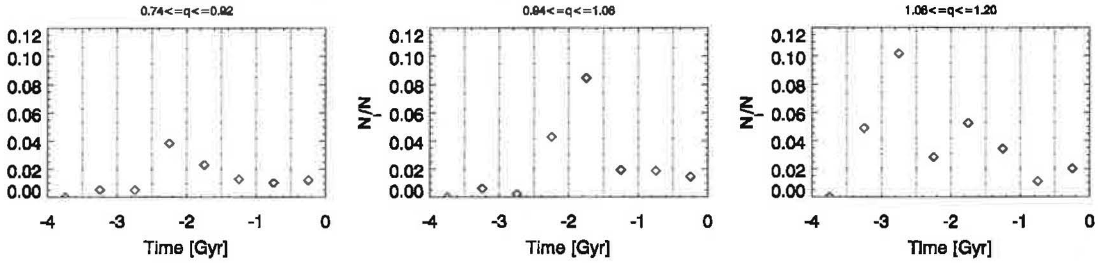

Figure 8.4: Relative number of the LMC and SMC test–particles strongly disturbed due to the Magellanic System interaction. Counts within 8 time intervals of 500 Myr and for model groups A (left), B (middle) and C (right) are plotted.

8.3 Representative Models

Here, we describe the models of highest fitness selected from each of the groups A, B and C. All of them are typical representatives of their model groups and we discuss their features with respect to the H I observational data. Tab. 8.2 summarizes the parameter values of the models.

8.3.1 Group A

The best model of the Magellanic System with an oblate MW halo is introduced in this section (model A). Fig. 8.5 depicts the time variation of the LMC, SMC galactocentric distance together with the LMC–SMC separation for the last 4 Gyr. The Clouds move on very different orbits. The apogalactic distance of the LMC decreases systematically during the evolutionary period, which clearly reflects the effect of dynamical friction. There is a gap between the periods of subsequent perigalactic approaches of the Clouds. While the last two perigalactica of the LMC are separated by ≈ 2.3 Gyr, it is not over ≈ 1.5 Gyr in the case of the SMC. Filled parts of the plot in Fig. 8.5 indicate that the Magellanic Clouds have reached the state of a gravitationally bound system during the last 4 Gyr. We define gravitational binding by the sum of the relative kinetic and gravitational potential energy of LMC and SMC as expressed by (7.1). Apparently, the LMC and SMC have been forming a bound couple since $T = -1.06$ Gyr. Nevertheless, the total lifetime of a bound LMC–SMC pair did not exceed 40 % of the entire evolutionary period we studied.

Fig. 8.5 allows for conclusions on major events that initialized the redistribution of the

LMC and SMC particles. The most significant change of the initial distribution of particles occurred as a result of the LMC–MW approach at $T \approx -2.4$ Gyr, and the preceding LMC–SMC encounter $T \approx -2.5$ Gyr. Later on, the particle redistribution continued due to tidal stripping by the MW. Fig. 8.6 shows the modeled distribution of integrated H I column density in the System. In order to enable comparison with the observed H I distribution, we plotted a normalized H I column density map. The technique used to convert a test-particle distribution into a smooth map of column densities is described in Sec. 6.4. Mass distribution of H I extends beyond the far tip of the observed Magellanic Stream (Fig. 7.5) in the model A. H I column density peaks can be found in Fig. 7.5 at the positions $l = 300°$, $b = -65°$ and $l = 45°$, $b = -82°$. The model A places local density maxima of H I close to those observed ones (relative angular distance is $\approx 10°$) to approximate positions $l = 325°$, $b = -70°$ and $l = 70°$, $b = -70°$, respectively. Note also the low-density distribution of matter spread along the great circle of $l = 270°$ (Fig. 8.6). The matter emanates from LMC near the Interface Region identified by Brüns et al. (2005) (Fig. 7.5). In general, the model overestimates the amount of matter in the Magellanic Stream. The Leading Arm consists only of LMC particles in this scenario. The modeled matter distribution covers a larger area of the plane of sky than what is observed. However, this is a common problem of previous test-particle models of the Magellanic System and is likely caused by

Model	A	B	C
q	**0.84**	**1.02**	**1.16**
FF	0.496	0.467	0.473
$\mathbf{r}_{\mathrm{LMC}}$[kpc]	$\begin{pmatrix}-1.26\\-40.50\\-26.87\end{pmatrix}$	$\begin{pmatrix}-0.90\\-40.31\\-26.88\end{pmatrix}$	$\begin{pmatrix}-0.63\\-40.03\\-26.92\end{pmatrix}$
$\mathbf{r}_{\mathrm{SMC}}$[kpc]	$\begin{pmatrix}13.16\\-34.26\\-39.77\end{pmatrix}$	$\begin{pmatrix}13.32\\-34.33\\-40.22\end{pmatrix}$	$\begin{pmatrix}13.92\\-34.04\\-39.86\end{pmatrix}$
$\mathbf{v}_{\mathrm{LMC}}$[km s^{-1}]	$\begin{pmatrix}44.0\\-169.8\\146.7\end{pmatrix}$	$\begin{pmatrix}18.5\\-169.3\\171.3\end{pmatrix}$	$\begin{pmatrix}5.8\\-169.2\\205.8\end{pmatrix}$
$\mathbf{v}_{\mathrm{SMC}}$[km s^{-1}]	$\begin{pmatrix}-37.2\\-60.2\\204.3\end{pmatrix}$	$\begin{pmatrix}-10.1\\-94.2\\270.0\end{pmatrix}$	$\begin{pmatrix}-47.5\\-13.2\\162.6\end{pmatrix}$
$m_{\mathrm{LMC}}[10^9 \mathrm{M}_\odot]$	24.46	19.86	19.01
$m_{\mathrm{SMC}}[10^9 \mathrm{M}_\odot]$	2.06	1.82	1.83
$r^{\mathrm{disk}}_{\mathrm{LMC}}$[kpc]	9.62	11.46	9.06
$r^{\mathrm{disk}}_{\mathrm{SMC}}$[kpc]	6.54	6.06	7.90
$\Theta^{\mathrm{disk}}_{\mathrm{LMC}}$	89°	98°	102°
$\Phi^{\mathrm{disk}}_{\mathrm{LMC}}$	274°	277°	281°
$\Theta^{\mathrm{disk}}_{\mathrm{SMC}}$	36°	49°	36°
$\Phi^{\mathrm{disk}}_{\mathrm{SMC}}$	229°	231°	224°

Table 8.2: Parameters of the best models in separate q categories.

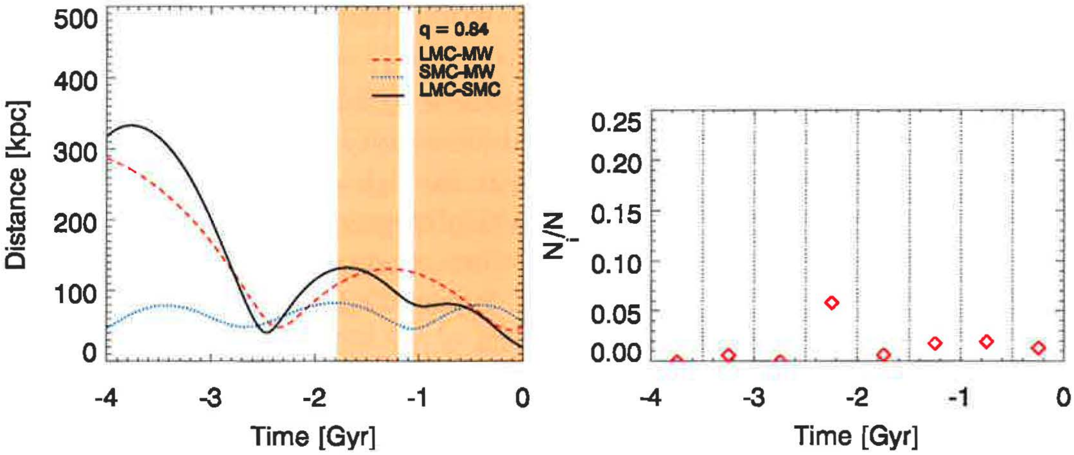

Figure 8.5: Left plot: Orbital evolution of the Clouds for the best GA fit from the model group A. The plot corresponds to an oblate halo of flattening $q = 0.84$. Time dependence of the LMC (dashed line), SMC (dotted line) galactocentric distances, and the LMC–SMC relative distance are plotted above. Plot areas with filling mark the time intervals when the Clouds were gravitationally bound to each other. Right plot: Relative number of LMC/SMC test–particles strongly disturbed due to the interaction in the Magellanic System. Counts within 8 time intervals of 500 Myr are plotted.

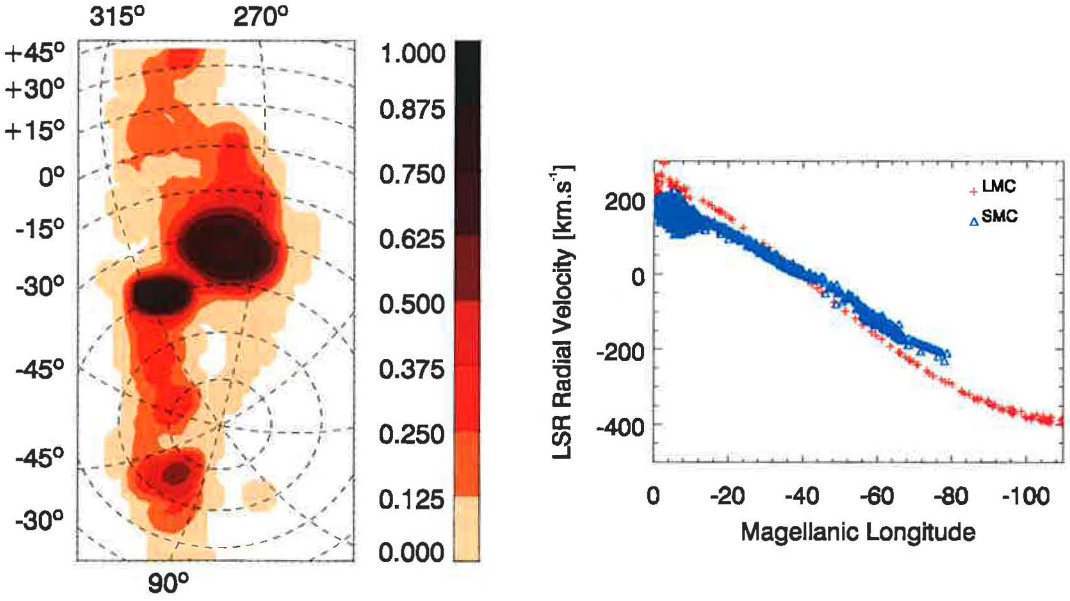

Figure 8.6: Left plot: Contour map of the modeled H I integrated relative column density. Data is projected on the sky plane. Galactic coordinates are used. Right plot: LSR radial velocity profile of the Magellanic Stream.

simplifications in the treatment of the physical processes. But also in general, successful reproduction of the Leading Arm has been a difficult task for all the models introduced so far.

The LSR radial velocity profile of the Magellanic Stream for the model A is shown in Fig. 8.6. The model reproduces the LSR radial velocity of the Stream matter as almost linear function of Magellanic Longitude with the high–negative velocity tip reaching $-400\,\mathrm{km\,s^{-1}}$. Such features are in agreement with observations (see Fig. 7.5). In contrast to GARDINER ET AL. (1994), the Magellanic Stream consists of both LMC and SMC particles. Fig. 8.6 denotes that the LMC and SMC Stream components cover different ranges of LSR radial velocities. The Stream component of the SMC origin does not extend to LSR radial velocities below the limit of $-200\,\mathrm{km\,s^{-1}}$. The major fraction of the LMC particles resides in the LSR radial velocity range from $-400\,\mathrm{km\,s^{-1}}$ to $-200\,\mathrm{km\,s^{-1}}$.

8.3.2 Group B

The best model of the group B (model B) corresponds to the MW DM halo flattening value $q = 1.02$. The initial condition set for the model B is listed in Tab. 8.2. The galactocentric distance of the Clouds and their spatial separation as functions of time are plotted in Fig. 8.7. Continuous decrease of the LMC and SMC galactocentric distances due to the dynamical friction is apparent for both LMC and SMC. A very close encounter of the Clouds with the relative distance $\Delta r \approx 10\,\mathrm{kpc}$ occurred at $T \approx -2.2\,\mathrm{Gyr}$. At similar moments of $T \approx -2.3\,\mathrm{Gyr}$ (LMC) and $T \approx -2.1\,\mathrm{Gyr}$ (SMC), the Clouds also reached perigalactica of their orbits. In general, both Clouds have been moving on orbits showing similar time dependence of their galactocentric distances, as indicated by Fig. 8.7.

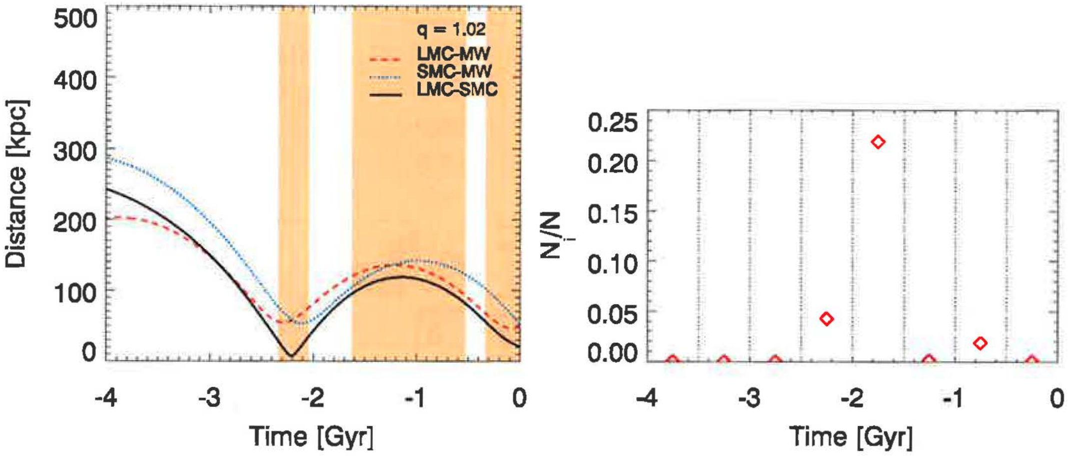

Figure 8.7: Left plot: Orbital evolution of the Clouds for the best GA fit from the model group B. The plot corresponds to a nearly spherical halo of flattening $q = 1.02$. Time dependence of the LMC (dashed line), SMC (dotted line) galactocentric distances, and the LMC–SMC relative distance are plotted above. Filled areas show time intervals when LMC and SMC formed a gravitationally bound couple. Right plot: Relative number of LMC/SMC test–particles strongly disturbed due to the interaction in the Magellanic System. Counts within 8 time intervals of 500 Myr are plotted.

Nevertheless, the position vectors of the Clouds evolved in significantly different ways. As consequence, the spatial separation of the Clouds varied within a wide range of values from $\Delta r \approx 10\,\mathrm{kpc}$ to $\Delta r \approx 250\,\mathrm{kpc}$. The Clouds have formed a gravitationally bound couple three times within the last 4 Gyr, and the total duration of such periods was 1.7 Gyr. Currently, the LMC and SMC are gravitationally bound in the model B.

The LMC–SMC encounter at $T \approx -2.2\,\mathrm{Gyr}$ caused distortion of the original particle disks of the Clouds. More than 25 % of the total number of the LMC and SMC particles were moved to significantly different orbits (for definition see Sec. 8.2) within the interval of 1 Gyr after the encounter (see Fig. 8.7). The following evolution of the particle distribution formed extended structures depicted in Fig. 8.8. There are two spatially separated components present in the modeled tail. The H I column density distribution map for the model B (see Fig. 8.8) shows a densely populated trailing stream parallel to the great circle of $l = 135°/315°$. It consists of the SMC particles torn–off from the initial disk $\approx 2\,\mathrm{Gyr}$ ago. Its far end is projected to the plane of sky close to the tip of the Magellanic Stream. However, the modeled increase of column density of matter toward the far end of the tail is a substantial drawback of the scenario B. The stream is extended into the SMC leading arm located between $l = 290°, b = -15°$ and $l = 290°, b = 45°$. The second component of the particle tail is of LMC origin and is spread over the position of the observed low–density gas distribution centered at $l = 80°, b = -50°$ (Fig. 7.5 or Fig. 7.5).

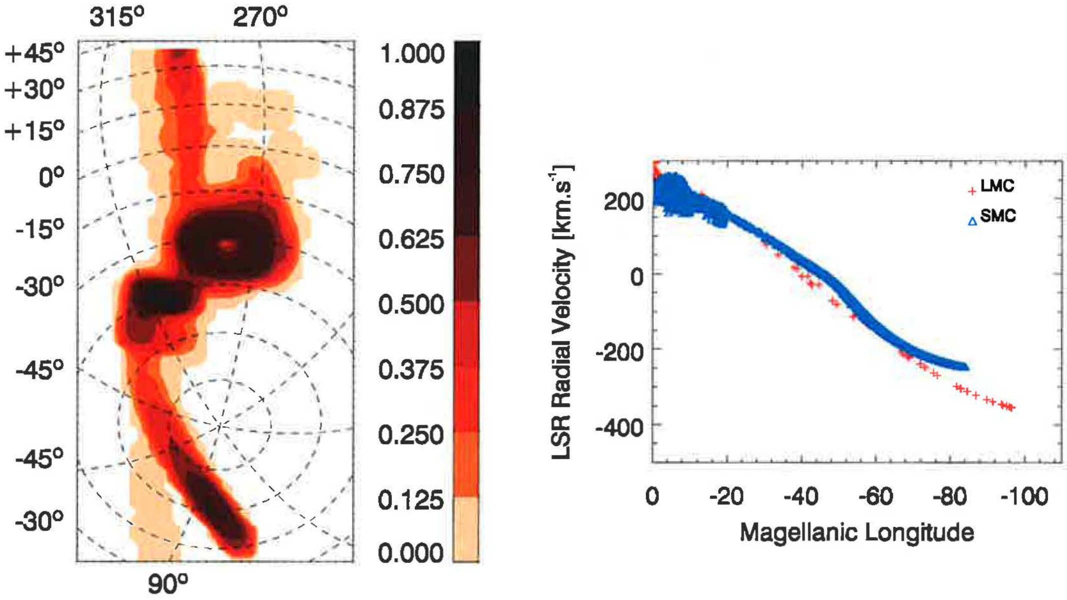

Figure 8.8: Left plot: Contour map of the modeled H I integrated relative column density. Data is projected on the plane of sky. Galactic coordinates are used. The dominant branch of the trailing stream is along the great circle denoted by $l = 135°/315°$. Right plot: LSR radial velocity profile of the Magellanic Stream.

The most significant structure at the leading side of the Magellanic System is the SMC stream introduced in the previous paragraph. Comparison between Fig. 7.5 and Fig. 8.8

indicates, that neither the projected position nor the integrated H I density distribution of the stream is in agreement with the observed Leading Arm. There was also a structure emanating from the leading edge of the LMC identified at approximate position $l = 270°, b = -15°$ (see Fig. 8.8). Regarding the H I data by BRÜNS ET AL. (2005), such an H I distribution is not observed. The LSR radial velocity profile of the trailing tail of the model B does not extend over the limit of $v_{\rm LSR} \approx -350\,{\rm km.s}^{-1}$ (Fig. 8.8). However, following the H I data, the far tip of the Stream should reach the LSR radial velocity $v_{\rm LSR} \approx -400\,{\rm km.s}^{-1}$ at the Magellanic Longitude $\approx -100°$.

8.3.3 Group C

Our last model group C assumes the presence of prolate MW DM halos. The best GA fit of the System (model C) is introduced in Tab. 8.2 reviewing its initial condition set. Concerning orbital motion of the Clouds, there is a significant difference between the LMC and SMC periods of perigalactic approaches during the last 4 Gyr. While the last period of the LMC exceeds 2.5 Gyr, the SMC orbital cycle is shorter than 1.5 Gyr. The relative distance of the Clouds remains over 70 kpc for $T < -0.4$ Gyr. They became a gravitationally bound couple 0.6 Gyr ago and this binding has not been disrupted (Fig. 8.9).

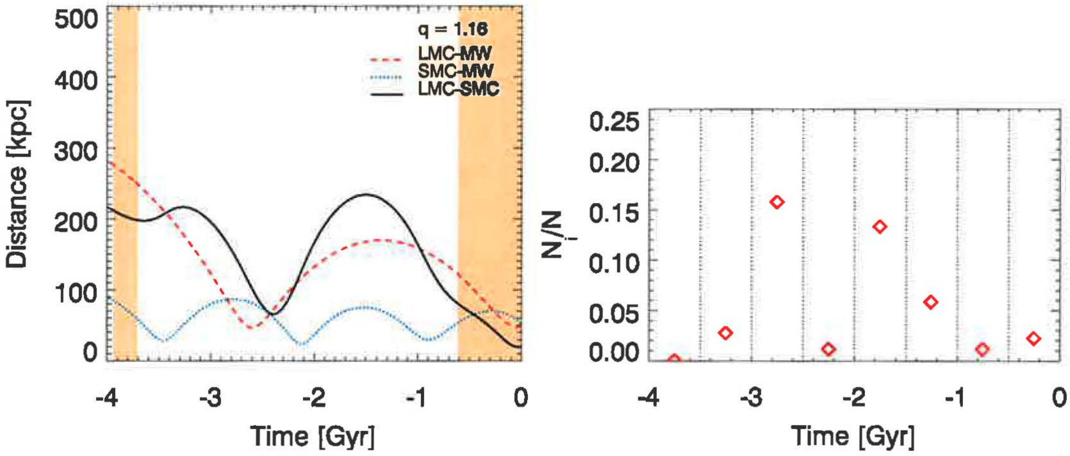

Figure 8.9: Left plot: Orbital evolution of the Clouds for the best GA fit from the model group C. The plot corresponds to a prolate halo of flattening $q = 1.16$. Time dependence of the LMC (dashed line), SMC (dotted line) galactocentric distances, and the LMC–SMC relative distance are plotted above. Periods when the Clouds formed a gravitationally bound couple are marked by filling. Right plot: Relative number of LMC/SMC test–particles strongly disturbed due to the interaction in the Magellanic System. Counts within 8 time intervals of 500 Myr are plotted.

Changes to the original LMC and SMC particle disks occurred especially due to the LMC–MW and SMC–MW encounters at $T < -2.0$ Gyr. Fig. 8.9 demonstrates the significance of different encounter events for particle redistribution. Note that raise of the number of disturbed particles is delayed with respect to the corresponding disturbing event. Subsequently, the evolution of particle structures continued under the influence of tidal stripping by the gravitational field of MW. The current distribution of matter in the model C is plotted in the form of a 2–D map in Fig. 8.10. The projection of the modeled trailing stream indicates that it occupies larger area of the data cube than the observed Magellanic Stream (compare Fig. 7.5 and Fig. 8.10). According to Fig. 7.5 the Magellanic Stream shows H I density peaks at $l = 300°$, $b = -65°$ and $l = 45°$, $b = -82°$. Our model C expects two local maxima of H I integrated column density in the tail. Their positions are shifted by $\approx 20°$ relatively to the peaks in Fig. 7.5. Additional comparison between the model and observations discovers that the model C overestimates the integrated column densities of H I in the Magellanic Stream. The matter located at the leading side of the Magellanic System is of SMC origin only. Similarly to the case of the trailing tail, the modeled amount of matter exceeds observational estimates for the Leading Arm.

Fig. 8.10 offers the LSR radial velocity profile of the Magellanic Stream in our model C. The measured minimum of the LSR radial velocity is $\approx -400\,\mathrm{km\,s^{-1}}$. The high negative LSR radial velocity at the far tip of the modeled Magellanic Stream does not exceed $\approx -300\,\mathrm{km\,s^{-1}}$, however. The observed H I emission intensity decreases towards the high negative velocity tip, which was not well reproduced by the model C.

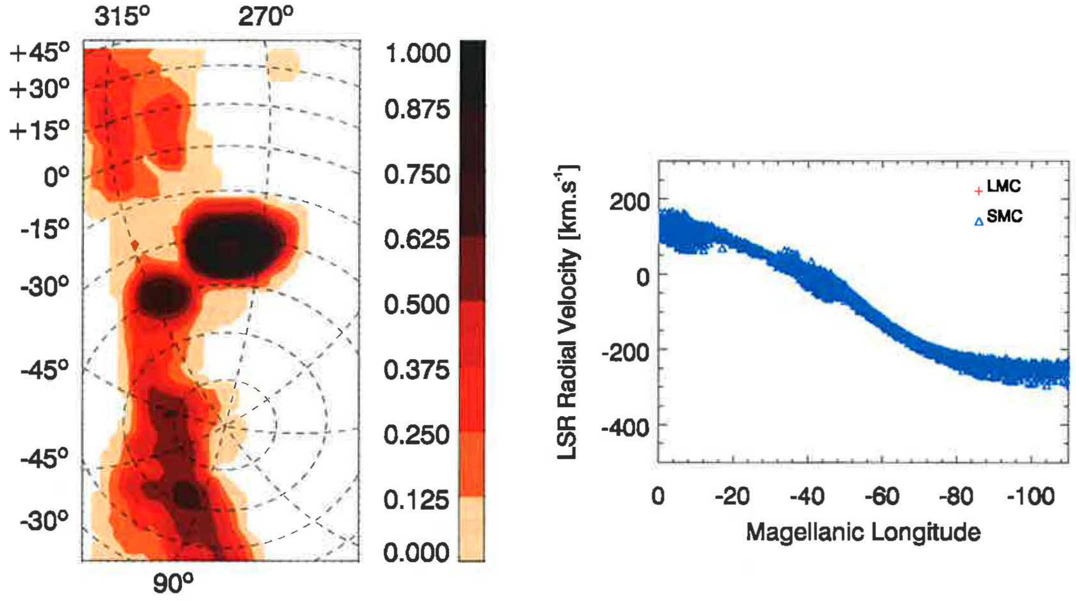

Figure 8.10: Left plot: Contour map of the modeled H I integrated relative column density. Data is projected on the sky plane. Galactic coordinates are used. Right plot: LSR radial velocity profile of the Magellanic Stream.

8.4 Orbits of the Magellanic Clouds

Exploration of the orbital motion of the Clouds shows similarity of the GA fits for oblate and prolate halos (models A and C). No close ($r < 10\,\mathrm{kpc}$) LMC–SMC encounters occurred for either of the models A and C. It is also notable that in the models with aspherical halos the SMC period of perigalactic approaches is significantly shorter than the period of the LMC and that the SMC remains closer than 100 kpc to the MW center during the last

4 Gyr. When the MW DM flattening $q \approx 1.0$, the LMC and SMC orbital cycle lengths were comparable for the model B. Independently of the MW halo shape, the LMC and SMC are currently forming a gravitationally bound couple in our models. However, the Clouds cannot be considered bound to each other during the entire period of the last 4 Gyr. This is in contrast with MURAI & FUJIMOTO (1980), GARDINER ET AL. (1994) or GARDINER ET AL. (1996) who argue that the LMC and SMC moving in the spherical halo have formed a gravitationally bound pair for at least several Gyr to allow for sufficient matter redistribution. We show that the structural resolution adopted by the above cited studies to make comparison between models and observations does not allow for such constraints on the orbital history of the Clouds. The GA search employed a 3–level detailed evaluation of modeled H I distribution with respect to high–resolution observational data (BRÜNS ET AL., 2005), which introduced significant improvement of previous approaches to compare observations and models. Nevertheless, there is still no clear indication that continuous gravitational binding of the Clouds covering the entire evolutionary period is necessary for successful reproduction of the observed data.

8.5 Magellanic Stream

8.5.1 Origin of the Matter

In our best model both SMC and LMC particles were present in the trailing stream. This is a common feature of the scenarios that were investigated. In general, the fraction of H I gas originating at the SMC exceeds the fraction of LMC matter in the Stream.

Following the models A and B, the formation of the Magellanic Stream did not start earlier than 2.5 Gyr ago. In the case of the models C, the age of the Stream is ≈ 3.5 Gyr. Both estimates are close to the epoch when a massive star formation burst in the LMC began (VAN DEN BERGH, 2000). Then the matter forming the Stream comes from the Magellanic Clouds containing stars, and we necessarily face the observational fact that there is no stellar content in the Magellanic Stream. Models for aspherical halos (A, C) indicate that the matter coming to the Magellanic Stream from the LMC originates in outer regions of its initial particle disk, while no matter was torn–off from the inner disk of radius $r_{\rm disk} \approx 5$ kpc that was the dominant region of star formation in the LMC. It is due to absence of close encounters in the Magellanic System.

In contrast to the models A and C, a dramatic encounter event between the Clouds occurred in the model B at ≈ -2.2 Gyr, when the internal structure of both disks was altered and also the matter from central areas of the LMC disk was transported to the Magellanic Stream. In such a case we expect a certain fraction of the matter of the Magellanic Stream to be in the form of stars, which is, however, not supported by observations.

8.5.2 Structure

MATHEWSON ET AL. (1977) observationally mapped the Magellanic Stream and discovered its clumpy structure consisting of six major H I clouds named MS I–VI. Recently, a more sensitive high–resolution H I survey of the Magellanic System by BRÜNS ET AL. (2005) showed that the above mentioned fragments of the Stream have to be considered density peaks of an otherwise smooth distribution of neutral hydrogen of column density decreasing towards the high–negative radial velocity tip of the Magellanic Stream. Our models corresponding to aspherical MW halos (A, C) placed local density maxima of H I close to the South Galactic pole. That result is supported by observations by BRÜNS ET AL. (2005). In this respect, the model B did not succeed and its projected distribution of H I in a trailing tail cannot be considered a satisfactory fit of the Magellanic Stream.

Our models overestimate the integrated relative column densities of HI in the part of the Magellanic Stream located between the South Galactic pole and the far tip of the Stream. There is also no indication of the H I density decrease as we follow the Stream further from the Magellanic Clouds. In general, all the models A, B and C predict the trailing tail to be of higher H I column densities and extended well beyond the far tip of the Magellanic Stream. Such behavior is a common feature of pure tidal evolutionary models of the Magellanic System and it is a known drawback of omitting dissipative properties of gaseous medium.

Regarding the LSR radial velocity measurements along the Magellanic Stream by BRÜNS ET AL. (2005), our models were able to reproduce some of their results. The far tip of the Magellanic Stream in the models A reaches the extreme negative LSR radial velocity of $-400\,\mathrm{km\,s^{-1}}$ known from H I observations. However, the highest negative LSR radial velocity does not drop below $-350\,\mathrm{km\,s^{-1}}$ for either prolate or nearly spherical halo configurations. Our previous discussion of various models of the Magellanic System denoted that successful reproduction of the high–negative LSR radial velocity at the far tip of the Magellanic Stream is one of the most challenging problems for such studies. Regarding our results, importance of the correct LSR radial velocity profile along the Magellanic Stream was emphasized again. Absence of H I between LSR radial velocities of $\approx -350\,\mathrm{km\,s^{-1}}$ and $\approx -400\,\mathrm{km\,s^{-1}}$ turned out to be the crucial factor decreasing the resulting fitness of examined evolutionary scenarios.

8.6 Leading Arm

Reproduction of the Leading Arm remains a difficult task for all the models of the Magellanic System that have been employed so far. Tidal models place matter to the leading side of the System, towards the Galactic equator, naturally as a result of the tidal stripping forming also the trailing tail. However, neither the projected shape of the modeled leading structures nor the H I density distribution in the regions having an observational counterpart can be considered sufficient (see e.g. GARDINER ET AL., 1994).

In every case A, B and C we were able to transport matter to the area of the Leading Arm. Nevertheless, the projected coverage of that region was more extended than what is observed. All the models contain a significant content of matter spread from the leading edge of the LMC across the Galactic equator, which has not been confirmed observationally. The model C reproduced the Leading Arm best. But the column density values of

H I in C are overestimated and we also could not avoid an additional low-density envelope surrounding the structure (Fig. 8.10).

8.7 Summary and Conclusions

In this chapter we focused especially on the flattening of the MW dark matter halo potential q. The range $0.74 \leq q \leq 1.20$ was studied. It is equivalent to the interval of the density flattening $0.31 \leq q_\rho \leq 1.37$ (see (3.7)).

We showed that creation of a trailing tail (Magellanic Stream) and a leading stream (Leading Arm) is quite a common feature of the LMC–SMC–MW interaction, and such structures were modeled across the entire range of halo flattening values. However, important differences exist between the models, concerning density distribution and kinematics of H I, and also dynamical evolution of the Magellanic System over the last 4 Gyr. In contrast to MURAI & FUJIMOTO (1980), GARDINER ET AL. (1994) or LIN ET AL. (1995), the Clouds do not have to be gravitationally bound to each other for the entire evolutionary period to produce the matter distribution that is in agreement with currently available H I data on the Magellanic System.

Overall agreement between the modeled and observed distribution of neutral hydrogen in the System is quantified by the fitness of the models. The fitness value is returned by a fitness function, that performs a very detailed evaluation of every model. Analysis of fitness as function of the halo flattening parameter q indicates, that the models assuming oblate DM halo of MW (models A) allow for better satisfaction of H I observations than models with other halo configurations.

We did not involve surveys of stellar populations in the Magellanic System into the process of fitness calculation. It is due to a nature of test–particle models that do not allow for distinguishing between stellar and gaseous content of studied systems. However, we still have to face one of the most interesting observational facts connected to the Magellanic Clouds – absence of stars in the Magellanic Stream (VAN DEN BERGH, 2000) – because both LMC and SMC contain stellar populations, and so every structure emanating from the Clouds should be contaminated by stars. It is an additional constraint on the models. It cannot be involved in fitness calculation because of the limits of our numerical code, but has to be taken into account.

Stellar populations of SMC are very young and the mass fraction in the form of stars is extremely low. Our models show that evolution of the Magellanic Stream has been lasting 2 Gyr at least (models B). Thus, the fraction of matter in the Magellanic Stream, that is of SMC origin, was torn off before significant star formation bursts occurred in SMC, and stars should not be expected in the Stream. Nevertheless, we found both LMC and SMC matter in the Magellanic Stream for every model of the System. Similarly to the case of SMC, if the LMC star formation activity was increased after the matter transport into the Magellanic Stream was triggered, stars would be missing in the Stream naturally. Such a scenario is doubtful though. Observational studies argue for a massive star formation burst started in LMC at ≈ -3 Gyr (see VAN DEN BERGH, 2000). But only presence of a prolate halo of MW (models C) enabled evolution of the Stream that began before the mentioned epoch. However, our results concerning LMC and SMC orbits introduced another acceptable solution to the problem of missing stars. We showed that evolution of the Clouds in aspherical MW DM halos (models A and C) does not lead to extremely close encounters disturbing inner parts of the LMC disk ($r_{\rm disk} < 5\,{\rm kpc}$). Since the distribution of gaseous matter in galaxies is typically more extended than the stellar content, the Magellanic Stream matter coming from outer regions of the Clouds does not necessarily have to contain a stellar fraction.

Previous discussion of stellar content of the Magellanic System supports discrimination of the configurations with nearly spherical halos (models B) that was discovered by the GA search. On the other hand many papers on the dynamical evolution of the Magellanic Clouds dealing with a spherical MW halo (MURAI & FUJIMOTO, 1980; GARDINER ET AL., 1994; BEKKI & CHIBA, 2005) argue, that the observed massive LMC star formation bursts 3 Gyr ago was caused by close LMC–SMC encounters. Our models B show close approaches of the Clouds $\Delta r \approx 10\,{\rm kpc}$ at around the mentioned time. For aspherical halos, such encounters do not induce the formation of particle streams. However, close LMC–MW and SMC–MW encounters appeared to be efficient enough to trigger massive matter redistribution in the System leading to formation of the observed structures. Then, they could also be responsible for triggering of star burst.

FUTURE PROSPECTS

We performed an extended analysis of the parameter space for the interaction of the Magellanic System with the Milky Way. The varied parameters cover the phase space parameters, the masses, the structure and the orientation of both Magellanic Clouds as well as the flattening of the dark matter halo of the Milky Way. The analysis was done by a specially adopted optimization code searching for a best match between numerical models and the detailed H I map of the Magellanic System by BRÜNS ET AL. (2005). The applied search algorithm is a genetic algorithm (GA) combined with a code based on the fast, but approximative restricted N–body method. By this, we were able to analyze more than 10^6 models which makes this study one of the most extended ones for the Magellanic System.

The agreement between our numerical models and the observations was measured by the fitness function FF. The detailed analysis of FF, that was introduced in Chapter 6, discovered a remarkable difference concerning the sensitivity of the H I distribution in the Magellanic System (i.e. the sensitivity of FF) to different parameters. While the specific choice for the orientation of the initial particle disk of LMC turned to be marginal, the spatial velocities of the Clouds played a key role concerning the proper reproduction of the observational data.

Following the results of the GA search of the parameter space, we performed a detailed analysis of the morphology and kinematics of H I in the Magellanic System with respect to the current motion of the Clouds. It was found out that the distribution of H I in the Magellanic Stream area is the main factor contributing to FF of the entire System and is notably sensitive to the variations in the spatial velocities of both LMC and SMC. In contrast to that, satisfaction of observational data was constantly insufficient for the region of the Leading Arm, and the corresponding FF_{LA} did not vary with changing velocities of the Clouds. We have shown that the models of low values of FF generally miss intense encounters that would lead to a significant disruption of either the LMC or SMC initial disk–like configuration of a particle distribution. However, the LMC–MW encounters at $-3.5 < T < -2\,\mathrm{Gyr}$ were efficient enough to disturb the outer region of the LMC disk, which lead to creation of a smooth low–density trailing tail, that satisfies the observed LSR radial velocity profile of the Magellanic Stream well. When the plateau of FF is reached the mutual approaches of SMC and MW, together with the LMC–SMC encounters lead to a very intense tidal stripping of the SMC particles. The encounters cause a very strong tidal force acting for a short time interval, which results into large variations of the stripping rates for SMC. Such a process is reflected by the clumpy distribution of H I column density. The best models studied here were able to produce trailing tails of correct large–scale kinematics and also of an inhomogeneous distribution of H I, which should be considered a notable reproduction of the Magellanic Stream. It turned out to be a very common result, that both the LMC and SMC particles contribute to the extended structures of the Magellanic System, namely to the Magellanic Stream. Moreover, we discovered a remarkably different influence of the LMC and SMC components on the kinematics and morphology of the System. It is very interesting that most studies published so far deal with pure either LMC or SMC Streams. That result is natural since often only LMC (e.g. LIN & LYNDEN–BELL, 1977; SOFUE, 1994; MASTROPIETRO ET AL., 2005; BEKKI & CHIBA, 2005) or SMC (see GARDINER ET AL., 1996; CONNORS ET AL., 2005) are treated as live systems. However, our study shows that creation of a one–component Magellanic Stream is a very unlikely case since both Clouds can serve as sources of matter.

Undoubtedly, the potential of MW plays a crucial role in the evolution of the Magellanic System. The features of the adopted logarithmic potential of the MW DM halo were described by the flattening parameter q. Since the flattening had to be treated differently from the remaining parameters, it was analyzed separately in Chapter 8. We showed that creation of a trailing tail (Magellanic Stream) and a leading stream (Leading Arm) is quite a common feature of the LMC–SMC–MW interaction, and such structures were modeled across the entire range of halo flattening values. However, important differences exist between the models, concerning density distribution and kinematics of H I, and also dynamical evolution of the Magellanic System over the last 4 Gyr. Analysis of fitness as function of the halo flattening parameter q indicates, that the models assuming oblate DM halo of MW allow for better satisfaction of H I observations than the models with other halo configurations. Additional arguments supporting our result came out of one of the most interesting observational facts connected to the Magellanic Clouds – absence of stars in the Magellanic Stream – because LMC contains old stellar populations, and so every structure emanating from the Clouds should be contaminated by stars. We showed that evolution of the Clouds in aspherical MW DM halos does not lead to extremely close encounters disturbing inner parts of the LMC disk. Since the distribution of gaseous matter in galaxies is typically more extended than the stellar content, the Magellanic Stream matter coming from outer regions of the Clouds does not necessarily have to contain a stellar fraction.

However, we should also point out that several drawbacks exist related to the method employed in this study. The most important problems remaining and possible ways to solve them will be summarized in the following paragraphs.

In order to optimize the performance of the GA, a computationally fast model of the Magellanic System was required. Therefore, complex N–body schemes involving self–consistent description of gravity and hydrodynamics were discriminated. On the other hand, correct description of physical processes dominating the evolution of the System was a crucial constraint on the model. The discussion of applicability of restricted N–body schemes on problems of galactic encounters showed that they allow for modeling of extended streams and tails. Nevertheless, also the models that involve hydrodynamical description of gaseous medium allowed for notable results. In general, there are strong arguments supporting the influence of ram pressure stripping on the evolution of the

Magellanic System, and so the dissipative properties of gas should be taken into account in the next generation of our model.

The DM halo of the Milky Way is considered axisymmetric and generally flattened in the model. It is a significant improvement of previous studies on the Magellanic System that assumed spherical halos. Our study indicates that an additional extension of the studied range of the halo flattening parameter q might introduce remarkable results. However, it is not feasible for the model of a logarithmic halo, that does not allow for $q < 1/\sqrt{2}$. Moreover, the recent results of both observations and numerical models argue for generally tri–axial DM halos. Thus, it is highly recommended to adopt a more elaborate and more general model of the DM halo potential.

It was already mentioned, that the impact of various parameters on the evolution of the Magellanic System shows notable differences across the studied parameter set. That fact suggests a promising way to optimize the search process itself by excluding those parameters playing a minor role, and thus to allow for a more detailed and extended analysis of the remaining parameters – namely the LMC and SMC velocity vectors, and the structural parameters of the DM halo of Galaxy.

REFERENCES

Alcock, C., Allsman, R. A., Alves, D., Axelrod, T. S., Becker, A. C., Bennett, B. C., Cook, K. H., Freeman, K. C., Griest, K., Guern, J., Lehner, M. J., Marshall, S. L., Minniti, D., Peterson, B. A., Pratt, M. R., Quinn, P. J., Rodgers, A. W., Sutherland, W., and Welch, D. L. (1997): The MACHO Project Large Magellanic Cloud Variable Star Inventory. III. Multimode RR Lyrae Stars, Distance to the Large Magellanic Cloud, and Age of the Oldest Stars. *Astrophys. J.*, **482**, 89–97 (Cited on page 49.)

Anderson, J., King, I. R. (2004): Erratum: "The Rotation of the Globular Cluster 47 Tucanae in the Plane of the Sky". *Astrophys. J.*, **128**, 950–950 (Cited on pages 51 and 52.)

Barnes, J., Hut, P. (1986): A Hierarchical $O(N \log N)$ Force–Calculation Algorithm. *Nature*, **324**, 446–449 (Cited on page 29.)

Barnes, T. G., Moffett, T. J., Gieren, W. P. (1993): A distance to the Cepheid HV 829 in the Small Magellanic Cloud. *Astrophys. J.*, **405**, L51–L53 (Cited on page 50.)

Bekki, K., Chiba, M. (2005): Formation and evolution of the Magellanic Clouds – I. Origin of structural, kinematic and chemical properties of the Large Magellanic Cloud. *Mon. Not. R. Astron. Soc.*, **356**, 680–702 (Cited on pages 31, 36, 115, 131 and 134.)

Bergeat, J., Knapik, A., Rutily, B. (1998): The PL relation of galactic carbon LPVs. The distance modulus to LMC. *Astron. Astrophys.*, **332**, L53–L56 (Cited on page 49.)

Binney, J. (1977): Dynamical friction in aspherical clusters. *Mon. Not. R. Astron. Soc.*, **181**, 735–746 (Cited on pages 41, 43 and 44.)

Binney, J., Tremaine, S. D. (1987): Galactic Dynamics, Princeton University Press, 1987. (Cited on pages 37, 43 and 47.)

Bosma, A. (1981): 21–cm line studies of spiral galaxies. II. The distribution and kinematics of neutral hydrogen in spiral galaxies of various morphological types. *AJ*, **86**, 1825–1846 (Cited on page 117.)

Brüns, C., Kerp, J., Staveley–Smith, L., Mebold, U., Putman, M. E., Haynes, R. F., Kalberla, P. M. W., Muller, E., Filipovic, M. D. (2004): The Parkes H I Survey of the Magellanic System. *Astron. Astrophys.*, **432**, 45–67 (Cited on pages 14, 15, 20, 21, 22, 23, 24, 25, 74, 77, 78, 83, 85, 86, 87, 100, 106, 107, 114, 118, 122, 126, 128, 129, 133, 145, 146, 148 and 150.)

Byrd, G., Valtonen, M., McCall, M., Innanen, K. (1994): Orbits of the Magellanic Clouds and Leo I in local group history. *Astron. J.*, **107**, 2055–2057 (Cited on pages 19 and 45.)

Caldwell, J. A. R., Laney, C. D. (1991): Cepheids in the Magellanic Clouds. In *The Magellanic Clouds*; Proceedings of the IAU Symposium no. 148, Kluwer Academic Publishers, Dordrecht, 1991, p.249 (Cited on page 18.)

Chandrasekhar, S. (1943): Dynamical Friction. I. General Considerations: the Coefficient of Dynamical Friction. *Astrphys. J.*, **97**, 255–262 (Cited on pages 43 and 44.)

Cole, A. A. (1998): Age, Metallicity, and the Distance to the Magellanic Clouds from Red Clump Stars. *Astrophys. J.*, **500**, L137–L140 (Cited on page 49.)

Connors, T. W., Kawata, D., Gibson, B. K. (2005): N–body simulations of the Magellanic Stream. *astro-ph/0508390*, **submitted to Mon. Not. R. Astron. Soc.**, (Cited on pages 30, 31, 115 and 134.)

de Grijs, R., Anders, P. (2006): How well do we know the age and mass distributions of the star cluster system in the Large Magellanic Cloud? *Mon. Not. R. Astron. Soc.*, **366**, 295–307 (Cited on page 26.)

DeJong, K. (1975): An Analysis of the Behavior of a Class of Genetic Adaptive Systems. PhD. Dissertation. Dept. of Computer and Communication Sciences, Univ. of Michigan, Ann Arbor. (Cited on pages 58, 69 and 70.)

Dopita, M. A., Lawrence, C. J., Ford, H. C., Webster, B. L. (1985): The kinematics and internal dynamics of planetary nebulae in the small Magellanic Cloud. *Astrophys. J.*, **296**, 390–398 (Cited on page 54.)

Dubinski, J., Carlberg, R. G. (1991): The structure of cold dark matter halos. *ApJ*, **378**, 496–503 (Cited on pages 117 and 118.)

Freire, P. C., Camilo, F., Kramer, M., Lorimer, D. R., Lyne, A. G., Manchester, R. N., D'Amico, N. (2003): Further results from the timing of the millisecond pulsars in 47 Tucanae. *Mon. Not. R. Astron. Soc.*, **340**, 1359–1374 (Cited on page 52.)

Frenk, C. S., White, S. D. M., Davis, M., Efstathiou, G. (1988): The formation of dark halos in a universe dominated by cold dark matter. *ApJ*, **327**, 507–525 (Cited on page 117.)

Fujimoto, M., Sofue, Y. (1976): Dynamical evolution of the triple system of the Galaxy, he Large and Small Magellanic Clouds. *Astron. Astrophys.*, **47**, 263–292 (Cited on page 30.)

Gardiner, L. T., Hawkins, M. R. S. (1991): Stellar populations and large–scale structure of the SMC. III – The geometry of the northern and north–western outlying regions. *Mon. Not. R. Astron. Soc.*, **251**, 174–191 (Cited on page 18.)

Gardiner, L. T., Sawa, T., Fujimoto, M. (1994): Numerical Simulations of the Magellanic System – Part One – Orbits of the Magellanic Clouds and the Global Gas Distribution. *Mon. Not. R. Astron. Soc.*, **266**, 567–582 (Cited on pages 14, 15, 30, 31, 36, 44, 50, 55, 77, 86, 114, 115, 124, 128, 129, 130 and 131.)

Gardiner, L. T., Noguchi, M. (1996): N–body simulations of the Small Magellanic Cloud and the Magellanic Stream. *Mon. Not. R. Astron. Soc.*, **278**, 191–208 (Cited on pages 14, 18, 30, 44, 55, 85, 114, 115, 128 and 134.)

Gieren, W. P., Fouqué, P., Gómez, M. (1997): Very Accurate Distances and Radii of Open Cluster Cephids from a Near–Infrared Surface Brightness Technique. *Astrophys. J.*, **488**, 74–88 (Cited on page 49.)

Goldberg, D. E. (1989): Genetic algorithms in search, optimization and machine learning, Addison–Wesley. (Cited on pages 61, 66 and 93.)

Gould, A., Uza, O. (1998): Upper Limit to the Distance to the Large Magellanic Cloud. *Astrophys. J.*, **494**, 118–124 (Cited on page 49.)

Hardy, E., Suntzeff, N. B., Azzopardi, M. (1989): The kinematics of the Small Magellanic Cloud from its field carbon stars. *Astrophys. J.*, **344**, 210–216 (Cited on page 54.)

Heller, P., Rohlfs, K. (1994): The dynamical evolution of the Magellanic System. *Astron. Astrophys.*, **291**, 743–753 (Cited on pages 31 and 114.)

Helmi, A. (2004): Is the dark halo of our Galaxy spherical? *Mon. Not. R. Astron. Soc.*, **351**, 643–648 (Cited on pages 47 and 118.)

Hernquist, L., Ostriker, J. P. (1992): A self–consistent field method for galactic dynamics. *Astrophys. J.*, **386**, 375–397 (Cited on page 29.)

Hindman, J. V., Kerr, F. J., McGee, R. X. (1963): A Low Resolution Hydrogen–line Survey of the Magellanic System. II. Interpretation of Results. *Australian J. Phys.*, **16**, 570 (Cited on pages 20 and 99.)

Holland, J. H. (1975): Adaptation in natural and artificial systems. An introductory analysis with applications to biology, control and artificial intelligence, University of Michigan Press. (Cited on pages 57, 58, 59, 60, 62, 63, 67 and 88.)

Hughes, S. M. G., Wood, P.R., Reid, N. (1991): Long–period variables in the Large Magellanic Cloud. III – Evidence of a kinematic spheroidal population. *Astron. J.*, **101**, 1304–1323 (Cited on page 54.)

Ibata, R., Lewis, G. F., Irwin, M., Totten, E., Quinn, T. (2001): Great Circle Tidal Streams: Evidence for a Nearly Spherical Massive Dark Halo around the Milky Way. *ApJ*, **551**, 294–311 (Cited on page 118.)

Irwin, M. J., Demers, Serge, Kunkel, W. E. (1990): A blue stellar link between the Magellanic Clouds. *Astron. J.*, **99**, 191–200 (Cited on page 32.)

Israel, F. P. (1997): H 2 and its relation to CO in the LMC and other magellanic irregular galaxies. *Astron. Astrophys.*, **328**, 471–482 (Cited on pages 22 and 26.)

Jacoby, G. H. (1997): What we can say about PN if their luminosity function distances are correct. In *The Magellanic Clouds*; Proceedings of the IAU Symposium no. 180, Kluwer Academic Publishers, Dordrecht, 1997, p.448 (Cited on pages 49 and 50.)

Jones, B. F., Klemola, A. R., Lin, D. N. C. (1994): Proper motion of the Large Magellanic Cloud and the mass of the galaxy. 1: Observational results. *Astron. J.*, **107**, 1333–1337 (Cited on pages 14, 50, 51, 52, 53 and 73.)

Kallivayalil, N., van der Marel, R. P., Alcock, C., Axelrod, T., Cook, K. H., Drake, A. J., Geha, M. (2006): The Proper Motion of the Large Magellanic Cloud Using HST. *ApJ*, **638**, 772–785 (Cited on pages 14, 51, 52, 53 and 73.)

Kallivayalil, N., van der Marel, R. P., Alcock, C. (2006): Is the SMC Bound to the LMC? The HST Proper Motion of the SMC. *astro-ph/0606240*, **submitted to ApJ**, (Cited on pages 14, 51, 52, 53 and 73.)

Kaluzny, J., Wysocka, A., Stanek, K. Z., Krzemiński, W. (1998): BVI CCD Photometry of the Globular Cluster 47Tuc. *Acta Astronomica*, **48**, 439–453 (Cited on page 50.)

Kawamura, A., Mizuno, N., Onishi, T., Mizuno, A., Fukui, Y. (2005): Molecular Clouds and Star formation in the Galaxy and the Magellanic System by NANTEN. Astrochemistry Throughout the Universe: Recent Successes and Current Challenges, International Astronomical Union. Symposium no. 231, 29 August – 2 September, 2005 in Asilomar, California, USA (Cited on page 26.)

Kazantzidis, S., Kravtsov, A.V., Zentner, A.R., Allgood, B., Nagai, D., Moore, B. (2004): The Effect of Gas Cooling on the Shapes of Dark Matter Halos. *ApJ*, **611**, L73–L76 (Cited on page 118.)

Kroupa, P., Rser, S., Bastian, U. (1994): On the motion of the Magellanic Clouds. *Mon. Not. R. Astron. Soc.*, **266**, 412 (Cited on pages 51, 52, 53 and 73.)

Kroupa, P., Bastian, U. (1997): The Hipparcos proper motion of the Magellanic Clouds. *New Astronomy*, **2 (1997)**, 77–90 (Cited on pages 14, 19, 51, 52, 53, 55, 73 and 89.)

Kroupa, P., Theis, C., Boily, C. M. (2005): The great disk of Milky–Way satellites and cosmological sub–structures. *Astron. Astrophys.*, **431**, 517–531 (Cited on page 118.)

Kunkel, W. E., Demers, S., Irwin, M. J., Albert, L. (1997): The Dynamics of the Large Magellanic Cloud Periphery: Mass Limit and Polar Ring. *Astrophys. J.*, **448**, L129–L132 (Cited on page 54.)

Laney, C. D., Stobie, R. S. (1994): Cepheid Period / Luminosity Relations in K H J and V. *Mon. Not. R. Astron. Soc.*, **266**, 441–454 (Cited on page 50.)

Lin, D. N. C., Lynden–Bell, D. (1977): Simulation of the Magellanic Stream to estimate the total mass of the Milky Way. *Mon. Not. R. Astron. Soc.*, **181**, 59–81 (Cited on pages 30, 31, 115 and 134.)

Lin, D. N. C., Lynden–Bell, D. (1982): On the proper motion of the Magellanic Clouds and the halo mass of our Galaxy. *Mon. Not. R. Astron. Soc.*, **198**, 707–721 (Cited on pages 14, 17, 30, 31 and 32.)

Lin, D. N. C., Jones, B. F., Klemola, A. R. (1995): The motion of the Magellanic clouds, origin of the Magellanic Stream, and the mass of the Milky Way. *Astrophys. J.*, **439**, 652–671 (Cited on pages 30, 55 and 130.)

Mastropietro, C., Moore, B., Mayer, L., Wadsley, J., Stadel, J. (2005): The gravitational and hydrodynamical interaction between the Large Magellanic Cloud and the Galaxy. *Mon. Not. R. Astron. Soc.*, **363**, 509–520 (Cited on pages 31, 36, 114, 115 and 134.)

Mathewson, D. S., Cleary, M. N., Murray, J. D. (1974): The Magellanic Stream. *Astron. J.*, **190**, 291–296 (Cited on pages 20, 23, 99, 107 and 110.)

Mathewson, D. S., Schwarz, M. P., Murray, J. D. (1977): The Magellanic stream – The turbulent wake of the Magellanic clouds in the halo of the Galaxy. *Astrophys. J.*, **217**, L5–L8 (Cited on page 128.)

Mathewson, D. S., Ford, V. L., Schwarz, M. P., Murray, J. D. (1979): The Magellanic Stream – Observational considerations. In: *The large–scale characteristics of the galaxy*; Proceedings of the Symposium, College Park, Md., June 12–17, 1978, p. 547–556 (Cited on page 24.)

Mathewson, D. S., Ford, V. L. (1984): H I surveys of the Magellanic System. In: *Structure and evolution of the Magellanic Clouds*; Proceedings of the IAU Symposium no. 108, D. Reidel Publishing Co., Dordrecht, 1984, p. 125–136 (Cited on page 31.)

McLaughlin, D. E. (1999): The Efficiency of Globular Cluster Formation. *Astrophys. J.*, **512**, L9–L12 (Cited on page 117.)

McNamara, D. (1997): Luminosities of SX Phoenicis, Large–Amplitude Delta Scuti, and RR Lyrae Stars. *Publications of the Astronomical Society of the Pacific*, **109**, 1221–1232 (Cited on page 49.)

Meatheringham, S. J., Dopita, M. A., Ford, H. C., Webster, B. L. (1988): The kinematics of the planetary nebulae in the Large Magellanic Cloud. *Astrophys. J.*, **327**, 651–663 (Cited on page 54.)

Meurer, G. R., Bicknell, G. V., Gingold, R. A. (1985): A drag dominated model of the Magellanic stream. *PASA*, **6, 2**, 195–198 (Cited on page 31.)

Muller, E., Staveley–Smith, L., Zealey, W. J. (2003): Detection of carbon monoxide within the Magellanic Bridge. *Mon. Not. R. Astron. Soc.*, **338, 3**, 609–615 (Cited on page 26.)

Murai, T., Fujimoto, M. (1980): The Magellanic Stream and the Galaxy with a Massive Halo. *Publ. Astron. Soc. Japan*, **32**, 581–603 (Cited on pages 14, 15, 30, 36, 44, 50, 86, 114, 128, 130 and 131.)

Murai, T., Fujimoto, M. (1984): The Magellanic Stream and its related problems. *Proceedings of the IAU Symposium No. 108, Dordrecht, D. Reidel Publishing Co.*, **115–123**, (Cited on page 30.)

Olling, R. P., Merrifield, M. R. (2000): Two measures of the shape of the dark halo of the Milky Way. *Mon. Not. R. Astron. Soc.*, **311, 2**, 361–369 (Cited on page 117.)

Ostriker, J. P., Peebles, P. J. E., Yahil, A. (1974): The size and mass of galaxies, and the mass of the universe. *Astrophys. J.*, **193, 2**, L1–L4 (Cited on page 117.)

Oudmaijer, R. D., Groenewegen, Martin A. T., Schrijver, H. (1998): The Lutz–Kelker bias in trigonometric parallaxes. *Mon. Not. R. Astron. Soc.*, **294**, L41–L46 (Cited on page 49.)

Panagia, N., Weiler, K. W., van Dyk, S. D., Montes, M. J., Sramek, R. A. (1998): Radio Supernovae as Distance Indicators. *Astrophys. J.*, **500**, 51–58 (Cited on page 49.)

Pedreros, M. H., Anguita, C., Maza, J. (2002): Proper Motion of the Large Magellanic Cloud Using QSOS as an Inertial Reference System: The Q0459-6427 Field. *Astron. J*, **123**, 1971–1977 (Cited on pages 51, 52 and 53.)

Peñarrubia, J., Just, A., Kroupa, P. (2004): *Mon. Not. R. Astron. Soc.*, **349, 2**, 747–756 (Cited on pages 36, 43 and 44.)

Rechenberg, I. (1965): Cybernetic Solution Path of an Experimental Problem, In: Evolutionary Computation – The Fossil Record, Edited by D. B. Fogel, 1998, IEEE Press. (Cited on page 57.)

Rechenberg, I. (1973): Evolutionsstrategie – Optimierung technischer Systeme nach Prinzipien der biologischen Evolution, Frommann Holzboog, 1973. (Cited on page 57.)

Reid, I. N., Strugnell, P. R. (1986): The luminosity and kinematics of RR Lyraes. II – RR Lyraes and the distance to the LMC. *Mon. Not. R. Astron. Soc.*, **221**, 887–896 (Cited on page 50.)

Burstein, D., Rubin, V. C. (1985): The distribution of mass in spiral galaxies. *Astrophys. J.*, **297**, 423–435 (Cited on page 117.)

Ruzicka, A. (2001): The system of the Milky Way, LMC and SMC: numerical test–particle model. *Astron. Gesellschaft Abstract Ser.*, **18**, 210–210 (Cited on page 77.)

Salaris, M., Cassisi, S. (1998): A new analysis of the red giant branch ‘tip’ distance scale and the value of the Hubble constant. *Mon. Not. R. Astron. Soc.*, **298**, 166–178 (Cited on page 49.)

Schommer, R. A., Suntzeff, N. B., Olszewski, E. W., Harris, H. C. (1992): Spectroscopy of giants in LMC clusters. II – Kinematics of the cluster sample. *Astron. J.*, **103**, 447–459 (Cited on page 54.)

Sellwood, J. A. (1980): Galaxy models with live halos. *Astron. Astrophys.*, **89**, 296–307 (Cited on page 29.)

Smith, H. A., Silbermann, N. A., Baird, S. R., Graham, J. A. (1992): Variable stars in the northeast arm/inner halo region of the Small Magellanic Cloud. *Astron. J.*, **104**, 1430–1457 (Cited on page 50.)

Stanimirovic, S., Staveley–Smith, L., Dickey, J. M., Sault, R. J., Snowden, S. L. (1999): The large–scale H I structure of the Small Magellanic Cloud. *Mon. Not. R. Astron. Soc.*, **302**, 417–436 (Cited on page 22.)

Staveley–Smith, L., Kim, S., Calabretta, M. R., Haynes, R. F., Kesteven, M. J. (2003): A new look at the large–scale H I structure of the Large Magellanic Cloud. *Mon. Not. R. Astron. Soc.*, **339**, 87–104 (Cited on page 22.)

Sofue, Y. (1994): Fate of the Magellanic Stream. *PASJ*, **46, 4**, 431–440 (Cited on pages 31, 115 and 134.)

Sugimoto, D., Chikada, Y., Makino, J., Ito, T., Ebisuzaki, T., Umemura, M. (1990): A Special–Purpose Computer for Gravitational Many–Body Problems. *Nature*, **6270**, 33 (Cited on page 29.)

Theis, Ch (1999): Modeling Encounters of Galaxies: The Case of NGC 4449. *Rev. Mod. Astron.*, **12**, 309 (Cited on pages 14, 35 and 71.)

Theis, Ch., Kohle, S. (2001): Multi–method–modeling of interacting galaxies. I. A unique scenario for NGC 4449? *Astron. Astrophys.*, **370**, 365–383 (Cited on pages 15, 71, 72, 73, 74 and 146.)

Toomre, A., Toomre, J. (1972): Galactic Bridges and Tails. *Astrophys. J.*, **178**, 623–666 (Cited on pages 13, 29, 30, 99, 113, 115 and 119.)

Van den Bergh, S. (2000): The galaxies of the Local Group, Cambridge University Press, 2000. (Cited on pages 14, 17, 18, 19, 22, 23, 26, 27, 48, 49, 50, 54, 55, 128, 130 and 150.)

van Leeuwen, F., Feast, M. W., Whitelock, P. A., Yudin, B. (1997): First results from HIPPARCOS trigonometrical parallaxes of Mira–type variables. *Mon. Not. R. Astron. Soc.*, **287**, 955–960 (Cited on page 49.)

Wahde, M. (1998): Determination of orbital parameters of interacting galaxies using a genetic algorithm. Description of the method and application to artificial data. *Astron. Astrophys.*, **132**, 417–429 (Cited on page 35.)

Walker, A. R., Mack, P. (1988): CCD photometry of the RR Lyrae stars in NGC 121 and the distance to the Small Magellanic Cloud. *Astron. J.*, **96**, 872–876 (Cited on page 50.)

Wall, M. (1996): GAlib: A C++ Library of Genetic Algorithm Components. `http://lancet.mit.edu/ga` (Cited on pages 15, 58, 69, 74, 145 and 146.)

Wannier P., Wrixon G. T. (1972): An Unusual High–Velocity Hydrogen Feature. *Astrophys. J.*, **173**, L117–L123 (Cited on pages 20, 23, 24, 99, 106, 109, 145 and 148.)

Wannier, P., Wrixon, G. T., Wilson, R. W. (1972): A Survey of Positive Velocity Neutral Hydrogen above the Galactic Plane. *Astron. Astrophys.*, **18**, 224 (Cited on pages 20, 24 and 99.)

Whitley, D. (1994): A Genetic Algorithm Tutorial. *Statistics and Computing*, **4**, 65–85 (Cited on pages 57, 60, 63, 70 and 146.)

Wood, P. R., Arnold, A., Sebo, K. M. (1997): Nonlinear Models of the Bump Cepheid HV 905 and the Large Magellanic Cloud Distance Modulus. *Astrophys. J.*, **485**, L25–L28 (Cited on page 49.)

Zentner, A. R., Kravtsov, A. V., Gnedin, O. Y., Klypin, A. A. (2005): The Anisotropic Distribution of Galactic Satellites. *Astrophys. J.*, **629**, 219–232 (Cited on page 118.)

Zwicky, F. (1933): Die Rotverschiebung von extragalaktischen Nebeln. *Helvetica Physica Acta*, **6**, 110–127 (Cited on page 117.)

LIST OF FIGURES

LIST OF TABLES

Astronomy & Astrophysics manuscript no. aa
(DOI: will be inserted by hand later)
June 27, 2006

Is the Milky Way Dark Matter Halo Flattened?

A. Růžička[1,2], J. Palouš[1] and C. Theis[3]

[1] Astronomical Institute, Academy of Sciences of the Czech Republic, Boční II 1401a, 141 31 Prague, Czech Republic
e-mail: `adam.ruzicka@gmail.com`
e-mail: `palous@ig.cas.cz`
[2] Faculty of Mathematics and Physics of the Charles University, Ke Karlovu 3, 121 16 Prague, Czech Republic
[3] Institut für Astronomie der Universität Wien, Türkenschanzstrasse 17, A-1180 Wien, Austria
e-mail: `theis@astro.univie.ac.at`

Received May 4, 2005; accepted XXX

Abstract. We performed an extended analysis of the parameter space for the interaction of the Magellanic System with the Milky Way. The varied parameters cover the phase space parameters, the masses, the structure and the orientation of both Magellanic Clouds as well as the flattening of the dark matter halo of the Milky Way. The analysis was done by a specially adopted optimization code searching for the best match between numerical models and the detailed H I map of the Magellanic System by Brüns et al. (2005). The applied search algorithm is a genetic algorithm combined with a code based on the fast, but approximative restricted N–body method. By this, we were able to analyze more than 10^6 models which makes this study one of the most extended ones for the Magellanic System. Here we focus on the flattening q of the axially symmetric MW dark matter halo potential, that is studied within the range $0.74 \le q \le 1.20$. We show that creation of a trailing tail (Magellanic Stream) and a leading stream (Leading Arm) is quite a common feature of the LMC–SMC–MW interaction, and such structures were modeled across the entire range of halo flattening values. However, important differences exist between the models, concerning density distribution and kinematics of H I, and also dynamical evolution of the Magellanic System. Detailed analysis of the overall agreement between modeled and observed distribution of neutral hydrogen shows that the models assuming oblate ($q < 1.0$) dark matter halo of the Galaxy allow for better satisfaction of H I observations than models with other halo configurations.

Key words. methods: N–body simulations – Galaxy: halo – galaxies: interactions – galaxies: Magellanic Clouds

1. Introduction

The idea of *dark matter* (DM) was introduced by Zwicky (1933). His dynamical measurements of the mass–to–light ratio of the Coma cluster gave larger values than those known from luminous parts of nearby spirals. That discrepancy was explained by presence of DM. Ostriker et al. (1974) proposed that DM is concentrated in a form of extended galactic halos. Analysis of rotation curves of spiral galaxies (Bosma 1981, Rubin & Burstein 1985) denotes that their profiles cannot be explained without presence of non–radiating DM. Hot X–ray emitting halos have been used to estimate total galactic masses (McLaughlin 1999). Corresponding mass–to–light ratios exceed the maximum values for stellar populations, and DM explains the missing matter naturally. The presence of DM halos is expected by the standard CDM cosmology model of hierarchical galaxy formation. The classical CDM halo profile (NFW) is simplified to be spherical. However, most CDM models expect even significant deviations from spherical symmetry of DM distribution in halos. The model of formation of DM halos in the universe dominated by CDM by Frenk et al. (1988) produced triaxial halos with preference for prolate configurations. Numerical simulations of DM halo formation by Dubinski & Carlberg (1991) are consistent with halos that are triaxial and flat, with (c/a) = 0.50 and (b/a) = 0.71. There are roughly equal numbers of dark halos with oblate and prolate forms.

Observationally, the measurement of the shape of a DM halo is a difficult task. A large number of various techniques found notably different values, and it is even not clear if the halo is prolate or oblate. Olling & Merrifield (2000) use two approaches to investigate the DM halo shape of the Milky Way (MW), a rotation curve analysis and the radial dependence of the thickness of the H I layer. Both methods lead consistently to flattened oblate halos.

Recently, the nearly planar distribution of the observed MW satellites, which is almost orthogonal to the Galactic plane, raised the question, if they are in agreement with cosmological CDM models (Kroupa et al. 2005) or if other origins have to be invoked. Zentner et al. (2005) claim that the disk–like distribution of the MW satellites can be explained, provided the halo of the MW is sufficiently prolate in agreement with their CDM simulations. On the other hand, it is

---

Send offprint requests to: A. Růžička

not clear, if there exists a unique prediction of the axis ratios from CDM simulations, as the scatter in axis ratios demonstrates (Dubinski & Carlberg 1991). Based on ΛCDM simulations Kazantzidis et al. (2004) emphasize that gas cooling strongly affects halo shapes with the tendency to produce rounder halos.

Another promising method to determine the Galactic halo shape are stellar streams, because they are coherent structures covering large areas in space. Thus, their shape and kinematics should be strongly influenced by the overall properties of the underlying potential. A good candidate for such an analysis is the stellar stream associated with the Sagittarius dwarf galaxy. By comparison with simulations Ibata et al. (2001) found that the DM halo is almost spherical in the galactocentric distance range from 16 to 60 kpc. However, Helmi (2004) warned that the Sagittarius stream might be dynamically too young to allow for constraints on the halo shape.

In this paper we use the Magellanic Stream in order to derive constraints on the halo shape of the MW. The basis are the new detailed H I observations of the Magellanic System (including the Large Magellanic Cloud (LMC) and the Small Magellanic Cloud (SMC)) by Brüns et al. (2005). As remnants of the LMC–SMC–MW interaction, extended structures connected to the System are observed. Among them, the *Magellanic Stream* – an H I tail originating in between the Clouds and spreading over ≈ 100° of the plane of sky – has been a subject of investigation for previous studies (see e.g. Fujimoto & Sofue 1976, Lin & Lynden-Bell 1977, Murai & Fujimoto 1980, Heller & Rohlfs 1994, Gardiner & Noguchi 1996, Bekki & Chiba 2005, Mastropietro et al. 2005). Due to the extended parameter space related to the interaction of three galaxies and also due to the high computational costs of fully self–consistent simulations, simplifying assumptions were unavoidable. Many simulations neglected the self–gravity of the individual stellar systems by applying a restricted N–body method similar to the method introduced by Toomre & Toomre (1972). None of these simulations considered the self–gravity of all three galaxies. Often only one galaxy is simulated including its self–gravity by means of a live disk and halo, whereas the other two galaxies are taken into account by rigid potentials of high internal symmetry. E.g. none of the simulations so far adopted a live dark matter halo of the Milky Way, but they applied (semi–)analytical descriptions for the *dynamical friction* between the Magellanic Clouds and the Milky Way. Also, a possible flattening of the MW halo has not been considered. Having the numerical difficulties in mind it is not surprising that a thorough investigation of the complete parameter space was impossible.

Modeling observed interacting galaxies means dealing with an extended high–dimensional space of initial conditions and parameters of the interaction. Wahde (1998) and Theis (1999) introduced a *genetic algorithm* (GA) as a robust search method to constrain models of observed interacting galaxies. The GA optimization scheme selects models according to their ability to match observations. Inspired by their results, we employed a simple fast numerical model of the Magellanic System combined with an implementation of a GA to perform the first very extended search of the parameter space for the interaction between LMC, SMC and MW. Here we present our results about the MW DM halo flattening values compatible with most detailed currently available H I Magellanic survey (Brüns et al. 2005, see Fig. 1, Fig. 2).

2. Magellanic Clouds and MW Interaction

2.1. Observations of the Magellanic System

The Milky Way together with its close dwarf companions LMC and SMC forms an interacting system. Hindman et al. (1963) observed the H I *Magellanic Bridge* (MB) connecting the Clouds. Another significant argument for the LMC–SMC–MW interaction was brought by Wannier & Wrixon (1972) and Wannier et al. (1972). Their H I observations of the Magellanic Clouds discovered large filamentary structures projected on the plane of sky close to the Clouds, and extended to both high negative and positive radial LSR velocities. Mathewson et al. (1974) detected another H I structure and identified a narrow tail emanating from the space between the LMC and SMC, spread over the South Galactic Pole. The tail was named the Magellanic Stream. A similar H I structure called the *Leading Arm* extends to the north of the Clouds, crossing the Galactic plane. A high–resolution, spatially complete H I survey of the entire Magellanic System done by Brüns et al. (2005, see Fig. 1 and Fig. 2) gives detailed kinematic information about the Clouds and the connected extended structures. It in-

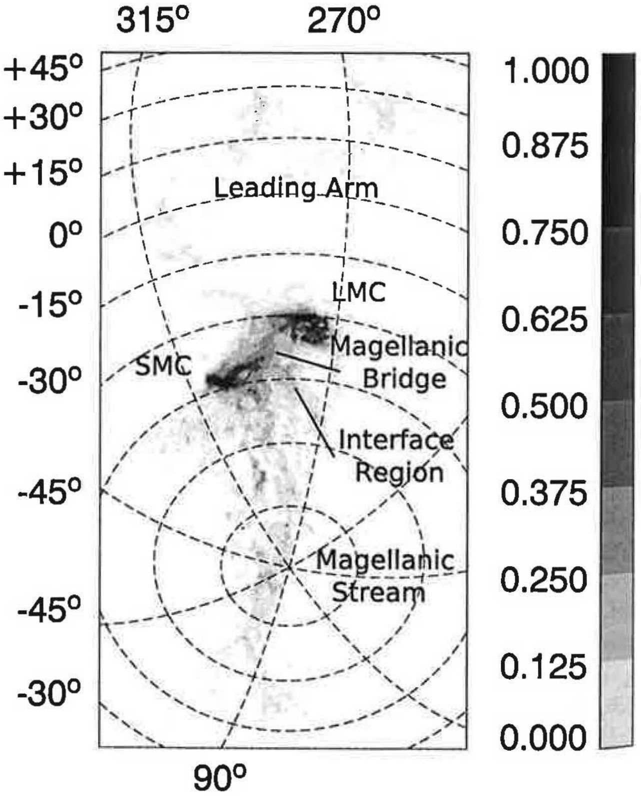

Fig. 1. Contour map of the observed H I integrated relative column density in the Magellanic System. Data by Brüns et al. (2005) is projected on the plane of sky. Galactic coordinates are used.

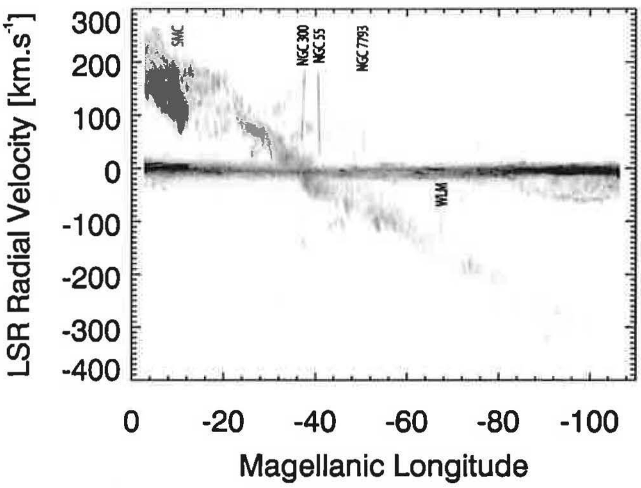

Fig. 2. LSR radial velocity of the Magellanic Stream as a function of Magellanic Longitude (see Wannier & Wrixon 1972). The observational data by Brüns et al. (2005) is plotted. Strong H I emission observed for $v_{\rm LSR} \approx 0\,{\rm km\,s^{-1}}$ comes from the MW. The map also shows the emission from the SMC, the galaxies NGC 300, NGC 55, and NGC 7793 from the Sculptor Group, and the Local Group galaxy WLM.

dicates that the observed features consist of the matter torn off the Magellanic Clouds and spread out due to the interaction between the LMC, SMC and MW.

2.2. Modeling of the Magellanic System

Toomre & Toomre (1972) have shown the applicability of *restricted N–body* models on interacting galaxies. In restricted N–body simulations, gravitating particles are replaced by *test–particles* moving in a time–dependent potential which is a superposition of analytic potentials of the individual galaxies. Such an approach maps the gravitational potential with high spatial resolution for low CPU costs due to the linear CPU scaling with the number of particles. However, the self–gravity of the stellar systems is not considered directly. E.g. the orbital decay of the Magellanic Clouds due to dynamical friction cannot be treated self–consistently in restricted N–body simulations, but has to be considered by (semi–)analytical approximative formulas.

First papers on the physical features of the interacting system of LMC, SMC and Galaxy used 3 D restricted N–body simulations to investigate the *tidal origin* of the extended Magellanic structures. Lin & Lynden–Bell (1977) pointed out the problem of the large parameter space of the LMC–SMC–MW interaction. To reduce the parameter space, they neglected both the SMC influence on the System and dynamical friction within the MW halo, and showed that such configuration allows for the existence of a LMC trailing tidal stream. The interaction between the Clouds was analyzed by Fujimoto & Sofue (1976) who assume the LMC and SMC to form a gravitationally bound pair for several Gyr, moving in a flattened MW halo. They identified some LMC and SMC orbital paths leading to creation of a tidal tail. Following studies by Murai & Fujimoto (1980, 1984), Lin & Lynden–Bell (1982), Gardiner et al. (1994) and Lin et al. (1995) extended and developed test–particle models of the LMC–SMC–MW interaction. The Magellanic Stream was reproduced as a remnant of the LMC–SMC encounter that was mostly placed to the time of −2 Gyr. The matter torn off was spread along the paths of the Clouds. The simulations also indicate that the major fraction of the Magellanic Stream gas stems from the SMC. The observed radial velocity profile of the Stream was modeled remarkably well. However, the smooth H I column density distribution did not agree with observations indicating apparently clumpy Magellanic Stream structure. Test–particle models place matter to the Leading Arm area naturally (see the study on the origin of tidal tails and arms by Toomre & Toomre 1972), but correspondence with observational data cannot be considered sufficient. Gardiner & Noguchi (1996) devised a scheme of the Magellanic System interaction implementing the full N–body approach. The SMC was modeled by a self–gravitating sphere moving in the LMC and MW analytic potentials. It was shown that the evolution of the Magellanic Stream and the Leading Arm is dominated by tides which supports the applicability of test–particle codes for modeling of extended Magellanic structures. Recently, the study by Connors et al. (2005) investigated the evolution of the Magellanic Stream as a process of tidal stripping of gas from the SMC. Their high–resolution N–body model of the Magellanic System based on ideas of Gardiner & Noguchi (1996) is compared to the data from the HIPASS survey. Involving pure gravitational interaction allowed for remarkably good reproduction of the Magellanic Stream LSR radial velocity profile. They were able to improve previous models of the Leading Arm. Similarly to the previous tidal scenarios, difficulties remain concerning overestimating of the H I column density toward the far tip of the Magellanic Stream. Connors et al. (2005) approximate both the LMC and Milky Way by rigid potentials and also do not study influence of non–spherical halo of MW.

Meurer et al. (1985) involved continuous ram pressure stripping into their simulation of the Magellanic System. This approach was followed later by Sofue (1994) who neglected presence of the SMC, though. The Magellanic Stream was formed of the gas stripped from outer regions of the Clouds due to collisions with the MW extended ionized disk. Heller & Rohlfs (1994) argue for a LMC–SMC collision 500 Myr ago that established the MB. Later, gas distributed to the inter–cloud region was stripped off by ram pressure as the Clouds moved through a hot MW halo. Generally, continuous ram pressure stripping models succeeded reproducing the decrease of the Magellanic Stream H I column density towards the far tip of the Stream. However, they are unable to explain the evidence of gaseous clumps in the Magellanic Stream. Gas stripping from the Clouds caused by isolated collisions in the MW halo was studied by Mathewson et al. (1984). The resulting gaseous trailing tail consisted of fragments, but such a method did not allow for reproduction of the column density decrease along Magellanic Stream. Recently, Bekki & Chiba (2005) applied a complex gas–dynamical model including star–formation to investigate the dynamical and chemical evolution of the LMC. They include self–gravity and gas dynamics by means of sticky particles, but they are also not complete: they assume a live LMC system, but SMC and MW were treated by static spherical potentials. Thus, dynamical friction of the LMC in the MW halo is only considered by an analytical formula and a possible flattening of the MW halo is not involved. Their model cannot investigate possible SMC origin of Magellanic Stream neither. Mastropietro et al. (2005) introduced their model of the Magellanic System including hydrodynamics (SPH) and full N–body description of gravity. They studied the interaction between the LMC and the MW. Similarly to Lin & Lynden–Bell (1977) and Sofue (1994) the presence of SMC was not taken into account. It was shown that the Stream, which sufficiently reproduces the observed H I column density distribution, might have been created without an LMC–SMC interaction. However, the history of the Leading Arm was not investigated.

In general, hydrodynamical models allow for better reproduction of the Magellanic Stream H I column density profile than tidal schemes. However, they constantly fail reproducing the Magellanic Stream radial velocity measurements and especially the high–negative velocity tip of Magellanic Stream. Both families of models suffer from serious difficulties when modeling the Leading Arm.

In order to model the evolution of the Magellanic System, the initial conditions and all parameters of their interaction have to be determined. Such a parameter space becomes quite extended. In the Magellanic System we have to deal with the orbital parameters and the orientation of the two Clouds, their internal properties (like the extension of the disk) and the properties of the MW potential. In total we have about 20 parameters (the exact number depends on the adopted sophistication of the model). Previous studies on the Magellanic Clouds, however, argued for very similar evolutionary scenarios of the system (e.g. Lin & Lynden–Bell 1982, Gardiner et al. 1994, Bekki & Chiba 2005). These calculations are based on additional assumptions concerning the orbits, or the internal structure and orientation of the Clouds, the potential of the Milky Way (mass distribution and shape), the treatment of dynamical friction in the Galactic halo or the treatment of self–gravity and gas dynamics in the Magellanic Stream. Some of them can be motivated by additional constraints. E.g. Lin & Lynden-Bell (1982) and Irwin et al. (1990) argue that the Clouds should have been gravitationally bound over the last several Gyr. However, in general the uniqueness of the adopted models is unclear, because a systematic analysis of the entire parameter space is still missing.

We explore the LMC–SMC–MW interaction parameter space that is compatible with the observations of the Magellanic System available up to date. Regarding the dimension and size of the parameter space, a large number of the numerical model runs have to be performed to test possible parameter combinations – no matter which kind of search technique is selected. In such a case, despite their physical reliability, full N–body models are of little use, due to their computational costs.

3. Method

In order to cope with the extended parameter space, neither a complete catalog of models nor a large number of computationally expensive self–consistent simulations can be performed – both due to numerical costs. However, a new numerical approach based on evolutionary optimization methods combined with fast (approximative) N–body integrators turned out to be a promising tool for such a task. In case of encounters between two galaxies Wahde (1998) and Theis (1999) showed that a combination of a genetic algorithm with restricted N–body simulations is able to reproduce the parameters of the interaction.

Here we apply the GA search strategy with a restricted N–body code for the Magellanic System. In the following sections we describe first our N–body calculations and then we explain briefly the applied genetic algorithm.

3.1. N–body simulations

Our simulations were performed by test–particle codes similar to the ones already applied to the Magellanic System by Murai & Fujimoto (1980) and Gardiner et al. (1994). But as an extension of these previous papers we allow for a flattened MW halo potential and a more exact formula for dynamical friction taking anisotropic velocity distributions into account.

For the galactic potentials we used the following descriptions: both LMC and SMC are represented by Plummer spheres. The potential of the DM halo of the Milky Way is modeled by a flattened axisymmetric logarithmic potential (Binney & Tremaine 1987)

$$\Phi_{\mathrm{L}} = \frac{1}{2} v_0{}^2 \ln\left(R_{\mathrm{c}}{}^2 + R^2 + \frac{z^2}{q^2}\right). \tag{1}$$

In agreement with Helmi (2004) we set $R_{\mathrm{c}} = 12\,\mathrm{kpc}$, $v_0 = \sqrt{2} \cdot 131.5\,\mathrm{km\,s^{-1}}$, and q describes the flattening of the MW halo potential. The corresponding flattening q_ρ of the density distribution associated with the halo potential follows

$$q_\rho{}^2 = \frac{1+4q^2}{2+3/q^2} \quad (R \ll R_{\mathrm{c}}), \tag{2}$$

$$q_\rho{}^2 = q^2\left(2 - \frac{1}{q^2}\right) \quad (R \gg R_{\mathrm{c}}). \tag{3}$$

Dynamical friction causes the orbital decay of the Magellanic Clouds. We adopted the analytic dynamical friction formula by Binney (1977). In contrast to the commonly used expression by Chandrasekhar (1943), it allows for an anisotropic velocity distribution. By comparison with N–body simulations of sinking satellites, Peñarrubia et al. (2004) showed that Binney's solution is a significant improvement of the standard approach with Chandrasekhar's formula.

Finally, we get the following equations of motion of the Clouds:

$$\frac{\mathrm{d}v_{\mathrm{LMC}}}{\mathrm{d}t} = -(\nabla\Phi_{\mathrm{L}} + \nabla\Phi_{\mathrm{SMC}}) + \frac{F_{\mathrm{DF}}}{m_{\mathrm{LMC}}}, \tag{4}$$

$$\frac{\mathrm{d}v_{\mathrm{SMC}}}{\mathrm{d}t} = -(\nabla\Phi_{\mathrm{L}} + \nabla\Phi_{\mathrm{LMC}}) + \frac{F_{\mathrm{DF}}}{m_{\mathrm{SMC}}}, \tag{5}$$

where $\Phi_{\rm LMC}$, $\Phi_{\rm SMC}$ are the LMC, SMC Plummer potentials, and $F_{\rm DF}$ is the dynamical friction force exerted on the Clouds as they move in the MW DM halo.

Our simulations were performed with the total number of 10 000 test–particles equally distributed to both Clouds. We start the simulation with test–particles in a disk–like configuration with an exponential particle density profile, and compute the evolution of the test–particle distribution up to the present time. Initial conditions for the starting point of the evolution of the System at the time –4 Gyr were obtained by the standard backward integration of equations of motion (see e.g. Murai & Fujimoto 1980, Gardiner et al. 1994). Basically, the choice for the starting epoch of this study originates in the fact that the MW, LMC and SMC form an isolated system in our model. Such an assumption was very common in previous papers on the Magellanic System (e.g. Murai & Fujimoto 1980, Gardiner et al. 1994, Gardiner & Noguchi 1996) and was motivated by insufficient kinematic information about the Local Group, that did not allow to estimate the influence of its members other than MW on the evolution of the Magellanic System. Our detailed analysis of the orbits of the LMC and SMC showed that the galactocentric distance of either of the Clouds did not exceed 300 kpc within the last 4 Gyr. Investigation of the kinematic history of the Local Group by Byrd et al. (1994) indicates, that the restriction of the maximal galactocentric radius of the Magellanic System to $R_{\rm max} \approx 300$ kpc when $T > -4$ Gyr lets us consider the orbital motion of the Clouds to be gravitationally dominated by the MW.

3.2. Genetic Algorithm Search

Genetic algorithms can be used to solve optimization problems like a search in an extended parameter space. The basic concept of GA optimization is to interpret natural evolution of a population of individuals as an optimization process, i.e. an increasing adaptation of a population to given conditions. In our case the conditions are to match numerical models to the observations. Each single point in parameter space defines uniquely one interaction scenario which can be compared with the observations (after the N–body simulation is performed). The quality of each point in parameter space (or the corresponding N–body model) can be characterized by the value of a *fitness function* (FF) which is constructed to become larger, the better the model matches the observations. A *population* consists of a set of points in parameter space (*individuals*). Each single parameter of an individual corresponds to a *gene*. A genetic algorithms recombines the genes of the individuals in different reproduction steps: First two individuals (*parents*) are selected with a probability growing with their fitness. Then the genes of the parents are recombined by application of reproduction operators mimicking *cross–over* and *mutation*. Often the reproduction is done for all members of a population. Then the newly created population corresponds to a next *generation*. The reproduction steps are then repeated until a given number of generations is calculated or a sufficient convergence is reached. More details about genetic algorithms can be found in Holland (1975) or Goldberg (1989). An application to interacting galaxies is described in Wahde (1998), Theis (1999) or Theis & Kohle (2001).

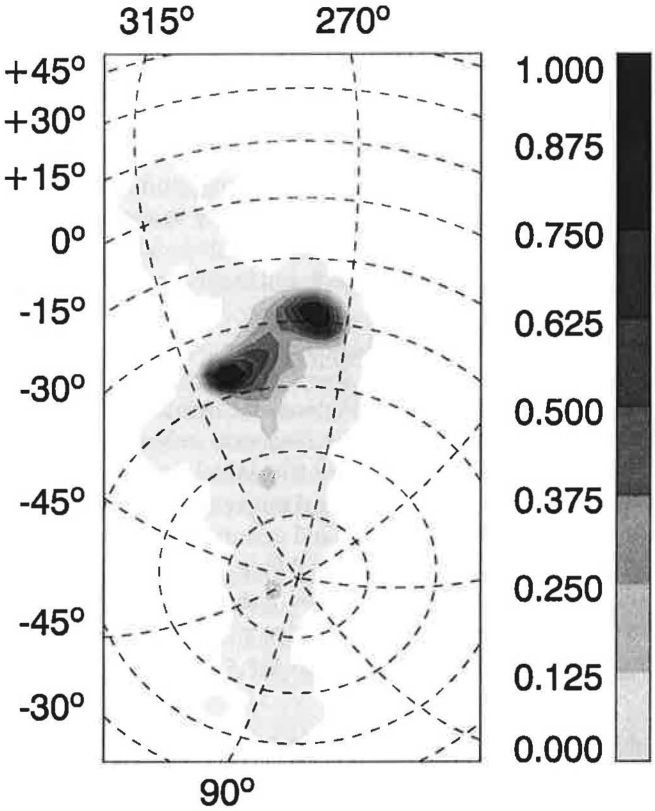

Fig. 3. Contour map of the observed H I integrated column density. The original data cube by Brüns et al. (2005) is modified by frequency filtering (see Appendix B) and integrated over all radial velocity channels. Contour map is projected on the plane of sky. Galactic coordinates are used.

Obviously, the evolutionary search for the optimal solution can be treated as a process of maximizing the fitness of individuals. The GA looks for maxima of the function assigning individuals their fitness values. It should be noted that the problem we want to solve only enters via the fitness function. Therefore, the choice of the fitness function is essential for the performance and the answer given by a GA.

For our calculations we used a fitness function consisting of three different parts corresponding to three different comparisons. These three fitness functions measure the quality of the numerical models for different aspects of the given H I data cube. The original 3D H I data cube together with its version modified for the purpose of efficient GA search are visualized in Fig. B.1. Two of the comparisons deal with the whole data cube: FF_2 denotes the rough occupation of cells in the data cube and is a measure for the agreement of the structural shape in the data cube. FF_3 compares the individual intensities in each cell of the data cube. The FF_3 definition basically follows the fitness function introduced in Theis (1999) or Theis & Kohle (2001) who found it an efficient GA driver for the galactic interaction problems they studied. However, if the fraction of the total volume of the system's data cube, that is occupied by the structures of special interest, is small (< 10% in the case of the Magellanic Stream and the Leading Arm), implementation of a structural search in the data (FF_2) preceding the fine comparison between modeled and observed data significantly improves the performance of the GA. Finally, FF_1 is introduced to take into account the velocity profile, i.e. the important constraint of the minimum velocity in the stream. All these three quality measures are combined to yield the final fitness of a model. Details can be found in the Appendix B.

3.3. The GA Parameter Space

In this paragraph we introduce the parameters of the Magellanic System interaction that were subject to our GA search. The parameters involve the initial conditions of the LMC and SMC motion, their total masses, parameters of mass distribution, particle disc radii and orientation angles, and also the MW dark matter halo potential flattening parameter. Tab. 1 summarizes the parameters of the interaction and introduces their current values. Models are described in a right–handed Cartesian coordinate system with the origin in the Galactic center. This system is considered to be an inertial frame, because we assume that $m_{\rm MW} \gg m_{\rm LMC}, m_{\rm SMC}$. Therefore, the center of mass of the system may be placed at the Galactic center. We assume the present position vector of the Sun $\boldsymbol{R}_\odot = (-8.5, 0.0, 0.0)$ kpc. In the following paragraphs we will discuss the parameters of the LMC–SMC–MW interaction and the determination of their ranges.

Table 1. Parameters of the MW–LMC–SMC interaction.

Param.	Value	
$r_{\rm LMC}$[kpc]	$\begin{pmatrix} \langle -1.5, -0.5\rangle \\ \langle -41.0, -40.0\rangle \\ \langle -27.1, -26.1\rangle \end{pmatrix}$	Current galactocentric position vectors
$r_{\rm SMC}$[kpc]	$\begin{pmatrix} \langle 13.1, 14.1\rangle \\ \langle -34.8, -33.8\rangle \\ \langle -40.3, -39.3\rangle \end{pmatrix}$	
$v_{\rm LMC}$[km s^{-1}]	$\begin{pmatrix} \langle -3, 85\rangle \\ \langle -231, -169\rangle \\ \langle 132, 206\rangle \end{pmatrix}$	Current velocity vectors
$v_{\rm SMC}$[km s^{-1}]	$\begin{pmatrix} \langle -112, 232\rangle \\ \langle -346, -2\rangle \\ \langle 45, 301\rangle \end{pmatrix}$	
$m_{\rm LMC}$[10^9M$_\odot$]	$\langle 15.0, 25.0\rangle$	Masses
$m_{\rm SMC}$[10^9M$_\odot$]	$\langle 1.5, 2.5\rangle$	
$\epsilon_{\rm LMC}$[kpc]	$\langle 2.5, 3.5\rangle$	Plummer sphere scale radii
$\epsilon_{\rm SMC}$[kpc]	$\langle 1.5, 2.5\rangle$	
$r^{\rm disk}_{\rm LMC}$[kpc]	$\langle 9.0, 11.0\rangle$	Particle disk radii
$r^{\rm disk}_{\rm SMC}$[kpc]	$\langle 5.0, 7.0\rangle$	
$\Theta^{\rm disk}_{\rm LMC}$	$\langle 87^\circ, 107^\circ\rangle$	Disk orientation angles
$\Phi^{\rm disk}_{\rm LMC}$	$\langle 261^\circ, 281^\circ\rangle$	
$\Theta^{\rm disk}_{\rm SMC}$	$\langle 35^\circ, 55^\circ\rangle$	
$\Phi^{\rm disk}_{\rm SMC}$	$\langle 220^\circ, 240^\circ\rangle$	
q	$\langle 0.74, 1.20\rangle$	MW DM halo potential flattening

The nature and distribution of dark matter in the Galaxy has been subject to intense research and a large number of models have been proposed. We probe the DM matter distribution by investigating the redistribution of matter in the Magellanic System due to the MW–LMC–SMC interaction, paying special attention to the features of the Magellanic Stream. That is similar to the method applied by Helmi (2004), who studied kinematic properties of the Sagittarius stream. In order to enable comparison with the results by Helmi (2004), we also adopted the axially symmetric logarithmic halo model of MW (Eq. 1) and the same values of the halo structural parameters R_c, v_0 with a similar range of studied values of the flattening q (see Tab. 1). We extended the range of q values tested by Helmi (2004) to the lower limit of $q = 0.74$, which is the minimal value acceptable for the model of a logarithmic halo (for a detailed explanation see Binney & Tremaine 1987). For every value of q a time–consuming calculation of parameters of dynamical friction is required (see Appendix A). To reduce the computational difficulties, the flattening q was treated as a discrete value with a step of $\Delta q = 0.02$, and the parameters of dynamical friction were tabulated. The upper limit of $q = 1.20$ was selected to enable testing of prolate halo configurations. Extension of the halo flattening range to higher values was not considered due to the computational performance limits of our numerical code.

The estimated ranges of the values of the remaining parameters are based on our observational knowledge in the Magellanic System. Galactocentric position vectors $\boldsymbol{r}_{\rm LMC}$ and $\boldsymbol{r}_{\rm SMC}$ agree with the LMC and SMC distance moduli measurements given by Van den Bergh (2000), who derived the mean values of distance moduli $\overline{(m-M)_0} = 18.50 \pm 0.05$ for LMC and $\overline{(m-M)_0} = 18.85 \pm 0.1$ for SMC, corresponding to the heliocentric distances of (50.1 ± 1.2) kpc and (58.9 ± 2.6) kpc, respectively. Only 2 of the 6 components of the LMC and SMC position vectors enter the GA search as free parameters, because the rest of them is determined by the projected position of the Clouds on the plane of sky, that is $l_{LMC} = 280^\circ\,27'$, $b_{\rm LMC} = -32^\circ\,53'$ and $l_{\rm SMC} = 302^\circ\,47'$, $b_{\rm SMC} = -44^\circ\,18'$.

Previous studies by Murai & Fujimoto (1980) and Gardiner et al. (1994) found that the correct choice of the spatial velocities is crucial for reproducing the observed H I structures. Kroupa & Bastian (1997) derived from an analysis of HIPPARCOS proper motions of LMC and SMC stars that $\boldsymbol{v}_{\rm LMC} = (+41 \pm 44, -200 \pm 31, +169 \pm 37)\,{\rm km\,s^{-1}}$ and $\boldsymbol{v}_{\rm SMC} = (+60 \pm 172, -174 \pm 172, +173 \pm 128)\,{\rm km\,s^{-1}}$. The large uncertainties in actual values of the LMC and SMC velocity vectors origin in the fact that the measured transverse velocities suffer from large rms errors, which is connected to large distance of LMC and SMC in combination with limited precision of proper motions in the HIPPARCOS catalog. To derive the actual initial conditions at the starting time of the simulation from the current positions and velocities of the Clouds, we employed the backward integration of equations of motion.

Current total masses $m_{\rm LMC}$ and $m_{\rm SMC}$ follow estimates by Van den Bergh (2000). In general, masses of the Clouds are functions of time and evolve due to the LMC–SMC exchange of matter, and as a consequence of the interaction between the Clouds and MW. Our test-particle model does not allow for a reasonable treatment of a time–dependent mass–loss. Therefore, masses of the Clouds are considered constant in time and their initial values at the starting epoch of our simulations are approximated by the current LMC and SMC masses. Regarding the large range of the LMC and SMC mass estimates available (for details see Van den Bergh 2000), $m_{\rm LMC}$ and $m_{\rm SMC}$ are also treated as free input parameters of our model that become subjects to the GA optimization. Their ranges that we investigated can be found in Tab. 1.

Scale radii of the LMC and SMC Plummer potentials $\epsilon_{\rm LMC}$, $\epsilon_{\rm SMC}$ are input parameters of the model describing the radial mass distribution in the Clouds. The study by Gardiner et al. (1994) used the values $\epsilon_{\rm LMC} = 3$ kpc and $\epsilon_{\rm SMC} = 2$ kpc. In order to investigate the influence of this parameter on the evolution of the Magellanic System, the Plummer radii were involved into the GA search and their values were varied within the ranges of the width of 1 kpc, including the estimates by Gardiner et al. (1994) (see Tab. 1).

Gardiner et al. (1994) analyzed the H I surface contour map of the Clouds to estimate the initial LMC and SMC disk radii entering their model of the Magellanic System as initial conditions. Regarding the absence of a clearly defined disk of the SMC, and possible significant mass redistribution in the Clouds during their evolution, the results require a careful treatment and a further verification. We varied the current estimates of disk radii $r^{\rm disk}_{\rm LMC}$, $r^{\rm disk}_{\rm SMC}$ as free parameters within the ranges introduced in Tab. 1, containing the values derived by Gardiner et al. (1994), and used them as initial values at the starting point of our calculations ($T = -4$ Gyr).

The orientation of the disks is described by two angles Θ and Φ defined by Gardiner & Noguchi (1996). Several observational determinations of the LMC disk plane orientation were collected by Lin et al. (1995). Its sense of rotation is assumed clockwise (Lin et al. 1995, Kroupa & Bastian 1997). Position angle of the bar structure in the SMC was used by Gardiner & Noguchi (1996) to investigate the current disk orientation. Their results allow for wide ranges of the LMC, SMC disk orientation angles (see Tab. 1) and so we investigated Θ and Φ by the GA search method, too. Similarly to Gardiner & Noguchi (1996) we use the current LMC and SMC disk orientation angles (Tab. 1) to approximate their initial values at $T = -4$ Gyr.

4. Results

We try to reproduce as closely as possible the column density and velocity distribution of H I in the Magellanic Stream and in the Leading Arm. The influence of actual distances to the LMC and SMC and of their present space velocity vectors is considered together with their masses and the past sizes and space orientations of the orginal disks. Here, we give the results of the search in the parameter space with the GA using the 3–component fitness function defined by Eq. B.1. In principle, the GA is able to find the global extreme of the FF if enough time is allowed for the evolution of the explored system (see Holland 1975). However, it may be very time–consuming to identify the single best fit due to a slow convergence of the FF. Therefore, to keep the computational cost reasonable, the maximum number of 120 GA generations to go through was defined.

In order to explore the FF of our system, we collected 123 GA fits of the Magellanic System resulting from repeated runs of our GA optimizer. Typically, identification of a single GA fit requires $\approx 10^4$ runs of the numerical model. Thus, due to the application of GA we were able to search the extended parameter space of the interaction and discover the most successful models of the System over the entire parameter space by testing $\approx 10^6$ parameter combinations. In the case of our 20–dimensional parameter space, simple exploration of every possible combination of parameters even on a sparse grid of e.g. 10 nodes per a dimension means 10^{20} runs of the model. Such a comparison clearly shows necessity of using optimization techniques and demonstrates computational efficiency of GA.

The fitness distribution for different values of the halo flattening parameter q is shown in Fig. 4. For every value of q, the model of the highest fitness is selected and its fitness value is plotted. Fig. 4 indicates that better agreement between the models and observational data was achieved generally for oblate halo configurations than for nearly spherical or prolate halos. The relative difference between the worst ($Fit_{\rm MIN} = 0.450; q = 1.14$) and the best ($Fit_{\rm MAX} = 0.496; q = 0.84$) model shown in Fig. 4 is $\Delta Fit = 0.09$. It reflects the fact, that each of the GA fits contains a trailing tail (Magellanic Stream) and a leading stream (Leading Arm), but there are fine differences between the resulting distributions of matter. One may note that the GA optimizer did not discover a model of fitness over 0.5 (the maximum reachable fitness value is 1.0 – see Appendix B). It is caused either by insufficient volume of the studied parameter space of the interaction, or by simplification of physical processes in our model (see Sec. 6), or by a combination of both

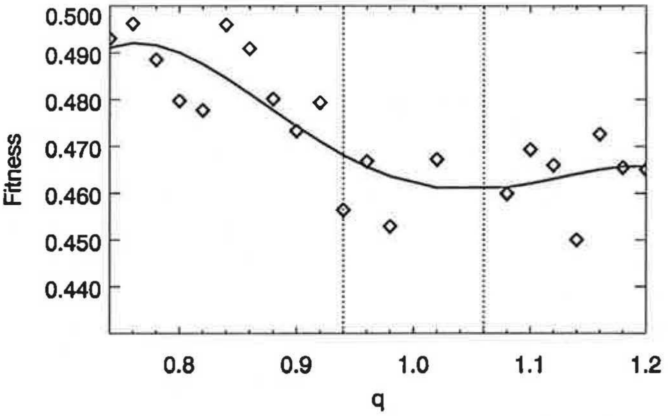

Fig. 4. Maximum values of fitness as function of the MW dark matter halo flattening q. The plot depicts the fitness of the best GA fit of the Magellanic System that was found for each of the MW dark matter halo flattening values that entered the GA search. The function is also approximated by its least–square polynomial fit. The values of q delimiting the model groups A, B and C (see Tab. 2) are emphasized by dotted lines.

reasons. That establishes an interesting problem and should become a subject to future studies.

We want to discuss our results with respect to the shape of the MW halo. Thus, all the GA fits are divided into three groups according to the halo flattening (see Tab. 2) to show differences or common features of models for oblate, nearly spherical and prolate halo configurations. The actual borders between the groups A, B and C were selected by definition and the way, so that the number of models in each of the groups allows for statistical treatment of the LMC, SMC orbital features and particle redistribution which will be introduced in Sec. 4.1.

Table 2. Three major groups according to the halo flattening q

Group	A	B	C
	$0.74 \le q \le 0.92$	$0.94 \le q \le 1.06$	$1.08 \le q \le 1.20$
N_i	101	10	12

4.1. Evolution

Close encounters of interacting galaxies often lead to substantial disruption of their particle disks forming tidal arms and tails subsequently (Toomre & Toomre 1972). Regarding that, the time dependence of the relative distance of the interacting pair is an interesting source of information on the system.

First of all, we examine the time distribution of the minima of the LMC–SMC relative distance. For each of the model groups mentioned in Tab. 2, we calculate the relative number of GA solutions having a minimum of the LMC–SMC relative distance within a given interval of 500 Myr. Fig. 5 shows such a distribution of fits for the total time interval of our simulations, which is 4.0 Gyr. The local maxima of the time distribution of the LMC–SMC distance minima are within the intervals ⟨−3.0, −2.0) Gyr and ⟨−0.5, 0.0) Gyr. For prolate halos ($q \ge 1.08$) there is no LMC–SMC distance minimum between -2.0 Gyr and -0.5 Gyr.

Subsequently, the mean values of the LMC–SMC distance minima are calculated for each of the time intervals defined above. Comparison of the results for oblate, nearly spherical and prolate DM halo configuration is available in Fig. 6. It was found that close ($\Delta r \approx 10$ kpc) LMC–SMC encounters do not occur in models with either oblate or prolate halos. If the MW DM halo shape is nearly spherical, disruption of the LMC and SMC initial particle distribution leading to creation of the observed H I structures occurred due to strong LMC–SMC interaction typically.

Another point of interest is the time dependence of the LMC and SMC test–particle redistribution during the evolutionary process. Fig. 7 offers the relative number of test–particles strongly disturbed, i.e. particles that reached the minimal distance of twice the original radii of their circular orbits around the LMC, SMC center, respectively, by the LMC–SMC–MW interaction in the defined time–intervals. Comparison between the plots in Fig. 6 and Fig. 7 shows that encounters of the Clouds are followed by delayed raise of the number of particles shifted to different orbits, typically. Another such events are induced by the interaction of the Clouds and MW. Disruption of the LMC and SMC disks triggers formation of the extended structures of the Magellanic System. Particles are assigned new orbits in the superimposed gravitational potential of the LMC, SMC and MW, and spread along the orbital paths of the Clouds. Our study shows that the formation of the Magellanic Stream and other observed H I features did not begin earlier than 2.5 Gyr ago for model groups A and B (see Fig. 7). Prolate halos (group C) allow for a mass redistribution in the system that started at $T < -3.5$ Gyr.

4.2. Representative Models

Here, we describe the models of highest fitness selected from each of the groups A, B and C. All of them are typical representatives of their model groups and we discuss their features with respect to the H I observational data. Tab. 3 summarizes the parameter values of the models.

Table 3. Parameters of the best models in separate q categories.

Model	A	B	C
q	**0.84**	**1.02**	**1.16**
Fit	0.496	0.467	0.473
$r_{\rm LMC}$[kpc]	$\begin{pmatrix} -1.26 \\ -40.50 \\ -26.87 \end{pmatrix}$	$\begin{pmatrix} -0.90 \\ -40.31 \\ -26.88 \end{pmatrix}$	$\begin{pmatrix} -0.63 \\ -40.03 \\ -26.92 \end{pmatrix}$
$r_{\rm SMC}$[kpc]	$\begin{pmatrix} 13.16 \\ -34.26 \\ -39.77 \end{pmatrix}$	$\begin{pmatrix} 13.32 \\ -34.33 \\ -40.22 \end{pmatrix}$	$\begin{pmatrix} 13.92 \\ -34.04 \\ -39.86 \end{pmatrix}$
$v_{\rm LMC}$[km s^{-1}]	$\begin{pmatrix} 44.0 \\ -169.8 \\ 146.7 \end{pmatrix}$	$\begin{pmatrix} 18.5 \\ -169.3 \\ 171.3 \end{pmatrix}$	$\begin{pmatrix} 5.8 \\ -169.2 \\ 205.8 \end{pmatrix}$
$v_{\rm SMC}$[km s^{-1}]	$\begin{pmatrix} -37.2 \\ -60.2 \\ 204.3 \end{pmatrix}$	$\begin{pmatrix} -10.1 \\ -94.2 \\ 270.0 \end{pmatrix}$	$\begin{pmatrix} -47.5 \\ -13.2 \\ 162.6 \end{pmatrix}$
$m_{\rm LMC}[10^9 {\rm M}_\odot]$	24.46	19.86	19.01
$m_{\rm SMC}[10^9 {\rm M}_\odot]$	2.06	1.82	1.83
$r^{\rm disk}_{\rm LMC}$[kpc]	9.62	11.46	9.06
$r^{\rm disk}_{\rm SMC}$[kpc]	6.54	6.06	7.90
$\Theta^{\rm disk}_{\rm LMC}$	89°	98°	102°
$\Phi^{\rm disk}_{\rm LMC}$	274°	277°	281°
$\Theta^{\rm disk}_{\rm SMC}$	36°	49°	36°
$\Phi^{\rm disk}_{\rm SMC}$	229°	231°	224°

4.2.1. Group A

The best model of the Magellanic System with an oblate MW halo is introduced in this section (model A). Fig. 8 depicts the time variation of the LMC, SMC galactocentric distance together with the LMC–SMC separation for the last 4 Gyr. The Clouds move on very different orbits. The apogalactic distance of the LMC decreases systematically during the evolutionary period, which clearly reflects the effect of dynamical friction. There is a gap between the periods of subsequent perigalactic approaches of the Clouds. While the last two perigalactica of the LMC are separated by ≈ 2.3 Gyr, it is not over ≈ 1.5 Gyr

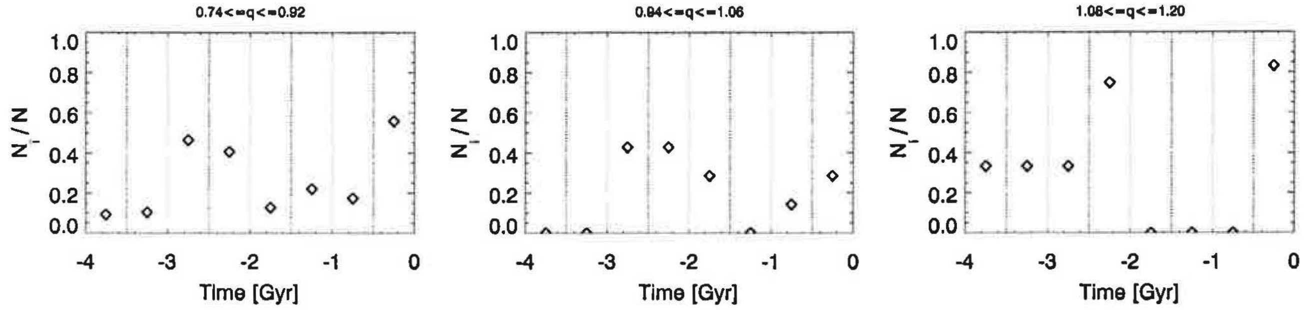

Fig. 5. Relative numbers of the Magellanic System GA models with LMC–SMC relative distance minima at given time interval for model groups A (left), B (middle) and C (right). The counts were made for 8 time intervals of 500 Myr covering the entire Magellanic evolution period of 4 Gyr investigated in our study.

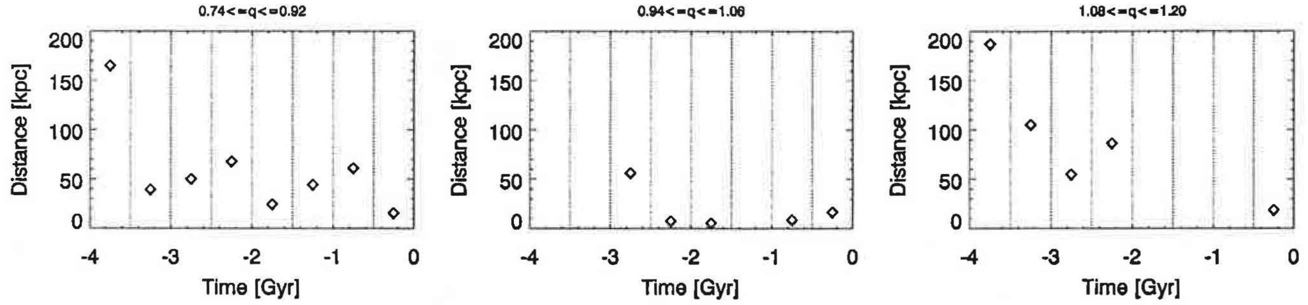

Fig. 6. Mean values of the LMC–SMC distance minima for model groups A (left), B (middle) and C (right) (Tab. 2) and for 8 time intervals of 500 Myr.

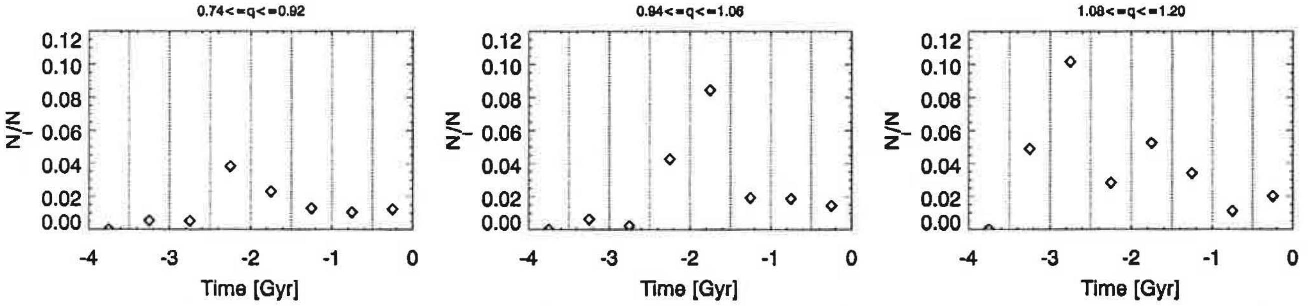

Fig. 7. Relative number of the LMC and SMC test–particles strongly disturbed due to the Magellanic System interaction. Counts within 8 time intervals of 500 Myr and for model groups A (left), B (middle) and C (right) are plotted.

in the case of the SMC. Filled parts of the plot in Fig. 8 indicate that the Magellanic Clouds have reached the state of a gravitationally bound system during the last 4 Gyr. We define gravitational binding by the sum of the relative kinetic and gravitational potential energy of LMC and SMC. The Clouds are bound when the total energy is negative. Specifically, the LMC and SMC have been forming a bound couple since $T = -1.06$ Gyr. Nevertheless, the total lifetime of a bound LMC–SMC pair did not exceed 40 % of the entire evolutionary period we studied.

Comparison between Fig. 8 and Fig. 9 allows for conclusions on major events that initialized the redistribution of the LMC and SMC particles. The most significant change of the initial distribution of particles occurred as a result of the LMC–MW approach at $T \approx -2.4$ Gyr, and the preceding LMC–SMC encounter $T \approx -2.5$ Gyr. Later on, the particle redistribution continued due to tidal stripping by the MW.

Fig. 10 shows the modeled distribution of integrated H I column density in the System. In order to enable comparison with the observed H I distribution, we plotted a normalized H I column density map. The technique used to convert a test–particle distribution into a smooth map of column densities is described in Appendix B. Mass distribution of H I extends beyond the far tip of the observed Magellanic Stream (Fig. 3) in the model A. H I column density peaks can be found in Fig. 3 at the positions $l = 300°$, $b = -65°$ and $l = 45°$, $b = -82°$. The model A places local density maxima of H I close to those observed ones (i.e. relative angular distance is $\approx 10°$) to approximate positions $l = 325°$, $b = -70°$ and $l = 70°$, $b = -70°$, respectively. Note also the low–density distribution of matter spread along the great circle of $l = 270°$ (Fig. 10). The matter emanates from the LMC near the position of the *Interface Region* identified by Brüns et al. 2005 (Fig. 1). In general, the model overestimates the amount of matter in the Magellanic

Stream. The Leading Arm consists only of LMC particles in this scenario. The modeled matter distribution covers a larger area of the plane of sky than what is observed. However, this is a common problem of previous test–particle models of the Magellanic System (see e.g. Murai & Fujimoto 1980, Gardiner et al. 1994) and is likely caused by simplifications in the treatment of the physical processes. But also in general, successful reproduction of the Leading Arm has been a difficult task for all the models introduced so far.

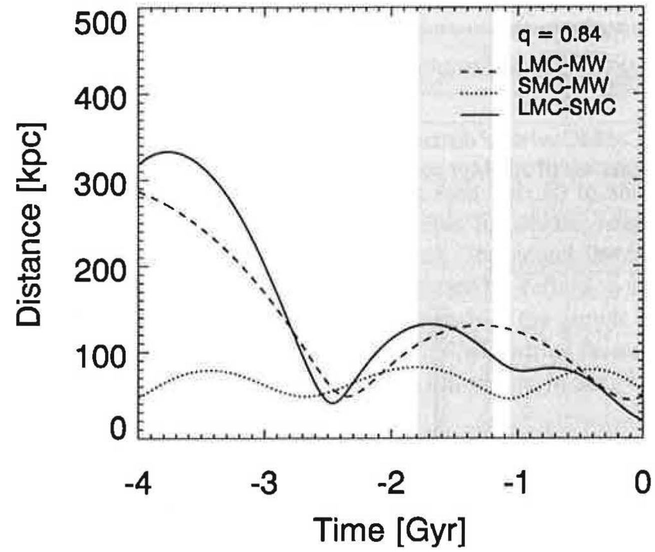

Fig. 8. Orbital evolution of the Clouds for the best GA fit from the model group A. The plot corresponds to an oblate halo of flattening $q = 0.84$. Time dependence of the LMC (dashed line), SMC (dotted line) galactocentric distances, and the LMC–SMC relative distance are plotted above. Plot areas with grey filling mark the time intervals when the Clouds were gravitationally bound to each other.

The LSR radial velocity profile of the Magellanic Stream for the model A is shown in Fig. 11. The model reproduces the LSR radial velocity of the Stream matter as almost linear function of Magellanic Longitude with the high–negative velocity tip reaching $-400\,\mathrm{km\,s^{-1}}$. Such features are in agreement with observations (see Fig. 2). In contrast to Gardiner et al. (1994), the Magellanic Stream consists of both LMC and SMC particles. Fig. 11 denotes that the LMC and SMC Stream components cover different ranges of LSR radial velocities. The Stream component of the SMC origin does not extend to LSR radial velocities below the limit of $-200\,\mathrm{km\,s^{-1}}$. The major fraction of the LMC particles resides in the LSR radial velocity range from $-400\,\mathrm{km\,s^{-1}}$ to $-200\,\mathrm{km\,s^{-1}}$.

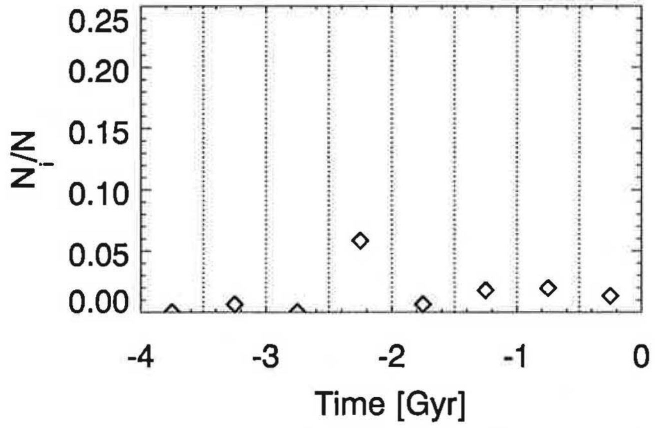

Fig. 9. Model A. Relative number of LMC/SMC test–particles strongly disturbed due to the interaction in the Magellanic System. Counts within 8 time intervals of 500 Myr are plotted.

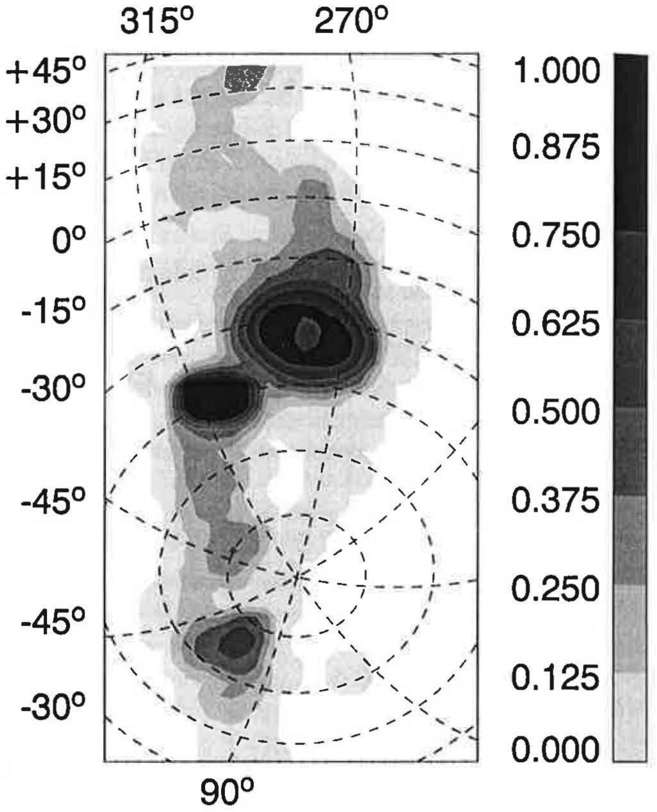

Fig. 10. Model A. Contour map of the modeled H I integrated relative column density. Data is projected on the sky plane. Galactic coordinates are used.

4.2.2. Group B

The best model of the group B (model B) corresponds to the MW DM halo flattening value $q = 1.02$. The initial condition set for the model B is listed in Tab. 3. The galactocentric distance of the Clouds and their spatial separation as functions of time are plotted in Fig. 12. Continuous decrease of the LMC and SMC galactocentric distances due to the dynamical friction is apparent for both LMC and SMC. A very close encounter of the Clouds with the relative distance $\Delta r \approx 10\,\mathrm{kpc}$ occurred at $T \approx -2.2\,\mathrm{Gyr}$. At similar moments of $T \approx -2.3\,\mathrm{Gyr}$ (LMC) and $T \approx -2.1\,\mathrm{Gyr}$ (SMC), the Clouds also reached perigalactica of their orbits. In general, both Clouds have been mov-

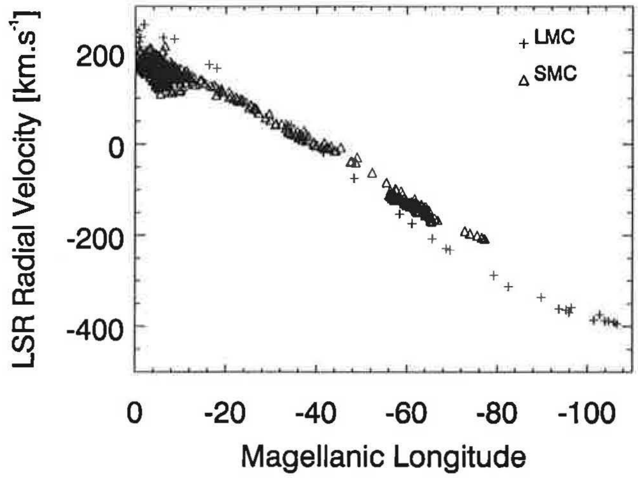

Fig. 11. Model A. LSR radial velocity profile of the Magellanic Stream.

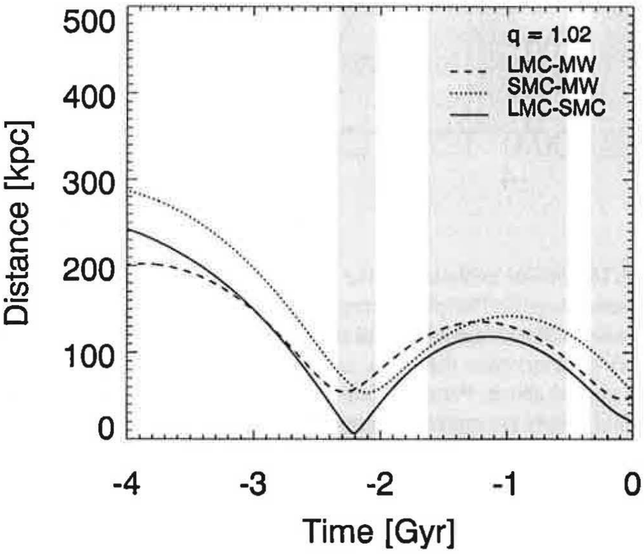

Fig. 12. Orbital evolution of the Clouds for the best GA fit from the model group B. The plot corresponds to a nearly spherical halo of flattening $q = 1.02$. Time dependence of the LMC (dashed line), SMC (dotted line) galactocentric distances, and the LMC–SMC relative distance are plotted above. Grey filled areas show time intervals when LMC and SMC formed a gravitationally bound couple.

ing on orbits showing similar time dependence of their galactocentric distances, as indicated by Fig. 12. Nevertheless, the position vectors of the Clouds evolved in significantly different ways. As consequence, the spatial separation of the Clouds varied within a wide range of values from $\Delta r \approx 10$ kpc to $\Delta r \approx 250$ kpc. The Clouds have formed a gravitationally bound couple three times within the last 4 Gyr, and the total duration of such periods was 1.7 Gyr. Currently, the LMC and SMC are gravitationally bound in the model B.

The LMC–SMC encounter at $T \approx -2.2$ Gyr caused distortion of the original particle disks of the Clouds. More than 25 % of the total number of the LMC and SMC particles were moved to significantly different orbits (for definition see Sec. 4.1) within the interval of 1 Gyr after the encounter (see Fig. 13).

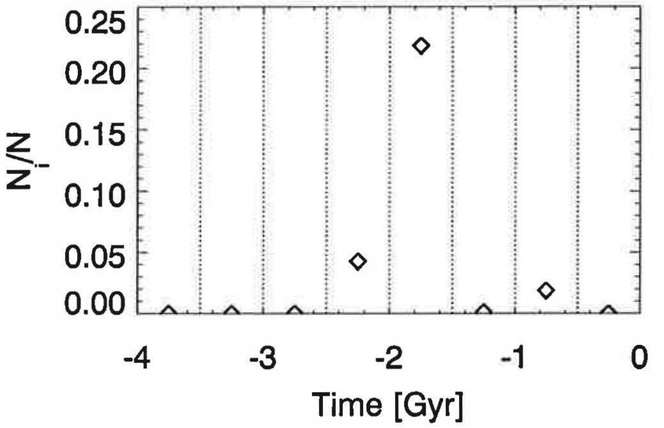

Fig. 13. Model B. Relative number of LMC/SMC test–particles strongly disturbed due to the interaction in the Magellanic System. Counts within 8 time intervals of 500 Myr are plotted.

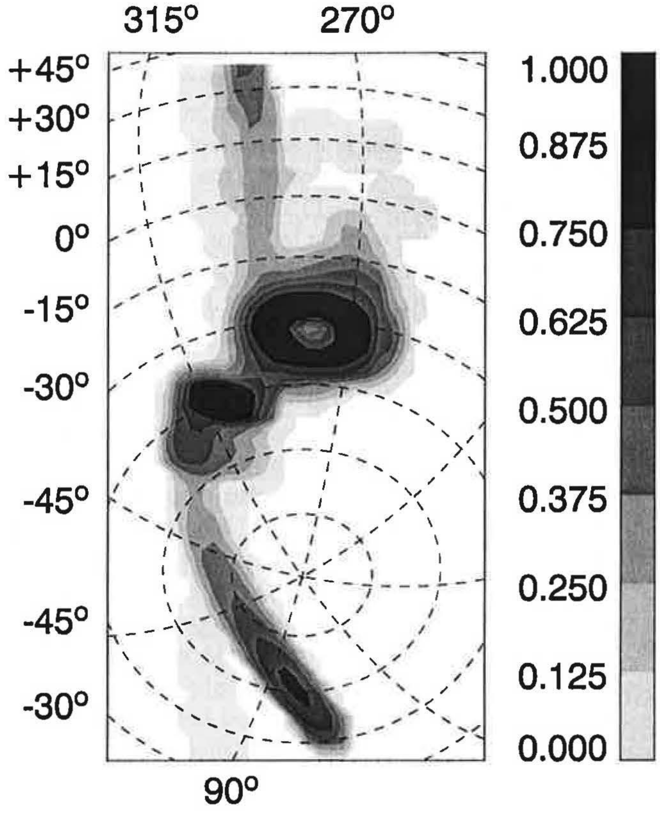

Fig. 14. Model B. Contour map of the modeled H I integrated relative column density. Data is projected on the plane of sky. Galactic coordinates are used. The dominant branch of the trailing stream is along the great circle denoted by $l = 135°/315°$.

The following evolution of the particle distribution formed extended structures depicted in Fig. 14. There are two spatially separated components present in the modeled tail. The H I column density distribution map for the model B (see Fig. 14) shows a densely populated trailing stream parallel to the great circle of $l = 135°/315°$. It consists of the SMC particles torn–off from the initial disk ≈ 2 Gyr ago. Its far end is projected

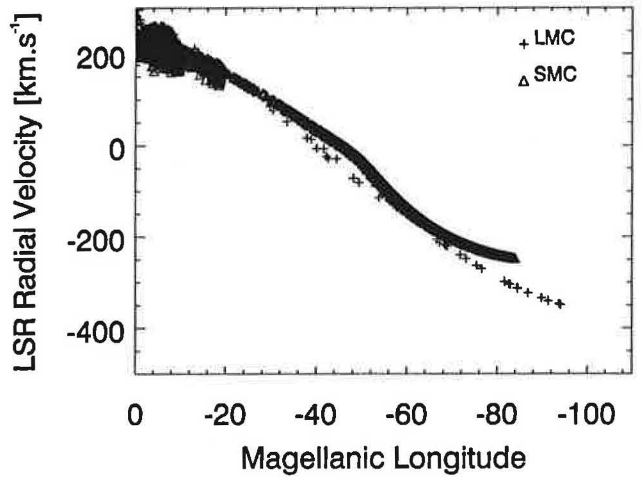

Fig. 15. Model B. LSR radial velocity profile of the Magellanic Stream.

to the plane of sky close to the tip of the Magellanic Stream. However, the modeled increase of column density of matter toward the far end of the tail is a substantial drawback of the scenario B. The stream is extended into the SMC leading arm located between $l = 290°, b = -15°$ and $l = 290°, b = 45°$. The second component of the particle tail is of LMC origin and is spread over the position of the observed low–density gas distribution centered at $l = 80°, b = -50°$ (Fig. 1 or Fig. 3).

The most significant structure at the leading side of the Magellanic System is the SMC stream introduced in the previous paragraph. Comparison between Fig. 3 and Fig. 14 indicates, that neither the projected position nor the integrated H I density distribution of the stream is in agreement with the observed Leading Arm. There was also a structure emanating from the leading edge of the LMC identified at approximate position $l = 270°, b = -15°$ (see Fig. 14). Regarding the H I data by Brüns et al. (2005), such an H I distribution is not observed. The LSR radial velocity profile of the trailing tail of the model B does not extend over the limit of $v_{\mathrm{LSR}} \approx -350\,\mathrm{km.s^{-1}}$ (Fig. 15). However, following the H I data, the far tip of the Stream should reach the LSR radial velocity $v_{\mathrm{LSR}} \approx -400\,\mathrm{km.s^{-1}}$ at the Magellanic Longitude $\approx -100°$.

4.2.3. Group C

Our last model group C assumes the presence of prolate MW DM halos. The best GA fit of the System (model C) is introduced in Tab. 3 reviewing its initial condition set. Concerning orbital motion of the Clouds, there is significant difference between the LMC and SMC periods of perigalactic approaches during the last 4 Gyr. While the last period of the LMC exceeds 2.5 Gyr, the SMC orbital cycle is shorter than 1.5 Gyr. The relative distance of the Clouds remains over 70 kpc for $T < -0.4$ Gyr. They became a gravitationally bound couple 0.6 Gyr ago and this binding has not been disrupted (Fig. 16).

Changes to the original LMC and SMC particle disks occurred especially due to the LMC–MW and SMC–MW encounters at $T < -2.0$ Gyr. Comparison between Fig. 16 and Fig. 17 demonstrates the significance of different encounter events for particle redistribution. Note that raise of the number of disturbed particles is delayed with respect to the corresponding disturbing event. Subsequently, the evolution of particle structures continued under the influence of tidal stripping by the gravitational field of MW. The current distribution of matter in the model C is plotted in the form of a 2–D map in Fig. 18. The projection of the modeled trailing stream indicates that it occupies larger area of the data cube than the observed Magellanic Stream (compare Fig. 3 and Fig. 18). According to Fig. 3 the Magellanic Stream shows H I density peaks at $l = 300°, b = -65°$ and $l = 45°, b = -82°$. Our model

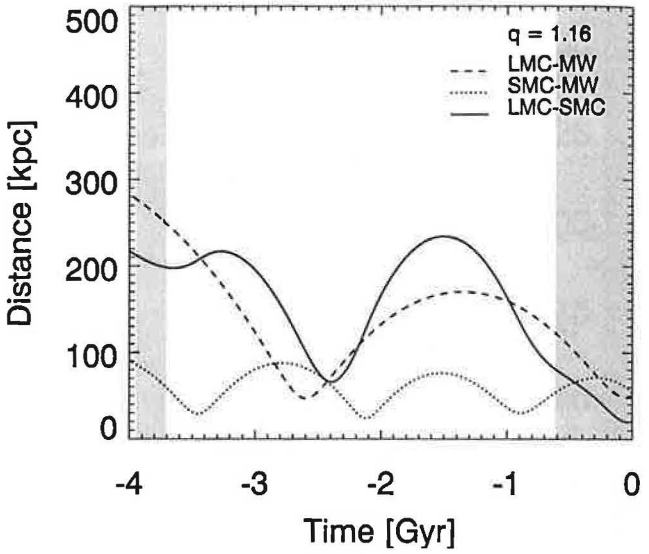

Fig. 16. Orbital evolution of the Clouds for the best GA fit from the model group C. The plot corresponds to a prolate halo of flattening $q = 1.16$. Time dependence of the LMC (dashed line), SMC (dotted line) galactocentric distances, and the LMC–SMC relative distance are plotted above. Periods when the Clouds formed a gravitationally bound couple are marked by grey filling.

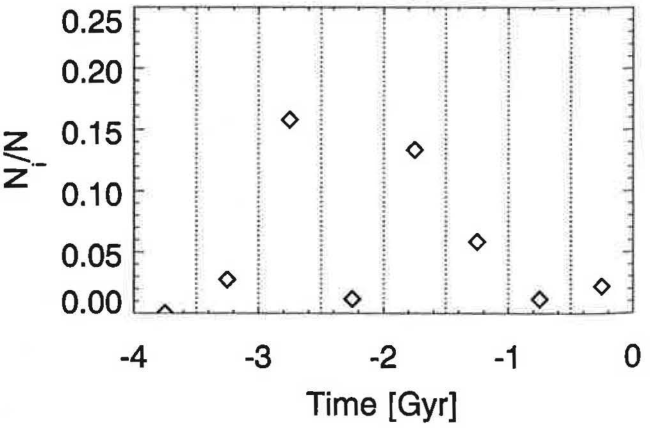

Fig. 17. Model C. Relative number of LMC/SMC test–particles strongly disturbed due to the interaction in the Magellanic System. Counts within 8 time intervals of 500 Myr are plotted.

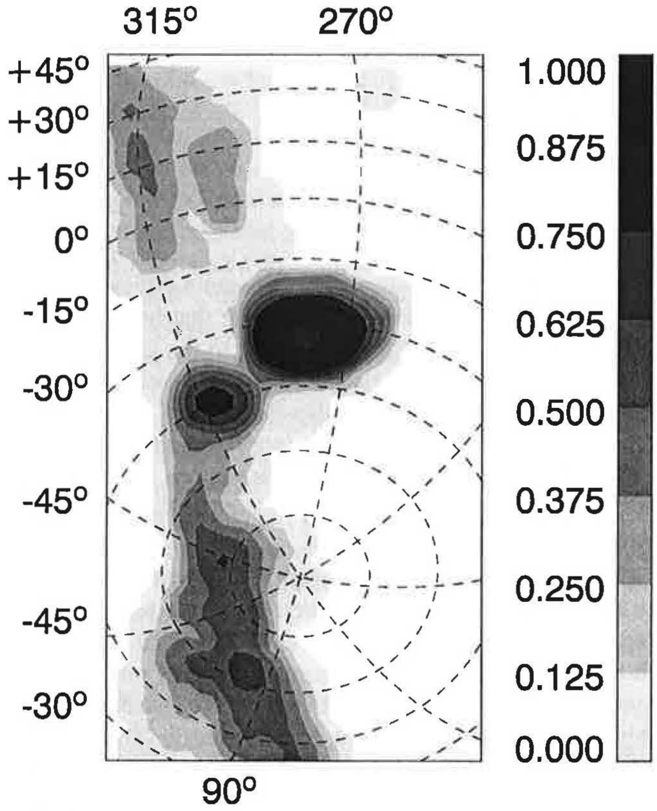

Fig. 18. Model C. Contour map of the modeled H I integrated relative column density. Data is projected on the sky plane. Galactic coordinates are used.

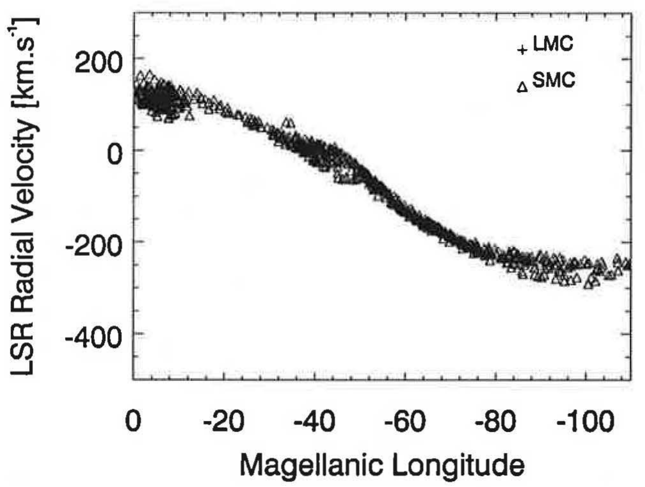

Fig. 19. Model C. LSR radial velocity profile of the Magellanic Stream.

C expects two local maxima of H I integrated column density in the tail. Their positions are shifted by ≈ 20° relatively to the peaks in Fig. 3. Additional comparison between the model and observations discovers that the model C overestimates the integrated column densities of H I in the Magellanic Stream. The matter located at the leading side of the Magellanic System is of SMC origin only. Similarly to the case of the trailing tail, the modeled amount of matter exceeds observational estimates for the Leading Arm.

Fig. 19 offers the LSR radial velocity profile of the Magellanic Stream in our model C. The measured minimum of the LSR radial velocity is ≈ $-400\,\mathrm{km\,s^{-1}}$. The high negative LSR radial velocity at the far tip of the modeled Magellanic Stream does not exceed ≈ $-300\,\mathrm{km\,s^{-1}}$, however. The observed H I emission intensity decreases towards the high negative velocity tip, which was not well reproduced by the model C.

5. Summary of the GA models

5.1. Orbits of the Magellanic Clouds

Exploration of the orbital motion of the Clouds shows similarity of the GA fits for oblate and prolate halos (models A and C). No close ($r < 10$ kpc) LMC–SMC encounters occurred for either of the models A and C. It is also notable that in the models with aspherical halos the SMC period of perigalactic approaches is significantly shorter than the period of the LMC and that the SMC remains closer than 100 kpc to the MW center during the last 4 Gyr. When the MW DM flattening $q \approx 1.0$, the LMC and SMC orbital cycle lengths were comparable for the model B. Independently of the MW halo shape, the LMC and SMC are currently forming a gravitationally bound couple in our models. However, the Clouds cannot be considered bound to each other during the entire period of the last 4 Gyr. This is in contrast with Murai & Fujimoto (1980), Gardiner et al. (1994) or Gardiner & Noguchi (1996) who argue that the LMC and SMC moving in the spherical halo have formed a gravitationally bound pair for at least several Gyr to allow for sufficient matter redistribution. We show that the structural resolution adopted by the above cited studies to make comparison between models and observations does not allow for such constraints on the orbital history of the Clouds. The GA search employed a 3–level detailed evaluation of modeled H I distribution with respect to high–resolution observational data (Brüns et al. 2005), which introduced significant improvement of previous approaches to compare observations and models. Nevertheless, there is still no clear indication that continuous gravitational binding of the Clouds covering the entire evolutionary period is necessary for successful reproduction of the observed data.

5.2. Origin of the matter in the Stream

In our best model both SMC and LMC particles were present in the trailing stream. This is a common feature of the scenarios that were investigated. In general, the fraction of H I gas originating at the SMC exceeds the fraction of LMC matter in the Stream.

Following the models A and B, the formation of the Magellanic Stream did not start earlier than 2.5 Gyr ago. In the case of the models C, the age of the Stream is ≈ 3.5 Gyr. Both estimates are close to the epoch when a massive star formation burst in the LMC began (Van den Bergh 2000). Then the matter forming the Stream comes from the Magellanic Clouds containing stars, and we necessarily face the observational fact that there is no stellar content in the Magellanic Stream. Models for aspherical halos (A, C) indicate that the matter coming to the Magellanic Stream from the LMC originates in outer regions of its initial particle disk, while no matter was torn–off from the inner disk of radius $r_{\rm disk} \approx 5$ kpc that was the dominant region of star formation in the LMC. It is due to absence of close encounters in the Magellanic System.

In contrast to the models A and C, a dramatic encounter event between the Clouds occurred in the model B at ≈ -2.2 Gyr, when the internal structure of both disks was altered and also the matter from central areas of the LMC disk was transported to the Magellanic Stream. In such a case we expect a certain fraction of the matter of the Magellanic Stream to be in the form of stars, which is, however, not supported by observations.

5.3. Structure of the Stream

Mathewson et al. (1977) observationally mapped the Magellanic Stream and discovered its clumpy structure consisting of six major H I clouds named MS I–VI. Recently, a more sensitive high–resolution H I survey of the Magellanic System by Brüns et al. (2005) showed that the above mentioned fragments of the Stream have to be considered density peaks of an otherwise smooth distribution of neutral hydrogen of column density decreasing towards the high–negative radial velocity tip of the Magellanic Stream. Our models corresponding to aspherical MW halos (A, C) placed local density maxima of H I close to the South Galactic pole. That result is supported by observations by Brüns et al. (2005). In this respect, the model B did not succeed and its projected distribution of H I in a trailing tail cannot be considered a satisfactory fit of the Magellanic Stream.

Our models overestimate the integrated relative column densities of H I in the part of the Magellanic Stream located between the South Galactic pole and the far tip of the Stream. There is also no indication of the H I density decrease as we follow the Stream further from the Magellanic Clouds. In general, all the models A, B and C predict the trailing tail to be of higher H I column densities and extended well beyond the far tip of the Magellanic Stream. Such behavior is a common feature of pure tidal evolutionary models of the Magellanic System and it is a known drawback of omitting dissipative properties of gaseous medium.

Regarding the LSR radial velocity measurements along the Magellanic Stream by Brüns et al. (2005), our models were able to reproduce some of their results. The far tip of the Magellanic Stream in the models A reaches the extreme negative LSR radial velocity of $-400\,\mathrm{km\,s^{-1}}$ known from H I observations. However, the highest negative LSR radial velocity does not drop below $-350\,\mathrm{km\,s^{-1}}$ for either prolate or nearly spherical halo configurations. Our previous discussion of various models of the Magellanic System denoted that successful reproduction of the high–negative LSR radial velocity at the far tip of the Magellanic Stream is one of the most challenging problems for such studies. Regarding our results, importance of the correct LSR radial velocity profile along the Magellanic Stream was emphasized again. Absence of H I between LSR radial velocities of $\approx -350\,\mathrm{km\,s^{-1}}$ and $\approx -400\,\mathrm{km\,s^{-1}}$ turned out to be the crucial factor decreasing the resulting fitness of examined evolutionary scenarios.

5.4. Leading Arm

Reproduction of the Leading Arm remains a difficult task for all the models of the Magellanic System that have been employed so far. Tidal models place matter to the leading side of the System, towards the Galactic equator, naturally as a result of the tidal stripping forming also the trailing tail. However, neither the projected shape of the modeled leading structures nor the H I density distribution in the regions having an observational counterpart can be considered sufficient (see e.g. Gardiner et al. 1994).

In every case A, B and C we were able to transport matter to the area of the Leading Arm. Nevertheless, the projected coverage of that region was more extended than what is observed. All the models contain a significant content of matter spread from the leading edge of the LMC across the Galactic equator, which has not been confirmed observationally. The model C reproduced the Leading Arm best. But the column density values of H I in C are overestimated and we also could not avoid an additional low–density envelope surrounding the structure (Fig. 18).

6. Uncertainties in our modeling

6.1. Missing physics

In order to optimize performance of the GA, a computationally fast model of the Magellanic System is required. Therefore, complex N–body schemes involving self–consistent description of gravity and hydrodynamics (see Bekki & Chiba 2005, Mastropietro et al. 2005) are discriminated. On the other hand, correct description of physical processes dominating the evolution of the System remains a crucial constraint on the model.

In Sec. 2.2 we discussed applicability of restricted N–body schemes on problems of galactic encounters and showed that they allow for modeling of extended streams and tails. Thus, we devised a restricted N–body code based on the numerical models by Murai & Fujimoto (1980) and Gardiner et al. (1994). The test–particle code interprets the observed large–scale structures such as the Magellanic Stream or the Leading Arm as products of tidal stripping in the Magellanic System.

Except tidal schemes, there have been used also ram pressure models in the previous studies on the Magellanic System (see Sec. 2.2). However, employing even a simple formula for ram pressure stripping would introduce other parameters including structural parameters of the distribution of gas in the MW halo and description of the gaseous clouds in the LMC and SMC. It would increase the dimension of the parameter space of the interaction and complicate the entire GA optimization process.

6.2. Mass and shape evolution of the Magellanic Clouds

The dark matter halo of the Milky Way is considered axisymmetric and generally flattened in our model. It is a significant improvement of previous studies of the Magellanic System that assumed spherical halos only. We were able to investigate the influence of the potential flattening parameter q on the evolution of the Magellanic System. However, both the mass and shape of the MW DM halo were fixed for the entire evolutionary period of 4 Gyr.

We did not take into account possible changes in mass and shape of the Clouds. Shape modification might become important for very close LMC–SMC encounters that are typical for the models with nearly–spherical MW DM halos. Peñarrubia et al. (2004) demonstrated that a relative mass–loss of a satellite galaxy moving through an extended halo strongly differs for various combination of its orbital parameters, shape and mass distribution of the halo, and cannot be described reliably by a simple analytic formula.

7. Summary and Conclusions

We performed an extended analysis of the parameter space for the interaction of the Magellanic System with the Milky Way. The varied parameters cover the phase space parameters, the masses, the structure and the orientation of both Magellanic Clouds as well as the flattening of the dark matter halo of the Milky Way. The analysis was done by a specially adopted optimization code searching for a best match between numerical models and the detailed HI map of the Magellanic System by Brüns et al. (2005). The applied search algorithm is a genetic algorithm combined with a code based on the fast, but approximative restricted N–body method. By this, we were able to analyze more than 10^6 models which makes this study one of the most extended ones for the Magellanic System.

In this work we focused especially on the flattening of the MW dark matter halo potential q. The range $0.74 \leq q \leq 1.20$ was studied. It is equivalent to the interval of the density flattening $0.31 \leq q_\rho \leq 1.37$ (see Eq. 3).

We showed that creation of a trailing tail (Magellanic Stream) and a leading stream (Leading Arm) is quite a common feature of the LMC–SMC–MW interaction, and such structures were modeled across the entire range of halo flattening values. However, important differences exist between the models, concerning density distribution and kinematics of H I, and also dynamical evolution of the Magellanic System over the last 4 Gyr. In contrast to Murai & Fujimoto (1980), Gardiner et al. (1994) or Lin et al. (1995), the Clouds do not have to be gravitationally bound to each other for the entire evolutionary period to produce the matter distribution that is in agreement with currently available H I data on the Magellanic System.

Overall agreement between the modeled and observed distribution of neutral hydrogen in the System is quantified by the fitness of the models. The fitness value is returned by a fitness function, that performs a very detailed evaluation of every model (Appendix B). Analysis of fitness as function of the halo flattening parameter q indicates, that the models assuming oblate DM halo of MW (models A) allow for better satisfaction of H I observations than models with other halo configurations.

We did not involve surveys of stellar populations in the Magellanic System into the process of fitness calculation. It is due to a nature of test–particle models that do not allow for distinguishing between stellar and gaseous content of studied systems. However, we still have to face one of the most interesting observational facts connected to the Magellanic Clouds – absence of stars in the Magellanic Stream (Van den Bergh 2000) – because both LMC and SMC contain stellar populations, and so every structure emanating from the Clouds should be contaminated by stars. It is an additional constraint on the models. It cannot be involved in fitness calculation because of the limits of our numerical code, but has to be taken into account.

Stellar populations of SMC are very young and the mass fraction in the form of stars is extremely low. Our models show that evolution of the Magellanic Stream has been lasting 2 Gyr at least (models B). Thus, the fraction of matter in the Magellanic Stream, that is of SMC origin, was torn off before significant star formation bursts occurred in SMC, and stars should not be expected in the Stream. Nevertheless, we found both LMC and SMC matter in the Magellanic Stream for every model of the System. Similarly to the case of SMC, if the LMC star formation activity was increased after the matter transport into the Magellanic Stream was triggered, stars would be missing in the Stream naturally. Such a scenario is doubtful though. Observational studies argue for a massive star formation burst started in LMC at ≈ -3 Gyr (see Van den Bergh 2000). But only presence of a prolate halo of MW (models C) enabled evolution of the Stream that began before the mentioned epoch. However, our results concerning LMC and SMC orbits introduced another acceptable solution to the problem of missing stars. We showed that evolution of the Clouds in aspherical MW DM halos (models A and C) does not lead to extremely close encounters disturbing inner parts of the LMC disk ($r_{\rm disk} < 5$ kpc). Since the distribution of gaseous matter in galaxies is typically more extended than the stellar content, the Magellanic Stream matter coming from outer regions of the Clouds does not necessarily have to contain a stellar fraction.

Previous discussion of stellar content of the Magellanic System supports discrimination of the configurations with nearly spherical halos (models B) that was discovered by the GA search. On the other hand many papers on the dynamical evolution of the Magellanic Clouds dealing with a spherical MW halo (Murai & Fujimoto 1980, Gardiner et al. 1994, Bekki & Chiba 2005) argue, that the observed massive LMC star formation bursts 3 Gyr ago was caused by close LMC–SMC encounters. Our models B show close approaches of the Clouds $\Delta r \approx 10$ kpc at around the mentioned time. For aspherical halos, such encounters do not induce the formation of particle streams. However, close LMC–MW and SMC–MW encounters appeared to be efficient enough to trigger massive matter redistribution in the System leading to formation of the observed structures. Then, they could also be responsible for triggering of star burst.

Acknowledgements. The authors gratefully acknowledge the support by the Czech–Austrian cooperation scheme AKTION (funded by the Austrian Academic Exchange Service ÖAD and by the program Kontakt of the Ministery of Education of the Czech Republic) under grant A–13/2005, by the Institutional Research Plan AV0Z10030501 of the Academy of Sciences of the Czech Republic and by the project LC06014 Center for Theoretical Astrophysics. We also thank Christian Brüns who kindly provided excellent observational data, and Matthew Wall for his unique C++ library for building reliable genetic algorithm schemes.

References

Bekki, K., Chiba, M. 2005, MNRAS, 356, 680–702

Binney, J. 1977, MNRAS, 181, 735–746

Binney, J., Tremaine, S. D. 1987, "Galactic Dynamics", Princeton University Press

Bosma, A. 1981, AJ, 86, 1825–1846

Brüns, C., Kerp, J., Staveley–Smith, L., et al. 2004, A & A, 432, 45–67

Byrd, G., Valtonen, M., McCall, M., Innanen, K. 1994, AJ, 107, 2055–2057

Chandrasekhar, S. 1943, ApJ, 97, 255–262

Connors, T. W., Kawata, D., Gibson, B. K. 2005, astro–ph/0508390, submitted to MNRAS

Dubinski, J., Carlberg, R. G. 1991, ApJ, 378, 496–503

Frenk, C. S., White, S. D. M., Davis, M., Efstathiou, G. 1988, ApJ, 327, 507–525

Fujimoto, M., Sofue, Y. 1976, A & A, 47, 263–292

Gardiner, L. T., Sawa, T., Fujimoto, M. 1994, MNRAS, 266, 567–582

Gardiner, L. T., Noguchi, M. 1996, MNRAS, 278, 191–208

Goldberg, D. E. 1989, "Genetic algorithms in search, optimization and machine learning", Addison–Wesley

Heller, P., Rohlfs, K. 1994, A & A, 291, 3, 743–753

Helmi, A. 2004, MNRAS, 351, 2, 643–648

Hindman, J. V., Kerr, F. J., McGee, R. X. 1963, Australian J. Phys., 16, 570

Holland, J. H. 1975, "Adaptation in natural and artificial systems. An introductory analysis with applications to biology, control and artificial intelligence", University of Michigan Press

Ibata, R., Lewis, G. F., Irwin, M., et al. 2001, ApJ, 551, 294–311

Irwin, M. J., Demers, S., Kunkel, W. E. 1990, AJ, 99, 191–200

Kazantzidis, S., Kravtsov, A.V., Zentner, A.R., Allgood, B. et al. 2004, ApJ, 611, L73–L76

Kroupa, P., Bastian, U. 1997, New Astron., 2 (1997), 77–90

Kroupa, P., Theis, C., Boily, C. M. 2005, A & A, 431, 517–531

Lin, D. N. C., Lynden–Bell, D. 1977, MNRAS, 181, 59–81

Lin, D. N. C., Lynden–Bell, D. 1982, MNRAS, 198, 707–721

Lin, D. N. C., Jones, B. F., Klemola, A. R. 1995, ApJ, 439, 652–671

Mastropietro, C., Moore, B., Mayer, L., et al. 2005, MNRAS, 363, 2, 509–520

Mathewson, D. S., Cleary, M. N., Murray, J. D. 1974, ApJ, 190, 291–296

Mathewson, D. S., Schwarz, M. P., Murray, J. D. 1977, ApJ, 217, L5–L8

Mathewson, D. S., Wayte, S. R., Ford, V. L., Ruan, K. 1984, PASA, 7, 1, 19–25

McLaughlin, D. E. 1999, ApJ, 512, L9–L12

Meurer, G. R., Bicknell, G. V., Gingold, R. A. 1985, PASA, 6, 2, 195–198

Murai, T., Fujimoto, M. 1980, PASJ, 32, 581–603

Murai, T., Fujimoto, M. 1984, Proceedings of the IAU Symposium No. 108, Dordrecht, D. Reidel Publishing Co., 115–123

Olling, R. P., Merrifield, M. R. 2000, MNRAS, 311, 2, 361–369

Ostriker, J. P., Peebles, P. J. E., Yahil, A. 1974, ApJ, 193, 2, L1–L4

Peñarrubia, J., Just, A., Kroupa, P. 2004, MNRAS, 349, 2, 747–756

Rubin, V. C., Burstein, D., 1985, ApJ, 297, 423–435

Sofue, Y. 1994, PASJ, 46, 4,431–440

Theis, Ch. 1999, Rev. Mod. Astron., 12, 309

Theis, Ch., Kohle, S. 2001, A & A, 370, 365–383

Toomre, A., Toomre, J. 1972, ApJ, 178, 623–666

Van den Bergh, S. 2000, "The galaxies of the Local Group", Cambridge University Press

Wahde, M. 1998, A & A, 132, 417–429

Wannier, P., Wrixon, G. T. 1972, ApJ, 173, 119

Wannier, P., Wrixon, G. T., Wilson, R. W. 1972, A & A, 18, 224

Zentner, A. R., Kravtsov, A. V., Gnedin, O. Y., Klypin, A. A., 2005, ApJ, 629, 219–232

Zwicky, F. 1933, Helvetica Physica Acta, 6, 110–127

Appendix A: Dynamical Friction

If the distribution function in velocity space is axisymmetric, the zeroth order specific friction force is (Binney 1977):

$$F^i_{\mathrm{DF}} = -\frac{2\sqrt{2\pi}\rho_{\mathrm{h}}(R,z)G^2M_{\mathrm{S}}\sqrt{1-e_{\upsilon}{}^2}\ln\Lambda}{\sigma_R{}^2\sigma_z}B_R\upsilon_i, \tag{A.1}$$

$$F^z_{\mathrm{DF}} = -\frac{2\sqrt{2\pi}\rho_{\mathrm{h}}(R,z)G^2M_{\mathrm{S}}\sqrt{1-e_{\upsilon}{}^2}\ln\Lambda}{\sigma_R{}^2\sigma_z}B_z\upsilon_z, \tag{A.2}$$

where $i = x, y$ and (σ_R, σ_z) is the velocity dispersion ellipsoid with ellipticity $e_{\upsilon}{}^2 = 1 - (\sigma_z/\sigma_R)^2$, $\ln\Lambda$ is the Coulomb logarithm (Chandrasekhar 1943) of the halo, M_{S} is the satellite mass and

$$B_R = \int_0^{\infty}\frac{\exp\left(-\frac{\upsilon_R^2/2\sigma_R^2}{1+q} - \frac{\upsilon_z^2/2\sigma_R^2}{1-e_{\upsilon}^2+q}\right)}{(1+q)^2(1-e_{\upsilon}^2+q)^{1/2}}dq, \tag{A.3}$$

$$B_z = \int_0^{\infty}\frac{\exp\left(-\frac{\upsilon_R^2/2\sigma_R^2}{1+q} - \frac{\upsilon_z^2/2\sigma_R^2}{1-e_{\upsilon}^2+q}\right)}{(1+q)(1-e_{\upsilon}^2+q)^{3/2}}dq, \tag{A.4}$$

where (υ_R, υ_z) are the components of the satellite velocity in cylindrical coordinates.

Appendix B: Fitness function

The behavior of the 3 D test–particle model of the Magellanic System is determined by a large set of initial conditions and parameters that can be viewed as a point (individual) in the system's high–dimensional parameter space. In the case of our task, the fitness of an individual means the ability of the numerical model to reproduce the observed H I distribution in the Magellanic Clouds if the individual serves as the input parameter set for the model. It is well known, that proper choice for FF is critical for the efficiency of GA and its convergence rate to quality solutions. After extended testing, we devised a three–component FF scheme. In order to discover possible unwanted dependence of our GA on the specific choice for the FF, both the following FF definitions were employed:

$$FF_a = FF_1 \cdot FF_2 \cdot FF_3, \tag{B.1}$$

$$FF_b = \frac{\sum\limits_{i=1}^{i=3} c_i \cdot FF_i}{\sum\limits_{i=1}^{i=3} c_i}, \tag{B.2}$$

where the components FF_1, FF_2 and FF_3 reflect significant features of the observational data and $c_1 = 1.0$, $c_2 = 4.0$ and $c_3 = 4.0$ are weight factors. Both the FFs return values from the interval $\langle 0.0, 1.0 \rangle$.

FF compares observational data with its models. In order to do that, resulting particle distribution has to be treated as neutral hydrogen and converted into H I emission maps for the defined radial velocity channels. In the following paragraphs we briefly introduce both the observed and modeled data processing.

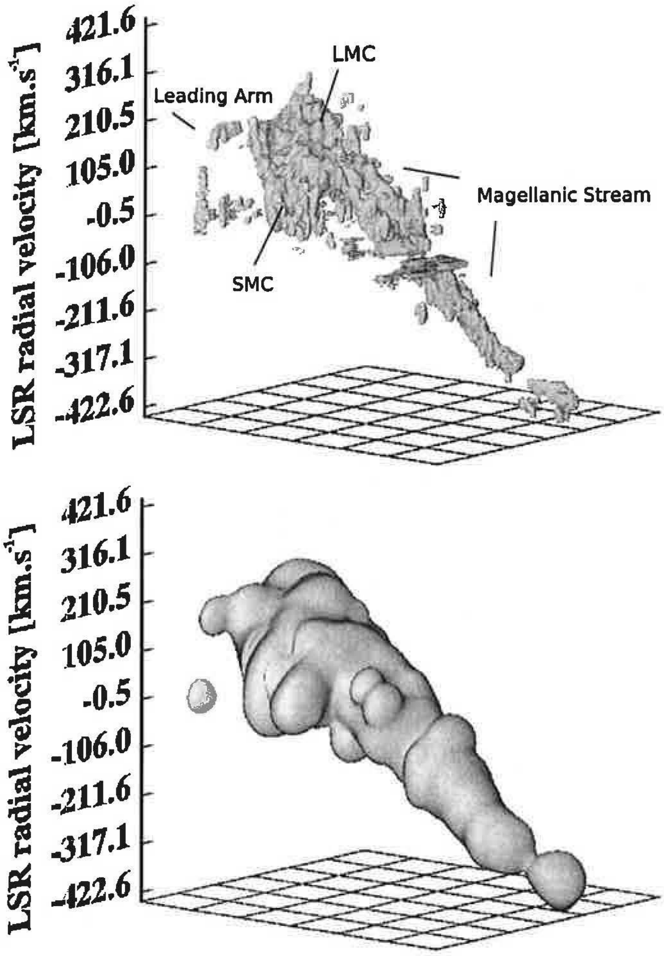

Fig. B.1. The figure depicts the original 3 D H I data cube by Brüns et al. (2005) (upper plot) together with the resulting data after median and Fourier filtering. Both images offer 3 D visualization of the column density isosurface $\Sigma_{\mathrm{H\,I}} = 0.2 \cdot 10^{18}\,\mathrm{cm}^{-2}$.

It was shown by Gardiner et al. (1994) and Gardiner & Noguchi (1996) that the overall H I distribution in the Magellanic System (Magellanic Stream, Leading Arm) can be considered a tidal feature. Following that result, an elaborate scheme of the original data (Brüns et al. 2005) manipulation was devised to emphasize large–scale features of the Magellanic H I distribution on one hand, and suppress small–scale structures on the other hand, since they originate in physical processes missing in our simple test–particle model. The observational data are stored as Flexible Image Transport System (FITS) format which let us apply standard image processing methods naturally. Fourier filter was selected for our task. It represents a frequency domain filter, and so it allows for an excellent control over the scale range of the image's structures to be conserved or filtered out. We removed the wavelengths below the limit of ≈ 10° projected on the sky–plane. The performance of Fourier filters suffers from the presence of abrupt changes of intensity, such as edges and isolated pixels. In order to enhance the efficiency of frequency filtering, it was preceded by an application of a spatial median filter to smear the original image on small scales. Subsequently, the H I column density is normalized. The resulting 3 D H I column density data cube together with the original data by Brüns et al. (2005) can be seen in Fig. B.1. To compare the modeled particle distribution with H I observations, we convert the distribution to a 3 D FITS image of column densities that are proportional to particle counts, since all the test–particles have the same weight factor assigned. Then, we have to interpolate missing data which is due to a limited number of particles in our simulations. Finally, the column density is normalized to the maximal value.

After discussing the data processing and manipulation, we will introduce the individual FF components FF_1, FF_2 and FF_3.

B.1. FF_1

The observed H I LSR radial velocity profile measured along the Magellanic Stream is a notable feature of the Magellanic System. It shows a linear dependence of LSR radial velocity on Magellanic Longitude, and a high negative velocity of $-400\,\mathrm{km\,s^{-1}}$ is reached at the Magellanic Stream far tip (Brüns et al. 2005). From the studies by Murai & Fujimoto (1980), Gardiner et al. (1994) and our modeling of various Magellanic evolutionary scenarios we know, that the linearity of the Magellanic Stream velocity profile shows low sensitivity to variation of initial conditions of the models. On the other hand, the slope of the LSR radial velocity function is a very specific feature, strongly dependent especially on the features of the orbital motion of the Clouds. Therefore, it turned out to be an efficient approach to test whether our modeled particle distribution was able to reproduce the high negative LSR redial velocity tip of the Magelanic Stream. Then, the first FF component FF_1 was defined as follows:

$$FF_1 = \frac{1}{1 + \left|\frac{v^{\mathrm{obs}}_{\mathrm{min}} - v^{\mathrm{mod}}_{\mathrm{min}}}{v^{\mathrm{obs}}_{\mathrm{min}}}\right|}, \tag{B.3}$$

where $v^{\mathrm{obs}}_{\mathrm{min}}$ and $v^{\mathrm{mod}}_{\mathrm{min}}$ are the minima of the observed LSR radial velocity profile of the Magellanic Stream and its model, respectively.

B.2. FF_2 and FF_3

The FF components FF_2 and FF_3 compare the observed and modeled H I column density distributions in the Magellanic System for 64 separate LSR radial velocity channels of width $\Delta v = 13.2\,\mathrm{km\,s^{-1}}$. For every velocity channel, H I column density values are available for $(64 \cdot 128)$ pixels covering the entire System. The above introduced 3 D data was obtained by modification of the original high–resolution H I data–cube by Brüns et al. (2005). Since test–particle model is not capable to reproduce small–scale features of the explored system, filtering and reduction of resolution of the original data were necessary prior to its use for the purpose of our GA search.

The second FF component analyzes whether there is a modeled H I emission present at the positions and LSR radial velocities where it is observed. Thus, we measure the relative spatial coverage of the System observed in H I emission by the modeled matter distribution for every LSR radial velocity channel. No attention is paid to specific H I column density values here. We only test, whether both modeled and observed emission is present at the same pixel of the position–velocity space. It can be expressed as

$$FF_2 = \frac{\sum\limits_{i=1}^{N_v}\sum\limits_{j=1}^{N_y}\sum\limits_{k=1}^{N_x} pix^{\mathrm{obs}}_{ijk} \cdot pix^{\mathrm{mod}}_{ijk}}{MAX\left(\sum\limits_{i=1}^{N_v}\sum\limits_{j=1}^{N_y}\sum\limits_{k=1}^{N_x} pix^{\mathrm{obs}}_{ijk}, \sum\limits_{i=1}^{N_v}\sum\limits_{j=1}^{N_y}\sum\limits_{k=1}^{N_x} pix^{\mathrm{mod}}_{ijk}\right)}, \tag{B.4}$$

where $pix^{\mathrm{obs}}_{ijk} \in \{0, 1\}$ and $pix^{\mathrm{mod}}_{ijk} \in \{0, 1\}$ indicate whether there is matter detected at the position [i, j, k] of the 3 D data on the observed and modeled Magellanic System, respectively. $N_v = 64$ is the number of separate LSR radial velocity channels in our data. $(N_x \cdot N_y) = (64 \cdot 128)$ is the total number of positions on the sky–plane for which observed and modeled H I column density values are available.

This binary comparison between the observed and modeled data introduces a problem of pure noise pixels present in the observed data cube, because they posses the same weight as the other data, despite their typically very low intensity. However, our treatment of the original high–resolution data by Brüns et al. (2005) involves spatial median filtering. It smears abrupt intensity changes and removes isolated pixels which handles the problem of pure–noise data pixels naturally. The subsequent Fourier filtering decreases the data resolution significantly, and that also strongly suppresses the influence of original noise pixels.

As the last step we compare the modeled matter density distribution to the observation. To do that, both modeled and observed H I column density values are scaled relatively to their maxima to introduce dimensionless quantities. Then, we get

$$FF_3 = \frac{1}{N_v \cdot N_x \cdot N_y} \sum_{i=1}^{N_v}\sum_{j=1}^{N_y}\sum_{k=1}^{N_x} \frac{1}{1 + \left|\sigma^{\mathrm{obs}}_{ijk} - \sigma^{\mathrm{mod}}_{ijk}\right|}, \tag{B.5}$$

where $\sigma^{\mathrm{obs}}_{ijk}$, $\sigma^{\mathrm{mod}}_{ijk}$ are normalized column densities measured at the position [j, k] of the i–th velocity channel of the observed and modeled data, respectively.